UNIVERSITY OF CRETE
DEPARTMENT OF PHYSICS

A study of the impact of aerosols on the energy budget of the atmosphere using satellite measurements of climatic parameters and computer models

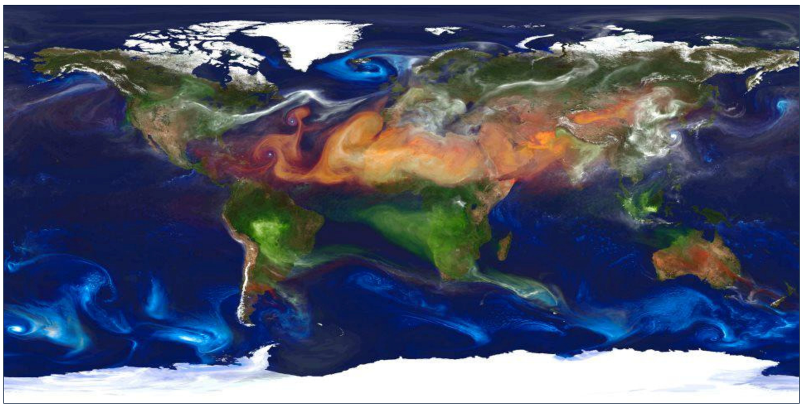

by

Nikolaos Benas

Thesis

submitted for the Degree of Doctor of Philosophy in Physics

Herakleion, 2013

University of Crete
Department of Physics

A study of the impact of aerosols on the energy budget of the atmosphere using satellite measurements of climatic parameters and computer models

by

Nikolaos Benas

Thesis

submitted for the Degree of Doctor of Philosophy in Physics

PhD Thesis

A study of the impact of aerosols on the energy budget of the atmosphere using satellite measurements of climatic parameters and computer models

Thesis Author:	N. Benas
Thesis Supervisor:	I. M. Vardavas
Thesis Committee:	N. Hatzianastassiou
	M. Kanakidou
	C. Matsoukas
	N. Mihalopoulos
	I. Papadakis
	X. Zotos
	I. M. Vardavas

Acknowledgements

I would like to thank my supervisor, Prof. Ilias M. Vardavas, for his valuable guidance, support and encouragement. Our meetings and discussions were always fruitful and motivating.

I am also grateful to Dr. Nektarios Chrysoulakis and the Regional Analysis Division of the Foundation for Research and Technology–Hellas, Institute of Applied and Computational Mathematics, for the continuous support throughout my research and the opportunity to expand my research area and interests.

I also wish to express my sincere thanks to Profs. N. Mihalopoulos and M. Kanakidou of the University of Crete, Department of Chemistry, for their support and for providing measurements from the Finokalia station.

Furthermore, I would like to thank Prof. N. Hatzianastassiou of the University of Ioannina, Department of Physics, and Prof. C. Matsoukas of the University of the Aegean, Department of Environment, for their helpful advice and suggestions.

I would also like to thank Dr. Andrew C. Banks of the Hellenic Centre for Marine Research, for making available observations from the AERONET and meteorological stations at HCMR in Crete.

Finally, I am grateful to my friends for their constant encouragement and support. I am also greatly indebted to my family, and particularly my parents, for their unwavering love, support and belief in me. It is to them that I dedicate this work.

Περίληψη

Ένα ντετερμινιστικό φασματικό μοντέλο διάδοσης ακτινοβολίας χρησιμοποιήθηκε για τον υπολογισμό του ισοζυγίου ακτινοβολίας στην ατμόσφαιρα της Γης, με βάση δορυφορικά δεδομένα αιωρούμενων σωματιδίων και ατμοσφαιρικών παραμέτρων, σε υψηλή χωρική ανάλυση και συχνότητα ανάκτησης, από τον αισθητήρα MODIS (Moderate Resolution Imaging Spectroradiometer).

Η μελέτη εστιάστηκε στην εκτίμηση της άμεσης επίδρασης (DRE) των αιωρούμενων σωματιδίων στις συνιστώσες του ισοζυγίου ακτινοβολίας. Λόγω της υψηλής χωρικής και χρονικής μεταβλητότητας των αιωρούμενων σωματιδίων, η DRE, η οποία αποτελεί κρίσιμη συνιστώσα της συνολικής επίδρασης των αιωρούμενων σωματιδίων στο κλίμα, χαρακτηρίζεται επίσης από μεγάλη μεταβλητότητα.

Εξετάστηκε επίσης η άμεση επίδραση των αιωρούμενων σωματιδίων στο ρυθμό φωτοδιάσπασης του τροποσφαιρικού όζοντος, $J(O^1D)$, ο οποίος αποτελεί βασικό μηχανισμό μείωσής του. Σημειώνεται ότι το τροποσφαιρικό όζον συνεισφέρει στο παγκόσμιο φαινόμενο του θερμοκηπίου. Έτσι, ο $J(O^1D)$ είναι μία σημαντική κλιματική παράμετρος, που πρέπει να μελετηθεί μέσω μοντελοποίησης, λόγω της απουσίας σταθμών μετρήσεων, και της πραγματοποίησής του σε μήκη κύματος μικρότερα από 330 nm, όπου η επίδραση των αιωρούμενων σωματιδίων είναι σημαντική.

Αξιολογήθηκε επίσης η άμεση επίδραση των αιωρούμενων σωματιδίων στη δυνητική εξάτμιση, η οποία ισούται με την πραγματική εξάτμιση σε ρηχές λίμνες, και αποτελεί καθοριστική παράμετρο του υδρολογικού κύκλου. Η DRE μειώνει τη δυνητική εξάτμιση μέσω της μείωσης της ηλιακής ακτινοβολίας που φτάνει στην επιφάνεια της Γης.

Οι προσομοιώσεις του μοντέλου πραγματοποιήθηκαν για την περίοδο 2000–2010, σε διάφορες περιοχές της Ελλάδας, που χαρακτηρίζονται από υψηλές συγκεντρώσεις αιωρούμενων σωματιδίων, με μοναδικά χαρακτηριστικά εποχικής διακύμανσης και προέλευσης. Δύο ερευνητικοί σταθμοί στην Κρήτη (ΕΛΚΕΘΕ/AERONET και Φινοκαλιά) επιλέχθηκαν λόγω της καταλληλότητας του νησιού για τη μελέτη των επεισοδίων σκόνης από τη Σαχάρα, τα οποία είναι συχνά στην ευρύτερη Ανατολική Μεσόγειο, και της διαθεσιμότητας επίγειων

μετρήσεων, που χρησιμοποιήθηκαν ως συμπληρωματικά δεδομένα εισόδου στο μοντέλο και για την αξιολόγηση των αποτελεσμάτων. Προσομοιώσεις πραγματοποιήθηκαν και πάνω από τέσσερεις λίμνες στην Κεντρική Ελλάδα, που αποτελούν τους κύριους ταμιευτήρες παροχής νερού στην Αθήνα, για την αξιολόγηση της επίδρασης των αιωρούμενων σωματιδίων στη δυνητική εξάτμιση.

Πραγματοποιήθηκε ανάλυση και επεξεργασία δεδομένων αιωρούμενων σωματιδίων, νεφών και ατμοσφαιρικών παραμέτρων από το MODIS, τα οποία είναι διαθέσιμα από το 2000, σε ανάλυση 10 km×10 km και 5 km×5 km, και χρησιμοποιήθηκαν ως δεδομένα εισόδου. Το μοντέλο λαμβάνει υπόψη όλες τις φυσικές παραμέτρους και διαδικασίες που επηρεάζουν σημαντικά τη διάδοση της ηλιακής ακτινοβολίας. Η DRE υπολογίζεται στην επιφάνεια της Γης, στο εσωτερικό της ατμόσφαιρας και στην κορυφή της.

Η κατερχόμενη ηλιακή ακτινοβολία που υπολογίστηκε από το μοντέλο, συγκρήθηκε επιτυχώς με επίγεια δεδομένα από τους σταθμούς ΕΛΚΕΘΕ και Φινοκαλιάς, όπως και ο J(O^{1}D) με βάση αντίστοιχα δεδομένα από τη Φινοκαλιά. Η ανάλυση της επίδρασης των αιωρούμενων σωματιδίων στο ισοζύγιο ακτινοβολίας, στο J(O^{1}D) και στη δυνητική εξάτμιση πραγματοποιήθηκε σε στιγμιαία/μέση ημερήσια, εποχική και ετήσια βάση. Ποσοτικοποιήθηκε επίσης η επίδραση των επεισοδίων σκόνης, ενώ εκτιμήθηκαν και αξιολογήθηκαν οι τάσεις μεταβολής κατά την εξεταζόμενη περίοδο, με βάση αντίστοιχες τάσεις και επιδράσεις παραγόντων, που περιλαμβάνουν τα αιωρούμενα σωματίδια, τα νέφη και το ολικό όζον.

Τα αποτελέσματα δείχνουν τάσεις μείωσης στα αιωρούμενα σωματίδια και στην επίδρασή τους, σε όλες τις περιοχές που εξετάστηκαν. Ωστόσο, οι αλλαγές στο ισοζύγιο ακτινοβολίας καθορίζονται και από άλλους παράγοντες: η αύξηση της νεφοκάλυψης στο σταθμό του ΕΛΚΕΘΕ αντιστάθμισε τα αποτελέσματα της μείωσης της DRE. Παρόμοια, αν και η DRE στο J(O^{1}D) μειώθηκε, ο J(O^{1}D) δεν αυξήθηκε όπως αναμενόταν, λόγω αύξησης του ολικού όζοντος στην ατμόσφαιρα. Η παρουσία των αιωρούμενων σωματιδίων μειώνει τη δυνητική εξάτμιση κατά περίπου 0.5 mm σε μέση ημερήσια βάση, φτάνοντας τα 2 mm το καλοκαίρι. Ωστόσο, μία τάση μείωσης των αιωρούμενων σωματιδίων βρέθηκε σε όλες τις λίμνες που εξετάστηκαν, κατά την περίοδο 2001–2010.

Ανάλογα με τη διαθεσιμότητα των δεδομένων εισόδου του μοντέλου, η μεθοδολογία που αναπτύχθηκε στην παρούσα εργασία μπορεί να εφαρμοστεί σε οποιαδήποτε περιοχή ειδικού ενδιαφέροντος στον πλανήτη.

Abstract

A deterministic spectral shortwave radiative transfer model was used for the computation of the Earth's atmospheric radiation budget, based on high temporal and spatial resolution satellite data of aerosols and atmospheric climatic parameters from the Moderate Resolution Imaging Spectroradiometer (MODIS) sensor.

The study focused on the evaluation of the aerosol direct radiative effect (DRE) on the radiation budget components. Due to the high spatial and temporal variability of aerosols, the DRE, which constitutes a crucial component of the overall effect of aerosols on climate, is thus also highly variable.

The aerosol direct effect on the tropospheric ozone photolysis rate, $J(O^1D)$, was also examined, being a dominant sink of tropospheric ozone. We note that tropospheric ozone contributes to the global greenhouse effect. Thus, $J(O^1D)$ is an important climatic parameter, which needs to be studied using modelling approaches, due to the scarcity of measuring stations, and because it takes place primarily below 330 nm, a spectral region where the aerosol effect is a key operating factor.

The aerosol direct effect on potential evaporation was also assessed. Potential evaporation equals actual evaporation in shallow lakes, and constitutes a crucial parameter of the hydrological cycle. The aerosol DRE decreases potential evaporation by decreasing the solar radiation reaching the Earth's surface.

The model runs were performed for the period 2000–2010 over several sites in Greece, which are characterised by high aerosol loads, with unique characteristics in terms of seasonal variation and origin. Two research stations in Crete (HCMR/AERONET and Finokalia), were selected due to the appropriateness of the island for studying Saharan dust episodes, which are frequent in the wider Eastern Mediterranean, and the availability of ground–based data for both model supplementary input and validation. The model was also run over four lakes in Central Greece, which constitute the main water supply reservoirs of the city of Athens, for the evaluation of the aerosol

effect on potential evaporation.

MODIS Level 2 data of aerosols, clouds and atmospheric parameters were analysed and processed, and used as input to the model. These data are available since 2000, on a daily basis and at $10\,\mathrm{km}\times 10\,\mathrm{km}$ and $5\,\mathrm{km}\times 5\,\mathrm{km}$ spatial resolution. The model takes into account all physical parameters and processes that affect significantly the solar radiation transfer. The aerosol DRE is determined at the Earth's surface, within the atmosphere and at the top of the atmosphere.

The model output downwelling shortwave radiation was successfully validated against ground–based measurements at the HCMR and Finokalia stations and at the four lakes in Central Greece. The model output $J(O^1D)$ was successfully validated against Finokalia station measurements. The analysis of the aerosol DRE on the model radiation budget, $J(O^1D)$ and potential evaporation was performed on an instantaneous/daily mean, seasonal and inter–annual basis. Dust event effects were also quantified, and trends during the period examined were assessed and evaluated in terms of corresponding trends and effects of operating factors, including aerosols, clouds and total ozone.

Results show a decreasing trend in aerosols and the corresponding DRE over all sites examined. Changes in the radiation budget components, however, are also controlled by other factors; an increase in cloud fraction over HCMR station counterbalanced the effect that the DRE reduction would have caused. Similarly, although the DRE on $J(O^1D)$ has decreased, $J(O^1D)$ has not increased as was expected, due to an increase in total atmospheric ozone. The presence of aerosols reduces potential evaporation by about 0.5 mm on a mean daily basis, reaching up to 2 mm in summer. However, a decreasing trend in the aerosol load and DRE was found over all lakes during the period 2001–2010.

Depending on the availability of model input data, the methodology developed in this study is applicable to any region of specific interest over the globe.

Contents

Introduction

Climate change predictions require knowledge of all the factors that control climate variability globally. Although the effects of greenhouse gases are known relatively accurately, due to their long lifetime and homogeneous global distribution, the effects of aerosols on climate remain uncertain due to their variability. An adequate representation of aerosol impacts on climate is required for more reliable predictions of future climate change, under different future emission scenarios.

The science of atmospheric aerosols has advanced significantly since the first observations of aerosol effects in the late 18th century, when volcanic ashes were linked to solar dimming and reduced air temperature (Franklin, 1784). However, until a few decades ago, the lack of sufficient aerosol measurements and uncertainties regarding their actual effects resulted in erroneous conclusions and exaggerated estimations of aerosol effects on climate (Weart, 2008).

The simultaneous development of both satellite and ground–based observations, in situ measurements and computational efficiency, improved aerosol monitoring and led the scientific community to a consensus regarding the categorization of the aerosol effects and the importance of their accurate estimation. However, a high degree of uncertainty remains; the Intergovernmental Panel on Climate Change (IPCC) Fourth Assessment Report (AR4) concluded that uncertainties associated with changes in Earth's radiation budget due to aerosols constitute the largest uncertainty in the radiative forcing of climate change, among factors that were assessed over the industrial period (IPCC, 2007).

Aerosol inherent characteristics, including their lifetime, which spans from a few days to a few weeks, and the spatial and temporal inhomogeneity of their sources and sinks, maintain this uncertainty. This highlights the importance for their continual and intensive spatial and temporal monitoring. Networks of ground–based aerosol monitoring stations offer high temporal resolution, but not adequate spatial distribution. Global aerosol monitoring can only be achieved using satellite derived measurements.

Polar orbiting satellite sensors scan the Earth's surface in 1–2 days, solving the problem of global coverage. However, the spatial resolution remains a crucial parameter: due to the highly variable aerosol distributions, the aerosol effects are much more pronounced on regional scales than on the global scale. In fact, although several models show good agreement in their representation of the global mean Aerosol Optical Thickness (AOT), which in general also agrees with satellite–derived values, large differences exist in model simulations of regional distributions of AOT (Remer et al., 2009). It can thus be insufficient or even misleading to place too much emphasis on a global average.

The Moderate Resolution Imaging Spectroradiometer (MODIS), developed for the National Aeronautics and Space Administration (NASA) Earth Observing System (EOS) Terra and Aqua satellites, provides a great opportunity for aerosol research. In particular, complete spectral coverage in key atmospheric bands has spurred the development of new spaceborne algorithms, while moderate but global spatial coverage (10 km × 10 km at nadir for aerosol parameters) allows for the implementation of retrieval algorithms at a higher spatial resolution than has previously been possible (Platnick et al., 2003).

High spatial resolution and global coverage are necessary but insufficient conditions for the assessment of aerosol effects on climate: both aerosol direct (interaction with atmospheric radiation through absorption and scattering) and indirect (modification of cloud properties and lifetime) effects, require additional modelling approaches. In particular, the aerosol direct effect is stronger at the Earth's surface compared to the Top of the Atmosphere (TOA), due to aerosol absorption (e.g. Zhou et al., 2005), also exerting large impacts within the atmosphere, to alter the atmospheric circulation patterns and water cycle (e.g. Remer et al., 2009). For the estimation of the aerosol direct effect and its consequences, the description of the radiation field interaction with aerosols and its subsequent modification, using an appropriate radiative transfer scheme, is also necessary.

The aerosol direct radiative effect modifies the solar radiation field in the atmosphere and has also an impact on other important atmospheric processes, including atmospheric photochemistry and the hydrological cycle. Specifically, the aerosol direct effect, being a key operating factor in the ultraviolet spectral region, affects the ultraviolet radiation reaching the Earth's surface, and consequently the tropospheric ozone photolysis rate, $J(O^1D)$. The importance of this effect and the need for its accurate assessment, are highlighted by the fact that tropospheric ozone acts both as an important greenhouse gas and as an indirect controller of greenhouse gas lifetimes (IPCC, 2007). Furthermore, the solar radiation reaching the Earth's surface is the dominant factor controlling the evaporation rate from oceans and lakes, which constitutes the main mechanism for the return of water to the atmosphere. By modifying the solar radiation field, the presence of aerosols will also modify this rate and consequently affect the water cycle. This effect is expected to be important especially in areas with high aerosol loads and limited water resources.

In the present work, high resolution MODIS daily data of aerosols, clouds and atmospheric parameters are used for the first time as input to a Shortwave (SW) spectral radiative transfer model, for the computation of the atmospheric radiation budget components and the corresponding aerosol direct radiative effect (DRE) and its anthropogenic component (direct radiative forcing, DRF) at $10\,\mathrm{km} \times 10\,\mathrm{km}$ spatial resolution. The aerosol DRE and DRF are computed in the SW range of wavelengths, since the corresponding effect is much smaller in the Longwave (LW), due to the rapid decrease of aerosol extinction with increasing wavelengths for most aerosol types. The FORTH radiative transfer model (Vardavas and Taylor, 2011), used here, has also been used in numerous studies in the past (e.g. Hatzianastassiou et al., 2005, 2004a,b), typically using climatological data at $2.5° \times 2.5°$ or $1° \times 1°$ latitude–longitude resolution, while it has also been successfully validated using ground–based measurements and intercompared against line–by–line models (Randles et al., 2013). The study focuses on the island of Crete, which is representative of the wider eastern Mediterranean basin, a region of high interest in terms of aerosol research, due to the variety of aerosol origins, mixture and composition (e.g. Lelieveld et al., 2002). The availability of MODIS data on a daily basis for over a decade (2000–present), allows the examination of both long–term trends and daily variations, including Saharan dust events, which prevail in this region.

Further to the study of the aerosol direct radiative effect per se, the consequences on $J(O^1D)$ and on the evaporation rate are also examined for the first time at this high spatial resolution. Specifically, $J(O^1D)$ is computed using the FORTH model, and the impact of aerosols is estimated and analysed. The aerosol direct effect and its long–term trends on potential evaporation are also investigated over four lakes in Greece, which constitute the main water supply of Athens.

The results presented in this study give insight to the aerosol direct effect and its consequences on aspects of atmospheric photochemistry and the water cycle, over a region very sensitive to climate change, due to the proximity of Sahara and the influence of the North Atlantic Oscillation, both of which control atmospheric moisture in the region. In addition, this approach offers the possibility of discriminating spatial patterns and procedures not evident using lower resolution data, in any place of interest, where MODIS satellite data are available.

In the chapters that follow, a description of the aerosol characteristics, properties and effects is first given, focusing on the direct effect, the importance of radiative transfer models for its evaluation and the eastern Mediterranean, as a region of high interest for its study (Chapter 1). The advances in aerosol remote sensing, both ground–based and satellite, which led to the present–day sophisticated monitoring instruments, are described in Chapter 2, along with the MODIS sensor and the corresponding products used here. Ground–based stations in Crete, related to aerosol monitoring and used for validation purposes, and the procedure used for the MODIS data pre–processing, are also described in this chapter. Chapter 3 provides a detailed description of the FORTH radiative transfer model, including its assumptions, approximations and accuracy. Chapter 4 presents the model results regarding the aerosol direct effect: validation of model output against ground measurements, sensitivity analysis, the aerosol direct effect during dust events, seasonal variation and trends. Estimation and validation of the aerosol effect on ozone photolysis at the Earth's surface are presented in Chapter 5, together with the effect of total column ozone on the photolysis and a trend analysis. Finally, Chapter 6 presents the methodology used for the estimation of potential evaporation, the aerosol effect and its trends, separately for each of the four lakes studied.

Bibliography

Franklin, B.: Meteorological Imaginations and Conjectures (Paper Read 1784), Memoirs of the Literary and Philosophical Society of Manchester 2nd ed., 1789, 373–377, 1784.

Hatzianastassiou, N., Fotiadi, A., Matsoukas, C., Pavlakis, K. G., Drakakis, E., Hatzidimitriou, D., and Vardavas, I.: Long–term global distribution of Earth's shortwave radiation budget at the top of atmosphere, Atmospheric Chemistry and Physics, 4, 1217–1235, 2004a.

Hatzianastassiou, N., Katsoulis, B. D., and Vardavas, I.: Global distribution of aerosol direct radiative forcing in the ultraviolet and visible arising under clear skies, Tellus B, 56B, 51–71, 2004b.

Hatzianastassiou, N., Matsoukas, C., Fotiadi, A., Pavlakis, K. G., Drakakis, E., Hatzidimitriou, D., and Vardavas, I.: Global distribution of Earth's surface shortwave radiation budget, Atmospheric Chemistry and Physics, 5, 2847–2867, doi:10.5194/acp-5-2847-2005, 2005.

IPCC: Climate Change 2007 - The Physical Science Basis: Working Group I Contribution to the Fourth Assessment Report of the IPCC, Cambridge University Press, 2007.

Lelieveld, J., Berresheim, H., Borrmann, S., Crutzen, P. J., Dentener, F. J., Fischer, H., Feichter, J., Flatau, P. J., Heland, J., Holzinger, R., Kormann, R., Lawrence, M. G., Levin, Z., Markowicz, K. M., Mihalopoulos, N., Minikin, A., Ramanathan, V., De Reus, M., Roelofs, G. J., Scheeren, H. a., Sciare, J., Schlager, H., Schultz, M., Siegmund, P., Steil, B., Stephanou, E. G., Stier, P., Traub, M., Warneke, C., Williams, J., and Ziereis, H.: Global air pollution crossroads over the Mediterranean., Science, 298, 794–799, doi:10.1126/science.1075457, 2002.

Platnick, S., King, M., Ackerman, S., Menzel, W., Baum, B., Riedi, J., and Frey, R.: The MODIS cloud products: algorithms and examples from

Terra, IEEE Transactions on Geoscience and Remote Sensing, 41, 459–473, doi:10.1109/TGRS.2002.808301, 2003.

Randles, C. A., Kinne, S., Myhre, G., Schulz, M., Stier, P., Fischer, J., Doppler, L., Highwood, E., Ryder, C., Harris, B., Huttunen, J., Ma, Y., Pinker, R. T., Mayer, B., Neubauer, D., Hitzenberger, R., Oreopoulos, L., Lee, D., Pitari, G., Di Genova, G., Quaas, J., Rose, F. G., Kato, S., Rumbold, S. T., Vardavas, I., Hatzianastassiou, N., Matsoukas, C., Yu, H., Zhang, F., Zhang, H., and Lu, P.: Intercomparison of shortwave radiative transfer schemes in global aerosol modeling: results from the AeroCom Radiative Transfer Experiment, Atmospheric Chemistry and Physics, 13, 2347–2379, doi:10.5194/acp-13-2347-2013, 2013.

Remer, L. A., Chin, M., DeCola, P., Feingold, G., Halthore, R., Kahn, R. A., Quinn, P. K., Rind, D., Schwartz, S. E., Streets, D., and Yu, H.: Executive Summary, in: Atmospheric Aerosol Properties and Climate Impacts, A Report by the U.S. Climate Change Science Program and the Subcommittee on Global Change Research, edited by Chin, M., Kahn, R. A., and Schwartz, S. E., National Aeronautics and Space Administration, Washington, D. C., USA, 2009.

Vardavas, I. and Taylor, F.: Radiation and Climate: Atmospheric Energy Budget from Satellite Remote Sensing, International Series of Monographs on Physics, OUP Oxford, 2011.

Weart, S.: The Discovery of Global Warming, New Histories of Science, Technology, and Medicine, Harvard University Press, 2008.

Zhou, M., Yu, H., Dickinson, R. E., Dubovik, O., and Holben, B. N.: A normalized description of the direct effect of key aerosol types on solar radiation as estimated from Aerosol Robotic Network aerosols and Moderate Resolution Imaging Spectroradiometer albedos, Journal of Geophysical Research: Atmospheres, 110, doi:10.1029/2005JD005909, 2005.

Chapter 1

Aerosols in a Changing Climate

1.1 Introduction

The first clues that aerosols, the solid and liquid particles suspended in the atmosphere, might affect the Earth's climate, came from volcanic eruptions, during the 18^{th} and 19^{th} centuries: volcanic dust was reported to dim the sunlight and reduce the air temperature (e.g. Franklin, 1784; Abbot and Fowle, 1913). As usually happens in scientific enquiries, even before the question regarding the interconnection between these phenomena was definitely answered, new questions had already emerged: If volcanic emissions can alter the climate, what about particles from other sources? Could human activity be such a source?

Lack of sufficient scientific data during the first decades of the 20^{th} century prevented researchers from addressing these questions, until almost the 1960s, when public concern started affecting the direction of aerosol research: understanding the interaction between aerosols and clouds, in the hope of manipulating the latter, the effects of contrails from an increasing fleet of jet air planes, airborne particles originating from nuclear weapon tests and ground level air pollution became primary areas of aerosol research. The increased focus on the aerosol pollution effects in urban areas, combined with measurements from both urban and remote sites, raised questions about possible world–wide effects (Weart, 2008).

In the early 1970s, when numerous scientists had already accepted that the regional to global aerosol effects are worth studying in more detail, the new question regarded the sign and magnitude of these effects, and their intercomparison with the corresponding greenhouse gases. First results showed that under specific circumstances, aerosols could produce a warming effect (e.g. Mitchell, 1970; Idso and Brazel, 1977), while the uncertainty on the magnitude of the generally accepted aerosol cooling effect, led to estimations that involved even a possible new ice age (Rasool and Schneider, 1971). Although the even less understood aerosol interaction with clouds (indirect effect, Section 1.2.3) added to the overall uncertainty, by the late 1970s, scientists with better data concluded that greenhouse warming would dominate as a climate forcing agent (Hansen et al., 1978).

In the late 1970s and early 1980s, computer models of aerosol direct effects on solar radiation started contributing to the scientific findings of the field (Section 1.3.1). The verification that sulfate aerosols, originating from volcanoes, could remain in the stratosphere for years, and the new theories of a possible "nuclear winter" (Kondratyev, 1988) and the dinosaur extinction due to a fatal planetary cooling caused by an asteroid impact (Alvarez et al., 1984), led the scientific interest to a planetary–scale viewpoint and awareness. However, this trend also led most scientists to treat aerosols as a globally uniform background, disregarding the spatial variability of aerosol emissions due to human activity (Weart, 2008).

By 1990, it was clear that global climate change was not a matter of CO_2 alone, and the role of aerosols had to be quantitatively estimated (Watson et al., 1990). A shift in viewpoint, now focusing on changes in the energy balance rather than attempting to calculate surface temperature changes only, accompanied by advances in laboratory instrumentation and aerosol remote sensing, led to the current wealth of methods, approaches and data available for aerosol research. While many uncertainties regarding the aerosol role and effects on climate remain (Figure 1.4), it is now clear that even for global–scale studies, the aerosol effects have to be examined on a local to regional scale.

1.2 Aerosol properties and effects

The term "atmospheric aerosol" encompasses a wide range of particle types, which have different compositions, sizes, shapes, and optical properties. Atmospheric aerosol particles are either natural (e.g. desert dust, sea salt, wildfire smoke, volcanic emissions) or anthropogenic (e.g. industrial emissions, combustion of fuels, biomass burning for agriculture, erosion due to land use changes). They are further categorized as primary (directly emitted) and secondary (formed in the atmosphere by gas–to–particle conversion processes, e.g. Seinfeld and Pandis, 2006). Since they are produced mainly at the Earth's surface, they are concentrated at the lowest layers of the troposphere, and usually near their production sources. However, their lifetime, which ranges between a few days and a few weeks, when combined with specific meteorological conditions, can lead to their lifting at several kilometers, and their transportation over long distances. The great variation of the aerosol spatial distribution is caused by the combination of the non–uniform distribution of their sources and sinks, their short lifetime and the different removal processes, which include dry deposition (gravitational settling especially of coarse particles), wet deposition (precipitation) and cloud processing (particles acting as cloud condensation nuclei (CCN)). Aerosols also exist in the stratosphere, originating primarily from volcanic eruptions. Although much less than tropospheric aerosols, their impact can be significant due to their longer lifetime and their global spreading (e.g. Lenoble et al., 2013).

1.2.1 Aerosol properties

The aerosol optical characteristics, which are used for the evaluation of their direct radiative effect, depend on the particles' chemical composition, their size and their shape. In turn, these physical characteristics depend on the aerosol origin, atmospheric processing and transport. This complexity in aerosol characteristics may refer to a single particle, which can be a mixture of different materials, or an aerosol layer, which usually contains particles of different sizes, compositions and origins. In addition, air humidity alters the aerosol optical properties, compared to laboratory measurements.

Aerosol sizes vary from a few molecules (10^{-3} µm) to a few tens of micrometers in radius. However, most of the aerosol mass is contained in the size range 0.05 to 10 µm, while this range also causes the major impact on radiation. According to their size, aerosol particles are categorized roughly into four modes: the nucleation mode comprises particles with diameters up to about 0.01 µm, the Aitken mode spans the size range from about 0.01 to 0.1 µm, the accumulation mode extends from 0.1 to 2.5 µm in diameter, while the coarse mode includes particles with diameter greater than 2.5 µm. Figure 1.1 shows typical examples of aerosol particles in each mode. A more general categorization divides aerosol particles into "fine" and "coarse" modes, with a 2.5 µm diameter separating the two modes. A detailed description of the aerosol size modes, composition and characteristics, can be found in Seinfeld and Pandis (2006).

Figure 1.1 also shows typical number and volume distributions of aerosols. While most particles have radii less than 0.1 µm (100 nm), the majority of the total volume is contributed by particles in the accumulation and coarse modes. For modelling purposes, mathematical expressions are used to represent the aerosol size distribution. The lognormal is a typical distribution, while the bimodal lognormal size distribution assumes a mixture of two different aerosol modes, namely a coarse mode with large particles and a fine

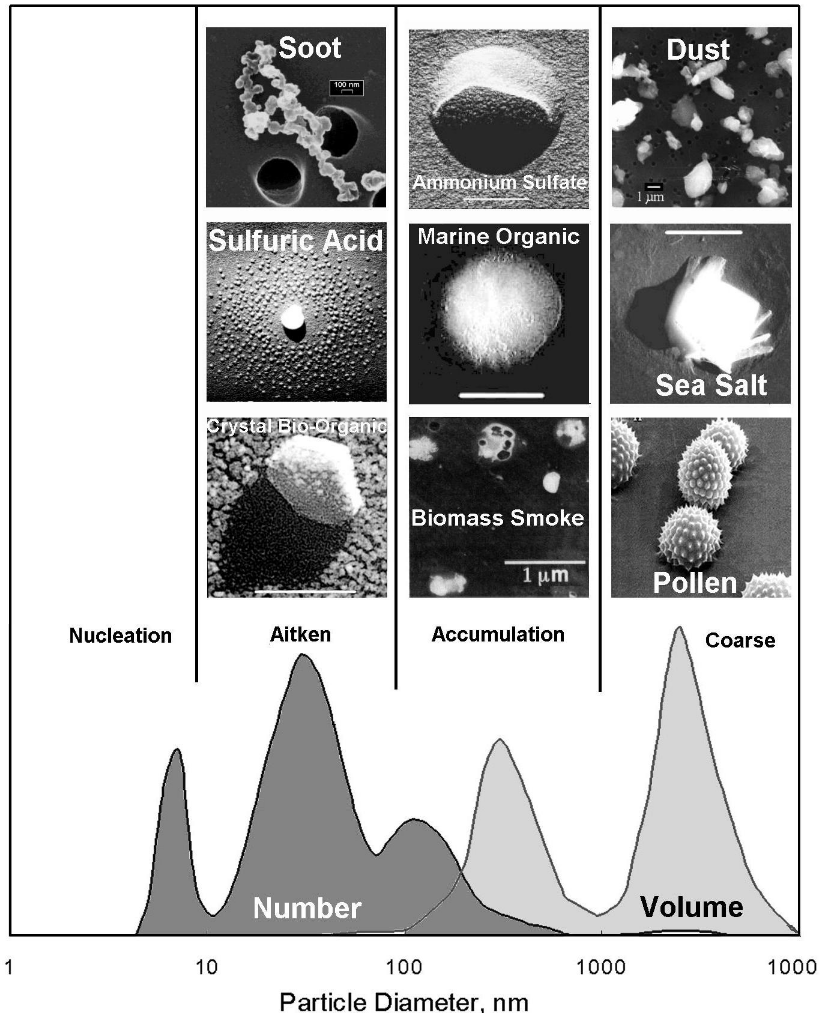

Figure 1.1: Typical examples of aerosol particles in the different size modes, along with the corresponding number and volume distributions (Heintzenberg et al., 2000).

mode with small particles. Although in nature aerosol size distributions are sometimes complex superpositions of different modes, the bimodal distribution is regarded as the most appropriate model in aerosol inversion algorithms (see e.g. Dubovik et al. (2002a), and references therein). Figure 1.2 shows an example of a bimodal distribution and its seasonal variation, reported by Fotiadi et al. (2006), using data from the FORTH–CRETE AERONET station (Section 2.4).

The aerosol optical properties required for the computation of the aerosol

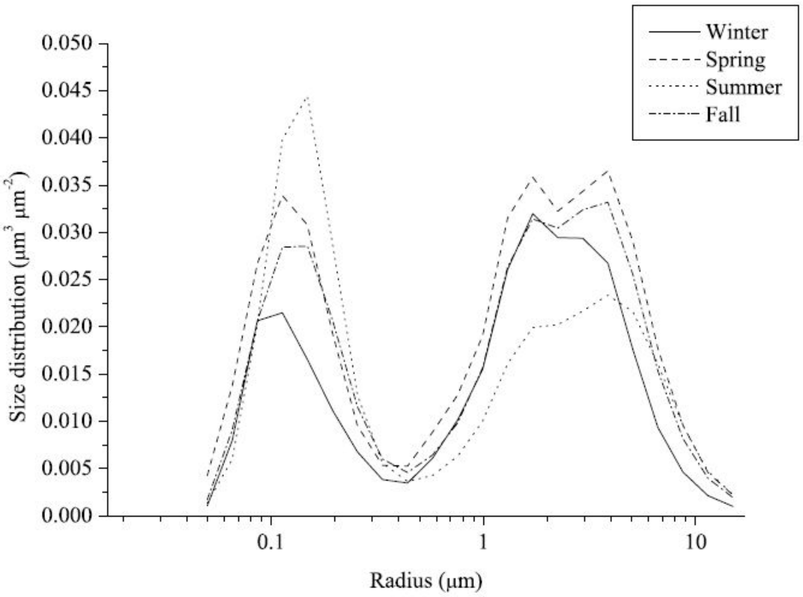

Figure 1.2: Seasonal variation of aerosol columnar volume size distribution at the FORTH–CRETE AERONET station (Fotiadi et al., 2006).

layer interaction with radiation and the evaluation of the corresponding aerosol direct effect (Section 1.2.2), are the AOT, the single scattering albedo, ω_{aer}, and the asymmetry parameter, g_{aer}. The AOT (also referred to as aerosol optical depth, AOD, in the literature) is a unitless measure of the amount of radiation incident on the aerosol layer, that is either scattered or absorbed by the aerosol particles. Formally, AOT is the integral of the aerosol extinction coefficient, or total effective cross–sectional area, along a path length through the atmosphere (see e.g. Vardavas and Taylor, 2011). The fraction of light that is scattered by the aerosol layer, compared to the total that is scattered and absorbed, is given by ω_{aer}: values of ω_{aer} range from 0 for totally absorbing particles to 1 for purely scattering ones. The asymmetry parameter, also known as asymmetry factor, gives a measure of the direction of the scattered radiation, compared to the incident one: the value of g_{aer} ranges from -1 for entirely back-scattering particles, to 0 for isotropic scattering, to 1 for entirely forward–scattering. A detailed description of the aerosol optical properties is given in Sections 3.6 and 3.8.

Aerosol effects range from local scale, relating to air quality and human health, to regional and global scales, constituting a crucial factor of global climate. According to the IPCC, a scientific body established by the United

Nations (UN) and the World Meteorological Organization (WMO) in 1988 in order to assess the information relevant to climate change and its environmental and socio–economic impacts, climate change related aerosol effects are categorized into direct, indirect and semi–direct (Forster et al., 2007).

1.2.2 Aerosol direct effect

The aerosol direct effect, also known as Direct Radiative Effect (DRE), is the mechanism by which aerosols alter the SW and LW radiative balance of the Earth–atmosphere system, through scattering and absorption of radiation (Figure 1.3). Aerosol DRE studies usually focus on the SW, since the corresponding effect is much smaller in the LW, due to the rapid decrease of aerosol extinction with increasing wavelengths for most aerosol types. Even for dust aerosol loads, the LW DRE is about 10% of the corresponding SW (Tanré et al., 2003).

The DRE is defined as the energy flux difference between an initial and a perturbed aerosol loading state, at a specified level in the atmosphere. It is usually estimated at the Earth's surface, at TOA and within the atmosphere, while the initial state usually refers either to the complete absence of aerosols, or to a typical pre–industrial year when human activity had not yet begun to exert an accelerated influence on the environment. Furthermore, in order to distinguish between natural and anthropogenic aerosol DRE, the latter is called Direct Radiative Forcing (DRF). The SW aerosol DRE is always negative at the Earth's surface, due to the reduction of the downwelling radiation. At TOA, the DRE is either negative or positive, depending on the surface brightness and the presence of clouds: while over dark surfaces, such as ocean and vegetation, the TOA DRE is negative (more radiation reflected back to space when aerosols are present), over bright surfaces, such as desert, snow and ice, the TOA DRE can become positive (e.g. Chylek and Wong, 1995; Haywood and Shine, 1995). The aerosol DRE can alter the atmospheric circulation and the water cycle, including precipitation patterns, on a variety of length and time scales (e.g. Ramanathan et al., 2001).

1.2.3 Aerosol indirect effect

The aerosol indirect effect is the mechanism by which aerosols modify the microphysical and hence the radiative properties, amount and lifetime of clouds (Forster et al., 2007). According to the IPCC Fourth Assessment Report (AR4), the indirect effect is split into the first and second indirect effects (Figure 1.3).

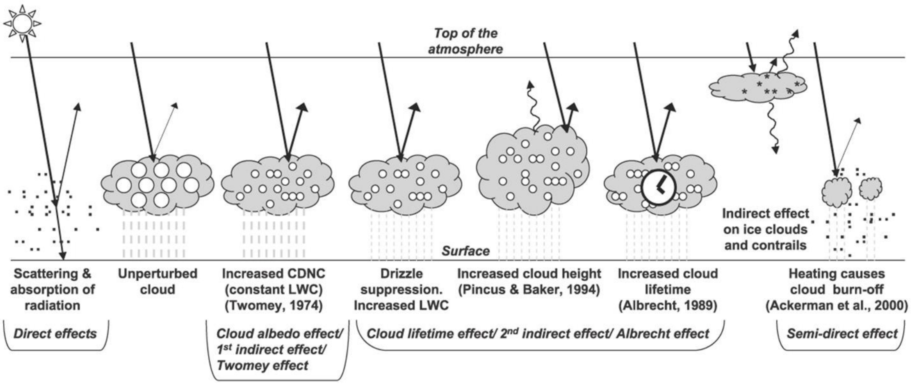

Figure 1.3: Schematic diagram showing the aerosol direct, indirect and semi–direct effects. Small black dots represent aerosols, circles represent cloud droplets, straight lines represent SW radiation, and wavy lines LW radiation. CDNC is cloud droplet number concentration and LWC is liquid water content. (From Forster et al. (2007), modified from Haywood and Boucher (2000)).

The first indirect effect, also known as "Twomey effect" (e.g. Twomey, 1977) or "cloud albedo effect" (e.g Lohmann and Feichter, 2005), is the microphysically induced effect on the cloud droplet number concentration and size, when the liquid water content is held fixed: aerosols, which act as cloud condensation nuclei (CCN), increase the number of cloud droplets, causing a reduction in the cloud droplet size. This in turn increases the cloud albedo (Ramaswamy et al., 2001). The second indirect effect, also known as "cloud lifetime effect" (e.g. Lohmann and Feichter, 2005) or "Albrecht effect" (Albrecht, 1989), is the effect on the cloud lifetime: increased aerosol loading causes the formation of smaller cloud droplets, which in turn decrease the precipitation efficiency and thereby prolong the cloud lifetime (Lohmann and Feichter, 2005). According to the IPCC AR4, while the cloud albedo effect is considered a purely radiative effect, the cloud lifetime effect involves feedbacks with the climate system that increase the uncertainties on its impacts. It is obvious, however, that the two indirect effects cannot be easily separated from each other: the processes that decrease the cloud droplet size per given liquid water content (albedo effect), also decrease precipitation production, presumably prolonging cloud lifetime (Denman et al., 2007).

1.2.4 Aerosol semi–direct effect

The aerosol semi–direct effect refers to the changes in atmospheric properties and cloud cover, caused by the absorption of SW radiation by aerosol particles: absorbing aerosols heat the surrounding air, preventing the condensation of water vapor into clouds, or dissipating existing ones. The overall result is a reduction in cloudiness (Ackerman et al., 2000). Furthermore, by heating an atmospheric layer, aerosols cause an enhancement in atmospheric stability and reduction in convection of moisture, which also result in reduced cloud formation (Koren et al., 2004). According to the IPCC Fourth Assessment Report, the aerosol semi–direct effect is not strictly considered as a radiative forcing agent, due to the interdependence between it and the hydrological cycle (Forster et al., 2007).

1.3 Studying the aerosol direct effect

For the study of aerosol effects, observations and measurements of aerosol amount, properties and distribution are necessary. Over the past decades, these measurements have substantially improved, based on advances in four main research fields (Remer et al., 2009): improvement of satellites and remote sensing techniques for retrieval of aerosol properties and their spatio–temporal distribution (Section 2.1.1), execution of numerous field campaigns in various aerosol regimes, establishment and continuous improvement of aerosol ground–based networks (Section 2.1.2), and development of enhanced instrumentation and retrieval algorithms which can determine various aerosol properties (e.g. Section 2.3). However, despite all these advances, the uncertainties regarding the aerosol effects remain high. Figure 1.4 shows the main radiative forcing components, along with their global mean values, their spatial scale and the corresponding level of scientific understanding in 2007 (Solomon et al., 2007). While it is clear that aerosols induce a negative radiative effect (cooling), the range of uncertainty is very high for both direct and indirect effects, and the corresponding scientific understanding remains medium to low.

The study of the aerosol direct effect can be broadly separated into two approaches, namely measurement–based and model–based estimations. The measurement–based approach relies on observations of aerosol properties from satellite sensors, ground instruments and field campaigns. When the aerosol optical properties required are available from observations, a Radiative Transfer Model (RTM) can be used for the estimation of the DRE at TOA and at the surface (e.g. Remer and Kaufman, 2006). Due to the lack

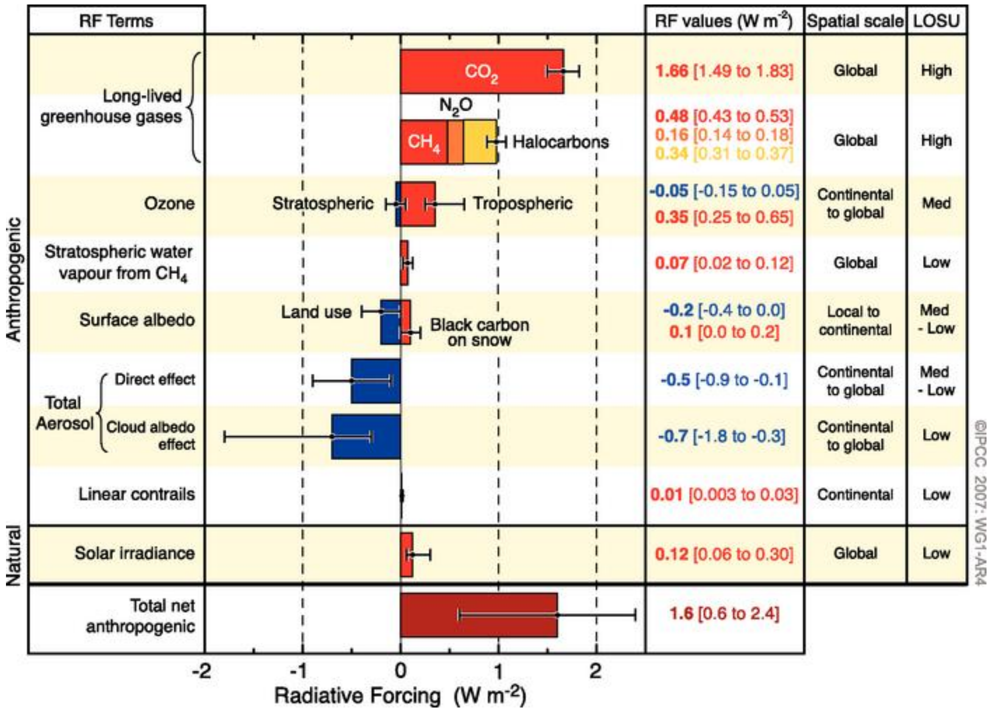

Figure 1.4: Global average values and uncertainty ranges of the main radiative forcing components. Their typical geographical extent (spatial scale) and level of scientific understanding (LOSU) are also shown (Solomon et al., 2007).

of sufficient satellite–derived aerosol optical properties to be used as input to the RTMs, satellite retrievals are usually integrated with corresponding data from model simulations (e.g. Yu et al., 2003, 2004).

The modelling approach is based on various types of models, which provide a variety of methods for understanding the aerosol effects on climate. Chemical Transport Models (CTMs) are used to test current understanding of the processes controlling aerosol spatial and temporal distributions, including aerosol and precursor emissions, chemical and microphysical transformations, transport and removal. CTMs are used to describe the global aerosol system and to make estimates of the DRE. The overall climate response to these effects is usually assessed by General Circulation Models (GCMs), which have the capability of including aerosol processes as a part of the climate system to estimate aerosol climate forcing, including the DRE, as well as aerosol–cloud interactions and feedbacks (Rind et al., 2009).

Climate models are essential tools for studying aerosols, when remote sensing or in situ measurements are not available: reproduction of the historical evolution of aerosol distribution and effects since the pre–industrial period, and estimation of future climatic scenarios, can only be assessed using models. The modelling approach has been substantially improved during the last two decades. The fact that in the IPCC First Assessment Report (Tegart et al., 1990) climate change simulations included only increases in greenhouse gases, is indicative of this progress. However, the role of aerosol remote sensing and RTMs remains crucial. In fact, along with the improvement of CTMs and GCMs, there has been a simultaneous shift of the present–day aerosol DRE estimation from model–based methods (as in the IPCC Third Assessment Report), to measurement–based methods (Yu et al., 2009).

Remotely sensed aerosol observations are required to provide both constraints and validation to the models: they can be compared with, or used in place of assumed model values, and are particularly important if the model is to be used in projections of future climate states that would result from assumed future scenarios. Validation of model output regarding aerosol properties is also based on aerosol measurements collocated in space and time. This interconnection explains the simultaneous progress in both models and aerosol remote sensing techniques (Section 2.1) during the past two decades.

In both approaches, measurement–based and model–based, RTMs are a prerequisite for the evaluation of the aerosol DRE. Reliable estimations of the effect of aerosols on solar radiation, compared to a hypothetical reference state (total absence of aerosols or pre–industrial aerosol concentrations), require a simulation of the solar radiation transfer through the atmosphere and its interaction with the aerosol particles, using an appropriate radiative transfer scheme.

1.3.1 Radiative Transfer Models

All RTMs are ultimately based on the fundamental equation of radiative transfer, which describes the modification of the radiation field as it traverses an atmosphere, due to absorption, scattering and emission effects from both the atmospheric molecules and the surface (e.g. Vardavas and Taylor, 2011).

A typical approximation in most one–dimensional RTMs is the “plane–parallel”, whereby the atmosphere is divided in simple, internally homogeneous layers, while temporal and horizontal variations are neglected. The plane–parallel approximation can be safely assumed, if the extent of the atmosphere is negligible compared to the planetary radius, as in the Earth’s case, it is expected however to produce systematic errors at large solar zenith angles, due to different atmospheric columns. In a plane–parallel atmosphere, aerosols can be represented as one (or more) scattering and absorbing layer(s). The aerosol DRE is then estimated as the difference between two model outputs, computed by including and omitting the aerosol layer(s), respectively.

Important characteristics of a RTM that determine its capabilities and accuracy include the spectral range and resolution (number of bands considered in the Ultraviolet (UV), visible and Near Infrared (NIR)), the approximation used to solve the radiative transfer equation, the multiple scattering and gaseous transmission (transmission database) schemes used, and the vertical resolution (number of atmospheric layers considered).

In terms of spectral resolution, the highest accuracy is achieved by line–by–line models (e.g. Edwards, 1992), which treat transmittance explicitly, by calculating the contribution of each spectral line for all molecules in each atmospheric layer. The data required for the theoretical calculations of molecular transmittances are available from databases such as the HIgh–resolution TRANsmission molecular absorption database (HITRAN, Rothman et al., 2009). For computationally more efficient calculations, the model spectral resolution is reduced, and replaced with parametrizations, which also reduce the accuracy. In models with lower spectral resolution, gaseous transmittance is generally achieved using either the correlated–k approximation (e.g. Lacis and Oinas, 1991) or the exponential–sumfit method (e.g. Wiscombe and Evans, 1977).

The most common approach for the solution of the radiative transfer equation is the two–stream approximation, whereby only two directions of the radiation field are considered, incoming and outgoing (e.g. Vardavas and Taylor, 2011). The two–stream approximation is computationally efficient and sufficiently accurate. Multi–stream approximations are used when higher accuracy is required, e.g. in line–by–line models (e.g. Randles et al., 2013). Multiple scattering schemes include the discrete–ordinate method (Stamnes et al., 1988), variations of the Eddington approximation (e.g. Joseph et al., 1976) and the matrix–operator method (Plass et al., 1973). As reported by Randles et al. (2013), most models use the Delta–Eddington approximation, described in detail in Section 3.11.

There are two main sources of uncertainties in estimates of the aerosol DRE using RTMs: a) uncertainties in the knowledge of aerosol optical properties and the way they are parameterized, and b) the treatment of radiative transfer, including the accuracy of the method, its spectral resolution and the treatment of molecular and multiple scattering. During the past decades, progress in both aerosol remote sensing (Sections 2.1.1 and 2.1.2) and computational methods, led to the simultaneous improvement of aerosol DRE estimations based on RTMs. Numerous RTM intercomparisons also helped to this end (Fouquart and Bonnel, 1991; Boucher et al., 1998; Halthore et al., 2005; Randles et al., 2013). The FORTH Radiative Transfer Model, described in detail in Chapter 3, was successfully tested and validated against line–by–line model results during the latest RTM intercomparison experiment (Randles et al., 2013).

1.4 Aerosols in the Eastern Mediterranean

In terms of climate change, the eastern Mediterranean region (Figure 1.5) is a sensitive area of high interest, especially due to the observed decreasing precipitation and increased droughts (Trenberth et al., 2007), and the consequent imminent desertification, which is also foreseen by future climatic projections (Meehl et al., 2007).

Numerous studies regarding aerosol characteristics and their effects have focused on this region, showing that it is multiply affected by air pollution from different sources and at different atmospheric levels. The main aerosol transport patterns include anthropogenic air pollution from Europe, which peaks in summer, and mineral dust from northern Africa and Middle East, especially during spring and autumn (e.g. Mihalopoulos et al., 1997; Formenti et al., 2001; Andreae et al., 2002; Lelieveld et al., 2002). Aerosols from sea spray and seasonal biomass burning (Formenti et al., 2002), and anthropogenic emissions from big cities, including Istanbul, Cairo and Athens (e.g. Kanakidou et al., 2011; Im and Kanakidou, 2012), also contribute to the overall aerosol load in the area. This complexity results in a mixture of aerosol types with different origins, compositions and characteristics. Subsequent studies have confirmed these findings, using both ground–based and satellite observations.

Aerosol data from various meteorological, lidar and Aerosol Robotic Network (AERONET) stations in the central and eastern Mediterranean, supplemented by satellite observations, have been used in the past to assess aerosol load, composition and seasonal variations. Major station locations include Athens (e.g. Papayannis et al., 2005; Papayannis and Balis, 1998), Thessaloniki (e.g. Koukouli et al., 2006; Balis et al., 2004), Crete (Section 2.4), Lampedusa (e.g. Pace et al., 2006; di Sarra et al., 2001), Erdemli (e.g. Vrekoussis et al., 2005; Kubilay et al., 2003), Nes Ziona and Sede Boker (e.g. Israelevich et al., 2003; Holben et al., 2001). The locations of these stations are shown in Figure 1.5. Studies focusing on these sites confirmed both the complex compositions and origins, and the very high aerosol loads, compared to other regions or the global average.

Although the above mentioned sites are representative of the wider eastern Mediterranean, the spatial distribution of aerosols and their DRE can

Figure 1.5: The eastern Mediterranean region and the locations of seven major aerosol research stations: Lampedusa, Thessaloniki, Athens, Crete, Erdemli, Nes Ziona and Sede Boker. (Image courtesy: NASA Blue Marble).

only be assessed using satellite–derived data and radiation transfer calculations. Hatzianastassiou et al. (2009) studied the spatial distribution of natural and anthropogenic aerosols in the eastern Mediterranean for the period 1980–2005, using AOT data from Total Ozone Mapping Spectrometer (TOMS) and MODIS sensors with 1° × 1° spatial resolution. They found strong spatial inhomogeneities and a significant seasonal cycle: the largest AOTs are reported over deserts and attributed to natural sources (desert dust), while large cities also exhibit large AOT values, due to local anthropogenic pollution sources. The intra–annual variation comprise maximum AOT values in spring, due to Saharan dust events, secondary maxima during summer, due to transport of continental aerosols from Europe, and minima in winter.

Papadimas et al. (2008) and Gkikas et al. (2009) found a similar intra–annual variation, examining the AOT spatial distribution over the broader Mediterranean basin for the 2000–2006 period, and the frequency and intensity of aerosol events for the 2000–2007 period, respectively, using MODIS Level 3 (1° × 1° spatial resolution) data. Papadimas et al. (2008) also reported a decreasing trend in AOT during summer, probably due to decreased emission rates of anthropogenic pollution, and a corresponding increase in winter, related to decreased precipitation. Furthermore, Gkikas et al. (2009) found a gradual decrease in the frequency of aerosol episodes, accompanied by an increase in their intensity.

Focusing on the AOT spatial distribution over Greece, Athanassiou et al. (2013) used higher resolution data (50 km × 50 km, derived from MODIS Level 2 10 km × 10 km data) for the 8–year period from March 2000 to February 2008, and found significant spatial and seasonal variability, including increasing AOT values from north to south, due to the presence of high loads of Saharan dust in Southern Greece, and high values in the eastern part of the Greek peninsula, due to high emissions of anthropogenic aerosols. They also report maximum AOT values in spring and summer and minimum in winter.

So far, the only study that has focused on the broader Mediterranean basin in order to estimate the aerosol DRE using satellite data and radiative transfer computations, was conducted by Papadimas et al. (2012). They calculated the aerosol DRE for the 7–year period from March 2000 to February 2007, at a spatial resolution of 2.5° × 2.5° latitude–longitude and on a monthly mean basis, using the FORTH RTM (Chapter 3) and aerosol data from MODIS Level 3 and Global Aerosol Data Set (GADS) (Köpke et al., 1997). They found that aerosols modify significantly the regional solar radiation budget, by inducing a planetary cooling, except for bright land surfaces, such as the desert and the Alps. The atmosphere is heated due to enhanced absorption, while the surface is cooled through reduced downwelling radiation. The maximum absolute DRE values were found in spring and summer, and the minimum in winter. Furthermore, they report a decreasing trend in the magnitude of DRE, due to decreasing aerosol load, which was attributed to reduced emissions of aerosols and aerosol precursors, combined with an increased aerosol removal by enhanced precipitation.

Both station and satellite based studies in the eastern Mediterranean, confirm the uniqueness of the island of Crete as an ideal site for aerosol research. The analysis and results presented in the following chapters, highlight the representativeness of Crete regarding the wider eastern Mediterranean, while ground–based data from FORTH–CRETE AERONET, Hellenic Centre for Marine Research (HCMR) and Finokalia stations on Crete (Section 2.4) are used both for validation purposes and as supplements to satellite model input data.

Bibliography

Abbot, C. G. and Fowle, F. E. J.: Volcanoes and Climate, Smithsonian Miscellaneous Collections, 60(29), 1–24, 1913.

Ackerman, A. S., Toon, O. B., Stevens, D. E., Heymsfield, A. J., Ramanathan, V., and Welton, E. J.: Reduction of Tropical Cloudiness by Soot, Science, 288, 1042–1047, doi:10.1126/science.288.5468.1042, 2000.

Albrecht, B. A.: Aerosols, Cloud Microphysics, and Fractional Cloudiness, Science, 245, 1227–1230, doi:10.1126/science.245.4923.1227, 1989.

Alvarez, W., Alvarez, L. W., Asaro, F., and Michel, H. V.: The End of the Cretaceous: Sharp Boundary or Gradual Transition?, Science, 223, 1183–1186, doi:10.1126/science.223.4641.1183, 1984.

Andreae, T. W., Andreae, M. O., Ichoku, C., and Maenhaut, W.: Light scattering by dust and anthropogenic aerosol at a remote site in the Negev desert, Israel, Journal of Geophysical Research, 107, doi:10.1029/2001JD900252, 2002.

Athanassiou, G., Hatzianastassiou, N., Gkikas, A., and Papadimas, C.: Estimating Aerosol Optical Depth Over the Broader Greek Area from MODIS Satellite, Water, Air and Soil Pollution, 224, 1–14, doi:10.1007/s11270-013-1605-2, 2013.

Balis, D. S., Amiridis, V., Nickovic, S., Papayannis, A., and Zerefos, C.: Optical properties of Saharan dust layers as detected by a Raman lidar at Thessaloniki, Greece, Geophysical Research Letters, 31, doi:10.1029/2004GL019881, 2004.

Boucher, O., Schwartz, S. E., Ackerman, T. P., Anderson, T. L., Bergstrom, B., Bonnel, B., Chylek, P., Dahlback, A., Fouquart, Y., Fu, Q., Halthore, R. N., Haywood, J. M., Iversen, T., Kato, S., Kinne, S., Kirkevag, A., Knapp, K. R., Lacis, A., Laszlo, I., Mishchenko, M. I., Nemesure, S., Ramaswamy, V., Roberts, D. L., Russell, P., Schlesinger, M. E., Stephens,

G. L., Wagener, R., Wang, M., Wong, J., and Yang, F.: Intercomparison of models representing direct shortwave radiative forcing by sulfate aerosols, Journal of Geophysical Research: Atmospheres, 103, 16 979–16 998, doi: 10.1029/98JD00997, 1998.

Chylek, P. and Wong, J.: Effect of absorbing aerosols on global radiation budget, Geophysical Research Letters, 22, 929–931, doi:10.1029/95GL00800, 1995.

Denman, K. L., Brasseur, G., Chidthaisong, A., Ciais, P., Cox, P. M., Dickinson, R. E., Hauglustaine, D., Heinze, C., Holland, E., Jacob, D., Lohmann, U., Ramachandran, S., da Silva Dias, P. L., Wofsy, S. C., and Zhang, X.: Couplings Between Changes in the Climate System and Biogeochemistry, in: Climate Change 2007: The Physical Science Basis. Contribution of Working Group I to the Fourth Assessment Report of the Intergovernmental Panel on Climate Change, edited by Solomon, S., Qin, D., Manning, M., Chen, Z., Marquis, M., Averyt, K. B., Tignor, M., and Miller, H. L., Cambridge University Press, Cambridge, United Kingdom and New York, NY, USA, 2007.

di Sarra, A., Di Iorio, T., Cacciani, M., Fiocco, G., and Fua, D.: Saharan dust profiles measured by lidar at Lampedusa, Journal of Geophysical Research: Atmospheres, 106, 10 335–10 347, doi:10.1029/2000JD900734, 2001.

Dubovik, O., Holben, B., Eck, T. F., Smirnov, A., Kaufman, Y. J., King, M. D., Tanré, D., and Slutsker, I.: Variability of Absorption and Optical Properties of Key Aerosol Types Observed in Worldwide Locations, Journal of the Atmospheric Sciences, 59, 590–608, 2002a.

Edwards, D. P.: GENLN2: a General Line–by–line Atmospheric Transmittance and Radiance Model: Version 3.0 Description and Users Guide, NCAR technical notes, Atmospheric Chemistry Division, National Center for Atmospheric Research, 1992.

Formenti, P., Andreae, M. O., Andreae, T. W., Galani, E., Vasaras, A., Zerefos, C., Amiridis, V., Orlovsky, L., Karnieli, A., Wendisch, M., Wex, H., Holben, B. N., Maenhaut, W., and Lelieveld, J.: Aerosol optical properties and large-scale transport of air masses: Observations at a coastal and a semiarid site in the eastern Mediterranean during summer 1998, Journal of Geophysical Research, 106, 9807–9826, doi:10.1029/2000JD900609, 2001.

Formenti, P., Reiner, T., Sprung, D., Andreae, M. O., Wendisch, M., Wex, H., Kindred, D., Dewey, K., Kent, J., Tzortziou, M., Vasaras, A., and Zerefos, C.: STAAARTE–MED 1998 summer airborne measurements over the Aegean Sea 1. Aerosol particles and trace gases, Journal of Geophysical Research: Atmospheres, 107, AAC 1–1 – AAC 1–15, doi: 10.1029/2001JD001337, 2002.

Forster, P., Ramaswamy, V., Artaxo, P., Berntsen, T., Betts, R., Fahey, D. W., Haywood, J., Lean, J., Lowe, D. C., Myhre, G., Nganga, J., Prinn, R., Raga, G., M., S., and Van Dorland, R.: Changes in Atmospheric Constituents and in Radiative Forcing, in: Climate Change 2007: The Physical Science Basis. Contribution of Working Group I to the Fourth Assessment Report of the Intergovernmental Panel on Climate Change, edited by Solomon, S., Qin, D., Manning, M., Chen, Z., Marquis, M., Averyt, K. B., Tignor, M., and Miller, H. L., Cambridge University Press, Cambridge, United Kingdom and New York, NY, USA, 2007.

Fotiadi, A., Hatzianastassiou, N., Drakakis, E., Matsoukas, C., Pavlakis, K. G., Hatzidimitriou, D., Gerasopoulos, E., Mihalopoulos, N., and Vardavas, I.: Aerosol physical and optical properties in the Eastern Mediterranean Basin, Crete, from Aerosol Robotic Network data, Atmospheric Chemistry and Physics, pp. 5399–5413, 2006.

Fouquart, Y. and Bonnel, B.: Intercomparing shortwave radiation codes for climate studies, Journal of Geophysical Research, 96, 8955–8968, 1991.

Franklin, B.: Meteorological Imaginations and Conjectures (Paper Read 1784), Memoirs of the Literary and Philosophical Society of Manchester 2nd ed., 1789, 373–377, 1784.

Gkikas, A., Hatzianastassiou, N., and Mihalopoulos, N.: Aerosol events in the broader Mediterranean basin based on 7–year (2000–2007) MODIS C005 data, Annales Geophysicae, 27, 3509–3522, doi:10.5194/angeo-27-3509-2009, 2009.

Halthore, R. N., Crisp, D., Schwartz, S. E., Anderson, G. P., Berk, A., Bonnel, B., Boucher, O., Chang, F.-L., Chou, M.-D., Clothiaux, E. E., Dubuisson, P., Fomin, B., Fouquart, Y., Freidenreich, S., Gautier, C., Kato, S., Laszlo, I., Li, Z., Mather, J. H., Plana-Fattori, A., Ramaswamy, V., Ricchiazzi, P., Shiren, Y., Trishchenko, A., and Wiscombe, W.: Intercomparison of shortwave radiative transfer codes and measurements, Journal of Geophysical Research: Atmospheres, 110, doi:10.1029/2004JD005293, 2005.

Hansen, J. E., Wang, W.-C., and Lacis, A. A.: Mount Agung Eruption Provides Test of a Global Climatic Perturbation, Science, 199, 1065–1068, 1978.

Hatzianastassiou, N., Gkikas, A., Mihalopoulos, N., Torres, O., and Katsoulis, B. D.: Natural versus anthropogenic aerosols in the eastern Mediterranean basin derived from multiyear TOMS and MODIS satellite data, Journal of Geophysical Research: Atmospheres, 114, doi:10.1029/2009JD011982, 2009.

Haywood, J. and Boucher, O.: Estimates of the direct and indirect radiative forcing due to tropospheric aerosols: A review, Reviews of Geophysics, 38, 513–543, doi:10.1029/1999RG000078, 2000.

Haywood, J. M. and Shine, K. P.: The effect of anthropogenic sulfate and soot aerosol on the clear sky planetary radiation budget, Geophysical Research Letters, 22, 603–606, doi:10.1029/95GL00075, 1995.

Heintzenberg, J., Raes, F., and Schwartz, S.: Atmospheric Chemistry in a Changing World, Chapter 4: Tropospheric Aerosols, URL `http://capita.wustl.edu/aerosolintegration/specialTopics/Integration/Capter4Drafts/CHAPTER4000708.htm`, 2000.

Holben, B. N., Tanré, D., Smirnov, A., Eck, T. F., Slutsker, I., Abuhassan, N., Newcomb, W. W., Schafer, J. S., Chatenet, B., Lavenu, F., Kaufman, Y. J., Castle, J. V., Setzer, A., Markham, B., Clark, D., Frouin, R., Halthore, R., Karneli, A., O'Neill, N. T., Pietras, C., Pinker, R. T., Voss, K., and Zibordi, G.: An emerging ground–based aerosol climatology: Aerosol optical depth from AERONET, Journal of Geophysical Research: Atmospheres, 106, 12 067–12 097, doi:10.1029/2001JD900014, 2001.

Idso, S. B. and Brazel, A. J.: Planetary Radiation Balance as a Function of Atmospheric Dust: Climatological Consequences, Science, 198, 731–733, doi:10.1126/science.198.4318.731, 1977.

Im, U. and Kanakidou, M.: Impacts of East Mediterranean megacity emissions on air quality, Atmospheric Chemistry and Physics, 12, 6335–6355, doi:10.5194/acp-12-6335-2012, 2012.

Israelevich, P. L., Ganor, E., Levin, Z., and Joseph, J. H.: Annual variations of physical properties of desert dust over Israel, Journal of Geophysical Research: Atmospheres, 108, doi:10.1029/2002JD003163, 2003.

Joseph, J. H., Wiscombe, W. J., and Weinman, J. A.: The Delta-Eddington Approximation for Radiative Flux Transfer, Journal of Atmospheric Sciences, 33, 2452–2459, 1976.

Kanakidou, M., Mihalopoulos, N., Kindap, T., Im, U., Vrekoussis, M., Gerasopoulos, E., Dermitzaki, E., Unal, A., Kocak, M., Markakis, K., Melas, D., Kouvarakis, G., Youssef, A. F., Richter, A., Hatzianastassiou, N., Hilboll, A., Ebojie, F., Wittrock, F., von Savigny, C., Burrows, J. P., Ladstaetter-Weissenmayer, A., and Moubasher, H.: Megacities as hot spots of air pollution in the East Mediterranean, Atmospheric Environment, 45, 1223–1235, doi:10.1016/j.atmosenv.2010.11.048, 2011.

Kondratyev, K. I. A.: Climate shocks: natural and anthropogenic, Wiley series in climate and the biosphere, Wiley, 1988.

Köpke, P., Hess, M., Schult, I., and Shettle, E. P.: Global Aerosol Data Set, MPI Report for Meteorology, Max–Planck–Institut für Meteorologie, 1997.

Koren, I., Kaufman, Y. J., Remer, L. A., and Martins, J. V.: Measurement of the Effect of Amazon Smoke on Inhibition of Cloud Formation, Science, 303, 1342–1345, doi:10.1126/science.1089424, 2004.

Koukouli, M. E., Balis, D. S., Amiridis, V., Kazadzis, S., Bais, A., Nickovic, S., and Torres, O.: Aerosol variability over Thessaloniki using ground based remote sensing observations and the TOMS aerosol index, Atmospheric Environment, 40, 5367–5378, doi:10.1016/j.atmosenv.2006.04.046, 2006.

Kubilay, N., Cokacar, T., and Oguz, T.: Optical properties of mineral dust outbreaks over the northeastern Mediterranean, Journal of Geophysical Research: Atmospheres, 108, doi:10.1029/2003JD003798, 2003.

Lacis, A. and Oinas, V.: A Description of the Correlated–k Distribution Method for Modeling Nongray Gaseous Absorption , Thermal Emission , and Multiple Scattering in Vertically Inhomogeneous Atmospheres, Journal of Geophysical Research, 96, 9027–9063, doi:10.1029/90JD01945, 1991.

Lelieveld, J., Berresheim, H., Borrmann, S., Crutzen, P. J., Dentener, F. J., Fischer, H., Feichter, J., Flatau, P. J., Heland, J., Holzinger, R., Kormann, R., Lawrence, M. G., Levin, Z., Markowicz, K. M., Mihalopoulos, N., Minikin, A., Ramanathan, V., De Reus, M., Roelofs, G. J., Scheeren, H. a., Sciare, J., Schlager, H., Schultz, M., Siegmund, P., Steil, B., Stephanou, E. G., Stier, P., Traub, M., Warneke, C., Williams, J., and Ziereis, H.: Global air pollution crossroads over the Mediterranean., Science, 298, 794–799, doi:10.1126/science.1075457, 2002.

Lenoble, J., Remer, L., and Tanré, D.: Aerosol Remote Sensing, Springer–Praxis books in environmental sciences, Springer, 2013.

Lohmann, U. and Feichter, J.: Global indirect aerosol effects: a review, Atmospheric Chemistry and Physics, 5, 715–737, 2005.

Meehl, G. A., Stocker, T. F., Collins, W. D., Friedlingstein, P., Gaye, A. T., Gregory, J. M., Kitoh, A., Knutti, R., Murphy, J. M., Noda, A., Raper, S. C. B., Watterson, I. G., Weaver, A. J., and Zhao, Z. C.: Global Climate Projections, in: Climate Change 2007: The Physical Science Basis. Contribution of Working Group I to the Fourth Assessment Report of the Intergovernmental Panel on Climate Change, edited by Solomon, S., Qin, D., Manning, M., Chen, Z., Marquis, M., Averyt, K. B., Tignor, M., and Miller, H. L., Cambridge University Press, Cambridge, United Kingdom and New York, NY, USA, 2007.

Mihalopoulos, N., Stephanou, E., Kanakidou, M., Pilitsidis, S., and Bousquet, P.: Tropospheric aerosol ionic composition in the Eastern Mediterranean region, Tellus B, 49, 314–326, 1997.

Mitchell, J.Murray, J.: A Preliminary Evaluation of Atmospheric Pollution as a Cause of the Global Temperature Fluctuation of the Past Century, in: Global Effects of Environmental Pollution, edited by Singer, S., pp. 139–155, Springer Netherlands, 1970.

Pace, G., di Sarra, A., Meloni, D., Piacentino, S., and Chamard, P.: Aerosol optical properties at Lampedusa (Central Mediterranean). 1. Influence of transport and identification of different aerosol types, Atmospheric Chemistry and Physics, 6, 697–713, doi:10.5194/acp-6-697-2006, 2006.

Papadimas, C. D., Hatzianastassiou, N., Mihalopoulos, N., Querol, X., and Vardavas, I.: Spatial and temporal variability in aerosol properties over the Mediterranean basin based on 6-year (2000-2006) MODIS data, Journal of Geophysical Research: Atmospheres, 113, doi:10.1029/2007JD009189, 2008.

Papadimas, C. D., Hatzianastassiou, N., Matsoukas, C., Kanakidou, M., Mihalopoulos, N., and Vardavas, I.: The direct effect of aerosols on solar radiation over the broader Mediterranean basin, Atmospheric Chemistry and Physics, 12, 7165–7185, doi:10.5194/acp-12-7165-2012, 2012.

Papayannis, A. and Balis, D.: Study of the structure of the lower troposphere over Athens using a backscattering lidar during the MEDCAPOT–TRACE experiment: measurements over a suburban area, Atmospheric Environment, 32, 2161–2172, 1998.

Papayannis, A., Balis, D., Amiridis, V., Chourdakis, G., Tsaknakis, G., Zerefos, C., Castanho, A. D. A., Nickovic, S., Kazadzis, S., and Grabowski, J.: Measurements of Saharan dust aerosols over the Eastern Mediterranean using elastic backscatter–Raman lidar, spectrophotometric and satellite observations in the frame of the EARLINET project, Atmospheric Chemistry and Physics, 5, 2065–2079, doi:10.5194/acp-5-2065-2005, 2005.

Plass, G. N., Kattawar, G. W., and Catchings, F. E.: Matrix operator theory of radiative transfer. 1: Rayleigh scattering, Applied Optics, 12, 314–329, doi:10.1364/AO.12.000314, 1973.

Ramanathan, V., Crutzen, P. J., Kiehl, J. T., and Rosenfeld, D.: Aerosols, Climate, and the Hydrological Cycle, Science, 294, 2119–2124, doi:10.1126/science.1064034, 2001.

Ramaswamy, V., Boucher, O., Haigh, J., Hauglustaine, D., Haywood, J., Myhre, G., Nakajima, T., Shi, G. Y., and Solomon, S.: Radiative Forcing of Climate Change, in: Climate Change 2001: The Scientific Basis. Contribution of working group I to the Third Assessment Report of the Intergovernmental Panel on Climate Change, edited by Houghton, J. T., Ding, Y., Griggs, D. J., Noguer, M., van der Linden, P. J., Dai, X., Maskell, K., and Johnson, C. A., pp. 349–416, Cambridge University Press, New York, 2001.

Randles, C. A., Kinne, S., Myhre, G., Schulz, M., Stier, P., Fischer, J., Doppler, L., Highwood, E., Ryder, C., Harris, B., Huttunen, J., Ma, Y., Pinker, R. T., Mayer, B., Neubauer, D., Hitzenberger, R., Oreopoulos, L., Lee, D., Pitari, G., Di Genova, G., Quaas, J., Rose, F. G., Kato, S., Rumbold, S. T., Vardavas, I., Hatzianastassiou, N., Matsoukas, C., Yu, H., Zhang, F., Zhang, H., and Lu, P.: Intercomparison of shortwave radiative transfer schemes in global aerosol modeling: results from the AeroCom Radiative Transfer Experiment, Atmospheric Chemistry and Physics, 13, 2347–2379, doi:10.5194/acp-13-2347-2013, 2013.

Rasool, S. I. and Schneider, S. H.: Atmospheric Carbon Dioxide and Aerosols: Effects of Large Increases on Global Climate, Science, 173, 138–141, doi:10.1126/science.173.3992.138, 1971.

Remer, L. A. and Kaufman, Y. J.: Aerosol direct radiative effect at the top of the atmosphere over cloud free ocean derived from four years of MODIS data, Atmospheric Chemistry and Physics, 6, 237–253, doi:10.5194/acp-6-237-2006, 2006.

Remer, L. A., Chin, M., DeCola, P., Feingold, G., Halthore, R., Kahn, R. A., Quinn, P. K., Rind, D., Schwartz, S. E., Streets, D., and Yu, H.: Executive Summary, in: Atmospheric Aerosol Properties and Climate Impacts, A Report by the U.S. Climate Change Science Program and the Subcommittee on Global Change Research, edited by Chin, M., Kahn, R. A., and Schwartz, S. E., National Aeronautics and Space Administration, Washington, D. C., USA, 2009.

Rind, D., Chin, M., Feingold, G., Streets, D., Kahn, R. A., Schwartz, S. E., and Yu, H.: Modeling the Effects of Aerosols on Climate, in: Atmospheric Aerosol Properties and Climate Impacts, A Report by the U.S. Climate Change Science Program and the Subcommittee on Global Change Research, edited by Chin, M., Kahn, R. A., and Schwartz, S. E., National Aeronautics and Space Administration, Washington, D.C., USA, 2009.

Rothman, L. S., Gordon, I. E., Barbe, A., Benner, D. C., Bernath, P. F., Birk, M., Boudon, V., Brown, L. R., Campargue, A., Champion, J.-P., Chance, K., Coudert, L. H., Dana, V., Devi, V. M., Fally, S., Flaud, J.-M., Gamache, R. R., Goldman, A., Jacquemart, D., Kleiner, I., Lacome, N., Lafferty, W. J., Mandin, J.-Y., Massie, S. T., Mikhailenko, S. N., Miller, C. E., Moazzen-Ahmadi, N., Naumenko, O. V., Nikitin, A. V., Orphal, J., Perevalov, V. I., Perrin, A., Predoi-Cross, A., Rinsland, C. P., Rotger, M., Šimečková, M., Smith, M. A. H., Sung, K., Tashkun, S. A., Tennyson, J., Toth, R. A., Vandaele, A. C., and Vander Auwera, J.: The HITRAN 2008 molecular spectroscopic database, Journal of Quantitative Spectroscopy and Radiative Transfer, 110, 533–572, doi:10.1016/j.jqsrt.2009.02.013, 2009.

Seinfeld, J. and Pandis, S.: Atmospheric chemistry and physics: from air pollution to climate change, Wiley Intersciencie publications, Wiley, 2006.

Solomon, S., Qin, D., Manning, M., Alley, R. B., Berntsen, T., Bindoff, N. L., Chen, Z., Chidthaisong, A., Gregory, J. M., Hegerl, G. C., Heimann, M., Hewitson, B., Hoskins, B. J., Joos, F., Jouzel, J., Kattsov, V., Lohmann, U., Matsuno, T., Molina, M., Nicholls, N., Overpeck, J., Raga, G., Ramaswamy, V., Ren, J., Rusticucci, M., Somerville, R., Stocker, T. F., Whetton, P., Wood, R. A., and Wratt, D.: Technical Summary, in: Climate Change 2007: The Physical Science Basis. Contribution of Working Group I to the Fourth Assessment Report of the Intergovernmental Panel on Climate Change, edited by Solomon, S., Qin, D., Manning, M., Chen, Z., Marquis, M., Averyt, K. B., Tignor, M., and Miller, H. L., Cambridge

University Press, Cambridge, United Kingdom and New York, NY, USA, 2007.

Stamnes, K., Tsay, S.-C., Jayaweera, K., and Wiscombe, W.: Numerically stable algorithm for discrete–ordinate–method radiative transfer in multiple scattering and emitting layered media, Applied Optics, 27, 2502–2509, doi:10.1364/AO.27.002502, 1988.

Tanré, D., Haywood, J., Pelon, J., Leon, J. F., Chatenet, B., Formenti, P., Francis, P., Goloub, P., Highwood, E. J., and Myhre, G.: Measurement and modeling of the Saharan dust radiative impact: Overview of the Saharan Dust Experiment (SHADE), Journal of Geophysical Research: Atmospheres, 108, doi:10.1029/2002JD003273, 2003.

Tegart, W., Sheldon, G., Griffiths, D., on Climate Change. Working Group II., I. P., Organization, W. M., Programme, U. N. E., and on Climate Change, I. P.: Climate change: the IPCC impacts assessments, Australian Govt. Pub. Service, 1990.

Trenberth, K. E., Jones, P. D., Ambenje, P., Bojariu, R., Easterling, D., Tank, A. K., Parker, D., Rahimzadeh, F., Renwick, J. A., Rusticucci, M., Soden, B., and Zhai, P.: Observations: Surface and Atmospheric Climate Change, in: Climate Change 2007: The Physical Science Basis. Contribution of Working Group I to the Fourth Assessment Report of the Intergovernmental Panel on Climate Change, edited by Solomon, S., Qin, D., Manning, M., Chen, Z., Marquis, M., Averyt, K. B., Tignor, M., and Miller, H. L., Cambridge University Press, Cambridge, United Kingdom and New York, NY, USA, 2007.

Twomey, S.: The Influence of Pollution on the Shortwave Albedo of Clouds, Journal of Atmospheric Sciences, 34, 1149–1154, 1977.

Vardavas, I. and Taylor, F.: Radiation and Climate: Atmospheric Energy Budget from Satellite Remote Sensing, International Series of Monographs on Physics, OUP Oxford, 2011.

Vrekoussis, M., Liakakou, E., Kocak, M., Kubilay, N., Oikonomou, K., Sciare, J., and Mihalopoulos, N.: Seasonal variability of optical properties of aerosols in the Eastern Mediterranean, Atmospheric Environment, 39, 7083–7094, doi:10.1016/j.atmosenv.2005.08.011, 2005.

Watson, R. T., Rhode, H., Oeschger, H., and Siegenthaler, U.: Greenhouse gases and aerosols, in: Climate Change: the IPCC Scientific Assessment, edited by Houghton, J. T., Jenkins, C. J., and Ephraums, J. J., pp. 1–40, Cambridge University Press, Cambridge, UK, 1990.

Weart, S.: The Discovery of Global Warming, New Histories of Science, Technology, and Medicine, Harvard University Press, 2008.

Wiscombe, W. J. and Evans, J. W.: Exponential–sum fitting of radiative transmission functions, Journal of Computational Physics, 24, 416–444, doi:10.1016/0021-9991(77)90031-6, 1977.

Yu, H., Dickinson, R. E., Chin, M., Kaufman, Y. J., Holben, B. N., Geogdzhayev, I. V., and Mishchenko, M. I.: Annual cycle of global distributions of aerosol optical depth from integration of MODIS retrievals and GOCART model simulations, Journal of Geophysical Research: Atmospheres, 108, doi:10.1029/2002JD002717, 2003.

Yu, H., Dickinson, R. E., Chin, M., Kaufman, Y. J., Zhou, M., Zhou, L., Tian, Y., Dubovik, O., and Holben, B. N.: Direct radiative effect of aerosols as determined from a combination of MODIS retrievals and GOCART simulations, Journal of Geophysical Research: Atmospheres, 109, D03206, doi:10.1029/2003JD003914, 2004.

Yu, H., Quinn, P. K., Feingold, G., Remer, L. A., Kahn, R. A., Chin, M., and Schwartz, S. E.: In Situ Measurements of Aerosol Properties, Burdens, and Radiative Forcing, in: Atmospheric Aerosol Properties and Climate Impacts, A Report by the U.S. Climate Change Science Program and the Subcommittee on Global Change Research, edited by Chin, M., Kahn, R. A., and Schwartz, S. E., National Aeronautics and Space Administration, Washington, D.C., USA, 2009.

Chapter 2

Aerosol Remote Sensing

2.1 Introduction

Aerosol remote sensing can be separated into two broad categories: space–based observations and ground–based measurements. During the past two decades, numerous field campaigns have also contributed to aerosol measurements, combining ground observations with satellite, aircraft or balloon data. However, these campaigns, each one focusing on a specific area of interest, provide limited data in terms of spatial and temporal coverage.

2.1.1 Aerosol monitoring from satellite observations

Inference of aerosol properties from satellites relies on the interaction of electromagnetic radiation scattered and/or absorbed by the atmospheric constituents and the Earth's surface. Radiation is received by two basic types of sensors: passive and active. Passive sensors record radiation emitted by the Sun and reflected back to the sensor, while active sensors receive energy emitted by the sensor itself (Lee et al., 2009).

Passive satellite remote sensing of aerosols has been performed for over three decades, although early aerosol monitoring from space used data from sensors that were designed for other purposes. The first satellite observation of aerosols was performed by the Multi–Spectral Scanner (MSS) sensor onboard NASA's Earth Resources Technology Satellite (ERTS–1, renamed Landsat); Griggs (1975) showed that the AOT could be estimated using a linear relationship which correlated the upwelling Earth–Atmosphere radiance and AOT. Validation of the satellite based AOT against ground measurements, made with a photometer at two test sites, determined a ±10% accuracy of the method.

The first operational aerosol product was generated based on data from the Advanced Very High Resolution Radiometer (AVHRR), launched in 1978 onboard TIROS–N satellite and originally intended for weather observations. Evolution of the AVHRR single–channel algorithm for AOT retrieval included several phases and was implemented in successive sensors launched on board National Oceanic and Atmospheric Administration (NOAA) satellites. The algorithm scaled the upwelling satellite radiances, over oceans and under cloud–free conditions, to AOT, using an RTM and assuming different types of aerosol models (Stowe et al., 1997). A dual–channel algorithm has also been implemented, which derived AOT at two wavelengths (0.65 and 0.85 µm) and the corresponding Angstrom exponent Å(Ignatov and Stowe, 2002).

The longest measurement record of global aerosols (over both ocean and land) from space has been provided by TOMS, onboard NASA's Nimbus–7 (1979–1992) and Earth Probe (1996–2006) satellites, which was replaced by the Ozone Monitoring Instrument (OMI) onboard NASA's Aura satellite in 2006. While TOMS was originally designed for ozone monitoring, the ratio of its 331 and 360 nm channels, which is sensitive to absorbing aerosols, was used for the derivation of an Aerosol Index, a measure of the presence of UV–absorbing aerosols, such as dust and soot (Hsu et al., 1996). AOT and single scattering albedo have also been derived from TOMS measurements, with uncertainties 20–30% and ±0.03, relative to AERONET observations, respectively (Torres et al., 2002, 2005).

While both the satellite sensor technology and the algorithms for aerosol retrieval were dramatically improved over the past 30 years, the underlying concept remains the same: the SW radiation detected by a satellite sensor is composed of solar radiation reflected by the Earth's surface as well as radiation scattered by the atmosphere in the direction of the sensor. Radiation reflected from the surface also interacts with the atmosphere, and thus its spectral and angular properties are affected both by the atmosphere and the surface. This radiation can either be absorbed by gases and aerosol particles, or scattered to the sensor through single backscattering by an aerosol particle or by a series of forward and/or backward scattering events in the atmosphere (King et al., 1999). After correcting for scattering and absorption by other atmospheric constituents, the signal contributed by atmospheric aerosol scattering needs to be decoupled from that contributed by surface reflectance.

The first algorithms developed, used radiation data from a single channel and retrieved AOT in the same wavelength (e.g. Nagaraja Rao et al., 1989; Stowe et al., 1997). These algorithms were limited to dark surfaces with low and uniform reflectivity, such as oceans, since, due to the lower reflection of the ocean's surface, the corresponding signal component is easily eliminated.

Inclusion of radiation measurements from more than one channel, allowed the retrieval of additional aerosol characteristics, such as the Angstrom exponent (e.g. King et al., 1999; Lee et al., 2009). Spectral information also allowed aerosol retrieval over dark land surfaces, such as green vegetation, whereby spectral characteristics of this land cover type, known a priori, are used in the algorithm to infer AOT over land (Kaufman et al., 1997a).

Most of the modern aerosol products are based on data from instruments with a single sampling of the angular domain, which suffer from the limitation of a priori assumptions about the spectral properties of the underlying surface. Use of multiple view–angle imagery allows an additional constraint to be placed, since the same area of surface is viewed through different atmospheric path lengths. The principal advantage of a multiple view–angle approach is that no a priori information of the surface spectrum is required and aerosol properties can be retrieved over all surface types, including bright surfaces, such as arid or snow covered land. Another main advantage is that, by eliminating the dark target limitations, the spatial resolution of the algorithm output can be significantly improved. A limitation of the angular approach is that the algorithms require accurate co–registration of the images acquired from multiple view angles. Several multi–angle approaches for aerosol retrieval have been developed in the past (e.g. Leroy et al., 1997; Martonchik et al., 1998; Grey et al., 2006; Diner et al., 2009; Frankenberg et al., 2012). Most of them use data from MISR (Multi–angle Imaging Spectroradiometer), POLDER (Polarization and Directionality of the Earth's Reflectances) and the Advanced Along–track Scanning Radiometer (AATSR) sensors. An algorithm recently developed by North et al. (2009), exploits the advantages of the multiple view–angle approach for aerosol retrieval, by synergistically combining data from the Medium Resolution Imaging Spectrometer (MERIS) and the AATSR sensors, both onboard the Envisat satellite. The MERIS/AATSR algorithm, along with a global validation of the retrieved AOT against AERONET and MODIS observations, are presented in Appendix A. The same synergy AOT data, along with MODIS AOT and atmospheric parameters, have been used for the estimation of Particulate Matter (PM) concentrations in Athens, Greece, using a multiple regression approach (Appendix B).

While only columnar information on aerosol parameters can be retrieved from passive sensors, the use of active sensors (lidars) allows the retrieval of information regarding the aerosol vertical distribution, through analysis of the lidar backscatter signal. The Cloud–Aerosol Lidar with Orthogonal Polarization (CALIOP) sensor onboard NASA's Cloud–Aerosol Lidar and Infrared Pathfinder Satellite Observations (CALIPSO) satellite, operational since 2006, is a typical example; its aerosol products include aerosol layer height, physical thickness and AOT (Winker et al., 2010, 2009).

2.1.2 Aerosol monitoring from ground measurements

Ground–based aerosol observations are based primarily on Sun photometry, whereby a photometer pointing at the Sun measures its direct radiance. Although the technology involved has substantially advanced (Holben et al., 1998) since the first analog instrument presented by Volz (1959), the physical principle and method used remain the same: the solar radiation measured at the surface is a function of the solar extraterrestrial radiation reaching the Earth's orbit, attenuated by absorption and scattering processes in the Earth's atmosphere. The spectral atmospheric extinction of the direct solar radiance is described by the Beer–Lambert–Bouguer exponential decay law:

$$I_\lambda = I_{0\lambda}\exp(-m\tau_\lambda), \tag{2.1}$$

where I_λ is the radiation measured at the sensor, $I_{0\lambda}$ the incoming radiation at TOA, m is the optical air mass, equal to $1/\cos z$, with z the solar zentih angle, and τ_λ the atmospheric extinction optical depth. Depending on the wavelength λ where the measurement takes place, the corresponding aerosol extinction optical depth can be inferred after removing the Rayleigh scattering and molecular absorption optical depths (Shaw, 1983).

Except for direct Sun measurements, valuable information regarding the aerosol properties can be obtained from sky (diffuse) radiance measurements. Several methods have been proposed (e.g. Nakajima et al., 1983, 1996; Dubovik and King, 2000), whereby sky radiance measurements in different angles on the almucantar plane (a circle on the celestial sphere parallel to the horizon, with altitude defined by the solar zenith angle), are combined with direct Sun measurements to retrieve aerosol information additional to the AOT. Aerosol parameters retrieved by inversion of such multi–angular and multi–spectral measurements of atmospheric radiances include particle size distribution, complex refractive index, phase function and single scattering albedo (Dubovik and King, 2000). As in satellite aerosol remote sensing, lidar measurements are also routinely used from ground stations to retrieve information on the aerosol vertical distribution.

Several networks of ground aerosol monitoring stations are presently operational, such as the AERONET (described in detail in Section 2.3), with stations worldwide, the Sky radiometer Network (SKYNET; Hashimoto et al., 2012; Kim et al., 2005), with stations located mainly in the Eastern Asia and Japan, and the China Aerosol Remote Sensing Network (CARSNET; Che et al., 2009). Aerosol vertical distribution information is also being monitored by lidar networks, such as the Micro Pulse Lidar Network (MPLNET, Welton et al., 2001), with numerous stations collocated with AERONET stations globally, the European Aerosol Research Lidar Network (EARLINET, Pappalardo et al., 2009), with 27 stations distributed over Europe and the Asian Dust and Aerosol Lidar Observation Network (AD-Net, Sugimoto et al., 2010), with about 20 stations in East Asia. Along with others, these networks are coordinated by the Global Atmosphere Watch (GAW) aerosol programme of the World Meteorological Organization, which has organized the GAW Aerosol Lidar Observation Network (GALION, Bösenberg and Hoff, 2007), a network of networks with primary objectives the harmonization and integration of aerosol measurements globally.

2.2 The MODIS sensor

MODIS is a sensor on board the NASA Earth Observing System (EOS) Terra and Aqua satellites (Salomonson et al., 1989; Barnes et al., 1998). A sketch of Terra satellite, with its technical characteristics and sensors, is shown in Figure 2.1. Terra was launched on December 18, 1999 and Aqua on May 4, 2002. Both satellites are polar orbiting at a height of about 700 km, with a wide swath (±55° or about 2330 km), which covers the entire Earth's surface every 1 to 2 days, while high latitude regions are covered more than once daily. Terra and Aqua cross the equator at approximately 10:30 and 13:30 local time, respectively. MODIS acquires data in 36 spectral bands, ranging from the visible through the NIR and mid–infrared to the thermal infrared (0.405-14.385 µm). MODIS data are being used operationally to provide a variety of geophysical parameters employed in monitoring the Earth's land, ocean and atmosphere. The MODIS 36 bands, their bandwidth and primary use are shown in Table 2.1 (MODIS, 2013). Their spatial resolution ranges between 250 m (bands 1–2), 500 m (bands 3–7) and 1000 m (bands 8–36). It should be noted that these pixel resolutions refer to the MODIS nadir view. Due to the Earth's spherical geometry and the wide MODIS swath, pixels increase to nearly their double size at the swath edges.

MODIS data files are stored in Hierarchical Data Format (HDF). Several parameters are grouped and stored in the same HDF file as Scientific Data Sets (SDS). Each file covers a five–minute time interval of measurements. There are three main levels of products generated from the data collected by the sensor. Level 1 products include scans of raw radiance measurements, geolocation, calibrated radiances and cloud mask. The Level 2 products comprise geophysical parameter data retrieved from the Level 1 data by application of geophysical parameter algorithms. Level 3 processing

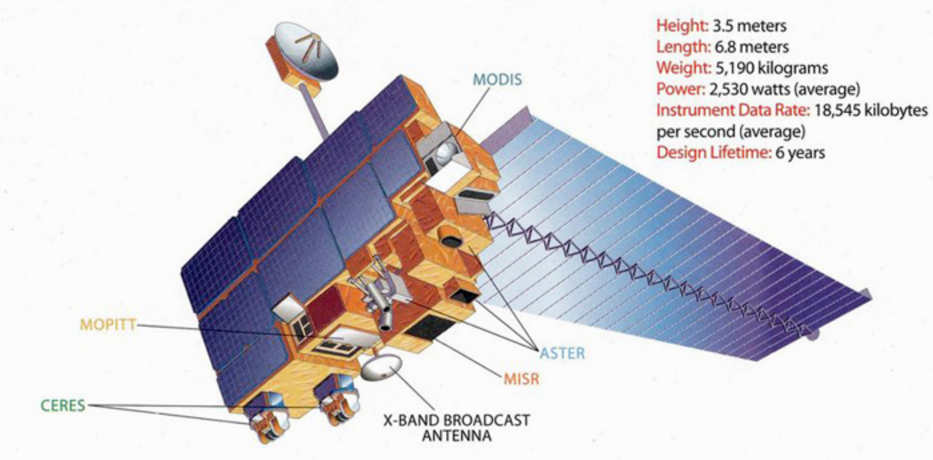

Figure 2.1: Artist's sketch of Terra spacecraft with technical specifications and instrument locations labelled. Credit: NASA.

uses Level 2 products to produce Earth–gridded geophysical parameter data, which have been statistically processed both spatially and temporally. Figure 2.2 shows the data processing architecture and data products that are used in processing MODIS atmospheric properties (adapted from Parkinson and Greenstone, 2000).

MODIS Level 2 data are categorized into 3 groups of products, namely Atmosphere, Land and Ocean parameters. The Level 2 Atmosphere parameters, used in this study, are further divided into 4 groups: the Aerosol, the Water Vapor, the Cloud and the Atmospheric Profile Products. A concise description of the MODIS atmosphere data products can be found in King et al. (2003).

2.2.1 The Aerosol product

MODIS Level 2 Aerosol products are derived separately over three environments: dark–surface (far from sun glint) ocean targets (Remer et al., 2005), dark surface land targets (Levy et al., 2007) and bright surfaces (deserts) land targets (Hsu et al., 2004). The products are organized in collections (Levy et al., 2009), whereby each successive collection consists of products that were generated by a major revision of the retrieval algorithm. While the algorithm was conceived and developed prior to Terra launch (Kaufman et al., 1997a; Tanré et al., 1997), and the latest operational collections are 005 and 051, the theoretical basis remains the same: the algorithm operates by matching observed spectral reflectance to Look–Up Table (LUT) that

Table 2.1: MODIS bands, bandwidths and primary applications (adapted from MODIS, 2013).

Band #	Bandwidth (μm)	Primary Use
1	0.620–0.670	Land/Cloud/Aerosols Boundaries
2	0.841–0.876	
3	0.459–0.479	Land/Cloud/Aerosols Properties
4	0.545–0.565	
5	1.230–1.250	
6	1.628–1.652	
7	2.105–2.155	
8	0.405–0.420	Ocean Color/ Phytoplankton/ Biogeochemistry
9	0.438–0.448	
10	0.483–0.493	
11	0.526–0.536	
12	0.546–0.556	
13	0.662–0.672	
14	0.673–0.683	
15	0.743–0.753	
16	0.862–0.877	
17	0.890–0.920	Atmospheric Water Vapor
18	0.931–0.941	
19	0.915–0.965	
20	3.660–3.840	Surface/Cloud Temperature
21	3.929–3.989	
22	3.929–3.989	
23	4.020–4.080	
24	4.433–4.498	Atmospheric Temperature
25	4.482–4.549	
26	1.360–1.390	Cirrus Clouds Water Vapor
27	6.535–6.895	
28	7.175–7.475	
29	8.400–8.700	Cloud Properties
30	9.580–9.880	Ozone
31	10.780–11.280	Surface/Cloud Temperature
32	11.770–12.270	
33	13.185–13.485	Cloud Top Altitude
34	13.485–13.785	
35	13.785–14.085	
36	14.085–14.385	

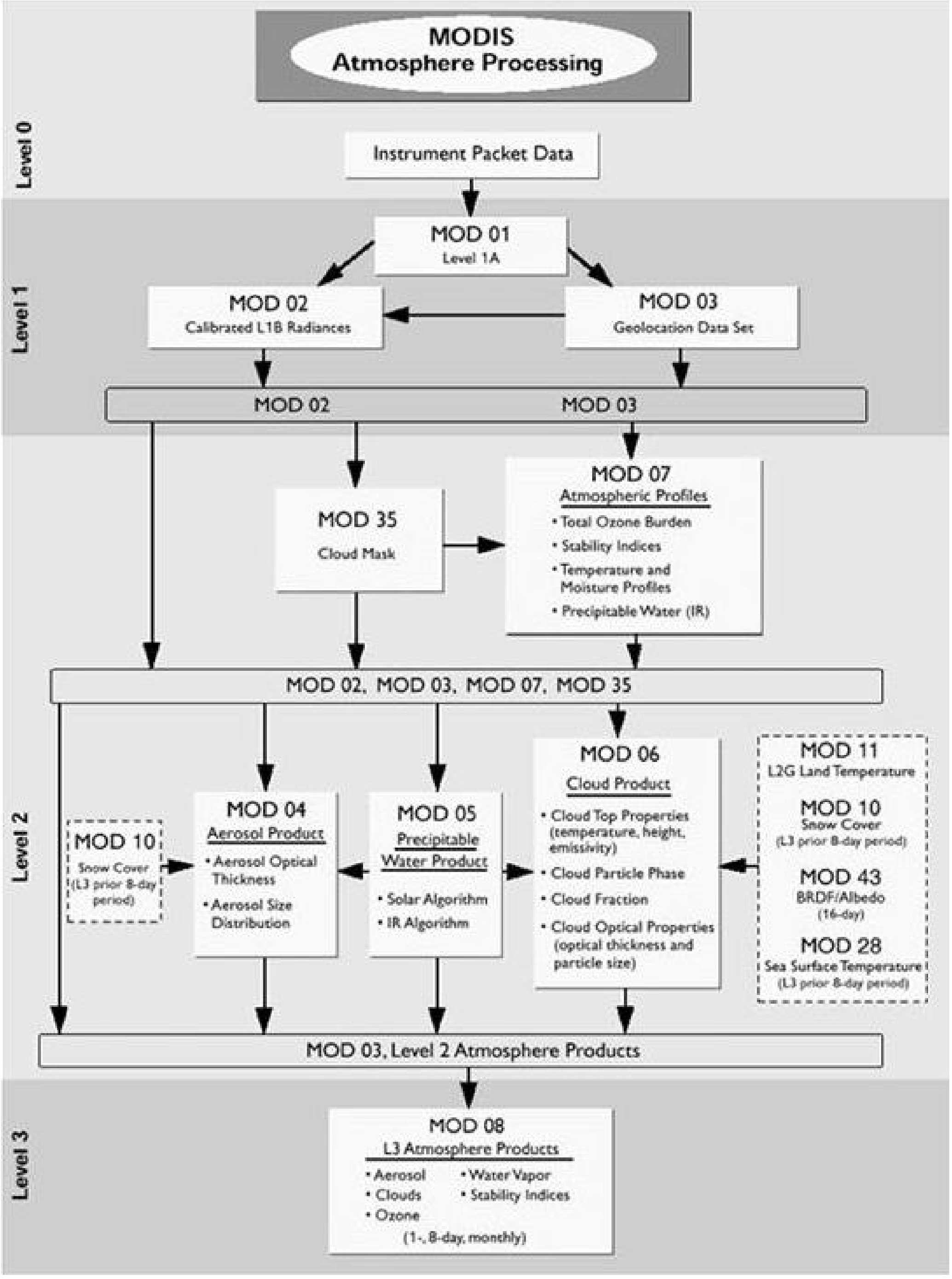

Figure 2.2: MODIS Atmosphere data processing architecture and products (Parkinson and Greenstone, 2000).

simulate spectral reflectance for expected aerosol conditions.

Both the land and ocean aerosol algorithms take as input the Level 1 calibrated and geolocated reflectances. Algorithm input also includes the Level 2 cloud mask product and the atmospheric profile product, as well as H_2O and O_3 profile data from the National Centres for Environmental Prediction (NCEP), as described in Remer et al. (2005). All reflectance pixels are aggregated in $10\,\text{km} \times 10\,\text{km}$ boxes. In bands with spatial resolution $500\,\text{m} \times 500\,\text{m}$, each $10\,\text{km} \times 10\,\text{km}$ box contains $20 \times 20 = 400$ pixels. Reflectances are corrected for atmospheric H_2O, O_3 and CO_2, while cloud mask data are used to mask cloudy and snow or ice covered pixels. The categorization of each initial pixel as a "land" or "water" pixel, also included in the cloud mask product, is used in the algorithm pre–processing: if all 400 pixels in the 10 km box are "water" pixels, the algorithm proceeds with the over-ocean retrieval. If any pixel is land, then it proceeds with the over-land retrieval (Levy et al., 2009).

Above land, in order to discard bright surfaces, only dark pixels are selected, based on their reflectance in band 7 (2.13 µm). To be selected, a pixel must fall within the range $0.01 \leq \rho_{2.13} \leq 0.25$. The selected pixels are then sorted based on their visible reflectance ($\rho_{0.66}$): the darkest 20% and brightest 50% are also discarded, to avoid possible contamination by clouds or cloud shadows. If at least 12 pixels remain (out of 400), mean reflectances are calculated at 0.47, 0.66 and 2.13 µm. The surface reflectances at 0.47 and 0.66 µm are then derived from the mean TOA reflectance at 2.13 µm, using the Kaufman et al. (1997a) empirical relationships. The 0.47 and 0.66 µm TOA and surface reflectances are used as input to the model LUT, to retrieve AOT values at the same wavelengths. The LUT comprises several aerosol models, with specific size distribution parameters and single scattering albedos (Table 1 in Remer et al., 2005). The algorithm output includes AOT at 0.47, 0.66 and 0.55 µm, inferred from the corresponding Angstrom exponent, as well as the fraction of AOT contributed by the fine mode (fine mode fraction). A detailed description of the algorithm is given in Remer et al. (2005).

Over ocean, after correcting radiances for atmospheric gases and cloud masking, two additional masks are applied, one for ocean contaminated by river sediments and the other for Sun glint, since the algorithm is designed to retrieve only over dark ocean (Remer et al., 2005). For the inversion procedure, all reflectances from MODIS bands 1–7 are used (Table 2.1). The LUT consists of four fine mode and five coarse mode aerosol models, and the solution, which results from minimizing an error metric, is a combination of a fine and a coarse mode. The algorithm output includes AOT at 7 wavelengths (bands 1–7), fine mode fraction and the aerosol effective radius, which is the ratio of the third and second moments of aerosol size distribution. The aerosol asymmetry factor, a crucial parameter for the radiation transfer computations described in Chapter 3, is also available over ocean at the same seven wavelengths, as a diagnostic parameter (Remer et al., 2005).

All collections of the MODIS Level 2 Aerosol product, both over land and ocean, have been thoroughly validated by the MODIS atmosphere science team as well as by independent researchers worldwide. Ichoku et al. (2002) developed a framework for the spatio–temporal intercomparison of MODIS AOT with corresponding AERONET measurements. The major validation studies (Chu et al., 2002; Ichoku et al., 2002, 2005; Remer et al., 2005; Levy et al., 2010) followed this framework and included data sets with thousands of pairs of MODIS and AERONET collocated AOT globally. This method, also used in the present study, is described in detail in Section 2.4.1.

2.2.2 The Cloud product

The MODIS Level 2 Cloud products include cloud detection and masking, cloud–top properties (pressure, temperature, effective emissivity), thermodynamic phase, and optical and microphysical properties (optical thickness, particle size, water path). With the exception of a 250 m cloud mask, all cloud products are at a scale of 1 or 5 km.

The Cloud Mask algorithm employs a variety of cloud detection tests, to indicate a level of confidence that MODIS is observing a clear or cloudy–sky scene. The algorithm uses 20 of the 36 MODIS bands to maximize reliable cloud detection (Ackerman et al., 2010). The product is derived globally during both day and night, at 1 km × 1 km pixel resolution.

Cloud–top properties and cloud amount are derived using the CO_2 slicing algorithm (Menzel et al., 1983; Wylie and Menzel, 1999), which takes advantage of the differing partial absorption in the MODIS infrared bands located within the broad 15 µm CO_2 absorption region (bands 31–36 in Table 2.1). Due to the difference in CO_2 absorption as the wavelength increases from 13.3 to 15 µm, each band is sensitive to a different level in the atmosphere, allowing the derivation of cloud–top properties in a wide range of pressure levels. The products are generated at 5 km × 5 km spatial resolution (Menzel et al., 2010).

While cloud–top properties retrieval is based on thermal infrared bands only, SW infrared and midwave infrared bands are also used for the retrieval of optical and microphysical properties. The retrieval is based on MODTRAN4 library calculations (Berk et al., 1998) of plane–parallel homogeneous clouds, considering different size distributions for liquid and ice clouds (Platnick et al., 2003; King et al., 1997). Cloud optical and microphysical properties are derived at 1 km × 1 km spatial resolution.

2.2.3 The Atmospheric Profile product

The Atmospheric Profile Product includes profiles of temperature and moisture, as well as surface temperature, total column ozone and precipitable water. The retrievals are performed using clear–sky radiances measured by MODIS at 5 km × 5 km spatial resolution, over land and ocean. The algorithm uses 11 bands (bands 25–36 in Table 2.1) for the derivation of the products. Since all these bands are in the infrared, the output is available for both day and night (Seemann et al., 2003).

The retrieval algorithm is based on a statistical regression between radiances and corresponding atmospheric profiles, utilizing a large sample of atmospheric temperature and moisture soundings, and collocated radiance observations. Since actual MODIS measurements are not always well collocated in space and time with radiosonde profiles, radiative transfer calculations are also involved. After the estimated atmospheric profiles are obtained, integration yields the total column ozone and precipitable water (Seemann et al., 2006; Borbas et al., 2011).

2.3 The AERONET stations network

AERONET is a global network of ground–based aerosol remote sensing automatic instruments established by NASA. Since the first documentation of the AERONET philosophy, instrumentation, processing system and database (Holben et al., 1998), the network has expanded by agencies, institutes and universities to approximately 400 stations in 50 countries (Figure 2.3).

AERONET station measurements are performed by spectral radiometers of the CIMEL CE–318 series. These instruments are solar–powered, robotically–pointed sun photometers, which perform both Sun and sky measurements. The direct Sun measurements are made in eight spectral bands (340, 380, 440, 500, 675, 870, 1020 and 1640 nm; the standard wavelengths are 440, 670, 870, 940 and 1020 nm), at 15–min intervals. Sky measurements are performed at 440, 670, 870 and 1020 nm.

AERONET uses a data collection system operating on geostationary satellites to automatically collect and process data from all network stations. Except for AOT retrieval from direct Sun measurements, the AERONET data processing system comprises referenced and generally accepted inversion algorithms for retrieval of aerosol optical and microphysical properties, by exploiting both Sun and sky measurements. The AERONET inversion

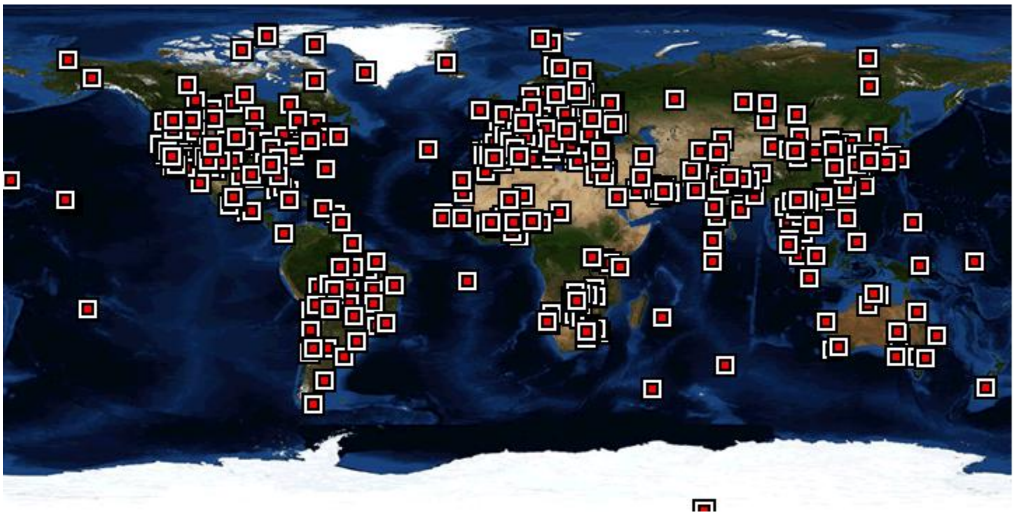

Figure 2.3: Global distribution of AERONET stations. The red squares on the map indicate the locations of AERONET sites. Credit: NASA.

products include aerosol size distribution, complex refractive index, phase function, single scattering albedo, asymmetry parameter, spectral and broadband fluxes (Dubovik and King, 2000; Dubovik et al., 2002b; Dubovik, 2004; Sinyuk et al., 2007).

AERONET has offered a standardization for ground–based aerosol measurements, processing and characterization. AERONET data have been used in numerous studies, primarily on local and regional scales, regarding air pollution, aerosol properties and effects on the atmospheric radiation budget. They also constitute the data set most widely used for validation of aerosol properties retrieved from satellite sensors.

2.4 Station measurements and MODIS observations in Crete

Crete is the largest and most southerly major island in Greece and is located on the border between the Aegean and Levantine sub–basins of the Eastern Mediterranean (Figure 2.4a). Ground–based data from three stations were used in the present study, either as input to the FORTH model or for validation purposes.

The FORTH–CRETE AERONET station (35 19’ 58” N, 25 16’ 55” E), is located on the northern coast of Crete, 15 km east from Herakleion, the

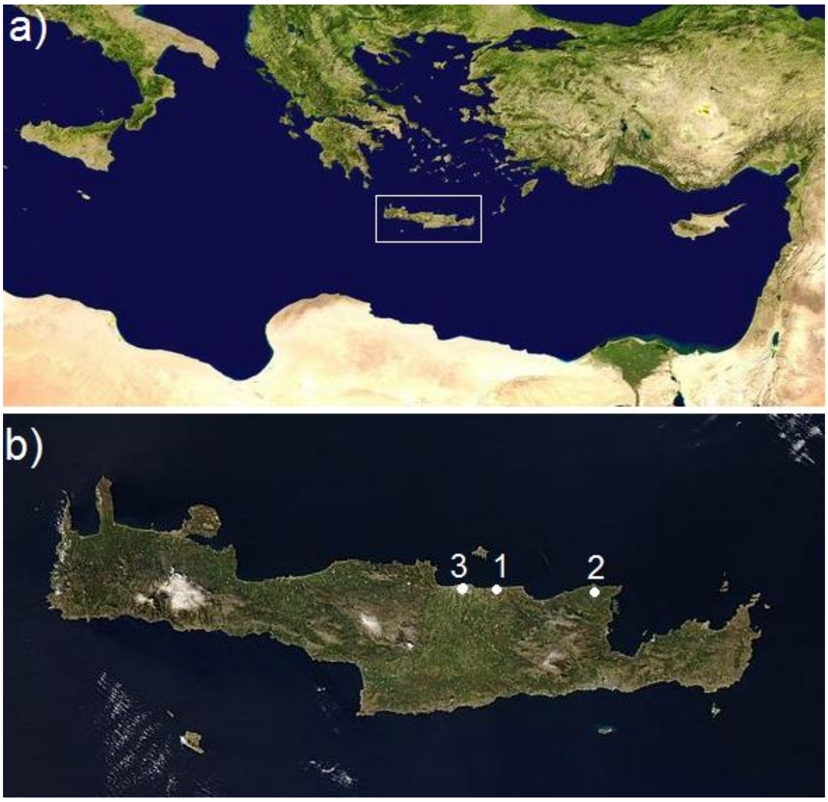

Figure 2.4: a) The location of Crete in the Eastern Mediterranean. b) The sites of FORTH–CRETE and HCMR stations (1), Finokalia Station (2) and the city of Herakleion (3). (Image credit: NASA Blue Marble).

largest city in Crete with a population of about 200,000 people (Figure 2.4b). The instrumentation, which operates since January 2003, is set up on the roof of the 20 m high building of the HCMR, which is 100 m from the coast. An analysis of the aerosol physical and optical properties measured at this station can be found in Fotiadi et al. (2006). Aerosol optical thickness data measured at the FORTH–CRETE AERONET station were used for validation of the corresponding MODIS Level 2 AOT data, as described in Section 2.4.2. Data of aerosol single scattering albedo, also provided by the FORTH–CRETE AERONET station, were used as input to the FORTH model, due to lack of corresponding satellite data. The incorporation procedure of these data in the model is described in detail in Section 3.8.

At HCMR meteorological station, which is collocated with the FORTH–CRETE AERONET station, downwelling shortwave radiation fluxes are being measured since June 2003, using a Kipp & Zonen CM11 pyranometer, with spectral range 310-2800 nm and 2% uncertainty. These measurements were used for validation of the corresponding FORTH model output, as described in Section 4.2.1.

Finokalia meteorological station, operated by the Environmental Chemical Processes Laboratory of the Department of Chemistry – University of Crete, is also located at a remote site of the northern coast of Crete, 70 km east of Herakleion (35 20' N, 25 40' E, 250 m altitude, Figure 2.4b). Details on the region and the prevailing atmospheric and meteorological conditions of the wider area are given in Mihalopoulos et al. (1997), Kouvarakis et al. (2000) and Gerasopoulos et al. (2005). Among other instruments, a CM3 pyranometer is installed in Finokalia since 2001, measuring the downwelling SW radiation at the 305-2800 nm spectral range, with 10% uncertainty. These data were also used for model validation (Section 4.2.1). Measurements of the surface ozone photolysis rate, $J(O^1D)$, have also been conducted in Finokalia during the period 2002–2006, and were used for validation of the FORTH model $J(O^1D)$ (Section 5.3.2). The ground measurements are performed using a 2π filter radiometer (Meteorologie Consult, Metcon, Germany), with a time resolution of 5 min. The accuracy of these measurements is estimated to be 15% and the precision better than 3% (Berresheim et al., 2003). More information regarding the instrument can be found in Gerasopoulos et al. (2012).

2.4.1 MODIS Level 2 data processing

Due to the polar orbits of both Terra and Aqua satellites, the orientation of all MODIS Level 2 swath data sets is not regular, depending on a 16–day repetition cycle of each specific satellite overpass trajectory. Moreover, due to the Earth's spherical geometry and the wide MODIS swath, pixel sizes increase near the swath edges. In the case of the Aerosol Product, the spatial resolution ranges between 10 km × 10 km at nadir and 20 km × 20 km at the edge of the swath. The corresponding spatial resolutions of all other data Products are 5 km × 5 km and 10 km × 10 km, respectively.

To acquire MODIS Level 2 data as input to the FORTH model over a site of interest, a procedure similar to the one described in Ichoku et al. (2002) for the validation of MODIS AOT against AERONET measurements, was used. The basis for this procedure is to identify within each MODIS image the pixel falling over the site of interest, by its longitude and latitude. If the parameter under consideration was successfully retrieved by the corresponding MODIS algorithm, this pixel value is used as input to the model. In case of MODIS algorithm failure, an $N \times N$ km^2 subset centered on that pixel is extracted, and its mean and standard deviation are computed. Following Ichoku et al.

Table 2.2: MODIS Level 2 Atmosphere Products and corresponding processed Scientific Data Sets.

Product	SDS name
Aerosol	Corrected_Optical_Depth_Land
	Corrected_Optical_Depth_Land_wav2p1
	Effective_Optical_Depth_Average_Ocean
	Optical_Depth_Small_Land
	Optical_Depth_Small_Average_Ocean
	Asymmetry_Factor_Average_Ocean
	Solar_Zenith
	Mean_Reflectance_Land
Cloud	Cloud_Fraction
	Cloud_Optical_Thickness
	Cloud_Phase_Infrared
	Cloud_Top_Pressure
Atmospheric Profile	Surface_Temperature
	Surface_Pressure
	Retrieved_Temperature_Profile
	Retrieved_Moisture_Profile
	Total_Ozone

(2002), a $\sim 50\,\mathrm{km} \times 50\,\mathrm{km}$ window size was selected for calculation of the mean values. This size corresponds to 5×5 pixels of Aerosol Product data ($10\,\mathrm{km} \times 10\,\mathrm{km}$ spatial resolution at nadir) and 10×10 pixels of all other Products data ($5\,\mathrm{km} \times 5\,\mathrm{km}$ spatial resolution at nadir). In order for the calculated mean value to be regarded as representative of this area and be used as input to the model, it is computed from a certain minimum number of values (20% of the pixels of this $\sim 50\,\mathrm{km}\times50\,\mathrm{km}$ grid). When this criterion is not fulfilled, a "no–data" value is assigned to the pixel of interest.

Table 2.2 shows the MODIS Level 2 Products and corresponding SDS parameter names, required as input to the FORTH model, which were processed using this method (see also Table 3.1). The runs were performed over all areas of interest covered in Chapters 4–6, namely FORTH–CRETE/HCMR stations (Chapter 4), Finokalia station (Chapters 4 and 5), and Marathonas, Yliki, Evinos and Mornos lakes (Chapter 6).

2.4.2 MODIS aerosol properties validation over Crete

Although the MODIS Level 2 AOT has been successfully validated in numerous studies based on thousands of AERONET collocated observations (Section 2.2.1), the overall performance may differ from site to site (Levy et al., 2010). In order to ensure the validity of the results reported here, MODIS AOT was validated against corresponding FORTH–CRETE AERONET measurements.

Following the Ichoku et al. (2002) approach, MODIS AOT averaged over a 50 km × 50 km area centered on the FORTH–CRETE AERONET station, was validated against temporal statistics from AERONET: the AERONET data acquired during the 1–hour period centered on the MODIS overpass time (±half hour) were used for the calculation of the AERONET mean AOT value. The justification is that, since air masses are constantly in motion, an air mass captured by MODIS across a certain horizontal span over the AERONET site, will be sampled by the sunphotometer during a certain time period. The MODIS AOT derived from the ocean algorithm was used, as suggested by Remer et al. (2002), for coastal and island stations.

For the validation of AOT, values at 675 and 870 nm from FORTH–CRETE AERONET station and at 660 and 865 nm from MODIS Terra and Aqua, were used. These channels are sufficiently similar for direct comparison. In Figure 2.5, the mean values of the 50 km × 50 km MODIS subset and the ±30 min temporal average of the corresponding AERONET data set are plotted. The error bars represent the respective spatial and temporal standard deviations. The red line is the linear regression fit, with the equation, determination coefficient and number of points used shown at the lower right corner. The agreement, as represented by the linear fit, is within the expected uncertainty of the MODIS retrieval algorithm over ocean ($\Delta\tau = \pm 0.03 \pm 0.05\tau$) for small values of AOT, as denoted by the dotted lines in the figures. The slight overestimation of AOT by MODIS might be partly explained by the slightly smaller observation wavelengths of MODIS than of AERONET.

The same validation procedure has been used for the cases of fine mode AOT and the asymmetry parameter g. Fine mode AOT validation was performed for the 0.47 and 0.50 µm wavelengths of MODIS and AERONET, respectively. The two data sets are not well correlated, with the determination coefficient being 0.38 and the slope equal to 0.59. These results show that MODIS tends to overestimate the fine mode AOT, as was shown by similar studies for dust–dominated aerosols (Santese et al., 2007; Kleidman et al., 2005). The MODIS asymmetry parameter was validated against the corresponding AERONET product at the two pairs of wavelengths used in the case

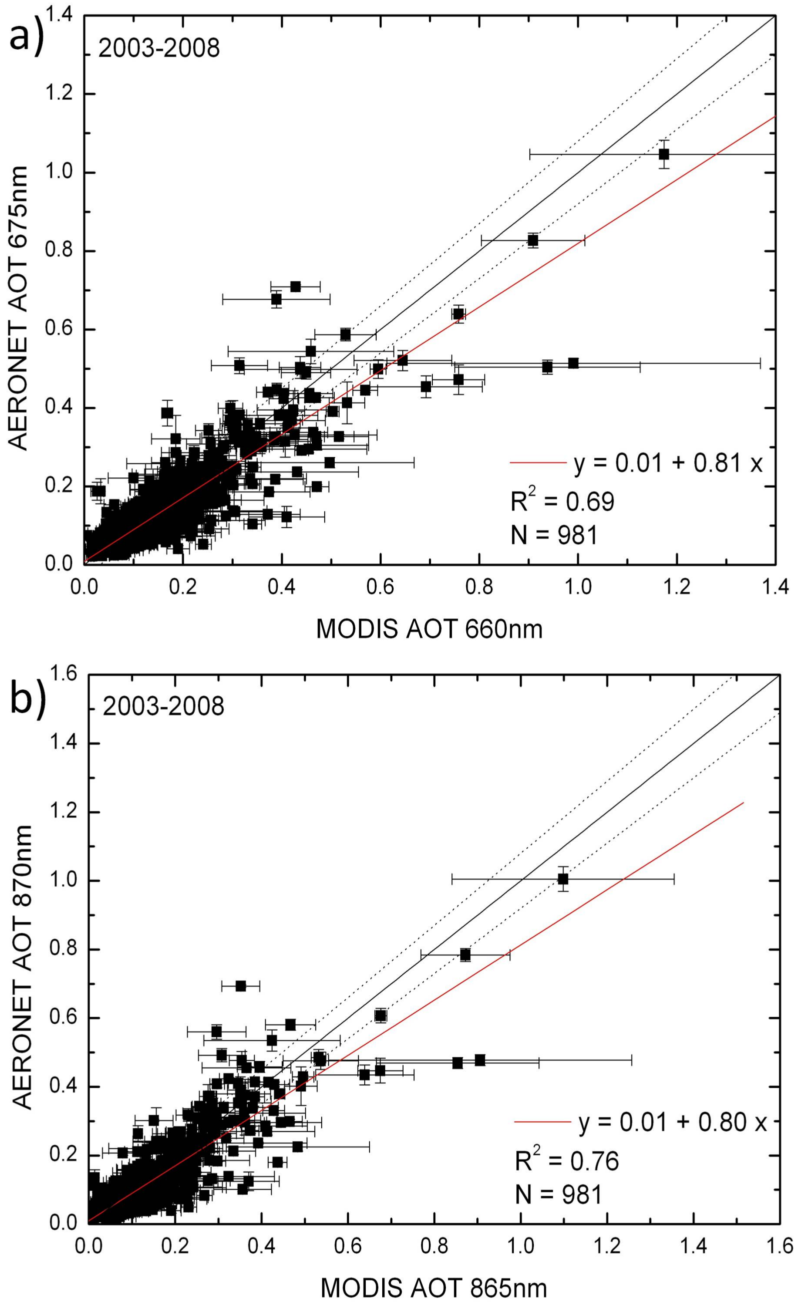

Figure 2.5: Scatter plots of means of AOT (660 nm (a) and 865 nm (b)) of MODIS 50 km × 50 km subsets against AOT (675 nm (a) and 870 nm (b)) of AERONET 1–hour subsets, for the period 2003-2008. The error bars represent the respective standard deviations. The red line is the linear regression fit, with the equation, determination coefficient and number of points used shown at the lower right corner. The dotted lines correspond to the expected uncertainty of the MODIS retrieval algorithm.

of the total AOT validation. While the two products are not well correlated at the 660 and 675 nm wavelengths ($R^2 = 0.39$, slope = 0.59), the correlation is improved at the 865-870 nm wavelengths ($R^2 = 0.51$, slope = 0.82). Nevertheless, the narrow value range of the asymmetry parameter and the sensitivity test performed for both these parameters (Section 4.2.3), suggest that the uncertainties associated with the MODIS data do not affect significantly the FORTH model results.

Bibliography

Ackerman, S., Frey, R., Strabala, K., Liu, Y., Gumley, L., Baum, B., and Menzel, P.: Discriminating Clear–sky from Cloud with MODIS: Algorithm Theoretical Basis Document (MOD35), Version 6.1, Cooperative Institute for Meteorological Satellite Studies, University of Wisconsin–Madison, 2010.

Barnes, W., Pagano, T., and Salomonson, V.: Prelaunch characteristics of the Moderate Resolution Imaging Spectroradiometer (MODIS) on EOS–AM1, IEEE Transactions on Geoscience and Remote Sensing, 36, 1088–1100, doi:10.1109/36.700993, 1998.

Berk, A., Bernstein, L. S., Anderson, G. P., Acharya, P. K., Robertson, D. C., Chetwynd, J. H., and Adler-Golden, S. M.: MODTRAN Cloud and Multiple Scattering Upgrades with Application to AVIRIS, Remote Sensing of Environment, 65, 367–375, 1998.

Berresheim, H., Plass-Dülmer, C., Elste, T., Mihalopoulos, N., and Rohrer, F.: OH in the coastal boundary layer of Crete during MINOS: Measurements and relationship with ozone photolysis, Atmospheric Chemistry and Physics, 3, 639–649, doi:10.5194/acp-3-639-2003, 2003.

Borbas, E., Seemann, S. W., Kern, A., Moy, L., Li, J., Gumley, L., and Menzel, W. P.: MODIS Atmospheric Profile Retrieval Algorithm Theoretical Basis Document, Collection 6, Version 7, 2011.

Bösenberg, J. and Hoff, R.: Plan for the implementation of the GAW Aerosol Lidar Observation Network GALION, World Meteorological Organization, (WMO/TD No. 1443), Hamburg, Germany, 2007.

Che, H., Zhang, X., Chen, H., Damiri, B., Goloub, P., Li, Z., Zhang, X., Wei, Y., Zhou, H., Dong, F., Li, D., and Zhou, T.: Instrument calibration and aerosol optical depth validation of the China Aerosol Remote Sensing Network, Journal of Geophysical Research: Atmospheres, 114, doi:10.1029/2008JD011030, 2009.

Chu, D. A., Kaufman, Y. J., Ichoku, C., Remer, L. A., Tanré, D., and Holben, B. N.: Validation of MODIS aerosol optical depth retrieval over land, Geophysical Research Letters, 29, 8007, doi:10.1029/2001GL013205, 2002.

Diner, D., Abdou, W., Ackerman, T., Crean, K., Gordon, H. R., Kahn, R. A., Martonchik, J. V., McMuldroch, S., Paradise, S. R., Pinty, B., Verstraete, M. M., Wang, M., and West, R. A.: MISR Level 2 Aerosol Retrieval Algorithm Theoretical Basis, JPL D–11400, Revision G, 2009.

Dubovik, O.: Optimization of Numerical Inversion in Photopolarimetric Remote Sensing, in: Photopolarimetry in Remote Sensing, edited by Videen, G., Yatskiv, Y., and Mishchenko, M., pp. 65–106, Kluwer Academic Publishers, Dordrecht, The Netherlands, 2004.

Dubovik, O. and King, M. D.: A flexible inversion algorithm for retrieval of aerosol optical properties from Sun and sky radiance measurements, Journal of Geophysical Research: Atmospheres, 105, 20 673–20 696, doi: 10.1029/2000JD900282, 2000.

Dubovik, O., Holben, B. N., Lapyonok, T., Sinyuk, A., Mishchenko, M. I., Yang, P., and Slutsker, I.: Non–spherical aerosol retrieval method employing light scattering by spheroids, Geophysical Research Letters, 29, 54–1–54–4, doi:10.1029/2001GL014506, 2002b.

Fotiadi, A., Hatzianastassiou, N., Drakakis, E., Matsoukas, C., Pavlakis, K. G., Hatzidimitriou, D., Gerasopoulos, E., Mihalopoulos, N., and Vardavas, I.: Aerosol physical and optical properties in the Eastern Mediterranean Basin, Crete, from Aerosol Robotic Network data, Atmospheric Chemistry and Physics, pp. 5399–5413, 2006.

Frankenberg, C., Hasekamp, O., O'Dell, C., Sanghavi, S., Butz, A., and Worden, J.: Aerosol information content analysis of multi–angle high spectral resolution measurements and its benefit for high accuracy greenhouse gas retrievals, Atmospheric Measurement Techniques, 5, 1809–1821, doi: 10.5194/amt-5-1809-2012, 2012.

Gerasopoulos, E., Kouvarakis, G., Vrekoussis, M., Kanakidou, M., and Mihalopoulos, N.: Ozone variability in the marine boundary layer of the eastern Mediterranean based on 7–year observations, Journal of Geophysical Research, 110, 1–12, doi:10.1029/2005JD005991, 2005.

Gerasopoulos, E., Kazadzis, S., Vrekoussis, M., Kouvarakis, G., Liakakou, E., Kouremeti, N., Giannadaki, D., Kanakidou, M., Bohn, B., and Mihalopoulos, N.: Factors affecting O_3 and NO_2 photolysis frequencies measured in the eastern Mediterranean during the five-year period 2002-2006, Journal of Geophysical Research: Atmospheres, 117, doi:10.1029/2012JD017622, 2012.

Grey, W. M. F., North, P. R. J., Los, S. O., and Mitchell, R. M.: Aerosol optical depth and land surface reflectance from multiangle AATSR measurements: Global validation and intersensor comparisons, IEEE Transactions on Geoscience and Remote Sensing, 44, 2184–2197, 2006.

Griggs, M.: Measurements of Atmospheric Aerosol Optical Thickness over Water Using ERTS–1 Data, Journal of the Air Pollution Control Association, 25, 622–626, doi:10.1080/00022470.1975.10470118, 1975.

Hashimoto, M., Nakajima, T., Dubovik, O., Campanelli, M., Che, H., Khatri, P., Takamura, T., and Pandithurai, G.: Development of a new data–processing method for SKYNET sky radiometer observations, Atmospheric Measurement Techniques, 5, 2723–2737, doi:10.5194/amt-5-2723-2012, 2012.

Holben, B. N., Eck, T. F., Slutsker, I., Tanré, D., Buis, J. P., Setzer, A., Vermote, E., Reagan, J. A., Kaufman, Y. J., Nakajima, T., Lavenu, F., Jankowiak, I., and Smirnov, A.: AERONET–A Federated Instrument Network and Data Archive for Aerosol Characterization, Remote Sensing of Environment, 66, 1–16, 1998.

Hsu, N., Tsay, S.-C., King, M., and Herman, J.: Aerosol properties over bright–reflecting source regions, IEEE Transactions on Geoscience and Remote Sensing, 42, 557–569, doi:10.1109/TGRS.2004.824067, 2004.

Hsu, N. C., Herman, J. R., Bhartia, P. K., Seftor, C. J., Torres, O., Thompson, A. M., Gleason, J. F., Eck, T. F., and Holben, B. N.: Detection of biomass burning smoke from TOMS measurements, Geophysical Research Letters, 23, 745–748, doi:10.1029/96GL00455, 1996.

Ichoku, C., Chu, D. A., Mattoo, S., Kaufman, Y. J., Remer, L. A., Tanré, D., Slutsker, I., and Holben, B. N.: A spatio-temporal approach for global validation and analysis of MODIS aerosol products, Geophysical Research Letters, 29, 8006, doi:10.1029/2001GL013206, 2002.

Ichoku, C., Remer, L. A., and Eck, T. F.: Quantitative evaluation and intercomparison of morning and afternoon Moderate Resolution Imaging Spectroradiometer (MODIS) aerosol measurements from Terra and Aqua, Journal of Geophysical Research: Atmospheres, 110, doi:10.1029/2004JD004987, 2005.

Ignatov, A. and Stowe, L.: Aerosol Retrievals from Individual AVHRR Channels. Part I: Retrieval Algorithm and Transition from Dave to 6S Radiative Transfer Model, Journal of Atmospheric Sciences, 59, 313–334, 2002.

Kaufman, Y. J., Tanré, D., Remer, L., Vermote, E., Chu, A., and Holben, B. N.: Operational remote sensing of tropospheric aerosol over land from EOS moderate resolution imaging spectroradiometer, Journal of Geophysical Research, 102, 17 051–17 067, 1997a.

Kim, D.-H., Sohn, B. J., Nakajima, T., and Takamura, T.: Aerosol radiative forcing over east Asia determined from ground-based solar radiation measurements, Journal of Geophysical Research: Atmospheres, 110, doi:10.1029/2004JD004678, 2005.

King, M., Menzel, W., Kaufman, Y., Tanré, D., Gao, B.-C., Platnick, S., Ackerman, S., Remer, L., Pincus, R., and Hubanks, P.: Cloud and aerosol properties, precipitable water, and profiles of temperature and water vapor from MODIS, IEEE Transactions on Geoscience and Remote Sensing, 41, 442–458, doi:10.1109/TGRS.2002.808226, 2003.

King, M. D., Tsay, S. C., Platnick, S. E., Wang, M., and Liou, K. N.: Cloud Retrieval Algorithms for MODIS: Optical Thickness, Effective Particle Radius, and Thermodynamic Phase. MODIS Algorithm Theoretical Basis Document No. ATBD–MOD–05, MOD06 - Cloud product, Goddard Space Flight Center, 1997.

King, M. D., Kaufman, Y. J., Tanré, D., and Nakajima, T.: Remote Sensing of Tropospheric Aerosols from Space: Past, Present, and Future., Bulletin of the American Meteorological Society, 80, 2229–2260, 1999.

Kleidman, R. G., O'Neill, N. T., Remer, L. A., Kaufman, Y. J., Eck, T. F., Tanre, D., Dubovik, O., and Holben, B. N.: Comparison of Moderate Resolution Imaging Spectroradiometer (MODIS) and Aerosol Robotic Network (AERONET) remote–sensing retrievals of aerosol fine mode fraction over ocean, Journal of Geophysical Research: Atmospheres, 110, doi:10.1029/2005JD005760, 2005.

Kouvarakis, G., Tsigaridis, K., Kanakidou, M., and Mihalopoulos, N.: Temporal variations of surface regional background ozone over Crete Island in the southeast Mediterranean, Journal of Geophysical Research, 105, 4399–4407, 2000.

Lee, K., Li, Z., Kim, Y., and Kokhanovsky, A.: Atmospheric Aerosol Monitoring from Satellite Observations: A History of Three Decades, in: Atmospheric and Biological Environmental Monitoring, edited by Kim, Y., Platt, U., Gu, M., and Iwahashi, H., pp. 13–38, Springer Netherlands, 2009.

Leroy, M., Deuze, J. L., Breon, F. M., Hautecoeur, O., Herman, M., Buriez, J. C., Tanre, D., Bouffies, S., Chazette, P., and Roujean, J. L.: Retrieval of atmospheric properties and surface bidirectional reflectances over land from POLDER/ADEOS, Journal of Geophysical Research: Atmospheres, 102, 17 023–17 037, doi:10.1029/96JD02662, 1997.

Levy, R. C., Remer, L. A., Mattoo, S., Vermote, E. F., and Kaufman, Y. J.: Second–generation operational algorithm: Retrieval of aerosol properties over land from inversion of Moderate Resolution Imaging Spectroradiometer spectral reflectance, Journal of Geophysical Research: Atmospheres, 112, doi:10.1029/2006JD007811, 2007.

Levy, R. C., Remer, L. A., Tanré, D., Mattoo, S., and Kaufman, Y. J.: Algorithm for remote sensing of tropospheric aerosol over dark targets from MODIS: Collection 005 and 051: Revision 2, February 2009, 2009.

Levy, R. C., Remer, L. A., Kleidman, R. G., Mattoo, S., Ichoku, C., Kahn, R., and Eck, T. F.: Global evaluation of the Collection 5 MODIS dark–target aerosol products over land, Atmospheric Chemistry and Physics, 10, 10 399–10 420, doi:10.5194/acp-10-10399-2010, 2010.

Martonchik, J. V., Diner, D. J., Kahn, R. A., Ackerman, T. P., Verstraete, M. M., Pinty, B., and Gordon, H. R.: Techniques for the retrieval of aerosol properties over land and ocean using multiangle imaging, IEEE Transactions on Geoscience and Remote Sensing, 36, 1212–1227, 1998.

Menzel, W. P., Smith, W. L., and Stewart, T. R.: Improved Cloud Motion Wind Vector and Altitude Assignment Using VAS, Journal of Applied Meteorology, 22, 377–384, 1983.

Menzel, W. P., Frey, R. A., and Baum, B. A.: Cloud Top Properties and Cloud Phase Algorithm Theoretical Basis Document, Version 8, Cooperative Institute for Meteorological Satellite Studies, University of Wisconsin–Madison, 2010.

Mihalopoulos, N., Stephanou, E., Kanakidou, M., Pilitsidis, S., and Bousquet, P.: Tropospheric aerosol ionic composition in the Eastern Mediterranean region, Tellus B, 49, 314–326, 1997.

MODIS: Technical Specifications, URL `http://modis.gsfc.nasa.gov/about/specifications.php`, accessed: 2013–06–19, 2013.

Nagaraja Rao, C. R., Stowe, L. L., and McClain, E. P.: Remote sensing of aerosols over the oceans using AVHRR data - Theory, practice and applications, International Journal of Remote Sensing, 10, 743–749, 1989.

Nakajima, T., Tanaka, M., and Yamauchi, T.: Retrieval of the optical properties of aerosols from aureole and extinction data, Applied Optics, 22, 2951–2959, 1983.

Nakajima, T., Tonna, G., Rao, R., Boi, P., Kaufman, Y., and Holben, B.: Use of sky brightness measurements from ground for remote sensing of particulate polydispersions, Applied Optics, 35, 2672–2686, 1996.

North, P., Grey, W., Heckel, A., Fischer, J., Preusker, R., and Brockmann, C.: MERIS/AATSR Synergy Algorithms for Cloud Screening, Aerosol Retrieval, and Atmospheric Correction. Algorithm Theoretical Basis Document Land Aerosol and Surface Reflectance ATBD. ESRIN Contract No. 21090/07/I–LG., 2009.

Pappalardo, G., Bösenberg, J., Amodeo, A., Ansmann, A., Apituley, A., Arboledas, L. A., Balis, D., Böckmann, C., Chaikovsky, A., Comeron, A., D'Amico, G., Freudenthaler, V., Grigorov, I., Hansen, G., Linnè, H., Kinne, S., Mattis, I., Mona, L., Mueller, D., Mitev, V., Nicolae, D., Papayannis, A., Perrone, M. R., Pietruczuk, A., Pujadas, M., Putaud, J.-P., Ravetta, F., Rizi, V., Simeonov, V., Spinelli, N., Trickl, T., Wandinger, U., and Wiegner, M.: EARLINET: the European Aerosol Research Lidar Network for the Aerosol Climatology on Continental Scale, in: American Institute of Physics Conference Series, edited by Nakajima, T. and Akemi Yamasoe, M., vol. 1100 of *American Institute of Physics Conference Series*, pp. 189–192, doi:10.1063/1.3116946, 2009.

Parkinson, C. and Greenstone, R.: EOS Data Products Handbook, vol. 2, Goddard Space Flight Center and Earth Observing System Program, NASA Goddard Space Flight Center, 2000.

Platnick, S., King, M., Ackerman, S., Menzel, W., Baum, B., Riedi, J., and Frey, R.: The MODIS cloud products: algorithms and examples from Terra, IEEE Transactions on Geoscience and Remote Sensing, 41, 459–473, doi:10.1109/TGRS.2002.808301, 2003.

Remer, L., Kaufman, Y. J., Tanré, D., Mattoo, S., Chu, D. A., Martins, J. V., Li, R.-R., Ichoku, C., Levy, R. C., Kleidman, R. G., Eck, T. F., Vermote, E., and Holben, B. N.: The MODIS Aerosol Algorithm, Products, and Validation, Journal of the Atmospheric Sciences, 62, 947–973, 2005.

Remer, L. A., Tanré, D., Kaufman, Y. J., Ichoku, C., Mattoo, S., Levy, R., Chu, D. A., Holben, B., Dubovik, O., Smirnov, A., Martins, J. V., Li, R.-R., and Ahmad, Z.: Validation of MODIS aerosol retrieval over ocean, Geophysical Research Letters, 29, MOD3–1–MOD3–4, doi:10.1029/2001GL013204, 2002.

Salomonson, V. V., Barnes, W., Maymon, P. W., Montgomery, H. E., and Ostrow, H.: MODIS: advanced facility instrument for studies of the Earth as a system, IEEE Transactions on Geoscience and Remote Sensing, 27, 145–153, doi:10.1109/36.20292, 1989.

Santese, M., De Tomasi, F., and Perrone, M. R.: Moderate Resolution Imaging Spectroradiometer (MODIS) and Aerosol Robotic Network (AERONET) retrievals during dust outbreaks over the Mediterranean, Journal of Geophysical Research, 112, 1–14, doi:10.1029/2007JD008482, 2007.

Seemann, S. W., Li, J., Menzel, W. P., and Gumley, L. E.: Operational Retrieval of Atmospheric Temperature, Moisture, and Ozone from MODIS Infrared Radiances., Journal of Applied Meteorology, 42, 1072–1091, 2003.

Seemann, S. W., Borbas, E. E., Li, J., Menzel, W., and Gumley, L. E.: MODIS Atmospheric Profile Retrieval Algorithm Theoretical Basis Document, Version 6, Space Science and Engineering Center, University of Wisconsin–Madison, 2006.

Shaw, G. E.: Sun Photometry, Bulletin of the American Meteorological Society, 64, 4–10, 1983.

Sinyuk, A., Dubovik, O., Holben, B., Eck, T. F., Breon, F.-M., Martonchik, J., Kahn, R., Diner, D. J., Vermote, E. F., Roger, J.-C., Lapyonok, T., and Slutsker, I.: Simultaneous retrieval of aerosol and surface properties from a combination of AERONET and satellite data, Remote Sensing of Environment, 107, 90–108, doi:10.1016/j.rse.2006.07.022, 2007.

Stowe, L. L., Ignatov, A. M., and Singh, R. R.: Development, validation, and potential enhancements to the second–generation operational aerosol product at the National Environmental Satellite, Data, and Information Service of the National Oceanic and Atmospheric Administration, Journal of Geophysical Research: Atmospheres, 102, 16 923–16 934, doi:10.1029/96JD02132, 1997.

Sugimoto, N., Matsui, I., Shimizu, A., Nishizawa, T., Hara, Y., and Uno, I.: Lidar network observation of tropospheric aerosols, in: Society of Photo–Optical Instrumentation Engineers (SPIE) Conference Series, vol. 7860 of *Society of Photo–Optical Instrumentation Engineers (SPIE) Conference Series*, doi:10.1117/12.869900, 2010.

Tanré, D., Kaufman, Y. J., Herman, M., and Mattoo, S.: Remote sensing of aerosol properties over oceans using the MODIS/EOS spectral radiances, Journal of Geophysical Research, 102, 16 971–16 988, 1997.

Torres, O., Bhartia, P. K., Herman, J. R., Sinyuk, A., Ginoux, P., and Holben, B.: A Long–Term Record of Aerosol Optical Depth from TOMS Observations and Comparison to AERONET Measurements., Journal of Atmospheric Sciences, 59, 398–413, 2002.

Torres, O., Bhartia, P. K., Sinyuk, A., Welton, E. J., and Holben, B.: Total Ozone Mapping Spectrometer measurements of aerosol absorption from space: Comparison to SAFARI 2000 ground–based observations, Journal of Geophysical Research: Atmospheres, 110, doi:10.1029/2004JD004611, 2005.

Volz, F. E.: Photometer mit Selen–photoelement zurspektralen Messung der Sonnenstrahlung und zer Bestimmung der Wallenlangenabhangigkeit der Dunsttrubung, Arch. Meteorol. Geophys. Bioklim., B10, 100–131, 1959.

Welton, E. J., Campbell, J. R., Spinhirne, J. D., and Scott, V. S.: Global monitoring of clouds and aerosols using a network of micro–pulse lidar systems, in: Lidar remote sensing for industry and environment monitoring, vol. 4153 of *Society of Photo–Optical Instrumentation Engineers*, pp. 151–158, 2001.

Winker, D. M., Vaughan, M. A., Omar, A., Hu, Y., Powell, K. A., Liu, Z., Hunt, W. H., and Young, S. A.: Overview of the CALIPSO Mission and CALIOP Data Processing Algorithms, Journal of Atmospheric and Oceanic Technology, 26, 2310–2323, doi:10.1175/2009JTECHA1281.1, 2009.

Winker, D. M., Pelon, J., Coakley, Jr., J. A., Ackerman, S. A., Charlson, R. J., Colarco, P. R., Flamant, P., Fu, Q., Hoff, R. M., Kittaka, C., Kubar, T. L., Le Treut, H., McCormick, M. P., Mégie, G., Poole, L., Powell, K., Trepte, C., Vaughan, M. A., and Wielicki, B. A.: The CALIPSO Mission: A Global 3D View of Aerosols and Clouds, Bulletin of the American Meteorological Society, 91, 1211–1229, doi:10.1175/2010BAMS3009.1, 2010.

Wylie, D. P. and Menzel, W. P.: Eight Years of High Cloud Statistics Using HIRS, Journal of Climate, 12, 170–184, 1999.

Chapter 3

The FORTH Radiative Transfer Model

3.1 Introduction

The FORTH model is a deterministic spectral radiative transfer model for computing the solar radiation budget components. Evolution of the model and its characteristics during the last 30 years can be traced in numerous past studies.

A one–dimensional spectral radiative–convective (RC) model with parameterizations, was developed by Vardavas and Carver (1984), to model both solar and terrestrial radiation transfer. Sample computations for the present Earth atmosphere were compared against contemporary studies, in terms of incoming and outgoing fluxes, heating and cooling rates, cloud effects, global albedo and the doubling of atmospheric carbon dioxide (CO_2), ammonia (NH_3) and methane (CH_4). This model formed the basis for later modifications and improvements, which led to the present FORTH model versions.

A simpler version of the RC model was developed by Vardavas (1987a), for computing the daily net all–wave radiation flux above a water surface, given the prevailing atmospheric conditions. This version was used in Vardavas (1987b) for the estimation of seasonal variations of net solar and net terrestrial radiation, and the Penman potential evaporation (Penman, 1948), for a water body located in northern Australia. Model results of radiation fluxes and evaporation were found to be in very good agreement with corresponding results from field studies and measurements. This version was also applied to four Australian lakes, representing different climatic conditions, by Vardavas and Fountoulakis (1996), and to Messara Valley of Crete (Vardavas et al., 1997), along with the modified version developed by Vardavas and Koutoulaki (1995).

Vardavas and Koutoulaki (1995) used the solar radiation transfer component of the model to estimate the radiation budget at the Earth's surface and at TOA for the northern hemisphere. The SW radiation was divided into two spectral bands, one for essentially the UV-visible wavelengths ($\lambda < 0.85\,\mu\text{m}$) accounting for about 60% of total solar incoming radiation, and a second band for the NIR wavelengths ($0.85\,\mu\text{m} \leq \lambda \leq 5\,\mu\text{m}$) accounting for about 40% of total solar radiation. Long term climatological data were used as input to the model, and the output was computed on a mean monthly basis for 10° latitudinal zones. A very good agreement of the model output TOA fluxes with the corresponding Earth Radiation Budget Experiment (ERBE) satellite data (Li and Leighton, 1993) was found. This version of the solar radiation transfer model was also tested according to the Intercomparison of Radiation Codes in Climate Models (ICRCCM) program (Fouquart and Bonnel, 1991). The model results were found to agree very well with the corresponding line–by–line model results of others.

Hatzianastassiou and Vardavas (1999, 2001) modified the previous model version, in order to incorporate the then available climatological data from the International Satellite Cloud Climatology Project (ISCCP), described in Schiffer and Rossow (1983) and Rossow and Schiffer (1991), as well as water vapour and temperature input data from the NCEP and National Center for Atmospheric Research (NCAR) data set. Using ISCCP–C2 and NCEP/NCAR data, available at $2.5° \times 2.5°$ spatial resolution, they calculated monthly mean radiation fluxes over both hemispheres, for the 1983–1990 period. Using the standard ISCCP cloud droplet spectrum and a Mie calculations code (Hatzianastassiou et al., 1997, 1998), they also incorporated in the model the spectral cloud optical properties for the entire UV–Visible and NIR spectrum. An equation for the estimation of the radiative forcing of a scattering and absorbing aerosol layer was also included in the model. The model surface radiation fluxes were validated through intercomparison with other model results, while the TOA outgoing fluxes were also validated against the ERBE corresponding data. The agreement between model output and ERBE data was improved, compared to previous model versions.

The same broadband model version was used in Hatzianastassiou et al. (2004a), for the estimation of the global distribution of the Earth's SW radiation budget at TOA, at $2.5° \times 2.5°$ spatial resolution and on a monthly mean basis, for the 1984–1997 period. Input data from the D2 series of ISCCP (Rossow et al., 1996), which were improvements over the previous C–series version, were supplemented by NCEP/NCAR atmospheric water vapour and temperature data. Aerosol effects on the SW radiation budget were incorporated in the model using the modified two–stream approximation, with aerosol optical parameters input data taken from the GADS (Köpke et al., 1997). Model results allowed the examination of seasonal and geographical distributions, intercomparison with ERBE data and results from other studies, trends and a sensitivity analysis of the TOA SW radiation budget. A decreasing trend in the tropical mean outgoing SW radiation at TOA was further investigated by Fotiadi et al. (2005). The corresponding model results at the Earth's surface (Hatzianastassiou et al., 2005), computed for the period 1984–2000, were validated at the grid cell level against two station networks, the Baseline Surface Radiation Network (BSRN, Ohmura et al. 1998) and the Global Energy Balance Archive (GEBA, Gilgen and Ohmura, 1999).

The same model version, along with the LW component and models for the estimation of heat fluxes and heat storage were used to study the heat budget of the Mediterranean (Matsoukas et al., 2005), and the Red and Black seas (Matsoukas et al., 2007). Additionally, correlations between the El Niño Southern Oscillation (ENSO) and surface SW radiation patterns over the tropical Pacific (Pavlakis et al., 2008), as well the effect of Arctic sea–ice on the absorbed solar radiation at the surface (Matsoukas et al., 2010), have been studied.

The importance of including aerosol effects in the model calculations was further investigated by Hatzianastassiou et al. (2004b). Using the spectral version of the model (computations at 115 wavelengths in the 0.20–0.85 µm), along with data from GADS, ISCCP–D2 and NCEP/NCAR, as described above, the aerosol direct radiative effect in the UV–Visible, under clear skies and for summer and winter conditions, was estimated on a global scale at 2.5° × 2.5° pixel size and compared against other similar studies. A sensitivity analysis on the aerosol DRE was also performed (Hatzianastassiou et al., 2004c), showing that the high spectral resolution for the estimation of aerosol effects is crucial, since the optical properties of aerosols are spectrally variable, making their interaction with solar radiation very sensitive to wavelength. The use of the spectral model for the study of aerosol effects on a global scale was extended in the solar NIR (Hatzianastassiou et al., 2007a), and complemented by Hatzianastassiou et al. (2007b), whereby global DRE monthly climatologies were produced, based on the 1984–1995 period, for winter and summer, for both clear and all–sky conditions. Computations were performed on a daily basis and at 1° × 1° spatial resolution.

Recently, the spectral version of the model was used for the computation of potential evaporation over land at 2.5° × 2.5° spatial resolution for the 25–year period 1983–2008 using ISCCP–D2, NCEP/NCAR and GADS data (Matsoukas et al., 2011), while MODIS Level 3 aerosol data were used along with GADS data, for the computation of the aerosol DRE on the solar radiation over the broader Mediterranean basin, on a monthly basis, for the 2000–2007 period and at 2.5° × 2.5° spatial resolution (Papadimas et al., 2012). The performance of the spectral model has recently been examined, along with 30 other global model radiative transfer schemes, during the aerosol model intercomparison initiative (AeroCom) Radiative Transfer Experiment (Randles et al., 2013). The model results showed very good agreement between the model and the corresponding benchmark results from high resolution, line–by–line radiation models.

The present, spectral version of the model has been developed to incorporate Level 2 daily data from the MODIS sensors on board NASA's Terra and Aqua satellites. The model spatial resolution has been increased, reaching up to 10 km × 10 km pixel size. This high spatial resolution offers the possibility of distinguishing patterns that could not be obvious in previous studies, where the resolution was lower, improving also the procedure of model validation against station measurements. The new version has also been adjusted to run in two separate modes, one for the evaluation of mean daily results and another for computations regarding the specific satellite overpass time. Modifications were also made to exploit the spectral resolution available from MODIS, regarding aerosol parameters and the surface reflectance. All model input data come from the MODIS daily Level 2 Atmosphere Products (Section 2.2), except for the aerosol single scattering albedo, which is supplemented by AERONET station data. The combination of MODIS Level 2 data set completeness, regarding the model required input data, along with their high spatial and temporal resolution, and the time period covered by MODIS measurements (2000–2012), renders the present model version suitable for studies over specific sites of interest, for both time-series/trends analysis and case studies.

3.2 Model overview

The model computations are performed separately for 118 wavelengths in the range 0.2–1.0 µm, and 10 spectral bands in the range 1.0–10 µm. The incoming solar irradiance at the top of the atmosphere is computed based on the spectral profile of Gueymard (2004), using a solar constant $S_{\odot} = 1367$ W m^{-2} (Hartmann, 1994; Willson, 1997) corrected for the Earth's elliptical orbit. For each wavelength and spectral band, a set of monochromatic radiative flux transfer equations is solved for an absorbing and multiple–scattering atmosphere, using the Delta–Eddington approximation method (Joseph et al., 1976) based on the Henyey–Greenstein phase function, which is an extension

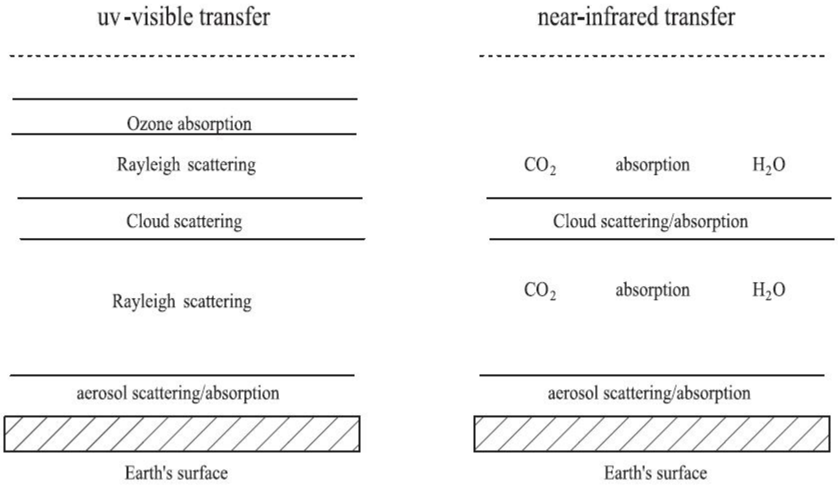

Figure 3.1: Scattering and absorption of UV–Visible and NIR solar radiation by the model atmospheric layers (Vardavas and Taylor, 2011).

of the Eddington method described in Shettle and Weinman (1970).

The model takes into account physical parameters and processes that affect significantly the solar radiation transfer: absorption by O_3 in the UV region between 0.2 and 0.35 µm (Hartley–Huggins bands) and in the visible, between 0.45 and 0.85 µm (Chappuis bands), and absorption in the NIR by water vapor (H_2O), methane (CH_4) and carbon dioxide (CO_2). The model also includes scattering and absorption by clouds and aerosols, Rayleigh scattering and surface reflection. The various atmospheric, cloud and surface properties required as input to the model, are shown in Table 3.1.

Depending on the part of the solar spectrum considered, the atmosphere

Table 3.1: Input data required to model the shortwave radiation budget.

Cloud Properties	Atmospheric Properties	Surface Properties
Amount	Temperature	Pressure
Scattering optical depth	Specific humidity	Temperature
Absorption optical depth	Atmospheric gases	Albedo
Top pressure	Aerosol optical depth	
Physical thickness	Aerosol asymmetry parameter	
Phase	Aerosol single scattering albedo	

is divided into different number of layers which determine the solar radiation transfer. In the UV–visible region, five layers are considered: an aerosol layer above the Earth's surface, Rayleigh scattering layers below and above a cloud layer and an ozone layer at TOA. In the NIR part the layers are: CO_2 and H_2O absorbing layers above and below clouds and a scattering and absorbing aerosol layer above the surface. The atmospheric layers considered by the model are shown in Figure 3.1. Model output fluxes include TOA incoming radiation, TOA outgoing, atmospheric absorption, Downwelling SW Radiation (DSR), surface absorption and net TOA incoming radiation.

Reflection of incident solar radiation from the Earth's surface is taken into account and the surface reflectivity, R_g, is computed considering four general types of surface: land, ocean, snow and ice. Then

$$R_g = f_{land}R_l + f_{ocean}R_o + f_{snow}R_s + f_{ice}R_i, \tag{3.1}$$

where f_i is the fractional coverage of the pixel's surface by each type i of reflecting surface. The ocean reflectivity, R_o, is computed using Fresnel reflection corrected for a non–smooth surface.

3.3 Incoming solar radiation

The solar spectrum used by the model is taken from Gueymard (2004). The original spectrum from Gueymard covers the spectral region from 0.5 nm to 280 nm in 1 nm steps, 280 to 400 nm in 0.5 nm steps, from 400 nm to 1705 nm in 1 nm steps, 5 nm steps from 1705 nm to 4000 nm, and variable steps beyond 4000 nm. The Gueymard solar spectrum is interpolated in the 118 wavelengths and 10 spectral bands used by the model. Figure 3.2 shows the original Gueymard spectrum (upper panel) and the interpolated values used as input to the model (lower panel). The correction for the Earth's elliptical orbit, described in this Section, is analysed in detail in Vardavas and Taylor (2011).

Due to the Earth's elliptical orbit, the incoming solar radiation at TOA varies with the time of year according to

$$S(t) = S_\odot \left(\frac{\bar{r}}{r(t)}\right)^2, \tag{3.2}$$

where $r(t)$ is the Sun–Earth distance and $\bar{r}$ is the mean Sun–Earth distance, equal to $0.5(r_p+r_a) = \alpha$ with r_p, r_a, the corresponding distances at perihelion (shortest) and aphelion (largest) and α the semi–major axis of the Earth's elliptical orbit.

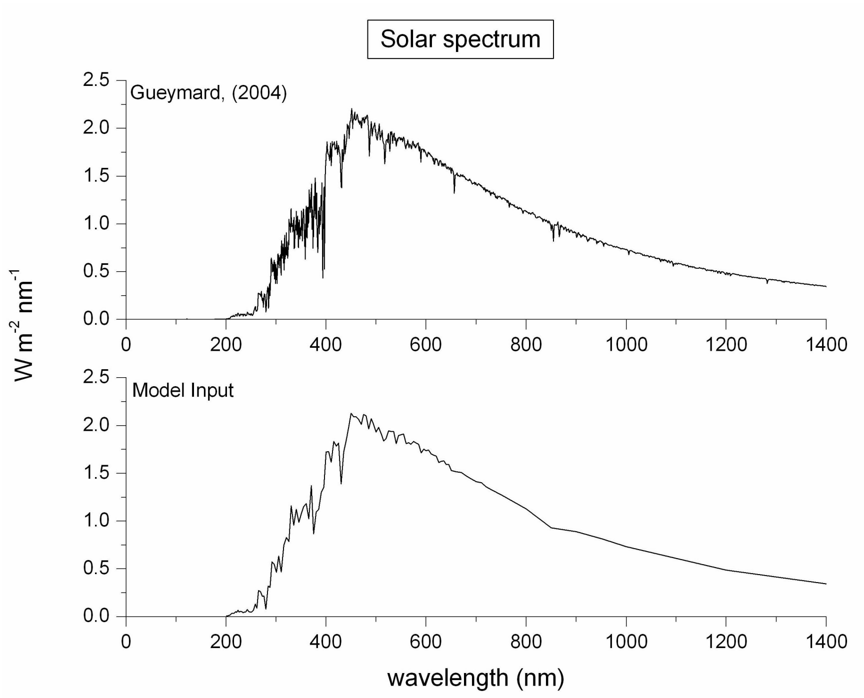

Figure 3.2: Solar spectrum, as given by Gueymard (2004) and the interpolated model input.

Representing the apparent orbit of the Sun in a geocentric system, the Earth's longitude of perihelion, $\bar{\omega}$, varies from 0 to 360° in about 21000 years, and is given by

$$\bar{\omega} = \bar{\omega}_0 + 9.44 \times 10^{-5}\pi(year - 2000), \tag{3.3}$$

where $\bar{\omega}_0 = 0.5725\pi$ is the value of $\bar{\omega}_0$ at the perigee of the celestial sphere, which corresponds to the perihelion of the Earth's orbit.

Assuming a fictitious mean Sun moving on the celestial equator at a uniform rate (i.e. circular motion), the mean Sun anomaly, g, is given by

$$g = L - \omega, \tag{3.4}$$

where L is the mean longitude of the Sun, given by

$$L(t) = L_0 + \frac{2\pi t_d}{P}, \tag{3.5}$$

with P the period of the Earth's orbit (365.256 days) and t_d the time in days from January 1$^{\text{st}}$, given by

$$t_d = n - 1 + t/24, \tag{3.6}$$

$n = 1$ on January 1^{st} and t is UT in hours. In Equation (3.4), ω is the solar longitude of the perigee, equal to $\bar{\omega} + \pi$. The true Sun anomaly, v, corresponding to the arc formed by the perihelion and the Sun's current position, is given by

$$v = g + 2e \sin g + \frac{5e^2}{4} \sin 2g, \tag{3.7}$$

where e is the eccentricity of the Earth, with a present mean value of 0.0167. The equation for the Sun–Earth distance is then given by

$$r = \frac{\alpha(1 - e^2)}{1 + e \cos v}. \tag{3.8}$$

The incoming solar flux, $F_{\odot}^{\downarrow}(t)$, above the Earth's atmosphere, at a particular location on Earth and at a particular time, is given by

$$F_{\odot}^{\downarrow}(t) = S_{\odot}\mu \left(\frac{\bar{r}}{r(t)} \right)^2, \tag{3.9}$$

with $\mu = \cos z$, z the solar zenith angle. In the case of model runs on an instantaneous basis, the solar zenith angle is available from MODIS for each pixel covered and corresponding time. In general, $\mu(t)$ can be calculated from

$$\mu(t) = A + B \cos\left[h(t)\right], \tag{3.10}$$

with

$$A = \sin\theta \sin\delta, \tag{3.11}$$

$$B = \cos\theta \cos\delta, \tag{3.12}$$

where θ is the latitude, δ the Sun's declination and h the hour angle. The Sun's declination is given by

$$\delta = \arcsin\left(\sin\varepsilon \sin\lambda\right), \tag{3.13}$$

where ε is the obliquity of the ecliptic, given by

$$\varepsilon(year) = \varepsilon_0 - 7.22 \times 10^{-7}\pi(year - 2000), \tag{3.14}$$

with $\varepsilon_0 = 0.13022\pi$, in the year 2000 AD, and $\lambda = v + \omega$, thus

$$\lambda = L + 2e \sin g + \frac{5e^2}{4} \sin 2g. \tag{3.15}$$

The hour angle h in Equation (3.10) is computed from

$$h(t) = \left(t - 12 + \frac{E}{15}\right)\frac{\pi}{12}, \tag{3.16}$$

where E, the equation of time, is equal to $L - \mathsf{a}$, with a, the solar right ascension, calculated from

$$\mathsf{a} = \lambda - u \sin 2\lambda + \frac{u^2}{2} \sin 4\lambda, \tag{3.17}$$

with

$$u = \tan^2\left(\frac{\varepsilon}{2}\right). \tag{3.18}$$

In the case of model runs on a mean daily basis, the incoming mean daily solar flux at TOA, on day n, is calculated from

$$F_{\odot}^{\downarrow}(t) = S_{\odot}\mu_n d_n \left(\frac{\bar{r}}{r_n}\right)^2, \tag{3.19}$$

where d_n is the day length, equal to $24H_n/\pi$, and the hour angle H_n is given by

$$H_n = \arccos\left(-\tan\theta \tan\delta\right). \tag{3.20}$$

The mean daily cosine of the solar zenith angle, μ_n, is calculated from

$$\mu_n = A_n + \frac{B_n \sin H_n}{H_n}. \tag{3.21}$$

3.4 Ultraviolet and visible molecular absorption and scattering

3.4.1 Ultraviolet and visible molecular absorption

The 0.2–1.0 µm spectral region corresponds to about 69% of the incoming solar radiation. The main atmospheric absorbers of solar UV–Visible radiation, included in the model, are O_3, O_2 and CO_2.

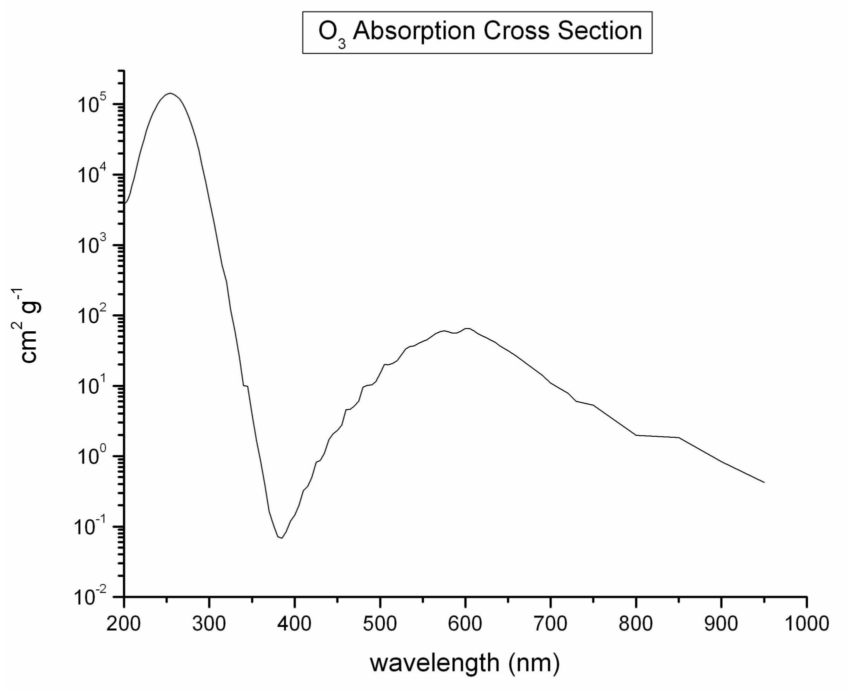

Figure 3.3: O_3 absorption cross section from Sander et al. (2006), interpolated at the model 118 wavelengths.

Ozone absorbs strongly in the wavelength region between 0.2 and 0.3 µm (Hartley bands). From 0.3 to 0.35 µm it absorbs in the relatively weak and temperature dependent Huggins bands. It also absorbs in the visible region between 0.41 and 0.85 µm in the Chappuis bands (see e.g. Vardavas and Taylor, 2011). Ozone absorption cross section is taken from the Jet Propulsion Laboratory (JPL) Chemical Kinetics and Photochemical Data for Use in Atmospheric Studies (Sander et al., 2006) and interpolated at the 118 model wavelengths. Figure 3.3 shows the corresponding spectral distribution in cm^2 g^{-1}.

The temperature dependence of the O_3 absorption cross section, $\sigma_\lambda(T)$, in the Hartley–Huggins bands, is taken into account according to Vardavas and Carver (1984), based on data from Bass and Paur (1981), whereby

$$\sigma_\lambda(T) = \sigma_\lambda(295\,\mathrm{K})r_\lambda(T), \tag{3.22}$$

with

$$r_\lambda(T) = \left\{ \begin{array}{ll} a_\lambda^{b+1}, & T \geq 243\,\mathrm{K} \\ a_\lambda e^{0.0477b}, & T < 243\,\mathrm{K}, \end{array} \right. \tag{3.23}$$

where

$$a_\lambda(T) = \begin{cases} -111.11\lambda^2 + 62.22\lambda - 7.711, & 0.28\,\mu\text{m} \le \lambda \le 0.35\,\mu\text{m} \\ 1, & 0.20\,\mu\text{m} \le \lambda < 0.28\,\mu\text{m}, \end{cases} \tag{3.24}$$

$$b = \frac{243 - T}{52}. \tag{3.25}$$

For the calculation of the surface O_3 photolysis rate, described in Chapter 5, Section 5.2, the temperature dependence of the O_3 absorption cross section was taken into account using linear interpolation between the two temperature values (at T=218 K and T=293–298 K) available from the Jet Propulsion Laboratory Chemical Kinetics and Photochemical Data for Use in Atmospheric Studies (Table 4–5 in Sander et al., 2006). In the model calculations, total ozone is distributed at the top atmospheric layer. Total ozone amount is available from MODIS Atmosphere Level 2 Products on a daily basis (Section 2.2.3).

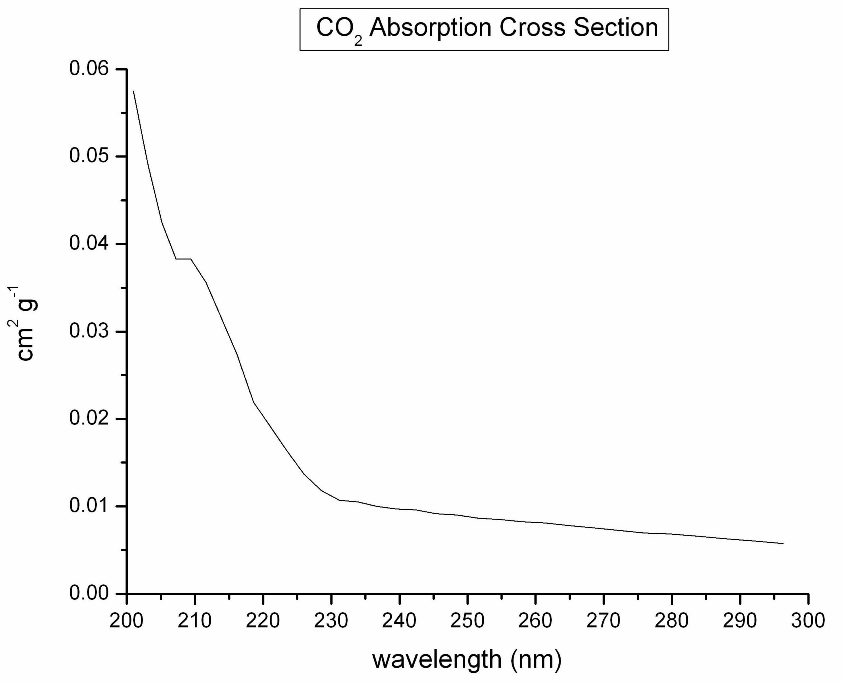

Figure 3.4: CO_2 absorption cross section (Karaiskou et al., 2004) interpolated at the model wavelengths.

While CO_2 is an important absorber in the NIR region, it also absorbs weakly in the UV region. Figure 3.4 shows the CO_2 absorption cross section in the UV region (cm^2 g^{-1}) used by the model. CO_2 absorption cross section data were taken from Karaiskou et al. (2004).

For CO_2, a total atmospheric amount is taken equal to 0.59 g cm^{-2}, corresponding to a fixed mixing ratio of 379 parts per million by volume (ppmv, 2005 value). CO_2 is distributed in all atmospheric layers, in proportion to the pressure differential.

Absorption by O_2 also takes place in the UV region, between 185 and 242 nm. This spectral interval corresponds to the Herzberg dissociation continuum, and is the main source of O atoms for altitudes below 60 km in the Earth's atmosphere (see e.g. Vardavas and Taylor, 2011). The absorption cross section of O_2 (cm^2) as a function of wavelength for the Herzberg continuum is given by

$$\sigma(x) = 7.5 \times 10^{-24} x \exp[-50(\ln x)^2], \tag{3.26}$$

where $x = 199/\lambda$, with λ in nm (Nicolet and Kennes, 1986). Figure 3.5 shows the corresponding spectral distribution (cm^2 g^{-1}) in the 200–242 nm region, where model computations take place.

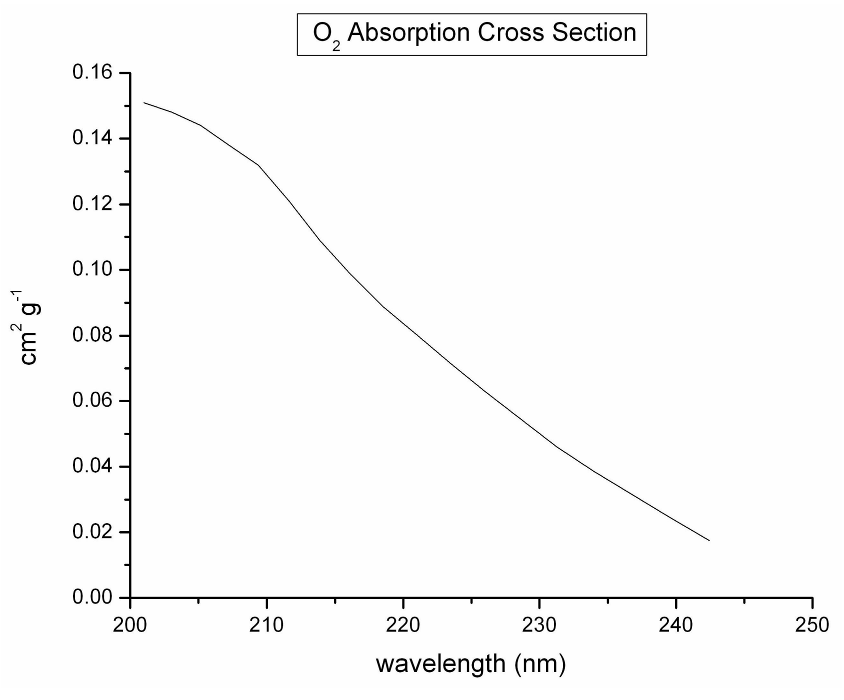

Figure 3.5: O_2 absorption cross section (Herzberg continuum), based on the Nicolet and Kennes (1986) formula.

O_2 is also distributed in all atmospheric layers in proportion to the pressure differential, while a constant amount, corresponding to 21% mixing ratio, is used.

The optical depth for molecular absorption, τ_{ma}, for each atmospheric layer and spectral wavelength, is computed as the sum of the products of the absorption cross sections σ_i (cm^2 g^{-1}) and the corresponding amounts y_i (g cm^{-2}):

$$\tau_{ma} = \sum \sigma_i y_i \tag{3.27}$$

3.4.2 Rayleigh scattering

As described in Vardavas and Taylor (2011), Rayleigh scattering by atmospheric molecules is important for wavelengths up to 1.0 µm, as the Rayleigh scattering cross–section decreases rapidly with wavelength. The real part of the refractive index of an atmosphere consisting of scattering molecules that are far apart is given by

$$n = 1 + 2\pi\alpha N, \tag{3.28}$$

where n is the number density of the molecules and α is called the polarizability of the molecules (van de Hulst, 1981). The Rayleigh scattering cross–section for a molecule is given by

$$\sigma_R = \frac{8\pi}{3} k^4 \alpha^2 \delta, \tag{3.29}$$

where $k = 2\pi/\lambda$, and λ is the wavelength in vacuum. The original result of Rayleigh was for spherical top molecules, so there is a small but significant correction δ for non–spherical molecules. The refractive indices of molecular gases at STP are tabulated, for example, in Allen (1973) and have the form

$$n_{STP} - 1 = A\left(1 + \frac{B}{\lambda^2}\right), \tag{3.30}$$

where λ is in µm. Thus, from (3.28) and (3.30) we can write

$$\alpha = \frac{A}{2\pi N_{STP}}\left(1 + \frac{B}{\lambda^2}\right). \tag{3.31}$$

If we replace k in the expression for the cross–section (3.29) we have

$$\sigma_R = \frac{128\pi^5\delta}{3\lambda^2}\alpha^2, \tag{3.32}$$

Table 3.2: Coefficients for computing the Rayleigh scattering cross–sections (Vardavas and Taylor, 2011)

Molecule	$A(\times 10^{-5})$	$B(\times 10^{-3})$	Δ	δ
N_2	29.06	7.70	0.0305	1.05
O_2	26.63	5.07	0.0540	1.10
Ar	29.06	7.70	0.0305	1.05
CO_2	43.9	6.4	0.0805	1.15
O_3	50.5	0.0	0.1189	1.23
H_2O	26.1	0.0	0.0199	1.034

and the cross–section (cm^2) can be computed from

$$\sigma_R = 4.577 \times 10^{-21} \frac{\delta}{\lambda^4} \left[A \left(1 + \frac{B}{\lambda^2} \right) \right]^2 \tag{3.33}$$

where λ is in µm, the coefficients A and B are tabulated in Allen (1973) for various molecules, while $\delta = (6+3\Delta)(6-7\Delta)$, where Δ is the depolarization factor, whose values are given in Table 3.2, together with the coefficients A and B for the molecules considered in the model.

In Figure 3.6, the Rayleigh scattering cross–sections (cm^2 g^{-1}) of these molecules in the 0.2–1.0 µm spectral region are shown.

For a mixture of atmospheric gases we obtain the Rayleigh cross–section from

$$\sigma_R = \sum_m \sigma_{Rm} n_m \tag{3.34}$$

where n_m is the mixing ratio by volume, of molecules m.

For the model computations, all Rayleigh scattering gases except O_3 are distributed in all atmospheric layers in proportion to the pressure differential. For the main atmospheric constituents, namely N_2, O_2 and Ar, constant mixing ratios are assumed, corresponding to 78%, 21% and 1%, respectively.

Table 3.3 summarizes the absorbing and scattering atmospheric gases in the UV–Visible spectral region, taken into account by the model. In order to assess the relative importance of each atmospheric gas, the downwelling UV–Visible radiation at the surface over HCMR station was calculated on a daily basis, for the period 2000–2010, first including all atmospheric gases and then disregarding each gas separately. Table 3.3 shows the resulting mean and standard deviation values (in percent) of the surface downwelling UV–Visible radiation attenuation due to each molecular gas. It is obvious from Table 3.3 that total ozone is the most important absorber, while the contributions of Ar, CO_2 and H_2O in this spectral region are almost insignificant.

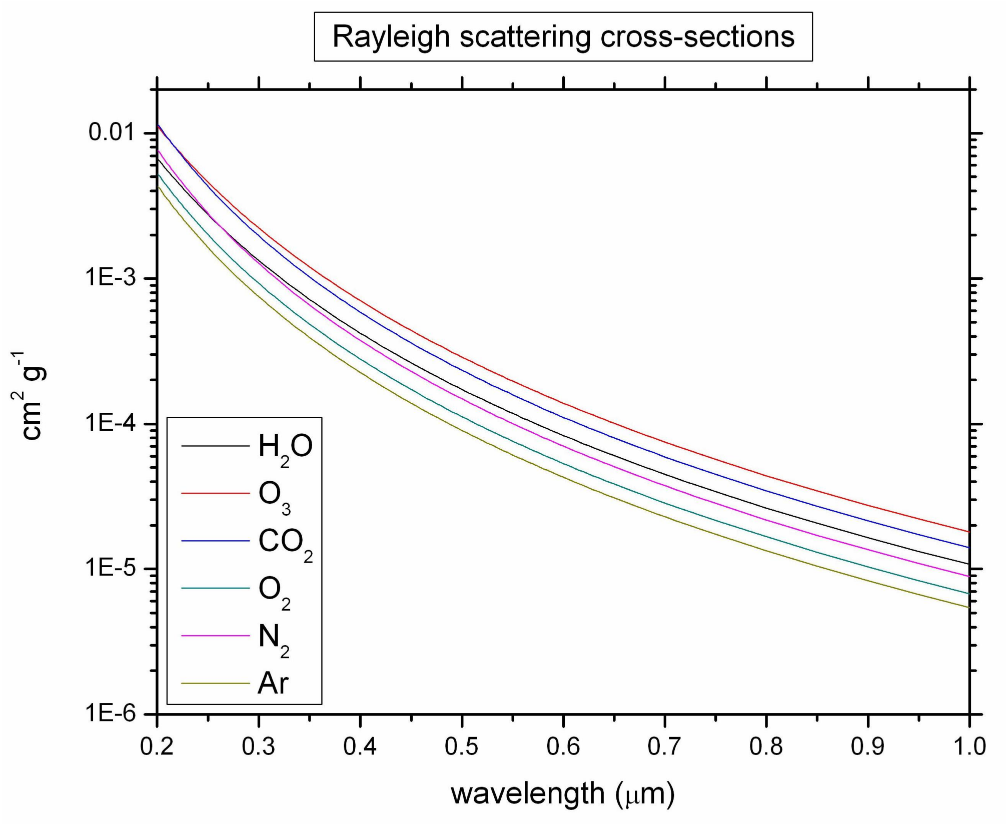

Figure 3.6: Rayleigh scattering cross–sections of the molecules considered by the model.

Table 3.3: Atmospheric gases in the UV–Visible: scattering, absorption and % effect on the downwelling surface radiation.

Atmospheric gas	Scattering	Absorption	% Effect in UV-Visible downwelling radiation at surface
N_2	✓		-6.09 ± 1.180
O_2	✓	✓	-1.06 ± 0.190
Ar	✓		-0.01 ± 0.005
CO_2	✓	✓	-0.01 ± 0.005
O_3	✓	✓	-3.16 ± 0.310
H_2O	✓		-0.02 ± 0.010

3.5 Near–infrared absorption

The 1.0–10 µm spectral region corresponds to about 31% of the incoming solar radiation. The most important absorbing gases in this spectral region, taken into account by the model, are H_2O, CO_2 and CH_4. Table 3.4 shows the 10 spectral bands, into which the 1.0–10 µm spectral region is divided, the incoming solar flux in each interval and the corresponding absorbing molecules.

Table 3.4: Distribution of the model 10 spectral bands in the near infrared region, incoming solar flux and main absorbers (adapted from Vardavas and Taylor, 2011).

Spectral interval	Wavelength (µm)	Solar flux (%)	Absorbing molecule
1	1.00-1.04	2.12	H_2O
2	1.04-1.22	7.55	H_2O
3	1.22-1.58	9.19	H_2O,CO_2
4	1.58-1.95	4.81	H_2O
5	1.95-2.12	1.24	H_2O,CO_2
6	2.12-2.61	2.41	H_2O
7	2.61-2.92	0.92	H_2O,CO_2
8	2.92-3.88	1.34	H_2O,CH_4
9	3.88-4.60	0.40	CO_2
10	4.60-9.52	0.64	H_2O,CH_4

To calculate the effect of molecular NIR absorption, the correlated–k approximation is used (Vardavas and Taylor, 2011), whereby the average transmissivity within a spectral interval is obtained from

$$t = \sum_n \alpha_n \exp{(-k_n y)}, \tag{3.35}$$

for an absorber amount y, in terms of effective monochromatic absorption coefficients, k_n, and associated discrete probability distribution weights α_n, with the normalization

$$\sum_n \alpha_n = 1. \tag{3.36}$$

The monochromatic radiation transfer is solved for each optical depth $\tau_n = k_n y$, for incoming solar flux $\alpha_n F_i$, where F_i is the flux contained in the spectral band i. For overlapping bands of two different molecules, namely for bands

3, 5, 7, 8 and 10 of Table 3.4, the transfer equation is solved for $\alpha_n \beta_m F_i$, with optical depth $\tau_{nm} = k_n y + l_m v$, for every combination of n and m, where l_m and v are the monochromatic absorption coefficients and absorber amount of the second molecule, respectively.

Values of α_n and k_n for H_2O, CO_2 and CH_4 and for each spectral interval were taken from Vardavas and Carver (1984). The H_2O content (g cm^{-2}) inside an atmospheric layer, which is defined by pressure levels p_1 and p_2 with $p_1 < p_2$ is calculated from

$$W_{H_2O} = -\int_{p_2}^{p_1} \eta(p)\mathrm{d}p/g, \tag{3.37}$$

where $\eta(p)$ is the water mixing ratio by mass and g the gravitational acceleration (Vardavas and Taylor, 2011). The CH_4 mixing ratio is set equal to 1.774 ppmv, corresponding to 10^{-3} g cm^{-2} (IPCC, 2007). CH_4 and CO_2 are also distributed in all atmospheric layers in proportion to the pressure differential.

Although the correlated–k method is an approximation compared to detailed line–by–line calculations, based for example on data from the HITRAN database (Rothman et al., 2009), several studies have shown that errors due to the correlated–k method are of the order of 1% or less, when compared with corresponding results from line–by–line calculations (e.g. Goody et al., 1989; Lacis and Oinas, 1991).

Table 3.5: Atmospheric absorbers in the NIR: % effect in the NIR downwelling surface radiation.

Atmospheric absorber	% Effect in NIR downwelling radiation at surface
H_2O	-31.65 ± 2.93
CO_2	-2.26 ± 0.21
CH_4	-0.31 ± 0.04

In Table 3.5, the effects of each absorbing gas in the NIR downwelling radiation at the surface are shown. Each effect was calculated as the mean difference between two model runs over HCMR station, for the period 2000–2010, using Terra MODIS data. In the first run, all near–infrared absorbers were included, while in the second, the amount of each gas under study was set equal to zero. It is apparent from Table 3.5 that water vapor is the main atmospheric absorber in the NIR, playing the most important role in the radiation budget in this spectral region.

3.6 Optical properties of atmospheric layers

The optical properties required for the radiation transfer solution in each atmospheric layer consist of the monochromatic extinction optical depth (or extinction optical thickness), τ_λ, single scattering albedo, ω_λ and asymmetry parameter (or asymmetry factor), g_λ.

The extinction optical depth is defined by

$$\tau_\lambda = \int_0^L \chi_\lambda(l)\mathrm{d}l, \tag{3.38}$$

where χ_λ is the extinction coefficient, or total effective cross–sectional area, for absorption and scattering of photons of wavelength λ by all particles, if the photons travel a distance L. Thus, $1/\chi_\lambda$ represents a characteristic length for the removal of photons of wavelength λ along their path, and the optical depth is the physical distance traversed by the photons in units of mean free path (see e.g. Vardavas and Taylor, 2011).

In atmospheres without significant macroscopic motions, χ_λ is isotropic and has two components, an absorption (κ_λ) and a scattering (σ_λ) component: $\chi_\lambda = \kappa_\lambda + \sigma_\lambda$. The single scattering albedo is defined as the probability of a photon undergoing a scattering event as opposed to an absorption event:

$$\omega_\lambda = \frac{\sigma_\lambda}{\kappa_\lambda + \sigma_\lambda} \tag{3.39}$$

The asymmetry factor, g, is defined by

$$g = \frac{1}{2}\int_{-1}^{1} p(\cos\vartheta)\cos\vartheta\mathrm{d}\cos\vartheta, \tag{3.40}$$

where $p(\cos\vartheta)$ is the phase function for coherent scattering (e.g Rayleigh and Mie scattering), and ϑ is the angle between incident and scattered radiation, given by Equation (3.57). Thus, g ranges between -1 and 1 and quantifies the extent of the non–isotropy of the scattering process, assuming the following characteristic values:

$$g = \begin{cases} 1 & \text{forward scattering} \\ 0 & \text{isotropic or symmetric scattering} \\ -1 & \text{backward scattering} \end{cases} \tag{3.41}$$

3.7 Cloud absorption and scattering

The presence of a cloudy sky part determines the number of atmospheric layers considered by the model, in both the UV–Visible and NIR spectral regions. In the UV–Visible case, the atmosphere is separated into five layers, while in the NIR four layers are considered. In both cases, the cloud layer is set below the top atmospheric layer (Figure 3.1).

Clouds are classified into three types and two phases: low, middle, high, and liquid and ice, respectively. The type classification is based on the ISCCP cloud classification scheme, whereby clouds are classified according to the cloud–top pressure: low level clouds have top pressures greater than or equal to 680 mbar, high level cloud–top pressures are less than 440 mbar and middle level cloud–top pressures lie between 440 and 680 mbar.

The cloud optical properties, required for the model computations, comprise cloud optical thickness, asymmetry parameter and single scattering albedo, as described in the previous Section. In the UV–Visible region, only scattering of solar radiation by clouds takes place, while in the NIR both scattering and absorption are considered. Of these parameters, MODIS provides only the cloud scattering optical depth, $\tau_c^s(UV\!-\!Visible)$, for the visible wavelengths 0.65 µm over land and 0.86 µm over ocean. This parameter is considered representative of the entire UV–Visible spectrum, since the cloud scattering optical depth in this spectral region is approximately independent of wavelength, as they have a particle–size distribution of sufficiently large radii when compared with the radiation wavelength (Vardavas and Taylor, 2011). The cloud scattering and absorption optical depths in the NIR, $\tau_c^s(NIR)$ and $\tau_c^a(NIR)$, are derived from the ratios $\tau_c^s(NIR)/\tau_c^s(UV - Visible)$ and $\tau_c^a(NIR)/\tau_c^s(UV - Visible)$, which resulted either from Mie scattering calculations or from existing parameterizations.

The cloud asymmetry parameter, g_c, is taken into account by computing values separately for the UV–Visible and NIR range of wavelengths, and for liquid and ice clouds. The computation is based on the parameterizations of Slingo (1989) for liquid clouds and Ebert and Curry (1992) for ice clouds. The cloud effective radius, needed for these computations, is set equal to 10 µm for liquid droplets and 30 µm for ice crystals, based on the ISCCP–D2 standard scheme (Hatzianastassiou et al., 2004a). The resulting g_c values, used by the model, for each cloud type, phase and spectral region, are shown in Table 3.6.

Table 3.6: Values of cloud asymmetry parameter, g_c, for low, middle and high clouds and for the UV–Visible and NIR ranges of wavelengths.

	low clouds (liquid)	middle clouds (liquid)	high clouds (ice)
UV-Visible	0.850	0.815	0.780
NIR	0.820	0.810	0.800

3.8 Aerosol absorption and scattering

The aerosol optical properties required as input to the model include the AOT, the asymmetry parameter, g_{aer}, and the single scattering albedo, ω_{aer}. AOT is available from MODIS Level 2 Atmosphere Products at seven wavelengths over ocean (0.47, 0.55, 0.66, 0.87, 1.24, 1.64 and 2.13 µm) and three wavelengths over land (0.47, 0.55 and 2.13 µm), while g_{aer} is also available over ocean at the same seven wavelengths and ω_{aer} data are available from the FORTH–CRETE AERONET station, at four wavelengths (0.44, 0.67, 0.87 and 1.02 µm), as described in detail in Chapter 2. Since the spectral model computations are performed for specific wavelengths and spectral intervals in the UV–Visible and NIR regions, the required AOT, g_{aer} and ω_{aer} are obtained through interpolation and extrapolation. Specifically, for the 0.20–0.47 µm region, linear extrapolation is used for g_{aer} and ω_{aer} (0.20–0.44 µm) and exponential extrapolation for AOT. In the 2.13–10 µm linear extrapolation is used for all three parameters (1.02–10 µm for ω_{aer}). Using values of AOT and ω_{aer} in each wavelength, the aerosol scattering (τ^s_{aer}) and absorption (τ^a_{aer}) optical depths are given by

$$\tau^s_{aer} = \omega_{aer} \times AOT, \tag{3.42}$$

$$\tau^a_{aer} = \tau^s_{aer} \times \frac{1-\omega_{aer}}{\omega_{aer}}, \tag{3.43}$$

where

$$\omega_{aer} = \frac{\tau^s_{aer}}{\tau^s_{aer} + \tau^a_{aer}}. \tag{3.44}$$

Aerosol scattering and absorption are considered in the layer above the Earth's surface, as shown in Figure 3.1. Aerosols within and above clouds are not considered, due to missing information. This introduces an underestimate of the aerosol effect in the case of absorbing aerosols above clouds

(Keil and Haywood, 2003). However, the MODIS algorithm does not retrieve aerosol properties if a cloud is detected (Remer et al., 2005).

The SW aerosol DRE (or ΔF) is estimated at TOA, at the Earth's surface and within the atmosphere, and is given by

$$\Delta F = F - F_{no-aerosol}, \tag{3.45}$$

where F and $F_{no-aerosol}$ are the SW radiative fluxes (W m^{-2}) computed with and without aerosols. Hence, the DRE components ΔF_{TOA}, ΔF_{AtmAb}, $\Delta F_{Surface}$ and $\Delta F_{NetSurface}$, represent the direct effect of aerosols on the net incoming (absorbed) radiation at TOA, within the atmosphere and at the Earth's surface (DSR and surface absorption). As far as ΔF_{TOA} is concerned, DRE is essentially the change of the outgoing (reflected) SW radiation at TOA, since the incoming extraterrestrial SW radiation is not affected by aerosols, and therefore ΔF_{TOA} is computed according to

$$\Delta F_{TOA} = F^{TOA}_{no-aerosol} - F^{TOA}. \tag{3.46}$$

The model computations are based on the SW radiation budget of the planet, whereby the net TOA incoming radiation equals the atmospheric plus the surface absorption:

$$\Delta F_{TOA} + \Delta F_{AtmAb} + \Delta F_{NetSurface} = 0. \tag{3.47}$$

3.9 Surface reflectivity

In previous model versions (e.g. Hatzianastassiou et al., 2004a), the surface reflectivity was computed based on Equation (3.1), considering four general types of surface: land, ocean, snow and ice. Fractional land cover data were taken from ISCCP, while values of surface reflectivity for each surface type were obtained from the literature, except for the ocean surface, where reflectivity R_o was computed using Fresnel reflection.

In the present study, the model is run over two coastal regions (HCMR and Finokalia meteorological stations in Crete) and four lakes (Marathonas, Yliki, Evinos and Mornos in mainland Greece). In the coastal regions, two types of surface are considered, namely land and ocean, while in the case of lakes only ocean reflectivity is used. Reflectivity over land is available from MODIS Level 2 Products at seven wavelengths (0.47, 0.55, 0.66, 0.87, 1.24, 1.64 and 2.13 µm). In order to estimate land surface reflectivity over the entire UV–Visible and NIR spectrum used by the model (0.2–10 µm), the following scheme is used: in the 0.2–0.3 µm region, a constant value $R_l = 0.1$

is used. In the 0.3–0.47 µm region, linear interpolation is applied between the 0.1 value at 0.3 µm and the daily variable MODIS value at 0.47 µm. In the 0.47–2.13 µm region, linear interpolation is applied, using the seven MODIS values available in this spectral interval, while for wavelengths greater than 2.13 µm linear extrapolation is used.

The ocean reflectivity, R_o, is computed as in previous model versions, using Fresnel reflection corrected for a non–smooth surface for an incident angle $\varphi = \cos^{-1}\mu$ from

$$R_o = 0.5\left[\left(\frac{\sin a}{\sin b}\right)^2 + \left(\frac{\tan a}{\tan b}\right)^2\right] + 0.016\cos\varphi, \tag{3.48}$$

where

$$a = \varphi - \sin^{-1}(\sin\varphi/1.333), \tag{3.49}$$

$$b = 2\varphi - a. \tag{3.50}$$

The term $0.016\cos\varphi$ is a correction applied to Fresnel reflectivity, in order to take into account surface roughness. It yields higher reflectivity of about 0.04 for incident radiation normal to the surface, compared to the smooth ocean surface case (Kondratyev, 1973). In the case of small lakes (Chapter 6), this correction term is not taken into account, since no surface roughness is expected.

3.10 Radiation transfer: multiple scattering solution for inhomogeneous atmospheric layers

The equation of transfer for diffuse radiation is

$$\mu\frac{\partial I_\lambda}{\partial \tau_\lambda} = -I_\lambda + S_\lambda, \tag{3.51}$$

where $I_\lambda(\tau_\lambda, \mu, \phi)$ is the radiance, S_λ the source function, τ_λ the extinction optical depth, $\mu = \cos\theta$, with θ the solar zenith angle and ϕ the azimuth angle (Vardavas and Taylor, 2011). For anisotropic scattering, the angle-dependent source function is generally expressed as

$$S_\lambda(\mu) = S_{e\lambda} + S_{s\lambda} + S_{i\lambda}, \tag{3.52}$$

where $S_{e\lambda}$, the thermal emission source function, equals zero, since the Earth's atmosphere does not emit ultraviolet or visible radiation. The scattering source function is

$$S_{s\lambda} = \frac{\omega_\lambda}{4\pi} \int_0^{2\pi} \int_{-1}^{1} P(\mu, \phi; \mu', \phi') I(\tau, \mu', \phi') \mathrm{d}\mu' \mathrm{d}\phi' \tag{3.53}$$

and the source function for the incoming direct solar radiation is

$$S_{i\lambda} = \frac{\omega_\lambda}{4\pi} P(\mu, \phi; \mu_0, \phi_0) F^{\downarrow}_{\mathrm{d}\lambda} \tag{3.54}$$

where

$$F^{\downarrow}_{\mathrm{d}\lambda} = S_{\odot\lambda} e^{-\tau_\lambda/\mu_0} \tag{3.55}$$

The phase function, $P(\mu, \phi; \mu', \phi')$, describes the probability of light incident at μ', ϕ', to be scattered in the direction μ, ϕ, and equals the redistribution function when scattering is coherent in frequency, such as Rayleigh and Mie (Vardavas and Taylor, 2011). Shettle and Weinman (1970) expressed the scattering phase function as a two–term truncated series of associated Legendre polynomials in the manner of Chandrasekhar (1960), to obtain

$$P(\vartheta) = 1 + 3g \cos\vartheta, \tag{3.56}$$

where g is the asymmetry parameter and ϑ the angle between incident and scattered radiances, given by

$$\cos\vartheta = \mu\mu' + (1 - \mu^2)^{\frac{1}{2}} (1 - \mu'^2)^{\frac{1}{2}} \cos(\phi - \phi'). \tag{3.57}$$

For an azimuthally–averaged radiation field, the phase function can also be averaged over the incoming azimuthal direction by replacing $\cos\vartheta$ given by Equation (3.57) to obtain

$$P(\mu\mu') = 1 + 3g\mu\mu'. \tag{3.58}$$

Eddington (1926) allowed for the anisotropy of the radiation field by expanding the radiance $I_\lambda(\tau, \mu)$ in terms of Legendre polynomials and showing that deep within an atmosphere a good approximation is to neglect higher order terms beyond the second. Thus, the Eddington approximation is to set

$$I_\lambda(\tau, \mu) = I_0(\tau) + I_1(\tau)\mu. \tag{3.59}$$

Using the phase function P and radiance I_λ given by equations (3.58) and (3.59), respectively, the scattering source function (3.53) becomes $S_{s\lambda} = \omega_\lambda(I_0 + I_1\mu)$. Substituting this equation, along with equations (3.58) and (3.59) in equation (3.51), we get the following equation of transfer:

$$\mu \frac{\mathrm{d}(I_0 + \mu I_1)}{\mathrm{d}\tau} = -(I_0 + \mu I_1) + \omega(I_0 + \mu I_1) + \frac{\omega}{4\pi} S_\odot e^{-\frac{\tau}{\mu_0}} (1 + 3g\mu\mu_0). \tag{3.60}$$

By integrating (3.60) and (3.60) times μ, both over μ, as in Shettle and Weinman (1970), we obtain the following pair of equations for I_0 and I_1:

$$\frac{\mathrm{d}I_1}{\mathrm{d}\tau} = -3(1-\omega)I_0 + \frac{3\omega}{4\pi}S_{\odot}e^{-\frac{\tau}{\mu_0}}, \tag{3.61}$$

$$\frac{\mathrm{d}I_0}{\mathrm{d}\tau} = -3(1-\omega g)I_1 + \frac{3\omega g\mu_0}{4\pi}S_{\odot}e^{-\frac{\tau}{\mu_0}}. \tag{3.62}$$

For internally homogeneous scattering and absorbing atmospheric layers ($\omega \neq 1$), the following solutions are appropriate within each layer $i (i = 1, \ldots, N)$:

$$I_0^i(\tau) = C_1^i e^{-k_i\tau} + C_2^i e^{+k_i\tau} - a_i e^{-\tau/\mu_0}, \tag{3.63}$$

$$I_1^i(\tau) = p_i(C_1^i e^{-k_i\tau} - C_2^i e^{+k_i\tau}) - \beta_i e^{-\tau/\mu_0}, \tag{3.64}$$

where $\tau_{i-1} < \tau < \tau_i$ and

$$k_i = [3(1-\omega_i)(1-\omega_i g_i)]^{1/2}, \tag{3.65}$$

$$p_i = [3(1-\omega_i)/(1-\omega_i g_i)]^{1/2}, \tag{3.66}$$

$$a_i = \frac{3\omega_i}{\pi}S_{\odot}\mu_0^2[1+g_i(1-\omega_i)]/4(1-k_i^2\mu_0^2), \tag{3.67}$$

$$\beta_i = \frac{3\omega_i}{\pi}S_{\odot}\mu_0^2[1+3g_i(1-\omega_i)\mu_0^2]/4(1-k_i^2\mu_0^2). \tag{3.68}$$

In order to determine C_1 and C_2 (and consequently I) in each layer, a system of $2N$ equations must be solved. These equations are formulated by the boundary conditions at TOA and at the surface, and the $I_0(\tau)$ and $I_1(\tau)$ continuity requirements between the layers. At TOA (layer 1), the downwelling diffuse irradiance is zero:

$$0 = 2\pi\int_0^1 (I_0 + \mu I_1)\mu\mathrm{d}\mu = \pi[I_0(0) + \frac{2}{3}I_1(0)] \Rightarrow$$

$$(1+\frac{2p_1}{3})C_1^1 + (1-\frac{2p_1}{3})C_2^1 = a_1 + 2\beta_1/3. \tag{3.69}$$

At the surface (layer N), the upwelling diffuse irradiance is equal to the product of the downwelling direct and diffuse irradiances, and the surface albedo. If τ^* is the extinction optical depth of the entire atmosphere and A the surface albedo:

$$\pi[I_0(\tau^*) - \frac{2}{3}I_1(\tau^*)] = A\left\{\pi\left[I_0(\tau^*) + \frac{2}{3}I_1(\tau^*)\right] + \frac{\mu_0 S_{\odot}}{\pi}e^{-\frac{\tau^*}{\mu_0}}\right\} \Rightarrow$$

$$\left[1 - A - \frac{2(1+A)p_N}{3}\right]e^{-k_N\tau^*}C_1^N + \left[1 - A + \frac{2(1+A)p_N}{3}\right]e^{+k_N\tau^*}C_2^N =$$

$$= \left[(1-A)a_N - \frac{2(1+A)\beta_N}{3} + A\frac{\mu_0 S_{\odot}}{\pi}\right]e^{-\frac{\tau^*}{\mu_0}}. \tag{3.70}$$

The remaining $2N-2$ equations are determined by requiring that $I_0(\tau)$ and $I_1(\tau)$ are continuous between layers:

$$I_0^i(\tau_i) = I_0^{i+1}(\tau_i), \tag{3.71}$$

$$I_1^i(\tau_i) = I_1^{i+1}(\tau_i), \tag{3.72}$$

with $i = 1, 2, \ldots, N-1$. Having formulated a system of $2N$ equations, the model solves for the $2N$ unknowns (C_1 and C_2 in each layer), using the LU decomposition method (Press, 2007). Direct and diffuse radiation fluxes at both TOA (layer 1) and the surface (layer N) are computed, while the radiation absorbed by the atmosphere is estimated through the radiation budget, whereby the net TOA incoming radiation equals the radiation absorbed by the surface and the atmosphere. For layer i, the diffuse irradiances are computed from

$$F(\tau) = 2\pi \int_0^{\pm 1} (I_0 + \mu I_1)\mu \mathrm{d}\mu = \pi[I_0(\tau) \pm \frac{2}{3} I_1(\tau)], \tag{3.73}$$

where $\mu > 0$ and $\mu < 0$ correspond to $F^{\downarrow}(\tau)$ and $F^{\uparrow}(\tau)$ (down and up welling irradiance, respectively).

Shettle and Weinman (1970) report that using the method described in this Section, irradiances are computed with an accuracy of several percent.

3.11 The Delta–Eddington approximation

Joseph et al. (1976) improved the truncated phase function approach by including a Dirac delta function forward scatter peak and a two–term expansion of the phase function:

$$P(\vartheta) \approx P_{\delta-Edd}(\vartheta) = 2f\delta(1-\cos\vartheta) + (1-f)(1+3g'\cos\vartheta), \tag{3.74}$$

where f is the fraction of scattered photons in the forward direction, while the Dirac delta function is defined by:

$$\delta(x) = \begin{cases} +\infty, & x = 0 \\ 0 & x \neq 0 \end{cases} \tag{3.75}$$

with the following main properties:

$$\int_{-\infty}^{+\infty} \delta(x)\mathrm{d}x = 1, \tag{3.76}$$

$$\int_{-\infty}^{+\infty} \delta(x-a) f(x) \mathrm{d}x = f(a). \tag{3.77}$$

Joseph et al. (1976) assumed that the original phase function that they were approximating was the Henyey–Greenstein (HG) phase function, P_{HG}. This phase function was introduced be Henyey and Greenstein (1941) and has the following form:

$$P_{HG} = \frac{1-g^2}{2(1+g^2-2g\cos\vartheta)^{\frac{3}{2}}}. \tag{3.78}$$

By varying the asymmetry factor g between -1 and 1, P_{HG} ranges from backscattering through isotropic scattering to forward scattering. Figure 3.7 shows how P_{HG} approximates the forward scattering peak, for three typical values of g.

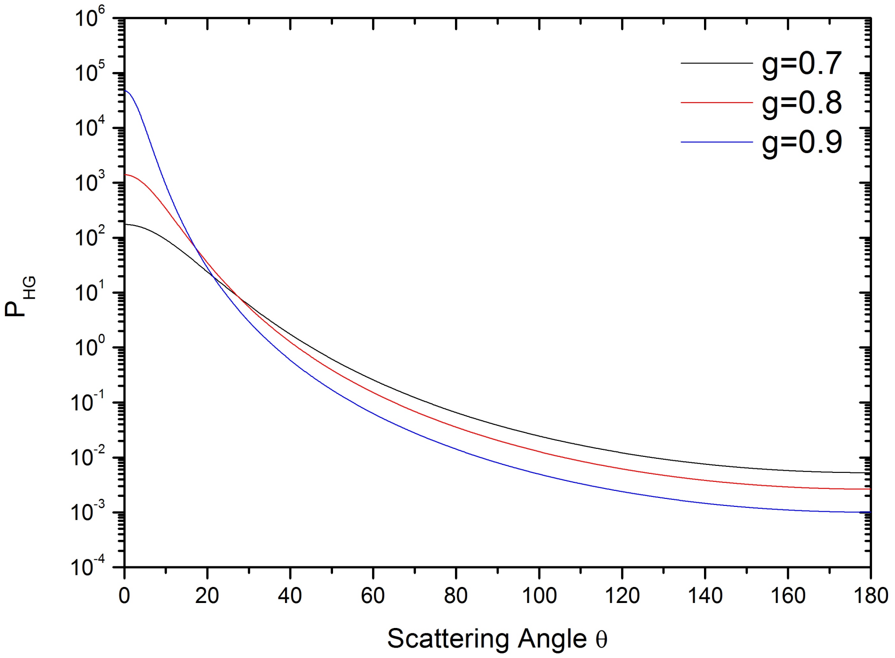

Figure 3.7: The Henyey–Greenstein phase function for three typical values of g (0.7,0.8,0.9).

Both van de Hulst (1968) and Hansen (1969) showed that, for flux computations, P_{HG} can be used in place of the more realistic phase functions from Mie theory (e.g. Vardavas and Taylor, 2011, p. 177, Lavvas, 2007, p. 233). Joseph et al. (1976) also showed that $P_{\delta-Edd}$ agrees with P_{HG} out to three terms, and the $P_{\delta-Edd}$ error grows smaller as $g \to 1$. Requiring that the second moment of $P_{\delta-Edd}$ be identical to the second moment of P_{HG}, they obtained $f = g^2$. By further requiring that $P_{\delta-Edd}$ has the same asymmetry factor as P_{HG}, they determined g':

$$g' = \frac{g-f}{1-f} = \frac{g}{1+g}. \tag{3.79}$$

The remaining Delta–Eddington simple transformations were obtained by inserting $P_{\delta-Edd}$ in the azimuthally averaged radiative transfer equation:

$$\tau' = (1-\omega f)\tau, \tag{3.80}$$

$$\omega' = \frac{(1-f)\omega}{1-\omega f}. \tag{3.81}$$

The solution to the Delta–Eddington approximation is equivalent to the Eddington approximation (Equations (3.63) and (3.64)), with g', τ', ω' replacing g, τ, ω. The Delta–Eddington approximation improves the accuracy achieved by the simple Eddington approximation. According to Joseph et al. (1976), the Delta–Eddington method predicts the radiative fluxes to an accuracy of better than 2.5%, with the average flux error being no larger than 0.5%. Errors tend to increase as the cosine of the solar zenith angle decreases, but for values of $\mu \geq 0.4$ the errors remain at their lowest levels.

3.12 Radiative transfer input parameters

The set of monochromatic radiative flux transfer equations described in the previous Sections is solved separately for each wavelength and spectral band, and for each atmospheric layer. The atmospheric constituents and processes in each layer, taken into account by the model, are shown in Figure 3.1. Generally, the atmospheric extinction optical depth in a layer and for a specific wavelength is given by

$$\tau = \tau_{cs} + \tau_{ca} + \tau_{aers} + \tau_{aera} + \tau_{ma} + \tau_R, \tag{3.82}$$

where τ_{cs} is the cloud scattering optical depth, τ_{ca} is the cloud absorption optical depth, τ_{aers} is the aerosol scattering optical depth, τ_{aera} is the aerosol absorption optical depth, τ_{ma} is that for molecular absorption and τ_R is that for Rayleigh or molecular scattering (Vardavas and Taylor, 2011). The single scattering albedo for each layer is

$$\omega = \omega_c + \omega_{aer} + \omega_R, \tag{3.83}$$

where $\omega_c = \tau_{cs}/\tau$, $\omega_{aer} = \tau_{aers}/\tau$, $\omega_R = \tau_R/\tau$. The asymmetry parameter is given by

$$g = \frac{g_c\omega_c + g_{aer}\omega_{aer} + g_R\omega_R}{\omega}, \tag{3.84}$$

with g_c and g_{aer} being the cloud and aerosol asymmetry factors, respectively, with the Rayleigh asymmetry factor $g_R = 0$. The parameters τ, ω and g constitute the input to the Delta–Eddington transformations.

Bibliography

Allen, C.: Astrophysical quantities, Athlone Press, 1973.

Bass, A. M. and Paur, R. J.: UV absorption cross sections for ozone: The temperature dependence, Journal of Photochemistry, 17, 141, 1981.

Chandrasekhar, S.: Radiative Transfer, Dover books on advanced mathematics, Dover Publ., 1960.

Ebert, E. E. and Curry, J. A.: A parameterization of ice cloud optical properties for climate models, Journal of Geophysical Research: Atmospheres, 97, 3831–3836, 1992.

Eddington, A.: The Internal Constitution of the Stars, Cambridge University Press, 1926.

Fotiadi, A., Hatzianastassiou, N., Matsoukas, C., Pavlakis, K. G., Drakakis, E., Hatzidimitriou, D., and Vardavas, I.: Analysis of the decrease in the tropical mean outgoing shortwave radiation at the top of atmosphere for the period 1984-2000, Atmospheric Chemistry and Physics, 5, 1721–1730, doi:10.5194/acp-5-1721-2005, 2005.

Fouquart, Y. and Bonnel, B.: Intercomparing shortwave radiation codes for climate studies, Journal of Geophysical Research, 96, 8955–8968, 1991.

Gilgen, H. and Ohmura, A.: The Global Energy Balance Archive, Bulletin of the American Meteorological Society, pp. 831–850, 1999.

Goody, R., West, R., Chen, L., and Crisp, D.: The correlated-k method for radiation calculations in nonhomogeneous atmospheres, Journal of Quantitative Spectroscopy and Radiative Transfer, 42, 539–550, 1989.

Gueymard, C. A.: The sun's total and spectral irradiance for solar energy applications and solar radiation models, Solar Energy, 76, 423–453, doi: 10.1016/j.solener.2003.08.039, 2004.

Hansen, J. E.: Exact and Approximate Solutions for Multiple Scattering by Cloudy and Hazy Planetary Atmospheres, Journal of Atmospheric Sciences, 26, 478–487, 1969.

Hartmann, D.: Global Physical Climatology, International Geophysics, Elsevier Science, 1994.

Hatzianastassiou, N. and Vardavas, I.: Shortwave radiation budget of the Northern Hemisphere using International Satellite Cloud Climatology Project and NCEP/NCAR climatological data, Journal of Geophysical Research, 104, 24 401–24 421, 1999.

Hatzianastassiou, N. and Vardavas, I.: Shortwave radiation Budget of the Southern Hemisphere using ISCCP C2 and NCEP-NCAR climatological data, Journal of Climate, 14, 4319–4329, 2001.

Hatzianastassiou, N., Wobrock, W., and Flossmann, A. I.: The role of droplet spectra for cloud radiative properties, Quarterly Journal of the Royal Meteorological Society, pp. 2215–2230, 1997.

Hatzianastassiou, N., Wobrock, W., and Flossmann, A. I.: The effect of cloud-processing of aerosol particles on clouds and radiation, Tellus B, 50, 478–490, 1998.

Hatzianastassiou, N., Fotiadi, A., Matsoukas, C., Pavlakis, K. G., Drakakis, E., Hatzidimitriou, D., and Vardavas, I.: Long–term global distribution of Earth's shortwave radiation budget at the top of atmosphere, Atmospheric Chemistry and Physics, 4, 1217–1235, 2004a.

Hatzianastassiou, N., Katsoulis, B. D., and Vardavas, I.: Global distribution of aerosol direct radiative forcing in the ultraviolet and visible arising under clear skies, Tellus B, 56B, 51–71, 2004b.

Hatzianastassiou, N., Katsoulis, B. D., and Vardavas, I.: Sensitivity analysis of aerosol direct radiative forcing in ultraviolet - visible wavelengths and consequences for the heat budget, Tellus B, 56B, 368–381, 2004c.

Hatzianastassiou, N., Matsoukas, C., Fotiadi, A., Pavlakis, K. G., Drakakis, E., Hatzidimitriou, D., and Vardavas, I.: Global distribution of Earth's surface shortwave radiation budget, Atmospheric Chemistry and Physics, 5, 2847–2867, doi:10.5194/acp-5-2847-2005, 2005.

Hatzianastassiou, N., Matsoukas, C., Fotiadi, A., Stackhouse, P. W. J., Koepke, P., Pavlakis, K. G., and Vardavas, I.: Modelling the direct effect of aerosols in the solar near-infrared on a planetary scale, Atmospheric Chemistry and Physics, 7, 3211–3229, doi:10.5194/acp-7-3211-2007, 2007a.

Hatzianastassiou, N., Matsoukas, C., Drakakis, E., Stackhouse, P. W. J., Koepke, P., Fotiadi, A., Pavlakis, K. G., and Vardavas, I.: The direct effect of aerosols on solar radiation based on satellite observations , reanalysis datasets , and spectral aerosol optical properties from Global Aerosol Data Set (GADS), Atmospheric Chemistry and Physics, pp. 2585–2599, 2007b.

Henyey, L. G. and Greenstein, J. L.: Diffuse radiation in the Galaxy, Astrophysical Journal, 93, 70–83, 1941.

IPCC: Climate Change 2007 - The Physical Science Basis: Working Group I Contribution to the Fourth Assessment Report of the IPCC, Cambridge University Press, 2007.

Joseph, J. H., Wiscombe, W. J., and Weinman, J. A.: The Delta-Eddington Approximation for Radiative Flux Transfer, Journal of Atmospheric Sciences, 33, 2452–2459, 1976.

Karaiskou, A., Vallance, C., Papadakis, V., Vardavas, I. M., and Rakitzis, T. P.: Absolute absorption cross–section measurements of CO_2 in the ultraviolet from 200 to 206 nm at 295 and 373 K, Chemical Physics Letters, 400, 30–34, 2004.

Keil, A. and Haywood, J. M.: Solar radiative forcing by biomass burning aerosol particles during SAFARI 2000: A case study based on measured aerosol and cloud properties, Journal of Geophysical Research: Atmospheres, 108, doi:10.1029/2002JD002315, 2003.

Kondratyev, K.: Radiation characteristics of the atmosphere and the earth's surface, Published for the National Aeronautics and Space Administration, by Amerind Pub. Co., New Delhi, 1973.

Köpke, P., Hess, M., Schult, I., and Shettle, E. P.: Global Aerosol Data Set, MPI Report for Meteorology, Max–Planck–Institut für Meteorologie, 1997.

Lacis, A. and Oinas, V.: A Description of the Correlated–k Distribution Method for Modeling Nongray Gaseous Absorption , Thermal Emission , and Multiple Scattering in Vertically Inhomogeneous Atmospheres, Journal of Geophysical Research, 96, 9027–9063, doi:10.1029/90JD01945, 1991.

Lavvas, P.: Spatial and temporal variability in the atmosphere and surface of Titan's atmosphere: Simulation and interpretation through space and ground–based observations, Ph.D. thesis, University of Crete, Department of Physics, 2007.

Matsoukas, C., Banks, A. C., Hatzianastassiou, N., Pavlakis, K. G., Hatzidimitriou, D., Drakakis, E., Stackhouse, P. W. J., and Vardavas, I.: Seasonal energy budget of the Mediterranean Sea, Journal of Geophysical Research, 110, 1–15, doi:10.1029/2004JC002566, 2005.

Matsoukas, C., Banks, A. C., Pavlakis, K. G., Hatzianastassiou, N., Stackhouse, P. W. J., and Vardavas, I.: Seasonal heat budgets of the Red and Black seas, Journal of Geophysical Research, 112, 1–15, doi:10.1029/2006JC003849, 2007.

Matsoukas, C., Hatzianastassiou, N., Fotiadi, A., Pavlakis, K. G., and Vardavas, I.: The effect of Arctic sea-ice extent on the absorbed (net) solar flux at the surface, based on ISCCP-D2 cloud data for 1983-2007, Atmospheric Chemistry and Physics, 10, 777–787, doi:10.5194/acp-10-777-2010, 2010.

Matsoukas, C., Benas, N., Hatzianastassiou, N., Pavlakis, K. G., Kanakidou, M., and Vardavas, I.: Potential evaporation trends over land between 19832008: driven by radiative fluxes or vapour-pressure deficit?, Atmospheric Chemistry and Physics, 11, 7601–7616, doi:10.5194/acp-11-7601-2011, 2011.

Nicolet, M. and Kennes, R.: Aeronomic problems of the molecular oxygen photodissociation. Part 1: The O_2 Herzberg continuum, Planetary and Space Science, 34, 1043–1059, 1986.

Papadimas, C. D., Hatzianastassiou, N., Matsoukas, C., Kanakidou, M., Mihalopoulos, N., and Vardavas, I.: The direct effect of aerosols on solar radiation over the broader Mediterranean basin, Atmospheric Chemistry and Physics, 12, 7165–7185, doi:10.5194/acp-12-7165-2012, 2012.

Pavlakis, K. G., Hatzianastassiou, N., Matsoukas, C., Fotiadi, A., and Vardavas, I.: ENSO surface shortwave radiation forcing over the tropical Pacific, Atmospheric Chemistry and Physics, 8, 5565–5577, doi:10.5194/acp-8-5565-2008, 2008.

Penman, H. L.: Natural Evaporation from Open Water, Bare Soil and Grass, Proceedings of the Royal Society of London. Series A. Mathematical and Physical Sciences, 193, 120–145, 1948.

Press, W.: Numerical Recipes 3rd Edition: The Art of Scientific Computing, Cambridge University Press, 2007.

Randles, C. A., Kinne, S., Myhre, G., Schulz, M., Stier, P., Fischer, J., Doppler, L., Highwood, E., Ryder, C., Harris, B., Huttunen, J., Ma, Y., Pinker, R. T., Mayer, B., Neubauer, D., Hitzenberger, R., Oreopoulos, L., Lee, D., Pitari, G., Di Genova, G., Quaas, J., Rose, F. G., Kato, S., Rumbold, S. T., Vardavas, I., Hatzianastassiou, N., Matsoukas, C., Yu, H., Zhang, F., Zhang, H., and Lu, P.: Intercomparison of shortwave radiative transfer schemes in global aerosol modeling: results from the AeroCom Radiative Transfer Experiment, Atmospheric Chemistry and Physics, 13, 2347–2379, doi:10.5194/acp-13-2347-2013, 2013.

Remer, L., Kaufman, Y. J., Tanré, D., Mattoo, S., Chu, D. A., Martins, J. V., Li, R.-R., Ichoku, C., Levy, R. C., Kleidman, R. G., Eck, T. F., Vermote, E., and Holben, B. N.: The MODIS Aerosol Algorithm, Products, and Validation, Journal of the Atmospheric Sciences, 62, 947–973, 2005.

Rossow, W., Walker, A. W., Beuschel, D. E., and Roiter, M. D.: International Satellite Cloud Climatology Project (ISCCP)), Documentation of new cloud data sets, World Meteorological Organization, 1996.

Rossow, W. B. and Schiffer, R. A.: ISCCP cloud products, Bulletin of the American Meteorological Society, 72, 2–20, 1991.

Rothman, L. S., Gordon, I. E., Barbe, A., Benner, D. C., Bernath, P. F., Birk, M., Boudon, V., Brown, L. R., Campargue, A., Champion, J.-P., Chance, K., Coudert, L. H., Dana, V., Devi, V. M., Fally, S., Flaud, J.-M., Gamache, R. R., Goldman, A., Jacquemart, D., Kleiner, I., Lacome, N., Lafferty, W. J., Mandin, J.-Y., Massie, S. T., Mikhailenko, S. N., Miller, C. E., Moazzen-Ahmadi, N., Naumenko, O. V., Nikitin, A. V., Orphal, J., Perevalov, V. I., Perrin, A., Predoi-Cross, A., Rinsland, C. P., Rotger, M., Šimečková, M., Smith, M. A. H., Sung, K., Tashkun, S. A., Tennyson, J., Toth, R. A., Vandaele, A. C., and Vander Auwera, J.: The HITRAN 2008 molecular spectroscopic database, Journal of Quantitative Spectroscopy and Radiative Transfer, 110, 533–572, doi:10.1016/j.jqsrt.2009.02.013, 2009.

Sander, S. P., Friedl, R. R., Ravishankara, A. R., Golden, D. M., Kolb, C. E., Kurylo, M. J., Molina, M. J., Moortgat, G. K., Keller-Rudek, H., J.Finlayson-Pitts, B., Wine, P. H., Huie, R. E., and Orkin, V. L.: Chemical Kinetics and Photochemical Data for Use in Atmospheric Studies, Evaluation Number 15, NASA/JPL Publication, 2006.

Schiffer, R. A. and Rossow, W. B.: The International Satellite Cloud Climatology Project (ISCCP): The first project of the World Climate Research Program, Bulletin of the American Meteorological Society, 64, 779–784, 1983.

Shettle, E. P. and Weinman, J. A.: The Transfer of Solar Irradiance Through Inhomogeneous Turbid Atmospheres Evaluated by Eddington's Approximation, Journal of Atmospheric Sciences, 27, 1048–1055, 1970.

Slingo, A.: A GCM Parameterization for the Shortwave Radiative Properties of Water Clouds., Journal of Atmospheric Sciences, 46, 1419–1427, 1989.

van de Hulst, H.: Light scattering by small particles, Structure of matter series, Dover Publications, 1981.

van de Hulst, H. C.: Asymptotic Fitting, a Method for Solving Anisotropic Transfer Problems in Thick Layers, Journal of Computational Physics, pp. 29–3061, 1968.

Vardavas, I.: A simple model for rapidly computing terrestrial flux, solar flux and global mean surface temperature, Ecological modelling, 35, 189–210, 1987a.

Vardavas, I.: Modelling the seasonal variation of net all-wave radiation flux and evaporation in a tropical wet-dry region, Ecological Modelling, 39, 247–268, 1987b.

Vardavas, I. and Carver, J.: Solar and terrestrial parameterizations for radiative-convective models, Planetary and Space Science, 32, 1307–1325, 1984.

Vardavas, I. and Fountoulakis, A.: Estimation of lake evaporation from standard meteorological measurements: application to four Australian lakes in different climatic regions, Ecological Modelling, 84, 139–150, 1996.

Vardavas, I. and Koutoulaki, K.: A model for the solar radiation budget of the northern hemisphere: Comparison with Earth Radiation Budget Experiment data, Journal of Geophysical Research, 100, 7303–7314, 1995.

Vardavas, I. and Taylor, F.: Radiation and Climate: Atmospheric Energy Budget from Satellite Remote Sensing, International Series of Monographs on Physics, OUP Oxford, 2011.

Vardavas, I., Papamastorakis, J., Fountoulakis, A., and Manousakis, M.: Water resources in the desertification-threatened Messara Valley of Crete: estimation of potential lake evaporation, Ecological Modelling, 102, 363–374, 1997.

Willson, R. C.: Total solar irradiance trend during solar cycles 21 and 22, Science, 277, 1963–1965, 1997.

Chapter 4

Aerosol Shortwave Direct Radiative Effect and Forcing

4.1 Introduction

In this chapter are presented the first results on the aerosol effect and forcing on local scales, based on the FORTH model runs with MODIS Level 2 climatic data at 10 km × 10 km resolution. These model runs can be applied to any region where MODIS data are temporally and spatially sufficient. The area of Crete and the FORTH–CRETE AERONET station have been selected due to the unique aerosol characteristics of the wider Eastern Mediterranean region (Section 1.4) and for validation of the model input and output data against ground–based station measurements. The DRE and DRF of aerosols are computed in the SW range of wavelengths. The corresponding effect is much smaller in the LW, due to the rapid decrease of aerosol extinction with increasing wavelength for most aerosol types. The FORTH model is used to compute the local distribution of all the SW radiation budget components above the FORTH–CRETE AERONET station. The radiation budget components are calculated on an instantaneous basis (satellite overpass time), spanning the 11–year period from February 2000 through December 2010.

The results presented in this chapter include validation of the FORTH model output DSR against in situ measurements from the HCMR and Finokalia stations, and sensitivity analysis tests regarding the aerosol optical parameters. The aerosol effect on the radiation budget is examined on an instantaneous basis (focusing on dust events) and on a mean annual and seasonal basis, for the evaluation of trends and seasonal characteristics. The method used for the estimation of the anthropogenic effect on the radiation budget (aerosol forcing or DRF), along with the corresponding results examined on a seasonal basis, are presented in Section 4.2.6, before the summary and conclusions.

4.2 Results

4.2.1 Model DSR validation against HCMR and Finokalia station measurements

Aerosol DRE cannot be directly validated against measurements. This can be only indirectly and partly achieved, through validation of radiation fluxes, and especially via comparison against real surface measurements of solar radiation. Surface measurement data were obtained from both HCMR and Finokalia meteorological stations, as described in Section 2.4. Figure 4.1 shows the model results of the instantaneous DSR at HCMR (FORTH-CRETE AERONET) station, against corresponding measurements from the station (spanning a ±15 min interval centred on the satellite overpass time), for the period 2003–2008, when both station and MODIS data are available. The model was run separately with MODIS Terra (Figure 4.1a) and Aqua (Figure 4.1b) data as input. The model DSR in both cases is in very good agreement with the ground–based measurements, as can be seen from the regression fit and the determination coefficients. Nevertheless, there is a bias of −72 and −52 W m^{-2}, which corresponds to 8.8% and 6.5% of the mean DSR values found, using Terra and Aqua MODIS data, respectively. This trend shows that the model tends to overestimate the DSR at the surface. Figure 4.2 shows the corresponding results for the DSR at Finokalia station. In this case, the bias is lower (−35 and −38 W m^{-2}), corresponding to 4.3% and 4.6% of the mean output DSR, using Terra and Aqua MODIS input, respectively. The validation of the model DSR against the FORTH–CRETE AERONET station has confirmed the tendency of the model to overestimate the DSR at the surface. The two data sets were well correlated, with a determination coefficient similar to the one obtained using HCMR and Finokalia station measurements ($R^2 = 0.77$).

4.2.2 Seasonal variation of the solar radiation budget

Based on the model output with and without aerosols on an instantaneous basis (Terra and Aqua overpass times), the seasonal variation of the main solar radiation budget components at HCMR station was computed. The incoming solar radiation at TOA is scattered and absorbed in the atmosphere,

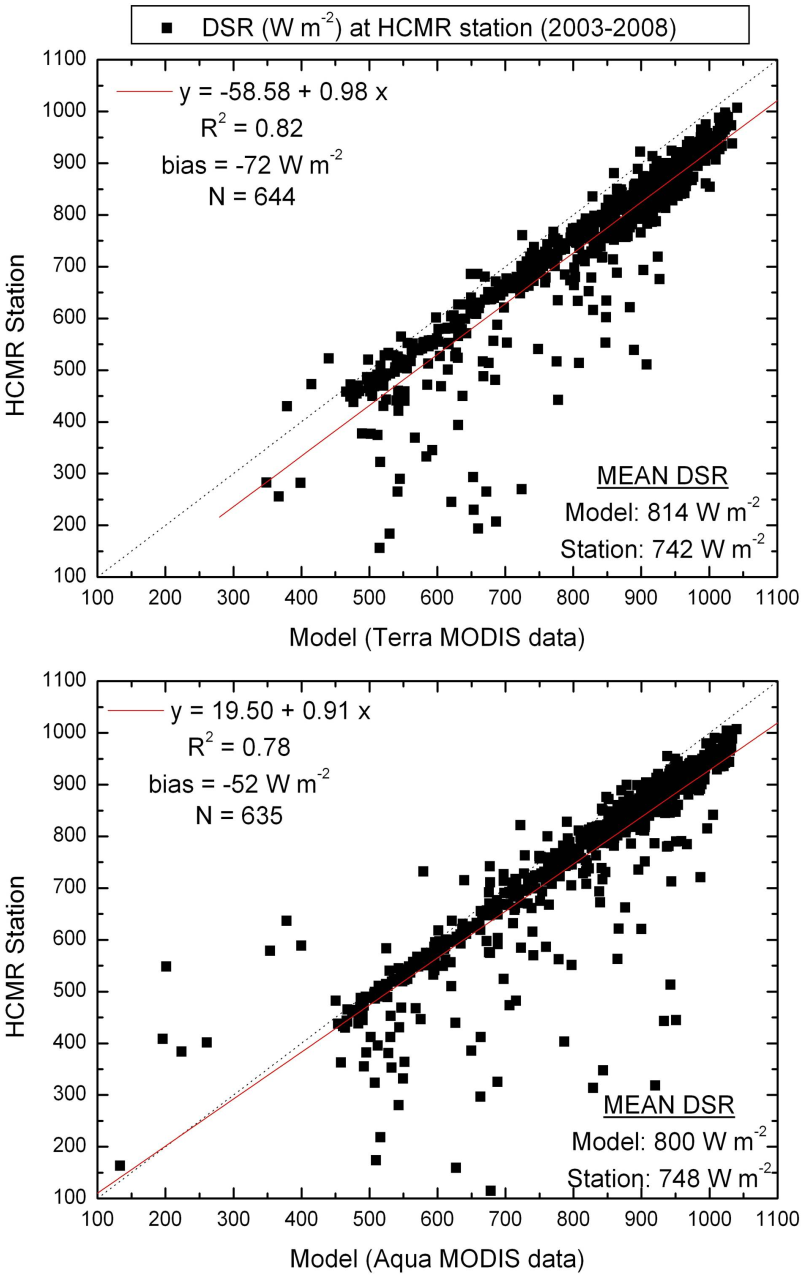

Figure 4.1: Scatter plots of the model instantaneous DSR using MODIS Terra (a) and Aqua (b) data, against corresponding ground–based measurements from the HCMR station, for the years 2003–2008. The lines are the linear regression fits, with the equations, determination coefficients, biases, number of points and mean DSR values shown.

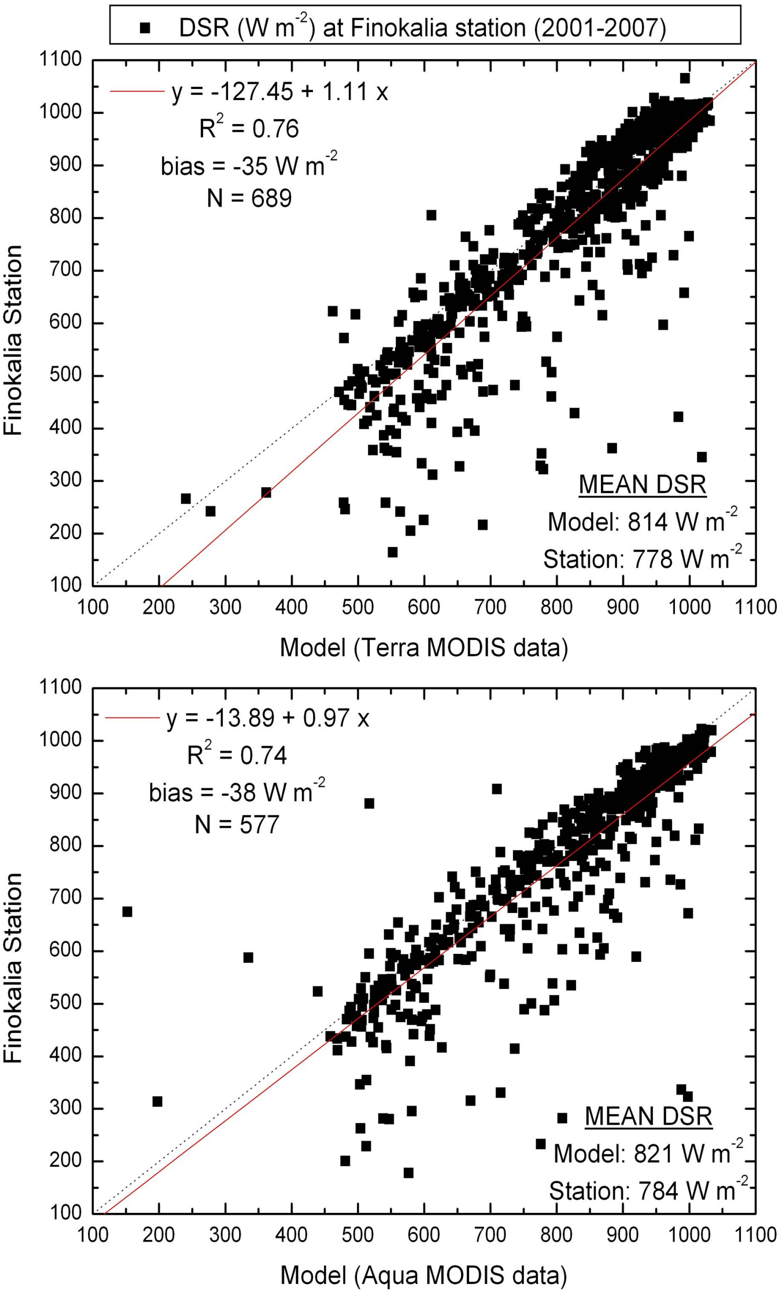

Figure 4.2: Scatter plots of the model instantaneous DSR using MODIS Terra (a) and Aqua (b) data, against corresponding ground–based measurements from the Finokalia station, for the years 2001–2007. The lines are the linear regression fits, with the equations, determination coefficients, biases, number of points and mean DSR values shown.

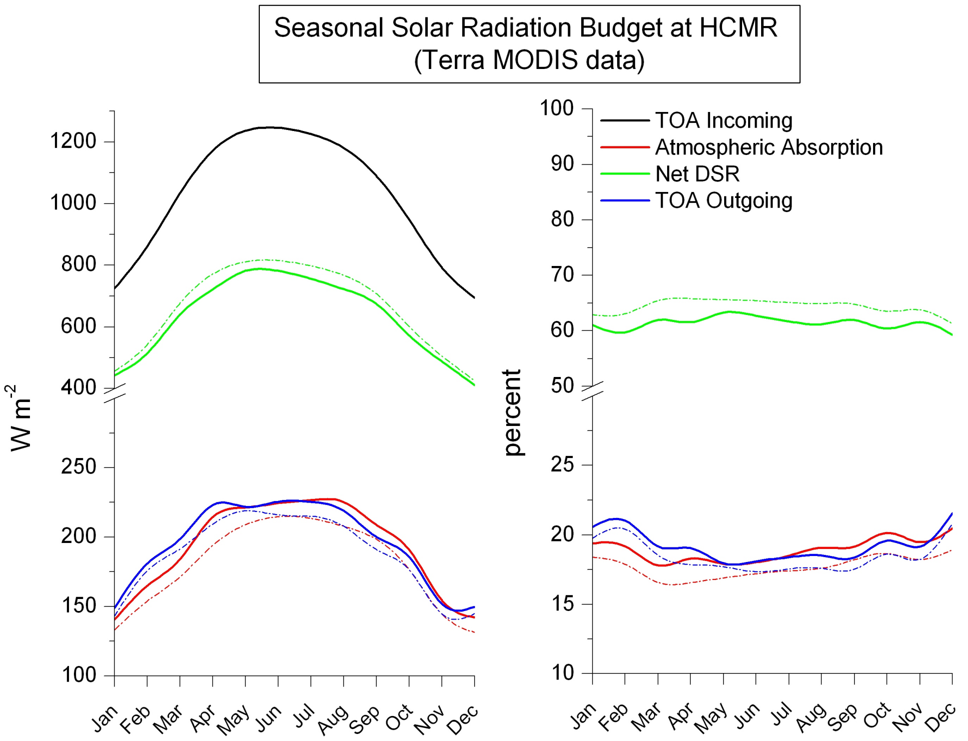

Figure 4.3: Seasonal variation of the solar radiation budget at HCMR station, in W m^{-2} (left panel) and % (right panel). The values are based on model computations on an instantaneous basis, using Terra MODIS input data. Dotted lines show the corresponding values without aerosols.

reflected and absorbed by the Earth's surface, while a fraction is reflected back to space. Due to conservation of energy, the sum of the radiation fluxes absorbed in the atmosphere and at the surface and the outgoing radiation at TOA always equal the total TOA incoming radiation. Figures 4.3 and 4.4 show the seasonal variation of these solar radiation budget components at HCMR station, based on Terra and Aqua MODIS data, respectively, in W m^{-2} and %. The incoming radiation at TOA ranges between ∼700 and 1250 W m^{-2}, with maximum values occurring in summer, due to smaller solar zenith angles. A similar seasonal variation is observed in the net DSR (surface absorption), atmospheric absorption and TOA outgoing components. The distribution of the incoming radiation in these components is almost constant throughout the year: about 60% is absorbed at the surface, 20% in the atmosphere, while about 20% is reflected back to space.

The model results without aerosols (dotted lines in Figures 4.3 and 4.4),

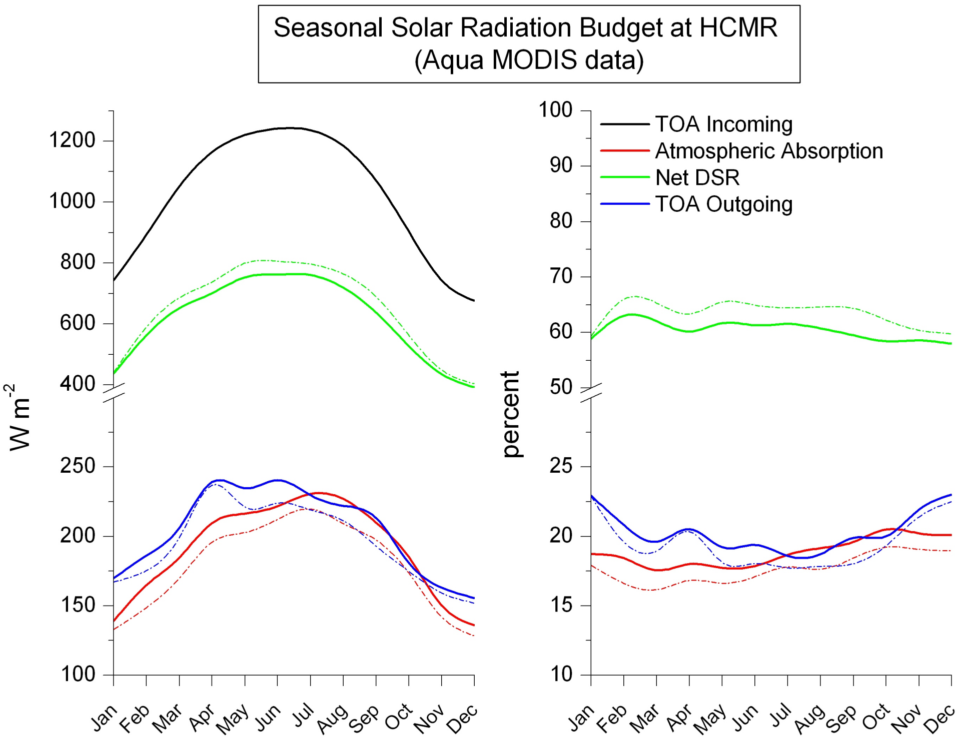

Figure 4.4: As in Figure 4.3, but based on Aqua MODIS input data.

show that at this site, aerosols cool the Earth–Atmosphere system, by increasing the radiation reflected back to space. They also cool the Earth's surface, by decreasing the net DSR through scattering and absorption of the DSR, while they cause a warming effect within the atmosphere. Aerosols increase multiple scattering within the atmosphere and together with their own absorption increase the probability of photon absorption within the atmosphere, leading to a warming effect.

4.2.3 Sensitivity analysis

To investigate the sensitivity of the model to the uncertainty of MODIS AOT, in the case of the HCMR station, the DSR was recalculated, using AOT values computed from the error limits of the MODIS retrieval algorithm ($\tau \pm \Delta\tau$, where τ is the AOT, and, according to Remer et al. (2005), $\Delta\tau = \pm 0.03 \pm 0.05\tau$ for AOT over ocean). The two new output datasets were then subtracted from the original model DSR output. Figure 4.5 shows the differences in the estimated DSR, when using the error limits of MODIS AOT

Table 4.1: Differences in model mean radiation budget components (in %) induced by variation of the aerosol optical properties (V is the variable and ΔV the amount of variation). Radiation budget components include DSR, atmospheric absorption (AtmAb) and TOA outgoing radiation. Mean values were computed from model calculations for the period 2000–2010, using Terra MODIS data.

V	ΔV	Δ(DSR)	Δ(AtmAb)	Δ(TOA)
AOT	$\pm 0.03 \pm 0.05\mathrm{AOT}$	∓ 0.8	± 1.6	± 1.0
fine mode AOT	±10%	∓ 0.2	± 0.6	± 0.2
g	±10%	± 0.6	∓ 0.1	∓ 2.0
ω	+10%	+1.9	−8.8	+3.3
ω	−10%	−2.6	+12.7	−5.0

retrieval algorithm instead of the AOT values, for Terra and Aqua MODIS. These differences range between almost 0.5% during summer and 1.5% in winter, when due to overcast conditions, they lead either to significantly small AOT or missing AOT retrievals from MODIS algorithm.

The same procedure was repeated for all components of the radiation budget, namely the DSR, net DSR, atmospheric absorption and outgoing radiation at TOA, and for all aerosol optical properties (AOT, fine mode AOT, asymmetry parameter g and single–scattering albedo ω). Table 4.1 shows the sensitivity results using Terra MODIS data only, since the corresponding results from Aqua MODIS were similar. The net DSR sensitivity results are also omitted, being identical with the corresponding results of DSR. As expected, an increase in AOT reduced the radiation reaching the Earth's surface, while atmospheric absorption and radiation reflected back to space were increased. The differences due to fine mode AOT variation were lower compared to those caused by the total AOT (mean DSR difference ~0.2%, reaching up to 1% in extreme cases), due to the lower fine mode AOT values. The asymmetry parameter +10% variation caused an increase in the surface DSR of the order of 0.6%, due to the increased aerosol forward scattering, with a small number of maximum differences ranging between 1.5 and 2.5%. This result, along with the small range of values of g (0.60–0.75), suggests that the use of MODIS g data does not affect the validity of the model output. Single–scattering albedo variations by +10% or −10% caused different results in the corresponding radiation budget outputs. In the case of +10% change in ω values, the output DSR increased by 1.9% on average, while atmospheric absorption decreased by 8.8% and the TOA outgoing radi-

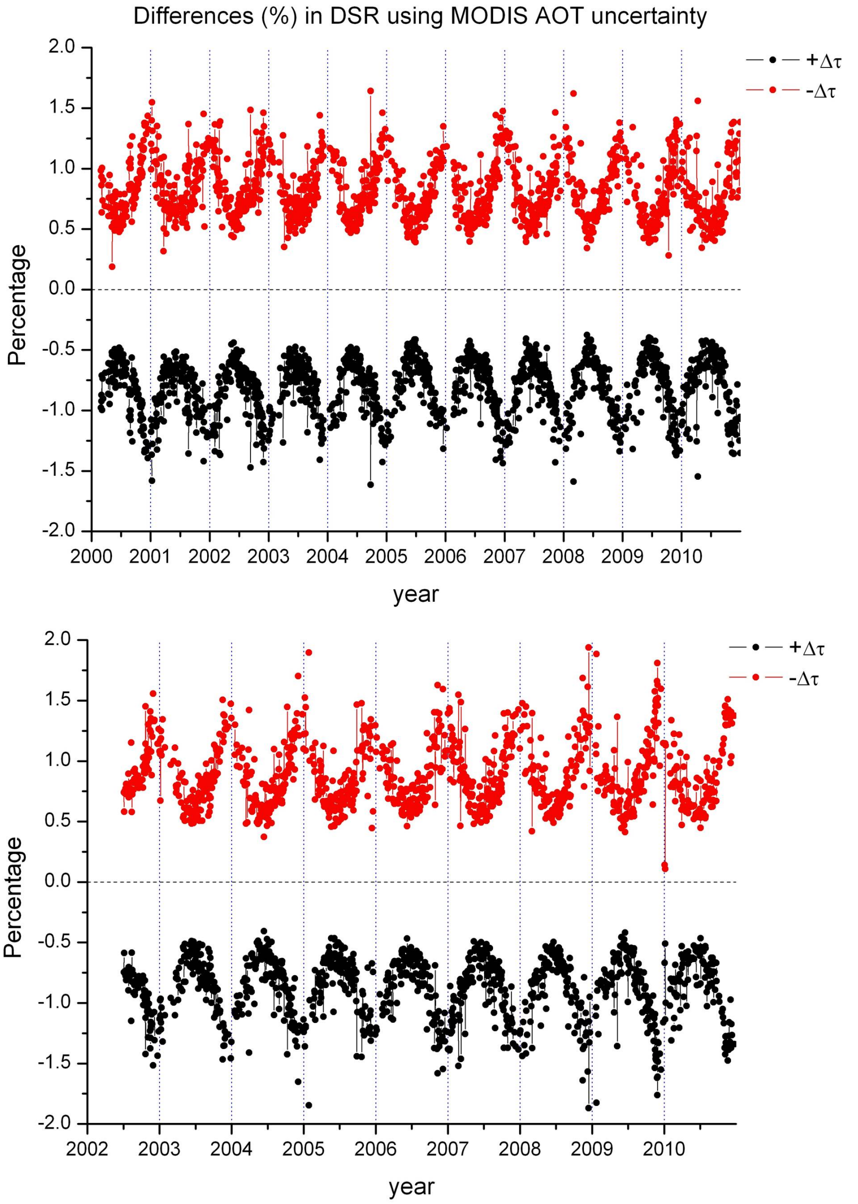

Figure 4.5: Time series of the differences in model instantaneous DSR (%), using Terra (a) and Aqua (b) MODIS AOT data and the error limits of the AOT retrieval algorithm ($\tau \pm \Delta\tau$), above the HCMR station, for the years 2000–2010.

ation increased by 3.3%, due to enhanced aerosol scattering. The variations appear larger when ω is reduced by 10%. This should be attributed to the typical values of ω, which usually exceed 0.9. Hence, an increase by 10% is actually less most of the times, since ω values cannot exceed 1.0. In reality, however, the smaller seasonal variation of ω and the uncertainties regarding its retrieval, as described in Dubovik and King (2000), suggest that possible variations of ω never reach values of 10%.

4.2.4 Time series of instantaneous aerosol DRE: Study of dust events

Figure 4.6 and Figure 4.7 show the instantaneous SW aerosol DRE (or ΔF, where F represents the radiation flux), at the surface ($\Delta F_{Surface}$), the net surface (surface absorption, $\Delta F_{NetSurface}$), within the atmosphere (ΔF_{AtmAb}) and at TOA (ΔF_{TOA}), for the corresponding years of available MODIS data over the HCMR station. The aerosol DRE generally takes higher values in summer, due to the larger incoming solar radiation and the clear–sky conditions prevailing during this season. Mean instantaneous values of DRE for the period 2000–2010, calculated from both output data sets (Aqua and Terra MODIS), are given in Table 4.2. The model DREs at the surface and at TOA were compared with the corresponding values available from the FORTH–CRETE AERONET station. The model output is well correlated with the AERONET output in the case of TOA DRE (R^2=0.67, slope=1.06). At the surface, the correlation is fair (R^2=0.50, slope=0.64), while the model tends to overestimate the surface DRE for small absolute values (less than -10 W m^{-2}).

Dust events, associated with coarse particles transported from the Sahara desert, enhance significantly the aerosol DRE, especially at the surface and

Table 4.2: Mean instantaneous values with standard deviations of DRE for the period 2000–2010, calculated from both output data sets (Aqua and Terra MODIS), for all days and dust events separately.

	DRE (W m^{-2})	
	All Days	Dust Events
$\Delta F_{Surface}$	-26 ± 16	-74 ± 21
$\Delta F_{NetSurface}$	-21 ± 13	-60 ± 17
ΔF_{AtmAb}	$+15 \pm 10$	$+44 \pm 14$
ΔF_{TOA}	$+6 \pm 5$	$+16 \pm 7$

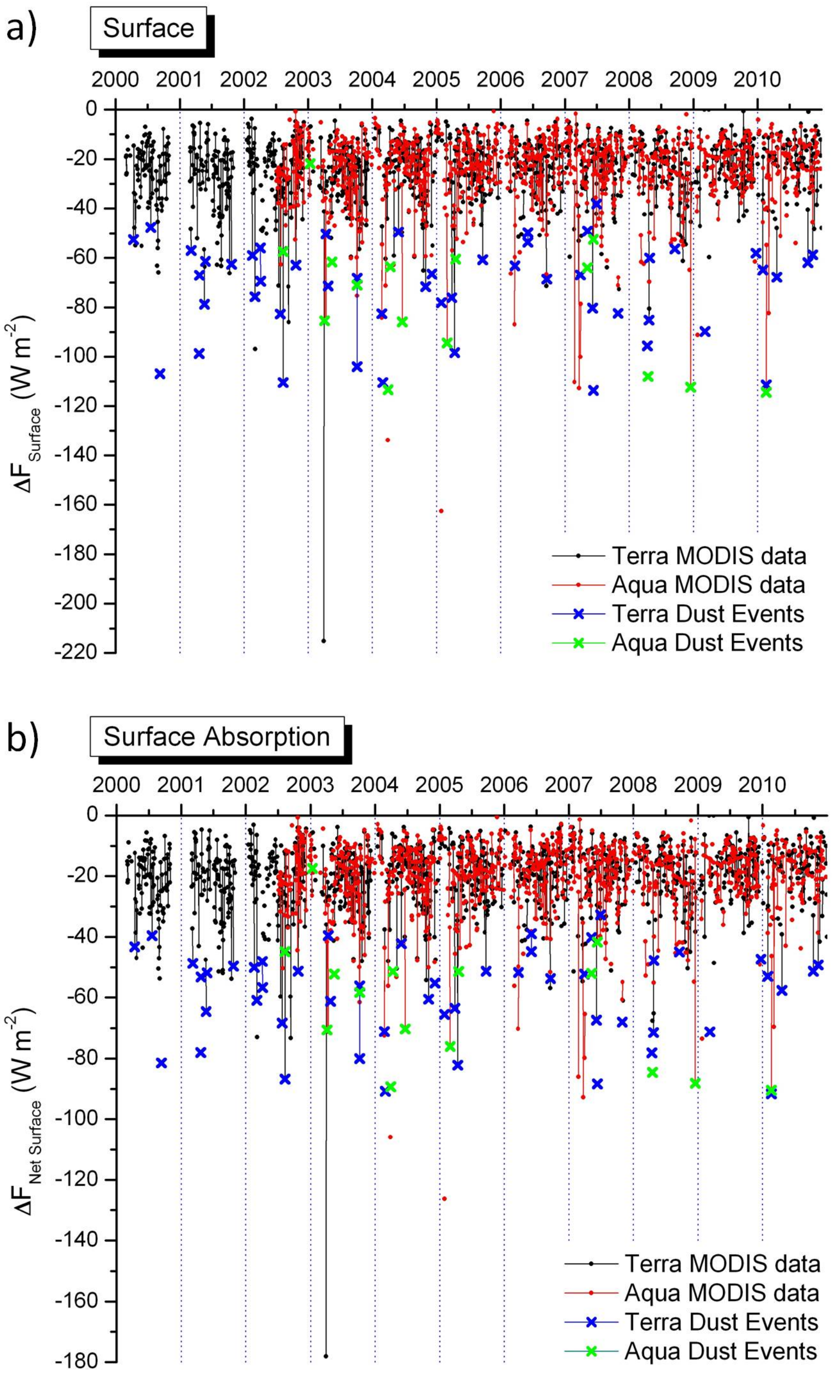

Figure 4.6: Time series of the instantaneous aerosol effect at the surface (incident (a) and absorbed (b) radiation), as computed from the model, based on MODIS Level 2 Terra and Aqua data, for the period 2000–2010, at the HCMR station.

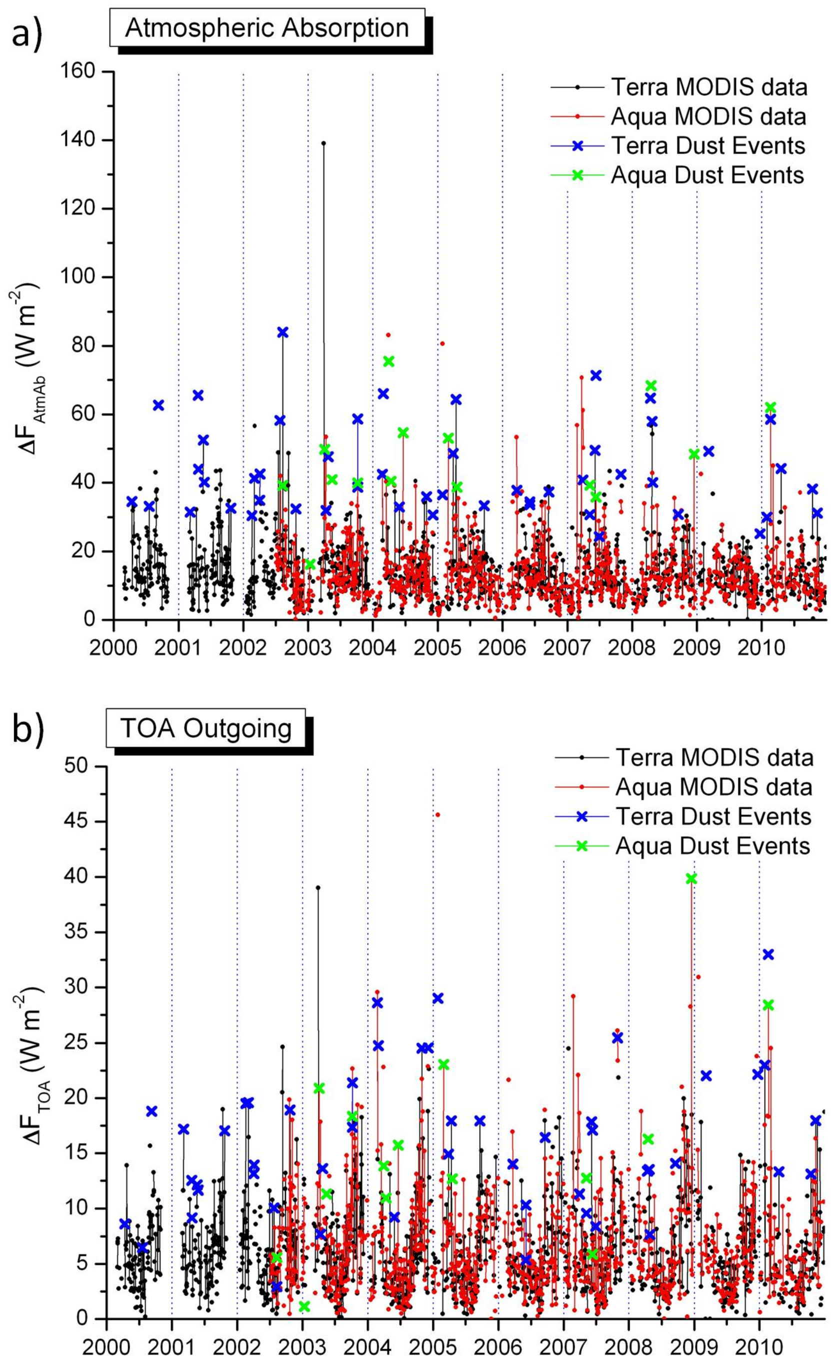

Figure 4.7: Time series of the instantaneous aerosol effect in the atmosphere (a) and at TOA (b), as computed from the model, based on MODIS Level 2 Terra and Aqua data, for the period 2000–2010, at the HCMR station.

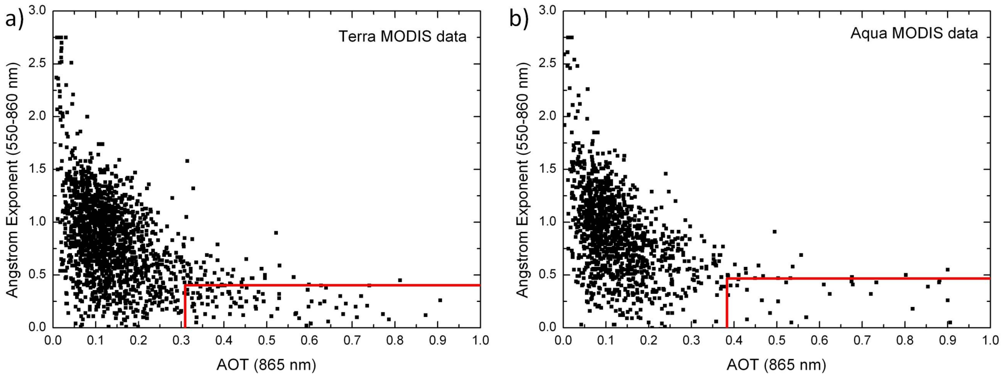

Figure 4.8: Scatter plots of the AOT at 865 nm versus Å at 550–860 nm from Terra (a) and Aqua (b) MODIS data over HCMR station. The red lines mark the areas where dust event criteria are met.

within the atmosphere. To further investigate dust events, they were first defined according to the following criteria: the AOT value should be greater than the mean AOT value for the whole period plus one standard deviation, and the Angstrom exponent (Å) less than the corresponding mean value for the whole period minus one standard deviation. Applying the above criteria to both Aqua and Terra MODIS (AOT at 865 nm and Å at 550–860 nm) and AERONET data (AOT at 1020 nm and Å at 440–870 nm), several cases were found, when dust events occurred. The scatter plots of the AOT versus Å, using Terra and Aqua MODIS data, are shown in Figure 4.8a and 4.8b, respectively. The red lines in these scatter plots mark the areas where the above mentioned dust event criteria are met.

These cases were further confirmed through back trajectories. Back trajectory calculations were made using the Hybrid Single Particle Lagrangian Integrated Trajectory (HYSPLIT) modeling system. This public domain model is documented in the international literature (Draxler and Hess, 1998). Figure 4.9 shows the seasonal distribution of the dust events detected during 2001–2010, from both Terra and Aqua MODIS data. Most of these events occur in spring, and secondarily in autumn.

The DRE on an instantaneous basis during dust events, when model results were available, is shown in Figures 4.6 and 4.7, in different symbols from the other days. Calculated from these cases, the mean values of the DRE on the radiation budget components during dust events are shown in Table 4.2. Mean values and standard deviations of the aerosol parameters (AOT, Å, g and ω) were also calculated for the entire time series and the dust event days separately. The mean AOT at 0.55 µm for the whole period examined was

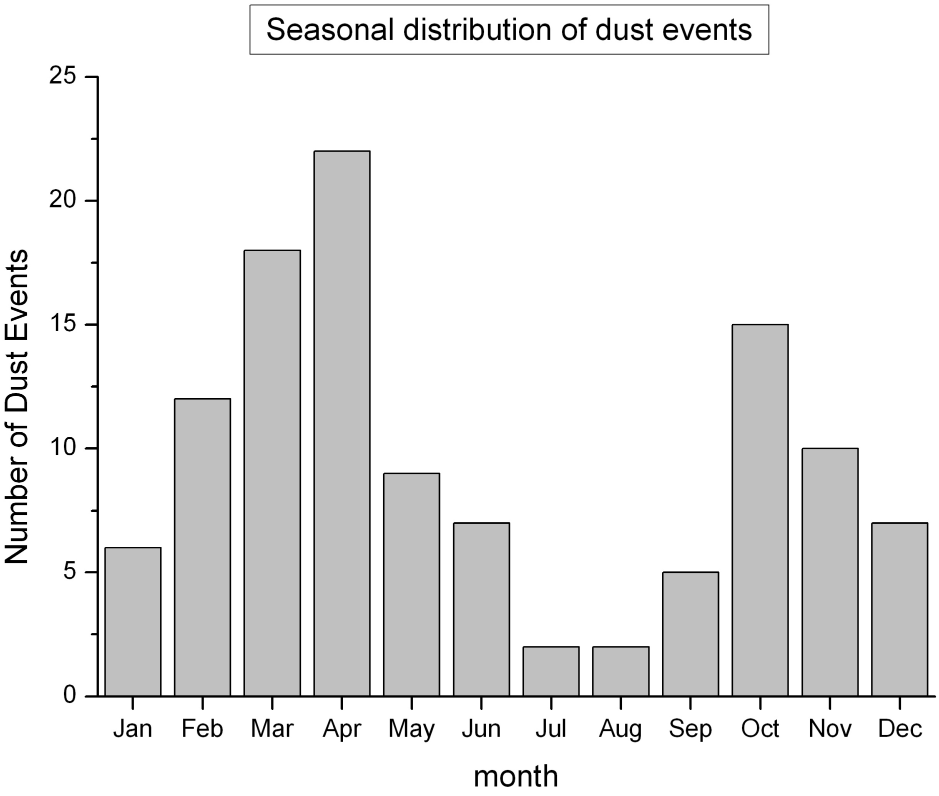

Figure 4.9: Seasonal distribution of dust events detected over HCMR station during the period 2001–2010, using both Terra and Aqua MODIS data.

0.21 ± 0.19, while during dust events it increased to 0.72 ± 0.66, exceeding 4.0 in some extreme cases. Values of AOT>1.0 during dust episodes have been reported in the past (e.g. Kaskaoutis et al., 2008; Tafuro et al., 2006). The asymmetry parameter at the same wavelength shows smaller variability, with values 0.71 ± 0.04 and 0.75 ± 0.02, respectively, reaching up to 0.78. Small variability was also found in the case of ω at 0.67 µm: 0.95 ± 0.02 and 0.96 ± 0.01 for the entire period and dust events, respectively. It should be mentioned that during dust episodes, the availability of ω data from the AERONET station was limited, with only 23 values found for the whole period examined. During dust events, Å decreased from 0.83 ± 0.42 for the entire period to 0.25 ± 0.12, as expected for dust particles with large radius. Similar values during dust outbreaks in Greece and the Central Mediterranean were reported by Kaskaoutis et al. (2008); Gómez-Amo et al. (2011) and Tafuro et al. (2006).

During these events, the decrease of the instantaneous DSR can range between -50 and -120 W m^{-2} and the corresponding decrease in surface absorption between -40 and -90 W m^{-2}, while the warming effect within the atmosphere ranges between 20 and 80 W m^{-2}. The outgoing radiation at TOA can be increased by up to 40 W m^{-2}. Similar results have been reported by Mallet et al. (2009), in a study of a dust event over West Africa. The maximum instantaneous DRE values, estimated by numerical simulations, were -172 and -26 W m^{-2} at the surface and at TOA, respectively. Gómez-Amo et al. (2011) also reported very high maximum DRE values during a 2007 Saharan dust event in the central Mediterranean: -224 W m^{-2} at the surface and -19 W m^{-2} at TOA. Haywood et al. (2003) found similar results, studying a Saharan dust episode over Cape Verde: the surface DRE of dust was shown to reach instantaneous values of approximately -130 W m^{-2}. Some of the dust event cases are shown in Table 4.3, along with the corresponding DRE and aerosol properties. Missing values are due to the lack of model input data.

4.2.5 Mean annual time series and trends

To investigate possible trends of the aerosol DRE during the period examined, annual mean values were calculated from the instantaneous values. In this analysis, annual mean values can be regarded as representative of the overpass time interval of each satellite. It should also be noted that successful model retrievals of the radiation budget and the corresponding DRE occur mainly in summer, autumn and spring, due to the more frequent availability of MODIS input data during these seasons. Hence, the results presented in this section should also be regarded as more representative of these seasons, compared to winter. Furthermore, the different distribution of days with model results in each year, could cause biases in the annual mean TOA incoming radiation and the corresponding radiation budget components. To avoid such complications, the radiation fluxes are presented as percentages of the corresponding TOA incoming fluxes, while the annual mean values of factors that affect the radiation budget, such as AOT and cloud fraction, were also computed from the same days with model output radiation fluxes.

Figure 4.10 shows this seasonal distribution of the model instantaneous results (in %), for the periods 2001–2010 for Terra MODIS data and 2003–2010 for Aqua MODIS, when complete annual results were available. This seasonal bias in annual time series and trends does not affect the significance of the results, since the highest aerosol loads and corresponding effects occur during these seasons, due to strong dust episodes taking place in spring and autumn, and high anthropogenic aerosol load in summer, as was shown by Fotiadi et al. (2006). Table 4.4 shows the monthly mean AOT values and the

Table 4.3: Characteristic dates of dust events and corresponding DRE (W m^{-2}) at the surface, within the atmosphere, at TOA and net surface, AOT and g at 550 nm, ω at 670 nm and Angstrom coefficient.

DRE	Surface		Atmosphere		TOA		NetSurface		AOT		g		ω		Å	
Dates	Terra	Aqua	Terra	Aqua	Terra	Aqua	Terra	Aqua	Terra	Aqua	Terra	Aqua	Terra	Aqua	Terra	Aqua
28/02/2004	-110		66		-25		-91		0.80		0.77		0.95		0.13	
29/03/2004		-113		75		-14		-89		0.87		0.75		0.95		0.43
18/06/2004		-86		55		-16		-70		0.82		0.74		0.96		0.44
26/01/2005	-78		37		-29		-66		0.49		0.75		0.95		0.12	
28/02/2005		-94		53		-23		-76		0.65		0.75		0.95		0.10
12/04/2005	-98		64		-18		-82		0.77		0.76		0.95		0.30	
26/02/2006		-66		34		-22		-56		0.44		0.74		0.95		0.48
10/06/2007	-114	-53	71	36	-17	-6	-88	-42	1.06	0.51	0.75	0.76	0.96	0.96	0.26	0.14

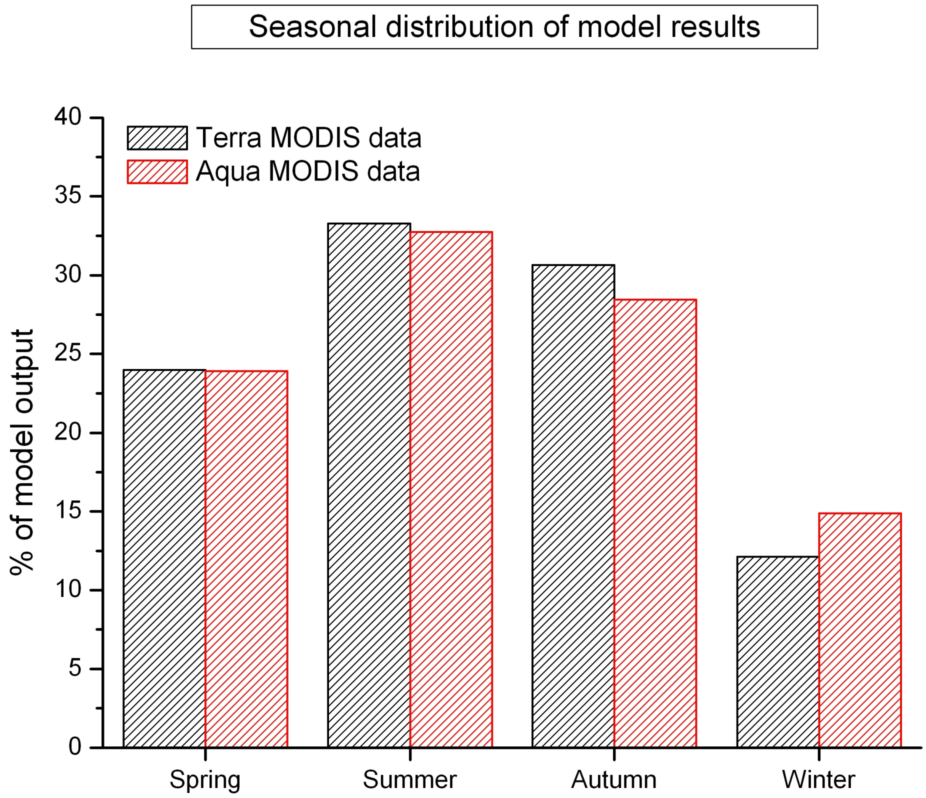

Figure 4.10: Seasonal distribution in % of the successful model computations during the periods 2001-2010 (Terra MODIS data) and 2003–2010 (Aqua MODIS data).

corresponding standard deviations from Terra and Aqua MODIS, calculated over the period examined. The results verify this seasonal behavior.

The annual mean aerosol DRE during 2001-2010 at surface (DSR and absorption), within the atmosphere and at TOA, is shown separately for Terra and Aqua MODIS data in Figure 4.11. An overall decreasing trend in DRE is obvious in both cases, and was quantified by applying linear regression. The corresponding % changes in DRE during the period examined are shown in Table 4.5. These decreases of DRE in all radiation budget components should be attributed to a corresponding significant decrease in AOT from both Terra and Aqua MODIS, shown in Figure 4.12 and Table 4.5. The trends in AOT and DRE found here, are in general agreement with the results presented by Papadimas et al. (2008, 2012), which showed that there is a decreasing trend in AOT and DRE values over the broader Mediterranean basin, using MODIS Level 3 data and examining the period from

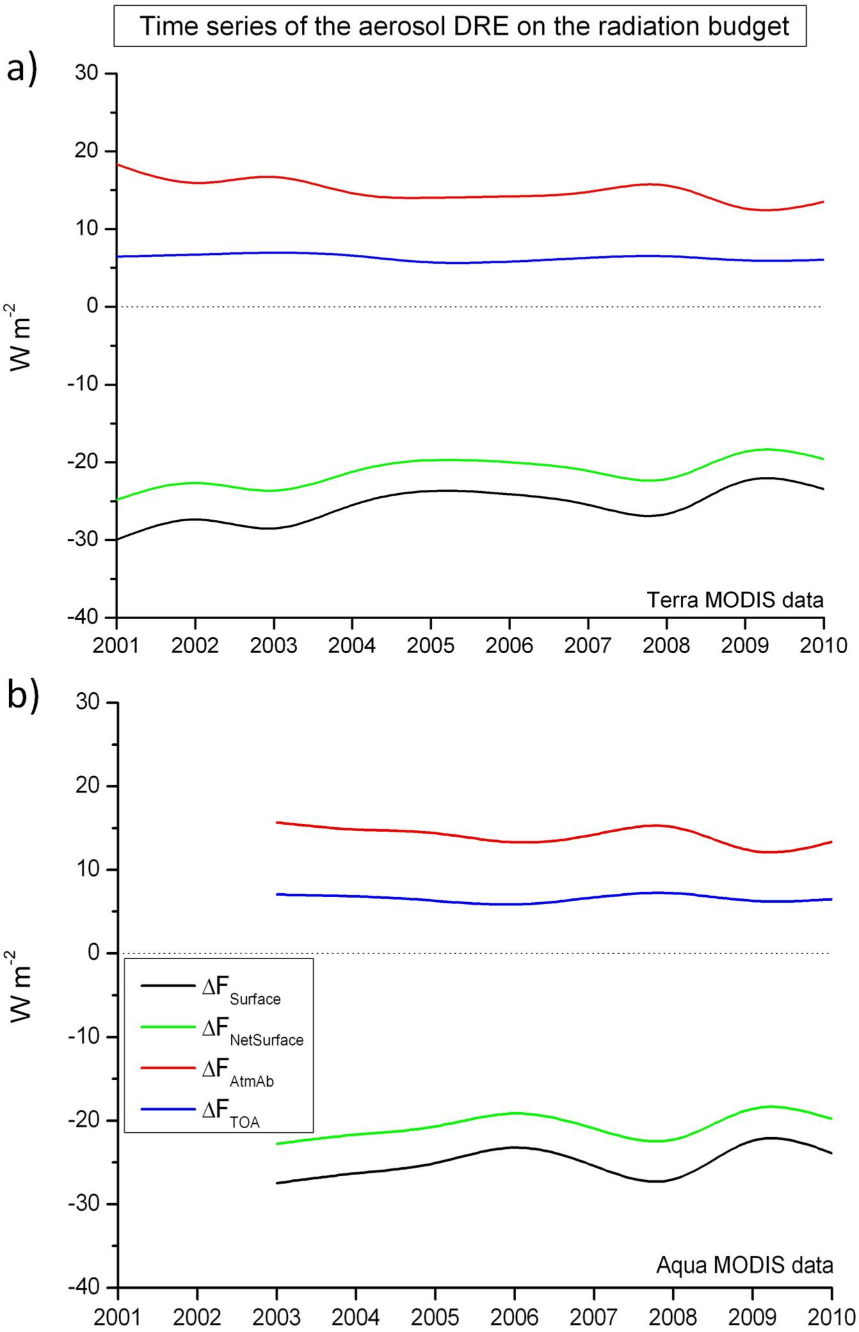

Figure 4.11: Time series of the annual mean aerosol DRE at surface (DSR and absorption), within the atmosphere and at TOA, using Terra (a) and Aqua (b) MODIS data.

Table 4.4: Monthly mean AOT and standard deviation from Terra and Aqua MODIS, calculated for the period 2000–2010.

Month	Terra MODIS AOT	Aqua MODIS AOT
January	0.14 ± 0.13	0.15 ± 0.14
February	0.20 ± 0.14	0.23 ± 0.42
March	0.25 ± 0.40	0.27 ± 0.40
April	0.29 ± 0.18	0.33 ± 0.44
May	0.26 ± 0.16	0.25 ± 0.17
June	0.20 ± 0.12	0.20 ± 0.11
July	0.21 ± 0.09	0.20 ± 0.08
August	0.22 ± 0.10	0.20 ± 0.09
September	0.22 ± 0.12	0.20 ± 0.09
October	0.21 ± 0.12	0.19 ± 0.11
November	0.17 ± 0.12	0.15 ± 0.09
December	0.16 ± 0.12	0.15 ± 0.11

2000 to 2006. These trends were attributed to reduced emissions of aerosols and aerosol precursors, but also to increased aerosol removal by enhanced precipitation.

While a decreasing AOT and corresponding aerosol DRE,assuming that other important parameters of the radiation budget remain unchanged during the period examined, are expected to increase the DSR and net DSR, by allowing more radiation to reach the surface, and decrease the atmospheric absorption and the radiation reflected back to space at TOA, the time series of the radiation fluxes from both Terra and Aqua MODIS appear contra-

Table 4.5: Changes (in %) in the annual mean aerosol DRE on the solar radiation budget and the corresponding AOT, during 2001–2010 (Terra MODIS) and 2003–2010 (Aqua MODIS). Statistically significant changes are shown in bold.

DRE	Terra MODIS	Aqua MODIS
$\Delta F_{\text{Surface}}$	**-19.6**	-11.3
$\Delta F_{\text{NetSurface}}$	**-19.1**	-11.1
ΔF_{AtmAb}	**-22.6**	-14.4
ΔF_{TOA}	-9.5	-3.7
AOT (0.55 µm)	**-19.4**	-15.2

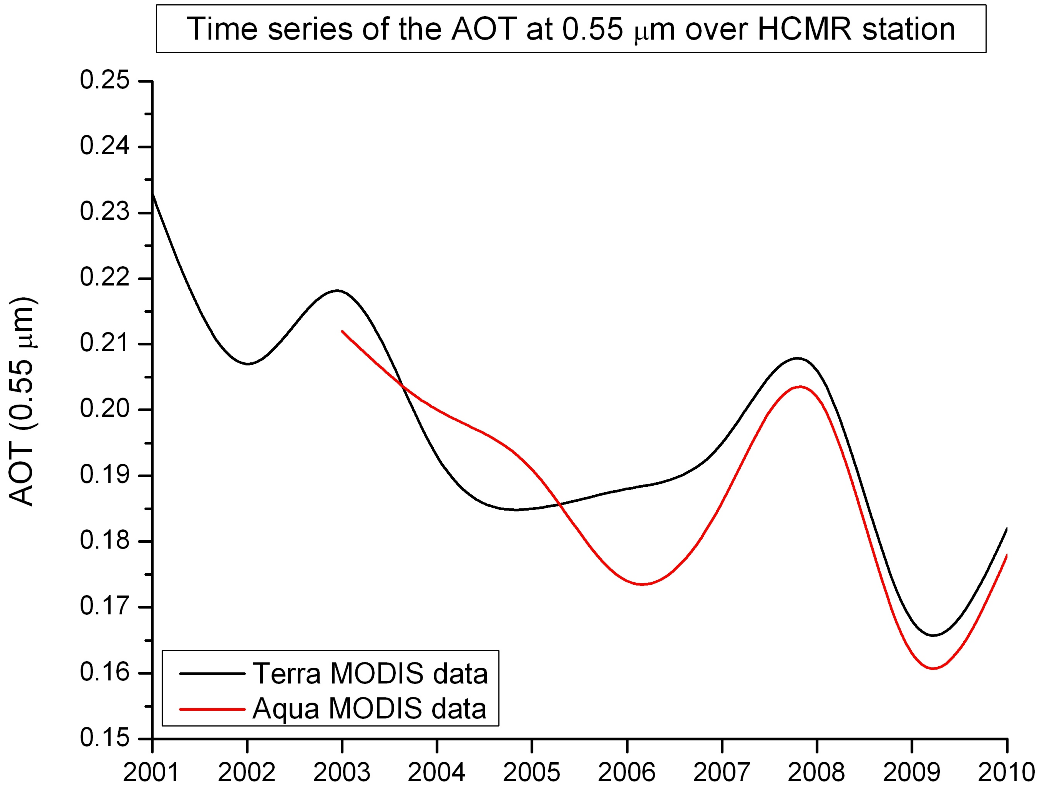

Figure 4.12: Time series of the annual mean AOT at 0.55 µm, using Terra and Aqua MODIS data.

dictory to this assumption (Figure 4.13a and b, respectively); The DSR, net DSR and atmospheric absorption have slightly decreased, while the TOA outgoing radiation has increased. Numerical values of these changes are given in Table 4.6. For the investigation of possible reasons that cause this behaviour in the radiation fluxes, the same time series analysis was performed for cloud fraction, along with a model sensitivity analysis. Figure 4.14 shows the time series of the annual mean cloud fraction over HCMR station using Terra and Aqua MODIS data for 2001–2010 and 2003–2010, respectively. By applying linear regression to these data, a significant increase in cloud fraction was found in both cases, equal to 15.4% and 13.4%, respectively (Table 4.5).

In order to verify that this increase in cloud fraction masked the expected increase in DSR and net DSR arising from the decrease in AOT and DRE, a model sensitivity analysis was performed, whereby the cloud fraction was increased by 10% and 15%, and the radiation budget results were compared against the corresponding original model output. The results, shown in Table

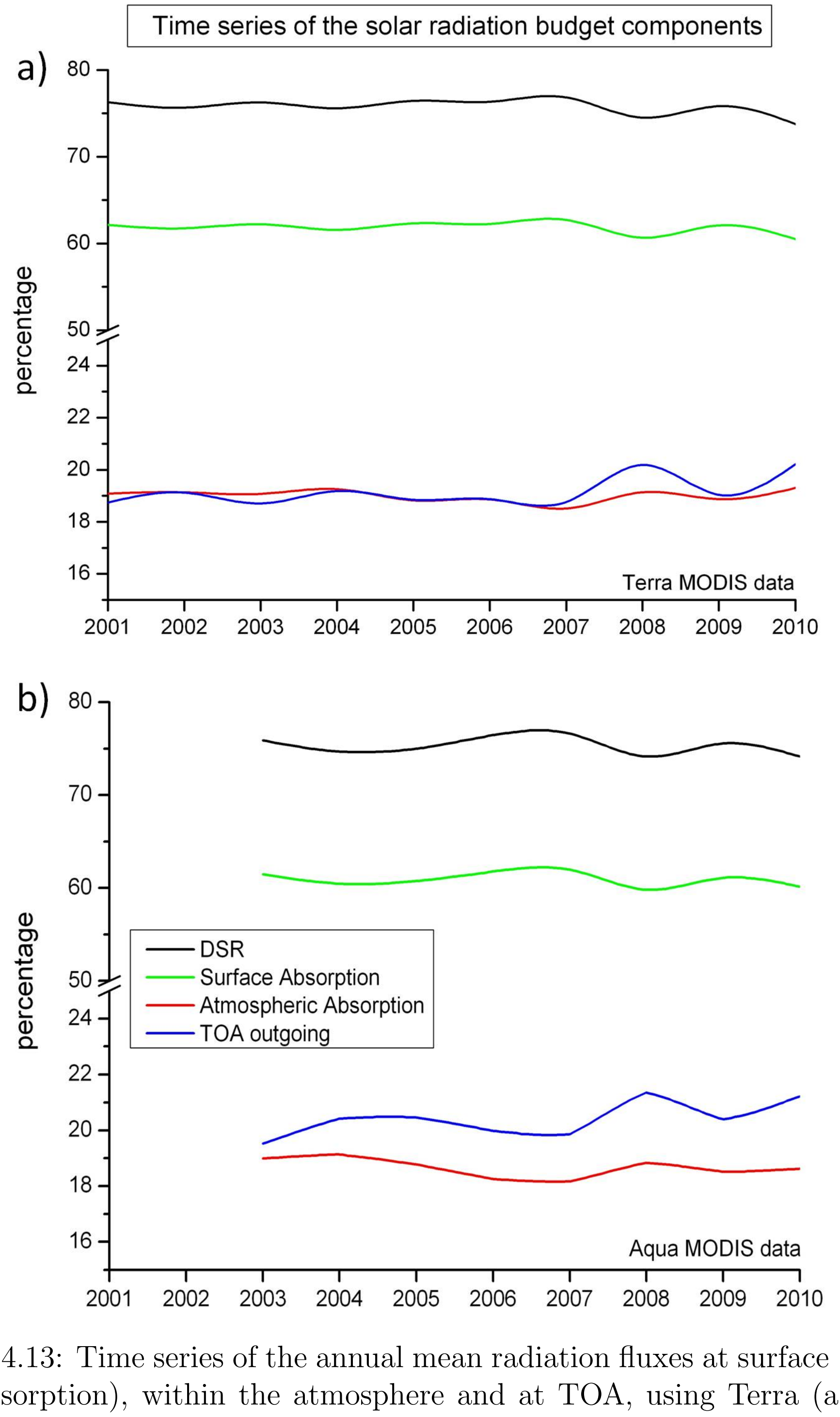

Figure 4.13: Time series of the annual mean radiation fluxes at surface (DSR and absorption), within the atmosphere and at TOA, using Terra (a) and Aqua (b) MODIS data.

Table 4.6: Changes (in %) in the annual mean components of the solar radiation budget and the cloud fraction during 2001–2010 (Terra MODIS) and 2003–2010 (Aqua MODIS).

	Terra MODIS	Aqua MODIS
DSR	-1.9	-1.1
Net DSR	-1.5	-1.2
Atmospheric Absorption	-0.5	-2.5
TOA Outgoing	+5.5	+6.0
Cloud Fraction	+15.4	+13.4

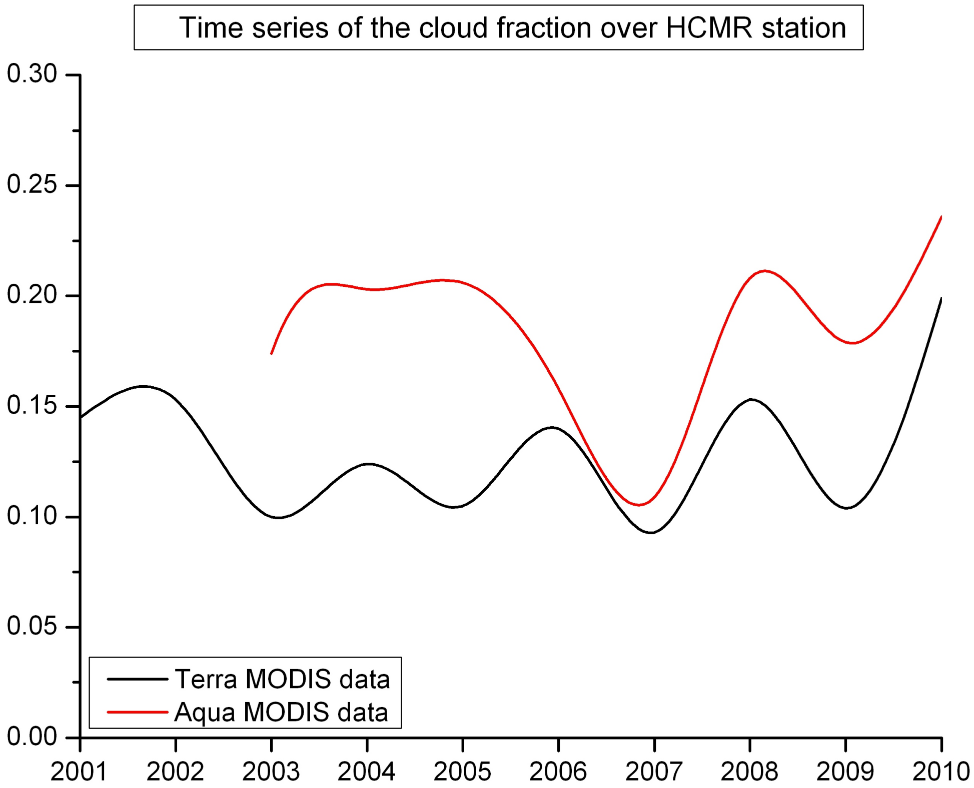

Figure 4.14: Time series of the annual mean cloud fraction, using Terra and Aqua MODIS data.

Table 4.7: Differences in model mean radiation budget components (in %) induced by variation of the cloud fraction. Radiation budget components include DSR, net DSR, atmospheric absorption (AtmAb) and TOA outgoing radiation. Mean values were computed from model calculations for the period 2000–2010, using Terra MODIS data.

Cloud Fraction	DSR	net DSR	AtmAb	TOA
+10	-2.4	-2.4	+0.7	+1.7
+15	-3.2	-3.2	+0.9	+2.3

4.7, imply that the 15% increase in cloud fraction, found during the period examined, counterbalanced the increase in DSR and net DSR that the AOT reduction would have caused, furthermore inducing a slight decrease (Table 4.6), while it has also masked a significant decrease in atmospheric absorption, and increased the TOA outgoing radiation.

4.2.6 Contribution of anthropogenic aerosols on DRE

The separation of total aerosol DRE into its natural and anthropogenic components is essential and very important in view of assessing human effects, through emissions of particulate matter (which may also influence natural aerosol events), on the extensively discussed current anthropogenic climate change. According to the literature, aerosols of anthropogenic origin are mainly composed of fine mode particles (Dubovik et al., 2002a; Kaufman et al., 2002). To investigate the inter–annual variation of the fine mode AOT, available from MODIS, and the fine mode fraction (FMF), calculated by dividing the fine mode AOT by the total AOT, the procedure described in the previous section was followed. Figure 4.15 shows the resulting time series of both fine mode AOT and FMF at 0.55 µm, over HCMR station, from Terra and Aqua MODIS data. As in the case of total AOT (Figure 4.12), the fine mode AOT has decreased significantly during the period examined. The FMF, however, has been slightly increasing until 2009, implying that the total AOT was decreasing more steeply than the fine mode AOT. This trend changed in 2010, when the total AOT increased (Figure 4.12), while the fine mode AOT continued to decrease, causing a significant reduction in FMF. The changes (in %) of fine mode AOT and FMF from Terra and Aqua MODIS during the entire period examined are shown in Table 4.8.

The technique used here to discriminate aerosols of anthropogenic origin was first implemented by Barnaba and Gobbi (2004), showing a good correspondence to the actual aerosol distribution, evaluated using other meth-

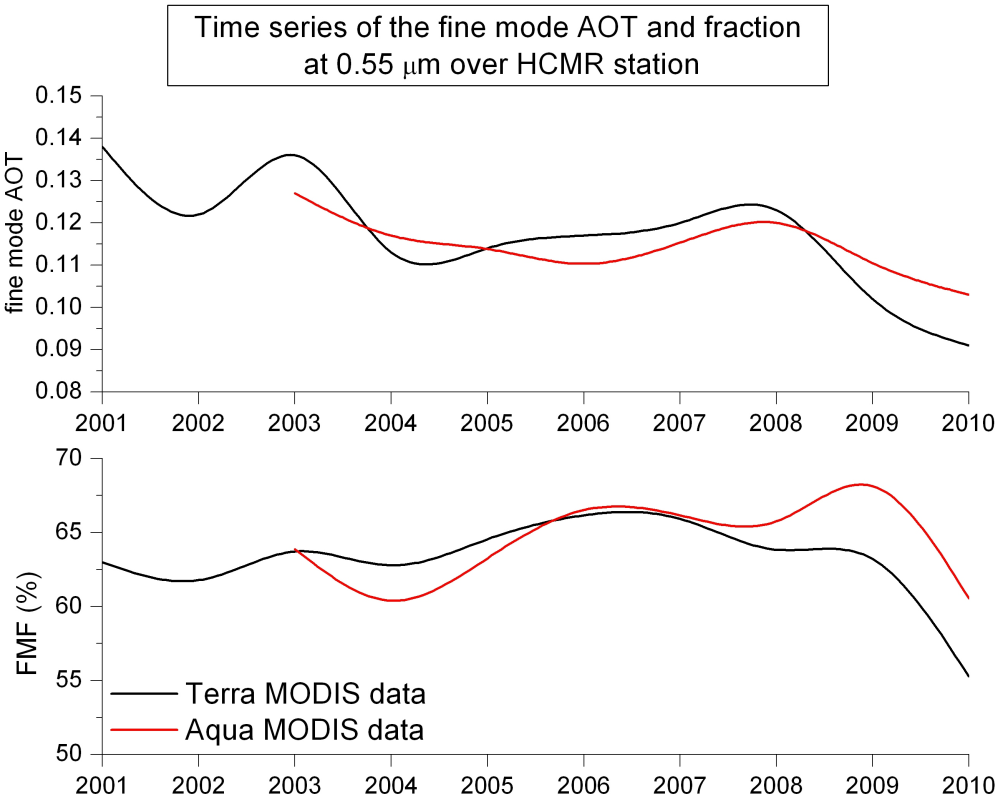

Figure 4.15: Time series of the annual mean fine mode AOT (a) and fraction (b) over HCMR station, at 0.55 µm, using Terra and Aqua MODIS data.

ods. To investigate the contribution of anthropogenic (mainly of fine mode) aerosols on the total DRE, the following method was used: For each day, the fine mode AOT at 0.55 µm was divided by the corresponding total AOT, to calculate the FMF. For the days that this fraction was greater than 0.7, fine mode particles were assumed to have prevailed and the asymmetry parameter g (taken from MODIS) and single–scattering albedo ω (from AERONET) during these days were assumed to be characteristic of the fine mode. In this section, AERONET Level 1.5 single–scattering albedo values were used, due to lack of sufficient temporal coverage from Level 2.0. For the days when the FMF was less than 0.7, a mixed aerosol load was assumed. To separate the anthropogenic component from the total aerosol DRE for days with mixed aerosol load, values of fine mode g, ω and AOT were also needed. While fine mode AOT is already available from MODIS on a daily basis, monthly averaged values of fine mode g and ω were used, computed from the days when the fine mode particles prevailed (FMF greater than 0.7).

Table 4.8: Changes (in %) in the annual mean fine mode AOT and fraction at 0.55 µm, during 2001–2010 (Terra MODIS) and 2003–2010 (Aqua MODIS). Statistically significant changes are shown in bold.

	Terra MODIS	Aqua MODIS
fine mode AOT	**-24.8**	-11.6
FMF	-4.1	+3.0

To investigate the optical characteristics of aerosols during anthropogenic events, the mean values of AOT at 0.55 µm, Å, g and ω, with the MODIS FMF greater than 0.7, were calculated. Fine mode AOT from both Terra and Aqua ranges between 0.12 ± 0.07, compared to the corresponding mean 0.21 ± 0.19 of total AOT for the same period. Å reaches up to 1.24 ± 0.68 for high FMF, from 0.83 ± 0.42 for the complete time series, while ω reduces to 0.89 ± 0.07, from a mean value of 0.95 ± 0.02. The asymmetry parameter exhibits smaller variance: 0.68 ± 0.07 for high anthropogenic aerosol loads, against 0.71 ± 0.04 for the whole period. A back trajectory analysis was conducted for the cases with FMF > 0.9. The results show that the Balkan area is the main source of these aerosol loads, with secondary sources being South Italy and Western Turkey.

The fine mode AOT at 0.55 µm was also examined on a seasonal basis and compared against the corresponding total AOT (Figure 4.16). Two distinct peaks in fine mode AOT appear in both Terra and Aqua MODIS, in April and August. The total AOT, however, is larger in April, compared to late summer and early autumn. This difference should be attributed to the contribution of Saharan dust events, which occur primarily in spring, and add a significant aerosol load to the total AOT.

The contribution of the fine mode aerosols to the total DRE was also examined on a seasonal basis, separately for Terra and Aqua. The results are shown in Figures 4.17 and 4.18, respectively. The DRE on net DSR peaks in spring in both cases, reaching almost -30 W m^{-2} on a monthly mean basis. This peak should be attributed to the combination of high natural and anthropogenic AOT values (Figure 4.16). The contribution of the fine mode aerosol on the surface absorption DRE, however, peaks in summer, due to the lower natural aerosol loads, compared to spring. The highest DRF on atmospheric absorption occurs also in summer; increased fine mode AOT, characterised by low values of ω, as mentioned before, causes increased absorption of radiation in the atmosphere. This characteristic also explains the reduced DRF on the TOA outgoing radiation, during summer: low values

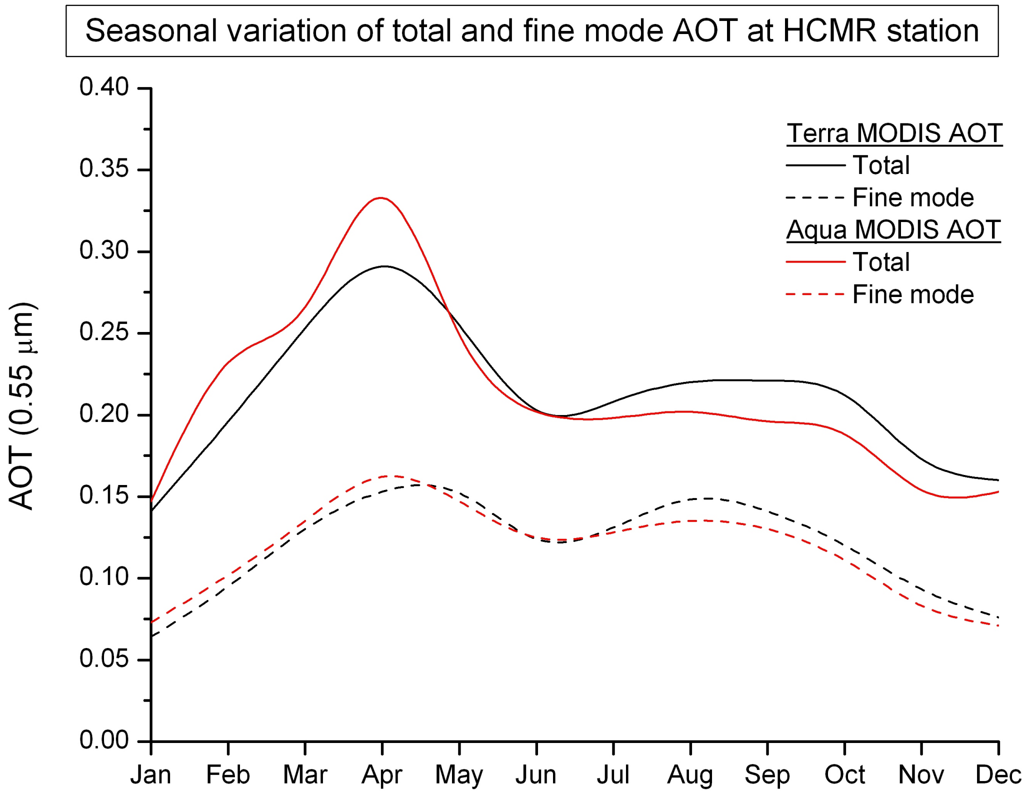

Figure 4.16: Seasonal variation of the total and fine mode AOT at 0.55 μm, over HCMR station, using Terra and Aqua MODIS data.

of ω result in less radiation scattered back at TOA from the aerosol layer.

4.3 Summary and conclusions

The FORTH model was used, along with MODIS Level 2 surface and atmospheric parameters, to compute the instantaneous SW radiation budget and aerosol DRE and DRF at the surface, within the atmosphere and at TOA, above HCMR station. The MODIS data were supplemented with data single–scattering albedo data from the FORTH–CRETE AERONET station. The model computations were performed for the 11–year period from 2000 to 2010. The results for the DSR were validated against HCMR and Finokalia stations data, showing that in general the model is able to predict the DSR in this region, with a negative bias of about 30 to 70 W m^{-2}.

The calculated instantaneous aerosol DRE at the surface, in the atmo-

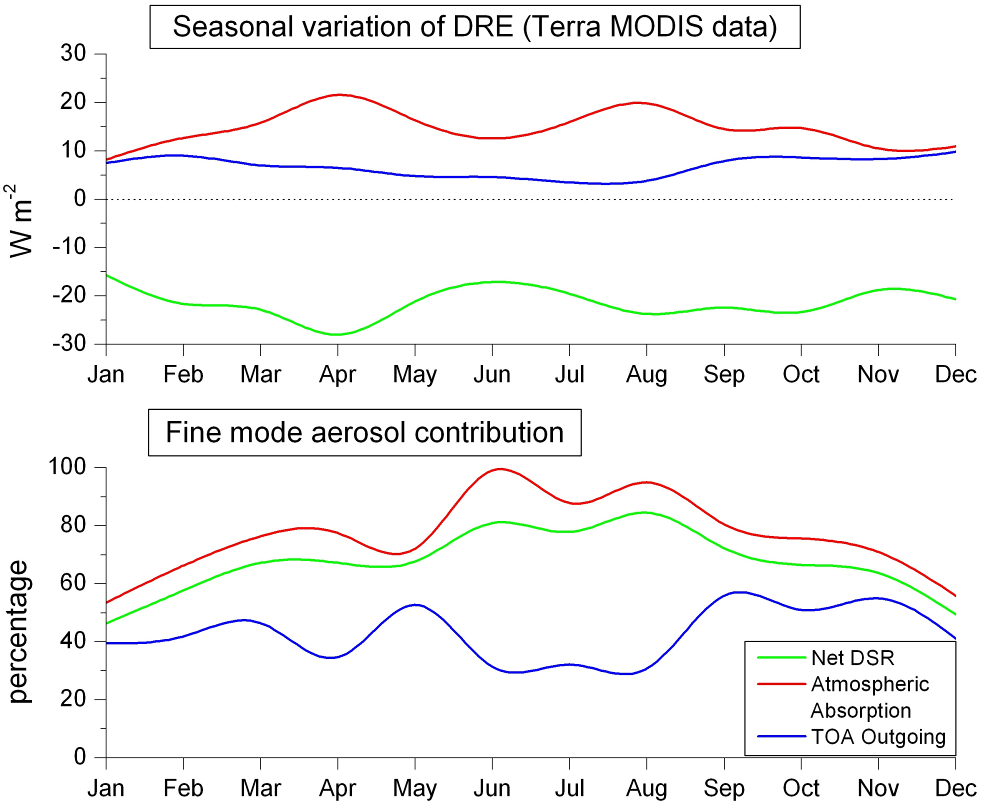

Figure 4.17: Seasonal variation of the DRE on net DSR, atmospheric absorption and TOA outgoing radiation (upper panel), and corresponding contribution of the fine mode aerosols (lower panel), at HCMR station, using Terra MODIS data.

sphere and at TOA, showed the significance of dust events in the region, when the DRE at the surface can induce surface cooling as high as -120 W m^{-2}. The maximum values observed, during dust events, of warming and cooling effects in the atmosphere and at TOA, are approximately 90 and -40 W m^{-2}, respectively. These large DRE values constitute an important modification factor of the local surface and atmospheric radiation budget which, given the key location of Crete, is representative of the eastern Mediterranean basin. The DRE is characterised by a seasonal pattern, with maximum values during spring, following the corresponding increase in AOT, which is caused by a combination of transported African dust, that occurs mainly in this season, with increased fine mode aerosol loads. A secondary maximum is also observed in late summer and early autumn, associated with anthropogenic aerosols.

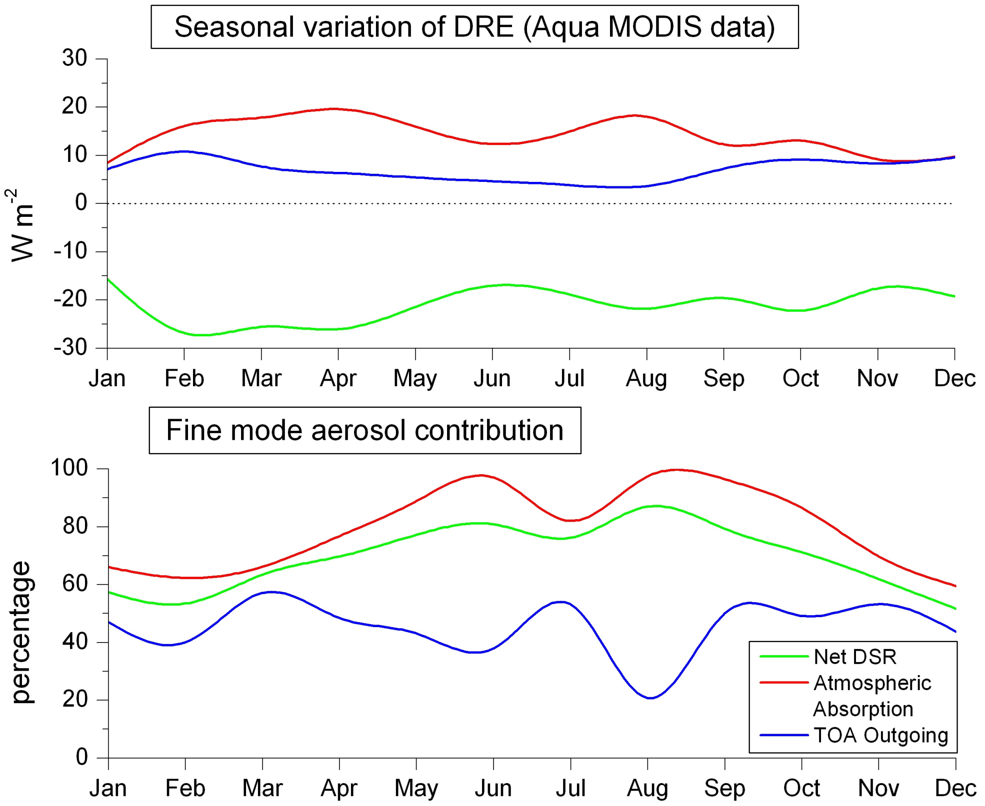

Figure 4.18: As in Figure 4.17, but based on Aqua MODIS data.

The linear regression analysis applied to the annual mean DRE total AOT and fine mode AOT, reveals a decreasing trend during the period examined, which is in agreement with similar previous results (e.g. Papadimas et al., 2008). The corresponding radiation budget trends, however, are also influenced by a significant increasing trend in cloud fraction.

The contribution of anthropogenic aerosols on the DRE at surface is highest during summer. Low values of single–scattering albedo in fine mode aerosols, associated with increased absorption of radiation, explain their significant contribution in atmospheric absorption, and the attenuation of radiation reflected back to space at TOA.

This version of the FORTH model can be used in the future at various sites of specific interest, regarding the direct effect of aerosols on the radiation budget, to investigate the local patterns of the DRE. This is important, especially in view of the assessment of aerosol DRE and DRF under different aerosol regimes, for example urban, remote continental, biomass burning or desert dust. Such future model computations can also benefit from the increased availability of vertically resolved aerosol information, provided by modern platforms like CALIPSO and CloudSat of A–train satellites. It is also very important to perform validations of computed fluxes against ground–based stations and satellite measurements, to ensure the validity of the results.

Bibliography

Barnaba, F. and Gobbi, G. P.: Aerosol seasonal variability over the Mediterranean region and relative impact of maritime , continental and Saharan dust particles over the basin from MODIS data in the year 2001, Atmospheric Chemistry and Physics, pp. 2367–2391, 2004.

Draxler, R. R. and Hess, G. D.: An overview of the HYSPLIT 4 modelling system for trajectories, dispersion and deposition, Australian Meteorological Magazine, 47, 295–308, 1998.

Dubovik, O. and King, M. D.: A flexible inversion algorithm for retrieval of aerosol optical properties from Sun and sky radiance measurements, Journal of Geophysical Research: Atmospheres, 105, 20 673–20 696, doi: 10.1029/2000JD900282, 2000.

Dubovik, O., Holben, B., Eck, T. F., Smirnov, A., Kaufman, Y. J., King, M. D., Tanré, D., and Slutsker, I.: Variability of Absorption and Optical Properties of Key Aerosol Types Observed in Worldwide Locations, Journal of the Atmospheric Sciences, 59, 590–608, 2002a.

Fotiadi, A., Hatzianastassiou, N., Drakakis, E., Matsoukas, C., Pavlakis, K. G., Hatzidimitriou, D., Gerasopoulos, E., Mihalopoulos, N., and Vardavas, I.: Aerosol physical and optical properties in the Eastern Mediterranean Basin, Crete, from Aerosol Robotic Network data, Atmospheric Chemistry and Physics, pp. 5399–5413, 2006.

Gómez-Amo, J., Pinti, V., Di Iorio, T., di Sarra, A., Meloni, D., Becagli, S., Bellantone, V., Cacciani, M., Fuà, D., and Perrone, M. R.: The June 2007 Saharan dust event in the central Mediterranean: Observations and radiative effects in marine, urban, and sub-urban environments, Atmospheric Environment, 45, 5385–5393, doi:10.1016/j.atmosenv.2011.06.045, 2011.

Haywood, J., Francis, P., Osborne, S., Glew, M., Loeb, N. G., Highwood, E. J., Tanré, D., Myhre, G., Formenti, P., and Hirst, E.: Radiative properties and direct radiative effect of Saharan dust measured by the C-130 aircraft during SHADE: 1. Solar spectrum, Journal of Geophysical Research, 108, doi:10.1029/2002JD002687, 2003.

Kaskaoutis, D., Kambezidis, H., Nastos, P., and Kosmopoulos, P.: Study on an intense dust storm over Greece, Atmospheric Environment, 42, 6884–6896, doi:10.1016/j.atmosenv.2008.05.017, 2008.

Kaufman, Y. J., Tanré, D., and Boucher, O.: A satellite view of aerosols in the climate system, Nature, 419, 215–223, 2002.

Mallet, M., Tulet, P., Serça, D., Solmon, F., Dubovik, O., Pelon, J., Pont, V., and Thouron, O.: Impact of dust aerosols on the radiative budget, surface heat fluxes, heating rate profiles and convective activity over West Africa during March 2006, Atmospheric Chemistry and Physics, 9, 7143–7160, doi:10.5194/acp-9-7143-2009, 2009.

Papadimas, C. D., Hatzianastassiou, N., Mihalopoulos, N., Querol, X., and Vardavas, I.: Spatial and temporal variability in aerosol properties over the Mediterranean basin based on 6-year (2000-2006) MODIS data, Journal of Geophysical Research: Atmospheres, 113, doi:10.1029/2007JD009189, 2008.

Papadimas, C. D., Hatzianastassiou, N., Matsoukas, C., Kanakidou, M., Mihalopoulos, N., and Vardavas, I.: The direct effect of aerosols on solar radiation over the broader Mediterranean basin, Atmospheric Chemistry and Physics, 12, 7165–7185, doi:10.5194/acp-12-7165-2012, 2012.

Remer, L., Kaufman, Y. J., Tanré, D., Mattoo, S., Chu, D. A., Martins, J. V., Li, R.-R., Ichoku, C., Levy, R. C., Kleidman, R. G., Eck, T. F., Vermote, E., and Holben, B. N.: The MODIS Aerosol Algorithm, Products, and Validation, Journal of the Atmospheric Sciences, 62, 947–973, 2005.

Tafuro, A. M., Barnaba, F., De Tomasi, F., Perrone, M. R., and Gobbi, G. P.: Saharan dust particle properties over the central Mediterranean, Atmospheric Research, 81, 67–93, doi:10.1016/j.atmosres.2005.11.008, 2006.

Chapter 5

Aerosol Effect on Surface Ozone Photolysis

5.1 Introduction

Ozone is the main atmospheric absorber of solar UV and visible radiation in the stratosphere. In the troposphere, O_3 acts both as a direct greenhouse gas, and as an indirect controller of greenhouse gas lifetimes. According to IPCC, it contributes about 0.35°C to the total 2.4°C rise due to greenhouse gases since pre–industrial times (see also Figure 1.4). The sources of tropospheric O_3 include in situ production by chemical reactions of precursor species (including CO and nitrogen oxides), and the transfer of stratospheric O_3 to the troposphere (IPCC, 2007). Due to its large spatial and temporal variability, it is studied primarily using CTMs. Results from these studies show that the modelled tropospheric O_3 abundances generally agree with observations and in most cases the net budgets are in balance. The individual budget components, however, vary greatly (Denman et al., 2007).

The photolysis of tropospheric O_3 constitutes its dominant sink, leading to different products, depending on the radiation wavelength. One of the key products is $O(^1D)$, which is produced by the photolysis reaction:

$$O_3 + h\nu \rightarrow O(^1D) + O_2, \tag{5.1}$$

primarily for wavelengths below 330 nm. The photolysis rate of O_3, $J(O^1D)$, is the inverse of the atmospheric lifetime of an O_3 molecule before photolysis occurs. Except in affecting the tropospheric O_3 concentration and its budget, the importance of $J(O^1D)$ lies also in providing the mechanism by which pollutants such as CO and CH_4 are removed from the lower atmosphere: the reaction of $O(^1D)$ with atmospheric water, forms hydroxyl–OH and hydroperoxyl–OH_2 radicals, which are highly reactive and constitute the primary oxidizing species in the lower atmosphere (Rohrer and Berresheim, 2006). Thus, possible changes in $J(O^1D)$ are expected to influence both the greenhouse effect and air pollution levels.

Several methods have been used in the past for the measurement of $J(O^1D)$, including chemical actinometry (e.g. Shetter et al., 1996; Blackburn et al., 1992) and filter radiometry (e.g. Gerasopoulos et al., 2006; Hofzumahaus et al., 1992), while spectral actinic fluxes have also been used, derived from spectral UV irradiance measurements (e.g. Bais et al., 2003; Kazadzis et al., 2004). Numerous campaigns have also focused on the study of $J(O^1D)$ (see Gerasopoulos et al., 2012, and references therein).

Atmospheric aerosols and total column ozone are amongst the important factors which determine $J(O^1D)$ in an area. The effect of aerosols on $J(O^1D)$ has been studied in the past, using either modelling methods (Li et al., 2011; Tie et al., 2005; Yang and Levy II, 2004), or direct comparisons between $J(O^1D)$ and AOT collocated station measurements (Gerasopoulos et al., 2012; Casasanta et al., 2011). This effect can also be deduced by the corresponding aerosol effect in the UV fluxes (Kerr, 2005; Balis et al., 2002), considering that reaction (5.1) takes place under the presence of UV radiation. The effect of total column ozone on $J(O^1D)$ is also caused by the high absorption at the same wavelengths, which reduces the amount of UV radiation that would otherwise reach the surface.

In terms of both aerosol load and total column ozone, the eastern part of the Mediterranean is a place of high interest. As described in Section 1.4, numerous studies have shown that aerosols play a crucial role in the radiative processes over the area, through their high temporal and spatial variability and their complex characteristics resulting from their mixed composition. Total column ozone also exhibits high variability in the area, as has been shown in the past (Demirhan et al., 2005; Hudson et al., 2003).

In the current chapter, the calculation of $J(O^1D)$ and the estimation of the aerosol and total ozone effects are presented. The computations are performed over Finokalia station, using the FORTH radiative transfer model (Chapter 3), and input data from MODIS Level 2 Collection 051 Atmosphere Products (Section 2.2). The area has been selected due to its representativeness of the wider Eastern Mediterranean. Additionally, $J(O^1D)$ measurements have been conducted in Finokalia during the period 2002–2006, rendering the area suitable for validation purposes (Section 2.4).

In the next section, the methodology for deriving $J(O^1D)$ and the aerosol and total ozone effects, using the FORTH model and MODIS Level 2 input data, are described. The results, including the total ozone validation against Thessaloniki station measurements, the model derived $J(O^1D)$ validation against Finokalia station measurements, trends of J(O^{1}D) during the period examined and the corresponding aerosol and total ozone effects are given in Section 5.3, before the summary and conclusions.

5.2 Calculation of J(O^{1}D)

For the computation of J(O^{1}D), input from the FORTH model output was used, specifically the enhancement factor for photolysis. The corresponding J(O^{1}D) values are computed on an instantaneous basis (satellite overpass time), spanning the 11–year period from February 2000 to December 2010. For the calculation of J(O^{1}D) (s^{-1}) the following formula was used, given by Vardavas and Taylor (2011):

$$j(z,t) = \int_{\lambda_a}^{\lambda_b} f_\lambda(z,t)\mu_0(t)S_{\odot\lambda}\sigma_\lambda(z)\Phi_\lambda(z)\mathrm{d}\lambda, \tag{5.2}$$

where z and t are the altitude and time, respectively, f_λ is the enhancement factor, μ_0 is the cosine of the solar zenith angle, $S_{\odot\lambda}$ is the spectral solar irradiance, σ_λ is the ozone absorption cross section and Φ_λ is the quantum yield, which represents the probability for a molecule that absorbs a photon to be photodissociated. The enhancement factor is given by

$$f_\lambda = \frac{4\pi\mathcal{J}_\lambda + \mu_0 F^{\downarrow}_{\mathrm{d}\lambda}}{\mu_0 S_{\odot\lambda}} \tag{5.3}$$

The total monochromatic solar flux for photolysis (also known as actinic flux), is $4\pi\mathcal{J}_\lambda + \mu_0 F^{\downarrow}_{\mathrm{d}\lambda}$, where $4\pi\mathcal{J}_\lambda$ is the spherically integrated over all solid angles diffuse radiation flux component and $\mu_0 F^{\downarrow}_{\mathrm{d}\lambda}$ the direct radiation flux component, with $F^{\downarrow}_{\mathrm{d}\lambda}$ given by equation (3.55). Hence, in the calculation of f_λ, all radiation components are taken into account: downwelling direct and diffuse radiation, as well as upwelling diffuse radiation.

The solar zenith angle is available from MODIS Level 2 Products, while the spectral solar irradiance, available from Gueymard (2004), is accounted for as described in Section 3.3. The ozone absorption cross section and quantum yield are available from the Jet Propulsion Laboratory Chemical Kinetics and Photochemical Data for Use in Atmospheric Studies (Tables 4–5 and 4–6 in Sander et al., 2006). The absorption cross section, which is temperature dependent, is calculated using linear interpolation between the two given values (at T=218 K and T=293–298 K), while the temperature dependence of the quantum yield is also taken into account, as recommended by Matsumi et al. (2002).

Since the AOT in the 300–320 nm range is crucial for the purposes of this study, the MODIS AOT (described in Section 2.2) is supplemented with daily AOT values at 340 nm from the FORTH–CRETE AERONET station, located about 50 km west of Finokalia station. The best fitting function to these 8 AOT values was estimated on a per–day basis, and the AOT at the 118 model wavelengths was calculated using this function. For the estimation of the aerosol effect on $J(O^1D)$ the model was run with and without aerosols, while all other input parameters remain unchanged. The aerosol effect is then given by

$$\Delta J(O^1D) = J(O^1D) - J(O^1D)_{\mathrm{no-aerosol}}, \tag{5.4}$$

where $J(O^1D)$ and $J(O^1D)_{\text{no-aerosol}}$ are the surface O_3 photolysis rates computed with and without aerosols, respectively. The estimation of the total column ozone effect on $J(O^1D)$ was based on sensitivity analysis.

5.3 Results

5.3.1 Validation of total column ozone

The MODIS Level 2 Total Ozone Product has been validated globally with OMI/TOMS data and also with ground based Brewer Measurements during a year long time period over Budapest, Hungary (Borbas et al., 2011). However, in order to further ensure the validity of the results, MODIS total ozone is validated against ground based measurements conducted at the University of Thessaloniki with a Brewer MKII spectrophotometer. Total ozone station data from Thessaloniki were available on a high temporal resolution daily and diurnal basis during the entire 11–year period studied. For each day, station data were used to compute the mean total ozone values corresponding to the Terra and Aqua overpass time intervals. These temporal mean values were validated against spatial mean MODIS total ozone values from a 50 km × 50 km area centered on the station coordinates. The validation results for Terra and Aqua separately are shown in Figure 5.1. The determination coefficients show that the station and satellite data correlate well. Nevertheless, a systematic bias of about 26 Dobson Units (DU) is detected in the case of Aqua: satellite data tend to underestimate total ozone, compared to the station measurements.

This systematic discrepancy between station and Aqua MODIS total ozone data, along with the high importance of total ozone in the calculation of $J(O^1D)$, discussed in Section 5.3.5, could lead to consequent systematic errors in $J(O^1D)$ calculated using Aqua MODIS data. For these reasons, only Terra MODIS data were used in the present study.

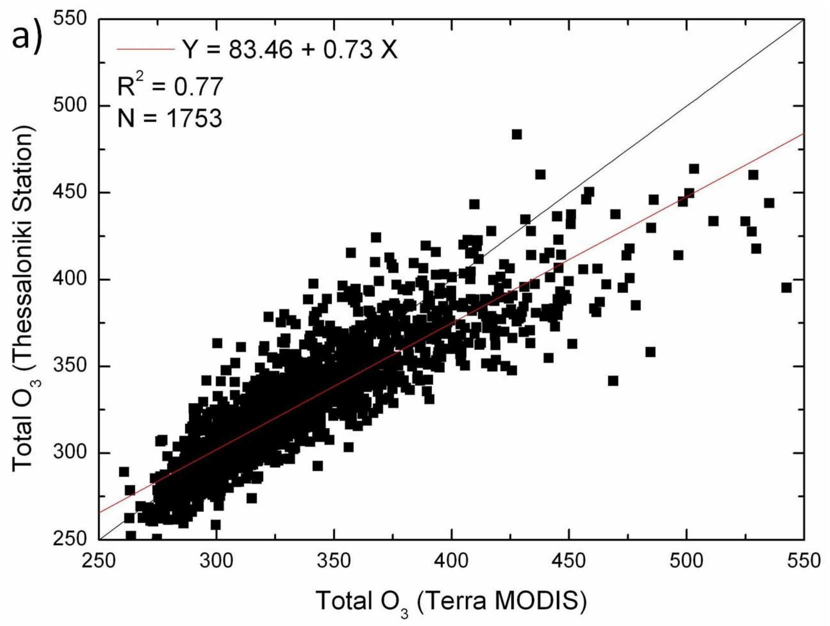

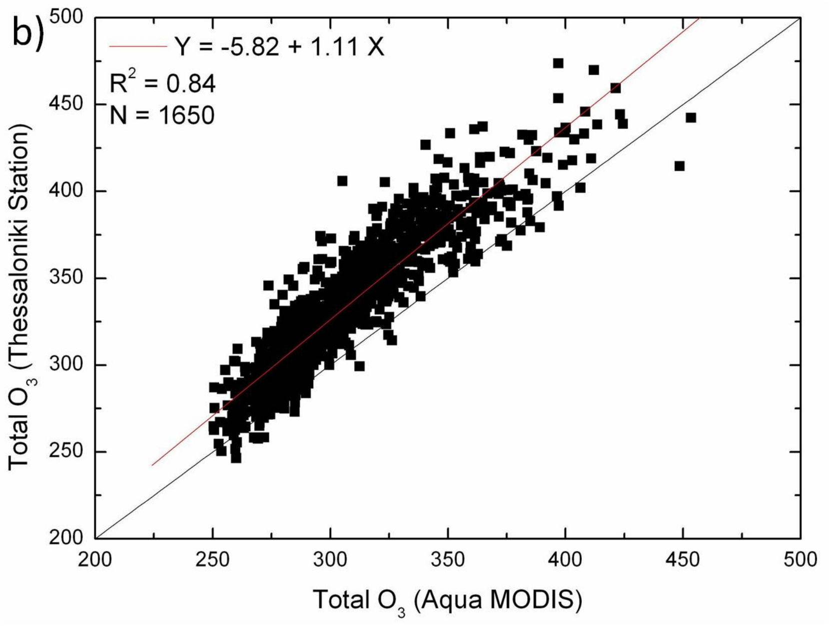

Figure 5.1: Scatter plots of the total column ozone in Dobson Units (DU) from MODIS Terra (a) and Aqua (b), against corresponding ground measurements from Thessaloniki station, for the years 2000-2010. The red lines are the linear regression fits, with the equations, determination coefficients and number of points shown.

5.3.2 Validation of J(O^1D)

In order to achieve a meaningful validation of the model J(O^1D) against Finokalia station measurements, a separate model run was performed, where f_λ was calculated taking into account only the downwelling direct and diffuse radiation. These calculations match the hemispherical (2π) setup of the station instrument. For the validation process, pairs of model and measured J(O^1D) with a time difference up to 5 minutes were used. The validation results, regarding all–sky conditions, are shown in Figure 5.2. In this scatter plot, the dotted line represents the 1:1 line and the solid line is the linear regression fit, while the error bars represent the 15% accuracy of the station measurements. The determination coefficient is high (0.87), while a small tendency of model J(O^1D) overestimation is observed, especially for high J(O^1D) values. Amongst different factors, differences can arise from the resolution of the atmosphere sampled by the satellites and the ground station sensor: while the satellite data cover a $50\,\mathrm{km} \times 50\,\mathrm{km}$ area, point measurements are determined by atmospheric processes occurring in a smaller area. Part of the scatter may also arise from clear/cloudy sky effects on the solar radiation direct component over the 5 minute ground station sensor integration time.

Taking into account the upwelling diffuse radiation, in addition to the downwelling direct and diffuse, in the computation of f_λ, the model derived J(O^1D) becomes higher compared to the station measurements, as expected. According to these results, shown in Figure 5.3, the fraction of the J(O^1D) values that can be attributed to the upwelling diffuse radiation ranges between about 9% and 16%, with a mean value of 12.4%.

To further ensure the validity of the model UV–B radiation at the surface, which is crucial for the reliability of the results, the calculation of J(O^1D) was repeated according to Equation (5.2), using the same model enhancement factor in the UV–B and MODIS solar zenith angle, but replacing σ_λ and Φ_λ with the corresponding values used by the Finokalia filter radiometer software, for the conversion of measured radiation to J(O^1D) measurements (Brock and Watson, 1980; Daumont et al., 1992). The similarity of the validation results using the two J(O^1D) outputs and the good correlation with J(O^1D) measurements in both cases ($R^2 = 0.88$ and slope $= 0.78$ in the second case), imply that the model radiation output in the UV–B range is reliable for the purposes of the present study.

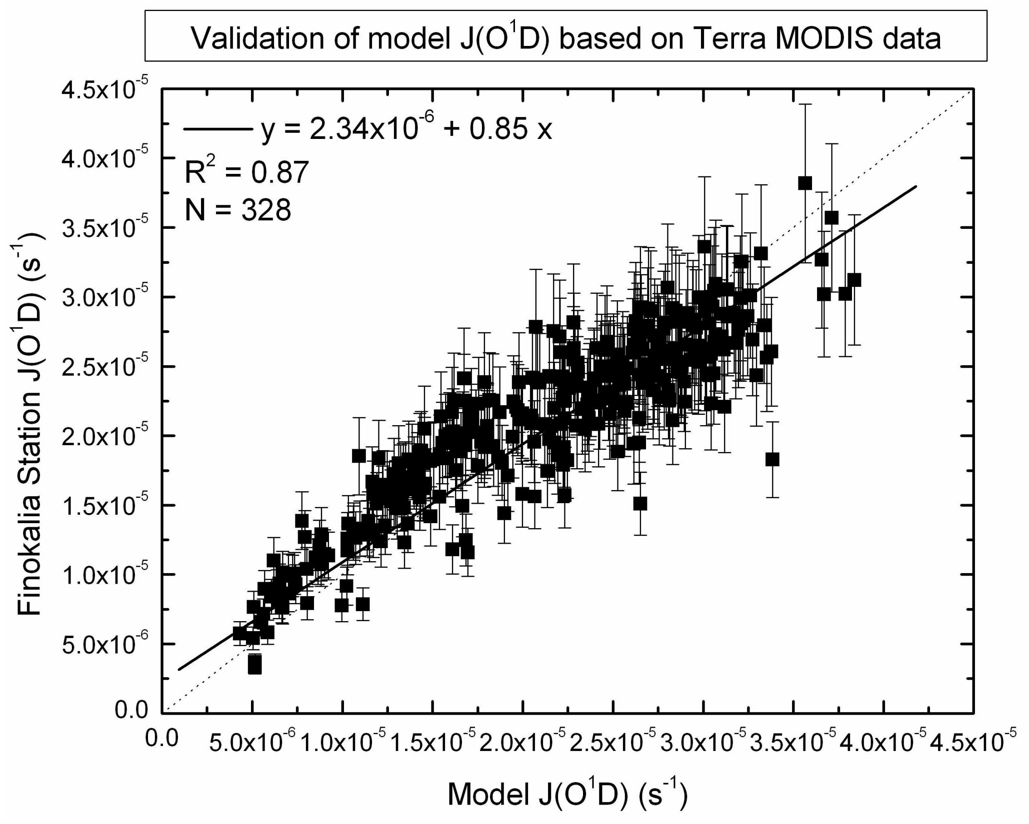

Figure 5.2: Scatter plot of the model instantaneous $J(O^1D)$ using MODIS Terra data, against corresponding ground measurements from the Finokalia station, for the years 2002-2006. The black line is the linear regression fit, with the equation, determination coefficient and number of points shown.

5.3.3 Trends in $J(O^1D)$

Considering monthly mean values of $J(O^1D)$, computed from daily local noon photolysis rates for the period when station measurements are available (2002–2006), no particular change is observed, as was reported by Gerasopoulos et al. (2012). In this study, possible changes using monthly mean values are investigated, computed for the time interval characteristic of Terra MODIS overpass times. Specifically, each daily value is computed as the average of the 5 minute measurements available during the ±30 minute period centered on the satellite overpass time. These daily values are then used for the computation of the corresponding monthly mean values. This approach offers the possibility of a meaningful comparison between station measurements and model results, while the latter are used to study the entire period

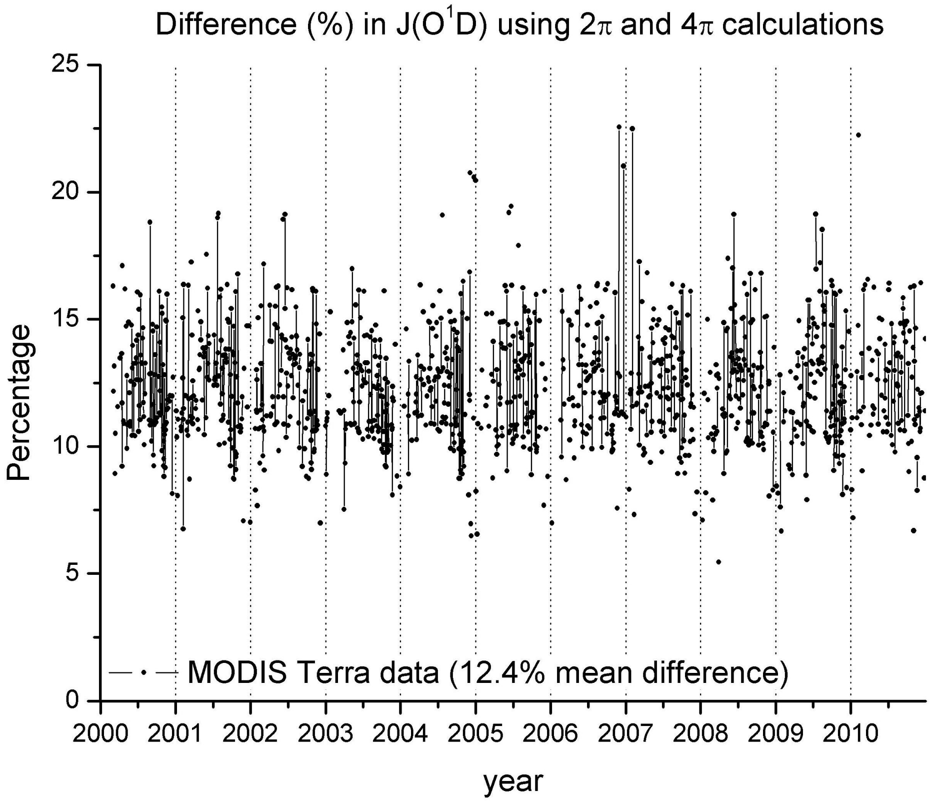

Figure 5.3: Time series of the daily percent difference between model and station J(O^{1}D), when computed using the 4π and 2π model configurations.

when MODIS data are available.

Figure 5.4 shows the time series of the model monthly mean J(O^{1}D), based on the 2π configuration, computed using Terra MODIS and the corresponding monthly mean values from Finokalia measurements for the period 2002–2006, when both model and station data are available. The seasonal variation of J(O^{1}D) is obvious, ranging between 5×10^{-6} s^{-1} in winter and 3×10^{-5} s^{-1} during summer, in agreement with Gerasopoulos et al. (2012). In order to perform a robust analysis, the deseasonalised time series were taken, normalized by the standard deviation, as explained in Matsoukas et al. (2011). Fitting linear trends to the normalized time series, both the station measurements and the model output showed no statistically significant change at the 95% confidence level for this specific 5–year period. However, when examining the entire 11–year period of the model J(O^{1}D) output (2000–2010), a statistically significant J(O^{1}D) decreasing trend appears. Figure 5.5 shows the time series of the model J(O^{1}D) monthly mean values, along with

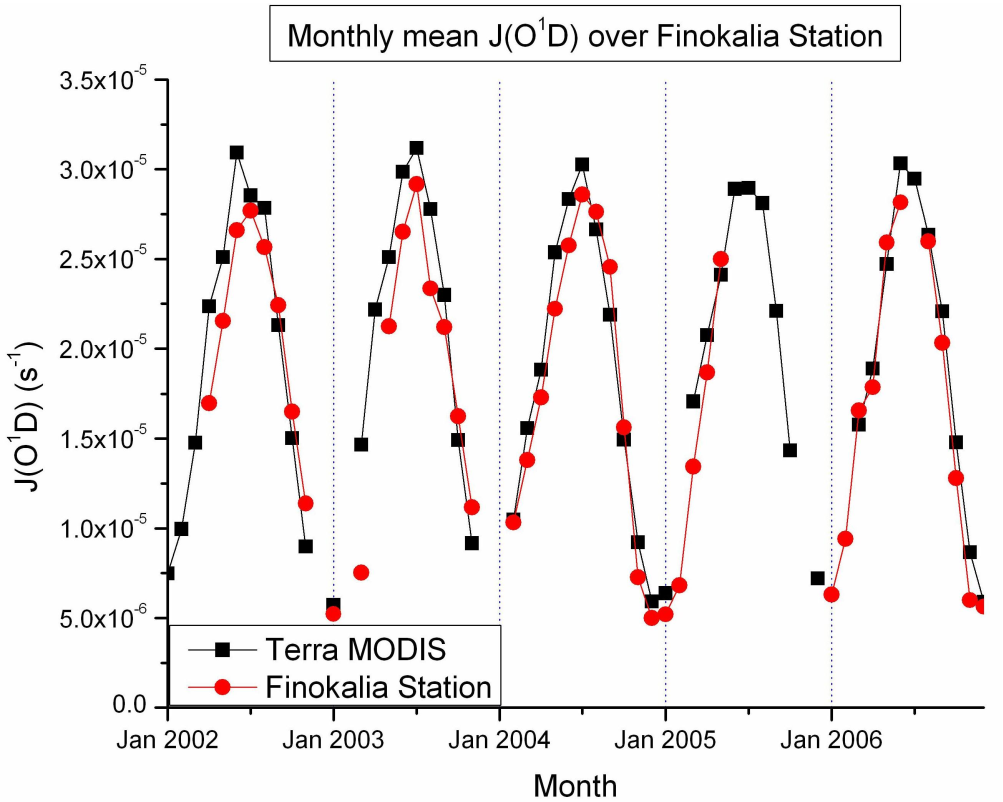

Figure 5.4: Times series of the model monthly mean J(O^{1}D), based on the 2π configuration, computed using Terra MODIS data, and the corresponding monthly mean values from Finokalia measurements for the period 2002–2006. The vertical lines are used to distinguish successive years.

the corresponding deseasonalised values and the linear regression fit. The trend appearing here corresponds to ~13% reduction in J(O^{1}D) during this period, and will be discussed further in the next sections.

5.3.4 Aerosol effects on J(O^{1}D)

Aerosol instantaneous effects

The aerosol effect on J(O^{1}D), ΔJ(O^{1}D), is caused by the corresponding changes in the radiative fluxes, included in the computation of f_λ (Equation 5.3), which occur when aerosols are not included in the model. These fluxes are predicted by the Delta-Eddington method to an accuracy of better than 2.5% (Joseph et al., 1976). This uncertainty causes a corresponding

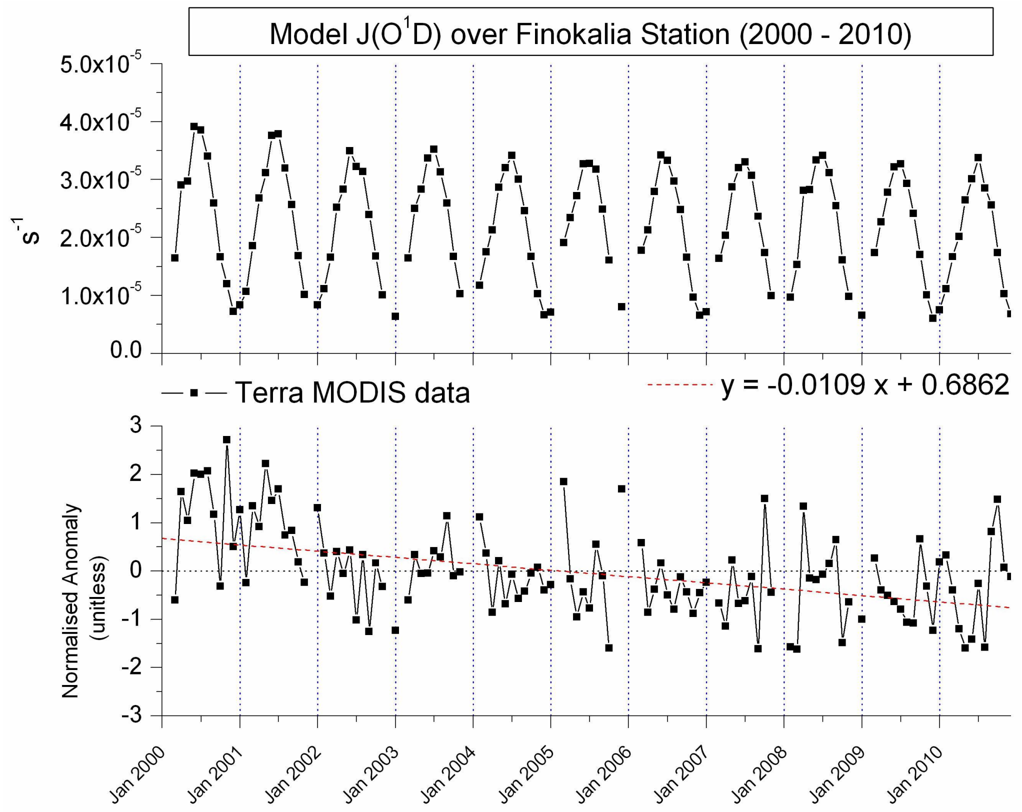

Figure 5.5: Time series of the model J(O^1D) monthly mean values along with the corresponding deseasonalised values and the linear regression fit. The vertical lines are used to distinguish successive years.

uncertainty of about 2% in the calculation of J(O^1D).

In order to investigate the way aerosols affect f_λ and consequently J(O^1D), the aerosol effect was examined separately on each component of f_λ, namely the direct downwelling radiation component, and the diffuse down and upwelling components for a typical day, when ΔJ(O^1D) was of the order of -5%. The results are shown in Figure 5.6.

Although the curves in Figure 5.6 are expected to vary on a day–by–day basis, depending on the values of solar zenith angle and total ozone, the analysis of various cases during different days showed that Figure 5.6 represents the typical aerosol effects on the radiation flux components and J(O^1D). The solid lines represent each output when aerosols are present, while the same color dashed lines correspond to the same output when the model was run without aerosols. The absence of aerosols causes an increase in the direct

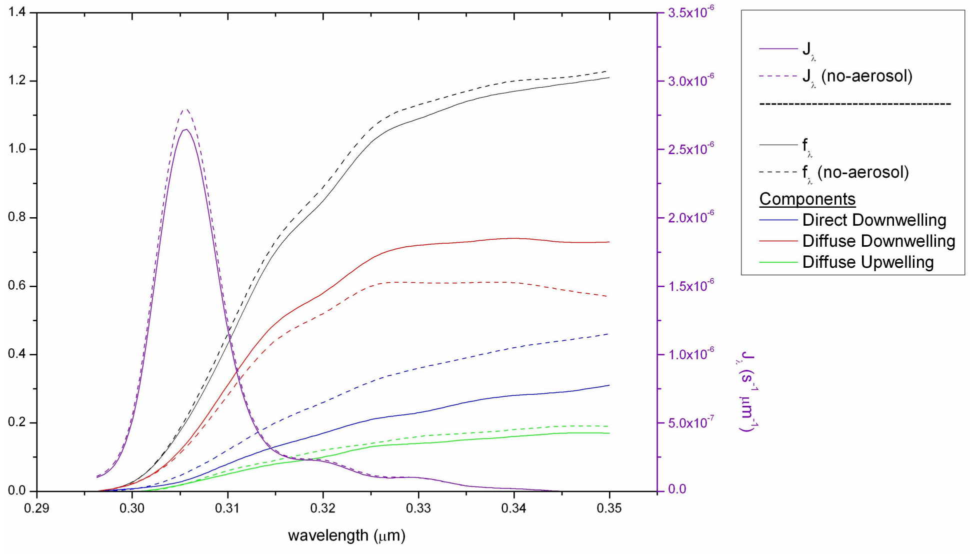

Figure 5.6: Aerosol effect on enhancement factor components for a typical day (ΔJ(O^{1}D) $\approx -5\%$), for the spectral region where J(O^{1}D) is computed, along with the spectral distribution of J_λ.

downwelling radiation reaching the surface, and a decrease in the diffuse downwelling. The upwelling diffuse radiation is slightly increased. The overall effect of these changes is an increase in f_λ in the absence of aerosols. Figure 5.6 also shows the spectral distribution of J(O^{1}D), J_λ. The peak of J_λ near 0.305 μm is the result of the rapidly increasing O$_3$ absorption cross section with decreasing wavelength in the Hartley–Huggins bands, combined with the decrease in f_λ to almost zero below 0.3 μm. The increased f_λ increases the corresponding values of J(O^{1}D), resulting in negative ΔJ(O^{1}D) values.

The time series of the instantaneous ΔJ(O^{1}D), computed as described in Section 5.2, is shown in Figure 5.7. The decrease in J(O^{1}D) is highly variable on a day to day basis, depending on the aerosol load. The median reduction in J(O^{1}D) due to aerosols, calculated from the entire period examined, is of the order of 2.3%. The computation of ΔJ(O^{1}D) on a per–day basis offers the possibility of studying the effects of Saharan dust events, which last 1–2 days and are common in the area, especially during spring and autumn. In order to define dust events, threshold criteria on the AOT and Angstrom exponent daily values provided by MODIS were used, while back–trajectory analysis was used to verify the dust episodes detected. This procedure is described in detail in Section 4.2.4. Detected ΔJ(O^{1}D) due to dust events

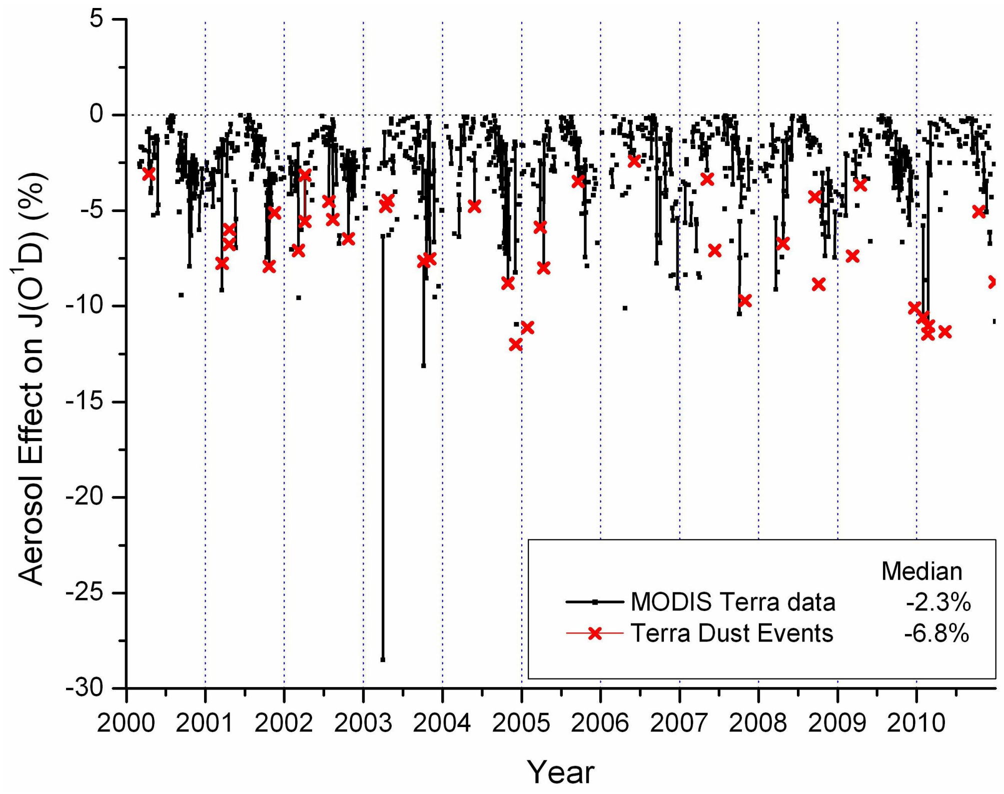

Figure 5.7: Time series of the daily aerosol effect on the model J(O^{1}D). The cases of the effect when dust events were detected and the corresponding median values are also shown. The vertical lines are used to distinguish successive years.

are shown in Figure 5.7 with different symbols. Due to the large effect on the DSR during these events, ΔJ(O^{1}D) exceeds -10% in many cases, with a median value of -6.8%. Gerasopoulos et al. (2012), have also reported aerosol effects on J(O^{1}D) reaching up to -40% in cases of high AOT. Large aerosol effects shown in Figure 5.7 but not identified as dust events were also examined using back–trajectory analysis. Several of these cases were attributed to forest fire smoke, transferred from the wider Balkan area (e.g. the 28% decrease in J(O^{1}D) detected in March 30th, 2003).

To further investigate the effect of the aerosol load on J(O^{1}D), a sensitivity analysis was performed: the model was run with the AOT varied by ±10%, and the resulting J(O^{1}D) output was compared against the corresponding results of the original model run. The analysis showed that the ±10% variation in AOT caused a corresponding $\mp 0.5 \pm 0.5\%$ change in

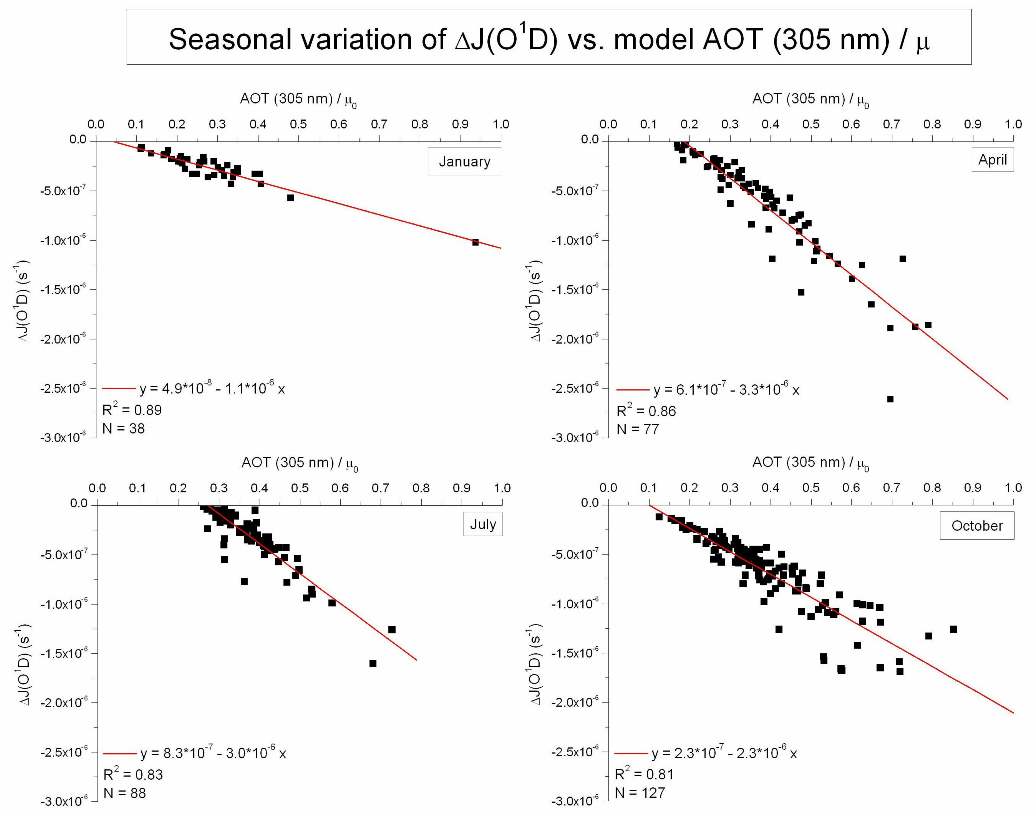

Figure 5.8: Scatter plots of the daily aerosol effect on J(O^{1}D) against model AOT at 305 nm divided by μ_0 for four characteristic months (January, April, July and October). The red lines are the linear regression fits, with the equations, determination coefficients and numbers of points shown.

J(O^{1}D). Furthermore, the relationship between the model input AOT at 305 nm, where J_λ peaks, and the corresponding change on J(O^{1}D), was directly examined.

Figure 5.8 shows the scatter plots of the AOT at 305 nm divided by the corresponding μ_0 in order to remove the seasonal effects, against ΔJ(O^{1}D) for January, April, July and October, which are characteristic of the seasonal variations. It is obvious from Figure 5.8 that larger optical path lengths (AOT/μ_0) induce larger aerosol effects. Figure 5.8 also shows that ΔJ(O^{1}D) also depends on the solar zenith angle: as the solar zenith angle moves towards the vertical ($\mu_0 = 0.93$ in July), the aerosol layer transmissivity goes to 1 for low optical paths, as can be seen from fig. 1 of Joseph et al. (1976), rendering ΔJ(O^{1}D) insignificant for AOT/μ_0 of about 0.3. However, as μ_0

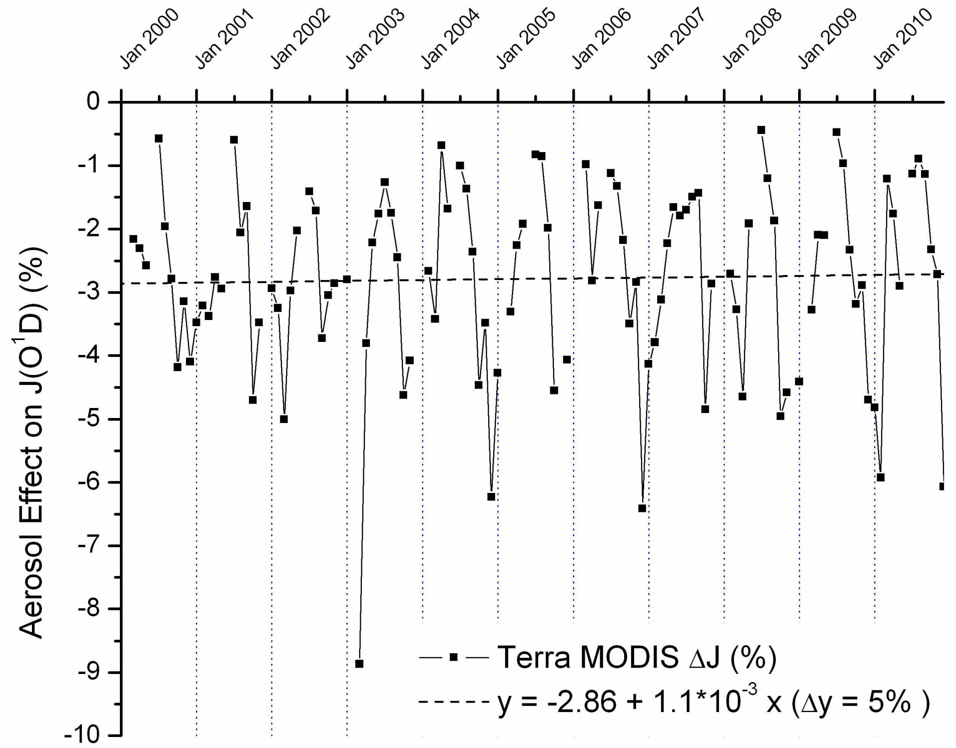

Figure 5.9: Time series of the monthly mean percent ΔJ(O^{1}D) from model output. The linear regression fit is also shown, while the vertical lines represent successive years.

decreases ($\mu_0 = 0.86, 0.69, 0.51$ in April, October and January respectively), transmissivity of the aerosol layer also decreases, and ΔJ(O^{1}D) becomes insignificant at progressively lower values of AOT/μ_0.

Aerosol monthly mean effects and trends

Model monthly mean values of ΔJ(O^{1}D) were computed from the daily values, for months with at least 5 daily values available, in order to ensure the validity of the results. Figure 5.9 shows the time series of the model monthly mean percent ΔJ(O^{1}D). High absolute ΔJ(O^{1}D) percent values in winter months are caused by the reduced radiation reaching the surface during this season. Although an overall decreasing trend is observed, no statistical significance in the 95% confidence level was found. This result suggests that the statistically significant decreasing trend in J(O^{1}D) found in the case of Terra cannot be attributed to aerosol effects. The seasonal percent variation

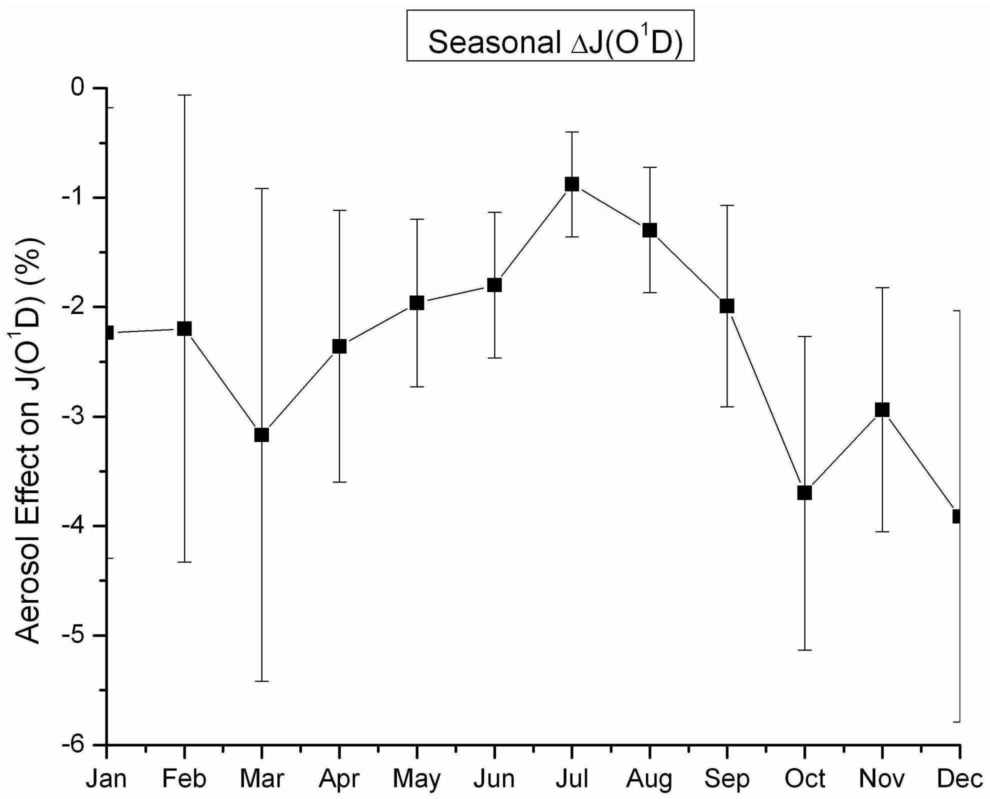

Figure 5.10: Seasonal variation of the aerosol effect on $J(O^1D)$ for Terra MODIS, computed from the period examined (2000-2010). The error bars represent the standard deviations of the mean monthly values computed from the Terra overpass time values.

of the aerosol effect on $J(O^1D)$ is shown in Figure 5.10. The higher aerosol percent effect in December should be attributed to the reduced radiation reaching the surface, as explained in the case of Figure 5.9. However, the large effects, appearing in spring, late summer and autumn, are caused by the large seasonal variation of the aerosol load in the region, due to increased dust events, as was shown in previous studies (e.g. Fotiadi et al., 2006).

5.3.5 Total column ozone effects on $J(O^1D)$

In order to further investigate the decreasing trend of $J(O^1D)$ (Section 5.3.3), the same analysis was conducted for the total column ozone, available from MODIS Level 2 Atmosphere Products over both Finokalia and Thessaloniki stations, and from Thessaloniki station ground measurements.

Total ozone monthly mean values over Finokalia station were computed and analyzed in the same way the J(O^1D) monthly mean values and trends were studied. Figure 5.11 shows the time series of the total ozone monthly mean values from Terra MODIS and the corresponding linear regression fit applied. The analysis of the deseasonalised time series showed that there is a statistically significant increasing trend: total ozone has increased by about 4.1% during the 11–year period examined. Figure 5.12 shows the time series of the monthly mean total ozone over Thessaloniki station for the period examined, from both Terra MODIS Level 2, and the corresponding station data. The trend analysis performed on the deseasonalised total ozone values is also shown. Both satellite and station data show a statistically significant increasing trend in total ozone, which corresponds to 5.7% and 1.2% increase for MODIS data and station measurements, respectively. A similar result was found by Meleti et al. (2009), examining the 1990–2006 period and total ozone calculated from measurements conducted from sunrise to sunset. The difference between MODIS and station data increasing rates in Figure 5.12 should be attributed to the higher MODIS total ozone values in 2009 and 2010, as it is implied from Figure 5.12 and was confirmed from a validation on a per–year basis.

In order to evaluate the total column ozone effect on J(O^1D) over Finokalia station, a sensitivity test was performed. The analysis showed that a 10% increase in total column ozone has a mean effect of about $-17 \pm 1\%$ in J(O^1D), while a corresponding reduction (-10%) causes an increase of $15 \pm 1\%$ in J(O^1D) on a mean basis. This sensitivity of J(O^1D) on total column ozone shows that the statistically significant decreasing trend in J(O^1D) over Finokalia can be attributed mainly to the corresponding increasing trend of total ozone during the same period.

5.4 Summary and conclusions

The FORTH model, described in Chapter 3, was used in order to compute the surface J(O^1D) in Finokalia meteorological station and evaluate the effects of aerosols and total column ozone. Model input data of $50\,\text{km} \times 50\,\text{km}$ spatial resolution, came from the MODIS Level 2 Atmosphere Products (Section 2.2). The study covered the 11-year period from 2000 to 2010. Satellite total column ozone data were validated against Thessaloniki station ground measurements, and the model computed J(O^1D) was validated against corresponding Finokalia station in situ instantaneous measurements from the period 2002-2006, showing very good correlation, with a small tendency of model J(O^1D) overestimation for high J(O^1D) values.

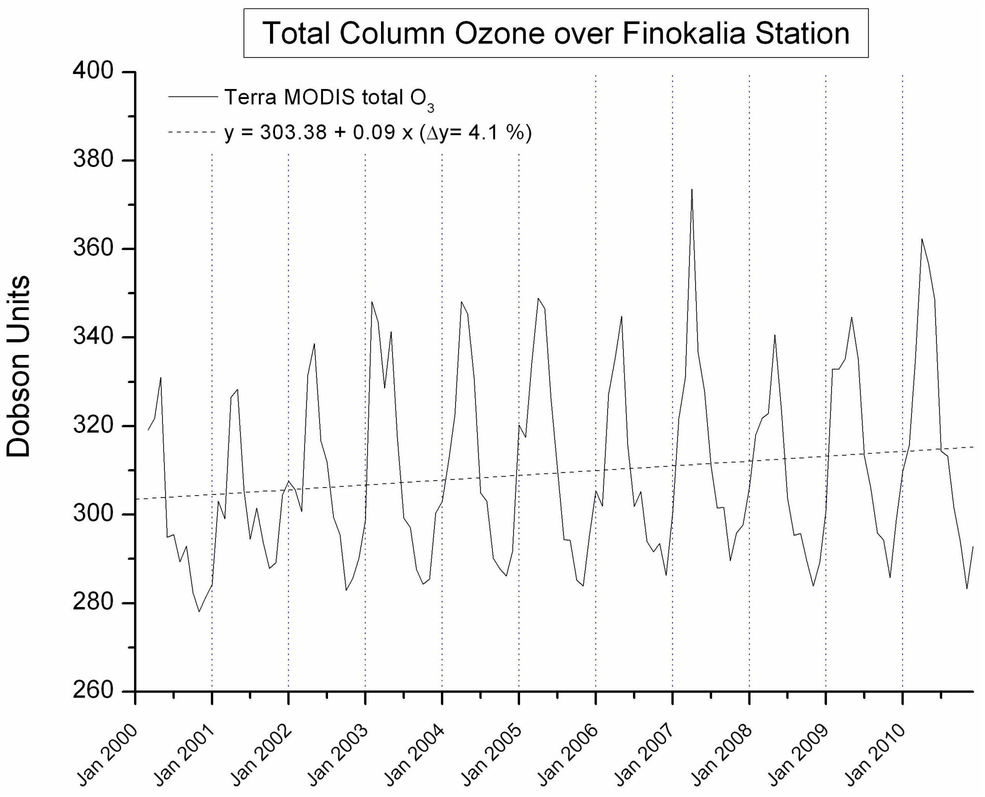

Figure 5.11: Time series of the total column ozone monthly mean values from Terra MODIS Level 2 data over Finokalia station, along with the corresponding linear regression fit. The vertical lines are used to distinguish successive years.

Linear regression applied to the deseasonalised monthly mean J(O^1D) values, computed from the instantaneous ones, showed a statistically significant decreasing trend in J(O^1D) during the hours before local noon (Terra overpass times). This trend has caused a 13% decrease in J(O^1D) during the period examined.

The aerosol effect on J(O^1D) was studied on a daily, monthly and seasonal basis. Aerosols cause a mean reduction in J(O^1D) of ~3% on an instantaneous basis, which can exceed 10% during Saharan dust events. Linear regression on monthly mean aerosol effect on J(O^1D) showed no statistically significant trend. High aerosol effects appear in spring and autumn, when the AOT assumes higher values, caused by frequent dust events during these seasons, while high winter percent effects are attributed to the reduced surface radiation during this season.

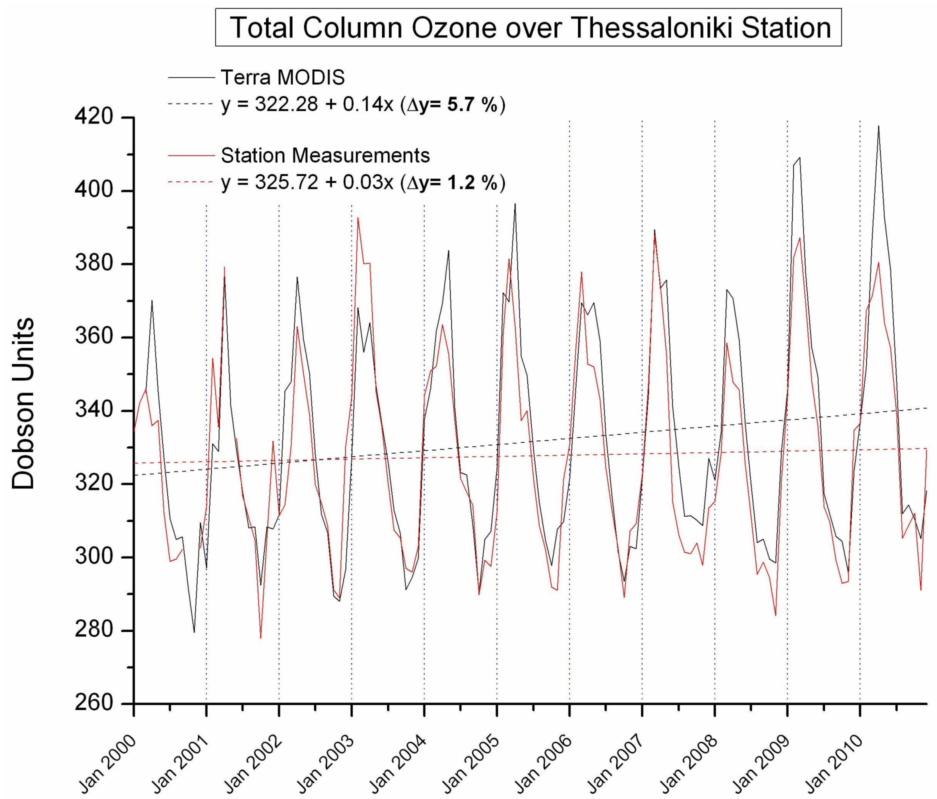

Figure 5.12: Timeseries of the monthly mean total ozone over Thessaloniki station for the period 2000–2010, from Terra MODIS and the corresponding station data. The trend analysis performed on the deseasonalised total ozone values is also shown. The vertical lines are used to distinguish successive years.

The total ozone trend analysis performed using Terra MODIS data is in agreement with the corresponding Thessaloniki station data: a statistically significant increasing trend appears during the hours before local noon, in both Thessaloniki and Finokalia stations. This trend has caused an increase of about 5% in total ozone during the period examined. The sensitivity analysis performed, showed that on a mean basis, a ±10% variation in total ozone causes a $\mp 15--17\%$ change in $J(O^1D)$, suggesting that the reduction in $J(O^1D)$ detected during the morning hours can be attributed mainly to the corresponding total column ozone increase detected using the same dataset.

Provided that the model input data and output are validated against ground measurements, and depending on the availability of AOT at 340 nm from an AERONET station, the same procedure could be used in the future at different sites of specific interest, for the calculation of $J(O^1D)$ and the estimation of aerosol and total column ozone effects.

Bibliography

Bais, A. F., Madronich, S., Crawford, J., Hall, S. R., Mayer, B., van Weele, M., Lenoble, J., Calvert, J. G., Cantrell, C. A., Shetter, R. E., Hofzumahaus, A., Koepke, P., Monks, P. S., Frost, G., McKenzie, R., Krotkov, N., Kylling, A., Swartz, W. H., Lloyd, S., Pfister, G., Martin, T. J., Roeth, E.-P., Griffioen, E., Ruggaber, A., Krol, M., Kraus, A., Edwards, G. D., Mueller, M., Lefer, B. L., Johnston, P., Schwander, H., Flittner, D., Gardiner, B. G., Barrick, J., and Schmitt, R.: International Photolysis Frequency Measurement and Model Intercomparison (IPMMI): Spectral actinic solar flux measurements and modeling, Journal of Geophysical Research: Atmospheres, 108, doi:10.1029/2002JD002891, 2003.

Balis, D. S., Zerefos, C., Kourtidis, K., Bais, A. F., Hofzumahaus, A., Kraus, A., Schmitt, R., Blumthaler, M., and Gobbi, G. P.: Measurements and modeling of photolysis rates during the Photochemical Activity and Ultraviolet Radiation (PAUR) II campaign, Journal of Geophysical Research, 107, doi:10.1029/2000JD000136, 2002.

Blackburn, T. E., Bairai, S. T., and Stedman, D. H.: Solar photolysis of ozone to singlet D oxygen atoms, Journal of Geophysical Research: Atmospheres, 97, 10 109–10 117, doi:10.1029/92JD00504, 1992.

Borbas, E., Seemann, S. W., Kern, A., Moy, L., Li, J., Gumley, L., and Menzel, W. P.: MODIS Atmospheric Profile Retrieval Algorithm Theoretical Basis Document, Collection 6, Version 7, 2011.

Brock, J. C. and Watson, R. T.: Laser flash photolysis of ozone: O(^{1}D) quantum yields in the fall–off region 297–325 nm, Chemical Physics, 46, 477–484, 1980.

Casasanta, G., di Sarra, A., Meloni, D., Monteleone, F., Pace, G., Piacentino, S., and Sferlazzo, D. M.: Large aerosol effects on ozone photolysis in the Mediterranean, Atmospheric Environment, 45, 3937–3943, doi:10.1016/j.atmosenv.2011.04.065, 2011.

Daumont, D., Brion, J., and Charbonnier, J.: Ozone UV spectroscopy I: Absorption cross-sections at room temperature, Journal of Atmospheric Chemistry, pp. 145–155, 1992.

Demirhan, D., Kahya, C., Topcu, S., and Incecik, S.: Total ozone variation in south eastern Europe, International Journal of Remote Sensing, 26, 3479–3486, doi:10.1080/01431160500076558, 2005.

Denman, K. L., Brasseur, G., Chidthaisong, A., Ciais, P., Cox, P. M., Dickinson, R. E., Hauglustaine, D., Heinze, C., Holland, E., Jacob, D., Lohmann, U., Ramachandran, S., da Silva Dias, P. L., Wofsy, S. C., and Zhang, X.: Couplings Between Changes in the Climate System and Biogeochemistry, in: Climate Change 2007: The Physical Science Basis. Contribution of Working Group I to the Fourth Assessment Report of the Intergovernmental Panel on Climate Change, edited by Solomon, S., Qin, D., Manning, M., Chen, Z., Marquis, M., Averyt, K. B., Tignor, M., and Miller, H. L., Cambridge University Press, Cambridge, United Kingdom and New York, NY, USA, 2007.

Fotiadi, A., Hatzianastassiou, N., Drakakis, E., Matsoukas, C., Pavlakis, K. G., Hatzidimitriou, D., Gerasopoulos, E., Mihalopoulos, N., and Vardavas, I.: Aerosol physical and optical properties in the Eastern Mediterranean Basin, Crete, from Aerosol Robotic Network data, Atmospheric Chemistry and Physics, pp. 5399–5413, 2006.

Gerasopoulos, E., Kouvarakis, G., Vrekoussis, M., Donoussis, C., Mihalopoulos, N., and Kanakidou, M.: Photochemical ozone production in the Eastern Mediterranean, Atmospheric Environment, 40, 3057–3069, doi:10.1016/j.atmosenv.2005.12.061, 2006.

Gerasopoulos, E., Kazadzis, S., Vrekoussis, M., Kouvarakis, G., Liakakou, E., Kouremeti, N., Giannadaki, D., Kanakidou, M., Bohn, B., and Mihalopoulos, N.: Factors affecting O_3 and NO_2 photolysis frequencies measured in the eastern Mediterranean during the five-year period 2002-2006, Journal of Geophysical Research: Atmospheres, 117, doi:10.1029/2012JD017622, 2012.

Gueymard, C. A.: The sun's total and spectral irradiance for solar energy applications and solar radiation models, Solar Energy, 76, 423–453, doi:10.1016/j.solener.2003.08.039, 2004.

Hofzumahaus, A., Brauers, B., Platt, U., and Callies, J.: Latitudinal variation of measured O3 photolysis frequencies J(O^1D) and primary OH production rates over the Atlantic Ocean between 50° N and 30° S, Journal of Atmospheric Chemistry, 15, 283–298, 1992.

Hudson, R. D., Frolov, A. D., Andrade, M. F., and Follette, M. B.: The Total Ozone Field Separated into Meteorological Regimes . Part I : Defining the Regimes, Journal of Atmospheric Sciences, 60, 1669–1677, 2003.

IPCC: Climate Change 2007 - The Physical Science Basis: Working Group I Contribution to the Fourth Assessment Report of the IPCC, Cambridge University Press, 2007.

Joseph, J. H., Wiscombe, W. J., and Weinman, J. A.: The Delta-Eddington Approximation for Radiative Flux Transfer, Journal of Atmospheric Sciences, 33, 2452–2459, 1976.

Kazadzis, S., Topaloglou, C., Bais, A. F., Blumthaler, M., Balis, D. S., Kazantzidis, A., and Schallhart, B.: Actinic flux and O^1D photolysis frequencies retrieved from spectral measurements of irradiance at Thessaloniki , Greece, Atmospheric Chemistry and Physics, 4, 2215–2226, doi:10.5194/acp-4-2215-2004, 2004.

Kerr, J. B.: Understanding the factors that affect surface ultraviolet radiation, Optical Engineering, 44, 041 002, doi:10.1117/1.1886817, 2005.

Li, G., Bei, N., Tie, X., and Molina, L. T.: Aerosol effects on the photochemistry in Mexico City during MCMA–2006/MILAGRO campaign, Atmospheric Chemistry and Physics, 11, 5169–5182, doi:10.5194/acp-11-5169-2011, 2011.

Matsoukas, C., Benas, N., Hatzianastassiou, N., Pavlakis, K. G., Kanakidou, M., and Vardavas, I.: Potential evaporation trends over land between 19832008: driven by radiative fluxes or vapour-pressure deficit?, Atmospheric Chemistry and Physics, 11, 7601–7616, doi:10.5194/acp-11-7601-2011, 2011.

Matsumi, Y., Comes, F. J., Hancock, G., Hofzumahaus, A., Hynes, A. J., Kawasaki, M., and Ravishankara, A. R.: Quantum yields for production of $O(^1D)$ in the ultraviolet photolysis of ozone: Recommendation based on evaluation of laboratory data, Journal of Geophysical Research: Atmospheres, 107, doi:10.1029/2001JD000510, 2002.

Meleti, C., Bais, A. F., Kazadzis, S., Kouremeti, N., Garane, K., and Zerefos, C.: Factors affecting solar ultraviolet irradiance measured since 1990 at

Thessaloniki, Greece, International Journal of Remote Sensing, 30, 4167–4179, doi:10.1080/01431160902822864, 2009.

Rohrer, F. and Berresheim, H.: Strong correlation between levels of tropospheric hydroxyl radicals and solar ultraviolet radiation, Nature, 442, 184–187, doi:10.1038/nature04924, 2006.

Sander, S. P., Friedl, R. R., Ravishankara, A. R., Golden, D. M., Kolb, C. E., Kurylo, M. J., Molina, M. J., Moortgat, G. K., Keller-Rudek, H., J.Finlayson-Pitts, B., Wine, P. H., Huie, R. E., and Orkin, V. L.: Chemical Kinetics and Photochemical Data for Use in Atmospheric Studies, Evaluation Number 15, NASA/JPL Publication, 2006.

Shetter, R. E., Cantrell, C. A., Lantz, K. O., Flocke, S. J., Orlando, J. J., Tyndall, G. S., Gilpin, T. M., Fischer, C. A., Madronich, S., Calvert, J. G., and Junkermann, W.: Actinometric and radiometric measurement and modeling of the photolysis rate coefficient of ozone to $O(^1D)$ during Mauna Loa Observatory Photochemistry Experiment 2, Journal of Geophysical Research: Atmospheres, 101, 14 631–14 642, doi:10.1029/96JD00211, 1996.

Tie, X., Madronich, S., Walters, S., Edwards, D. P., Ginoux, P., Mahowald, N., Zhang, R., Lou, C., and Brasseur, G.: Assessment of the global impact of aerosols on tropospheric oxidants, Journal of Geophysical Research: Atmospheres, 110, doi:10.1029/2004JD005359, 2005.

Vardavas, I. and Taylor, F.: Radiation and Climate: Atmospheric Energy Budget from Satellite Remote Sensing, International Series of Monographs on Physics, OUP Oxford, 2011.

Yang, H. and Levy II, H.: Sensitivity of photodissociation rate coefficients and O_3 photochemical tendencies to aerosols and clouds, Journal of Geophysical Research, 109, 1–12, doi:10.1029/2004JD005032, 2004.

Chapter 6

Aerosol Effect on Potential Evaporation

6.1 Introduction

The hydrological cycle describes the processes that control the transportation of water from oceans and continents to the atmosphere, and its return, mainly via precipitation and rivers, to the oceans. Climate warming is expected to significantly alter the hydrological cycle in different ways, which depend on local and regional climate changes (e.g. Bengtsson, 2010). The Mediterranean basin is one of the areas where numerous studies, including past observations and future projections, suggest that these changes are expected to manifest themselves strongly, especially as decreased precipitation rates, increased droughts and water deficits, and consequent desertification (e.g. Trenberth et al., 2007; Meehl et al., 2007).

Evaporation from oceans and lakes is a crucial parameter of the hydrological cycle, since it constitutes the main mechanism for the return of water to the atmosphere. Moreover, evaporation from a lake is a primary factor controlling the local water budget, and its changes become highly important, especially when connected to human activities, such as water supply and irrigation. Hence, the evaluation of evaporation from a lake, its possible changes and the corresponding assessment of the factors affecting it, are significant in a wider context. Over small, shallow lakes, where heat storage considerations can be ignored from the factors affecting the evaporation rates, the Penman Potential Evaporation (PE) can be assumed to be the actual lake evaporation (Penman, 1948).

In the present chapter, the PE and the corresponding aerosol effect are evaluated over four lakes in Central Greece, which constitute the main water

Figure 6.1: The broader area of Central Greece and the locations of the four lakes studied. The area of Athens is also shown.

supply reservoirs for the city of Athens (Evinos, Mornos, Marathonas and Yliki, Figure 6.1). PE is determined by two factors: the available energy for evaporation, and the lake to atmosphere water vapour transfer. The available energy relies on the net SW and LW fluxes at the surface of each lake. Hence, the FORTH RTM (Chapter 3) is used for the SW budget computations, supplemented by corresponding LW model output data. This approach allows the computation of the aerosol effect on PE, through the corresponding DRE. The study examines the PE and the aerosol effect on a daily, monthly and seasonal basis, the corresponding trends and the factors affecting them, using MODIS input data from the decade 2001–2010.

In the next section, the methodology for the calculation of the PE and the aerosol effect, the surface and LW data which supplement the model output and the assumptions made, are described in detail. The results, including the model DSR validation against surface measurements, the seasonal variation of PE, the aerosol daily effects, focusing on dust events, and the decadal trends of PE, aerosols and operating factors, are presented in Section 6.3, before the summary and conclusions.

6.2 Methodology and input data

6.2.1 Calculation of potential evaporation

The methodology for the calculation of PE, described in this section, has also been described in detail in Vardavas (1987b).

The net solar flux on a water surface is the dominant source of energy which determines the evaporation rate on any given day. The water surface net infrared emission reduces this heat input while wind flux above the surface removes water vapor and so enhances the evaporation rate. In Penman's equation, the potential evaporation rate (mm day^{-1}) for a free water surface, with no heat advection or storage, is expressed as (Penman, 1948):

$$PE = \left(\frac{\Delta}{\Delta + \gamma}\right) E_s + \left(\frac{\gamma}{\Delta + \gamma}\right) E_a \tag{6.1}$$

where E_s is the evaporation due to solar heating and E_a the contribution due to the wind. In equation (6.1), γ is the psychrometric constant (mbar K^{-1}) given by Brutsaert (2010):

$$\gamma = \frac{c_p p M_d}{L M_v} \tag{6.2}$$

where c_p is the specific heat of air and equal to 0.24 cal g^{-1} K^{-1}, p the surface atmospheric pressure (mbar), M_d and M_v are the mean molecular weights of dry air and water vapour, respectively, so that $M_v/M_d = 0.622$, and L the latent heat of evaporation (cal g^{-1}) given by:

$$L = 597.3 - 0.553(T - T_0) \tag{6.3}$$

where $T_0 = 273.15$ K. The parameter Δ represents the slope of the saturation vapour pressure e_s with respect to T and can be computed from:

$$\Delta = \frac{\mathrm{d}e_s}{\mathrm{d}T}, \tag{6.4}$$

with the saturation vapour pressure at T given by:

$$\ln e_s = a_1 - \frac{a_2}{T} + a_3 \ln T, \tag{6.5}$$

and thus

$$\Delta = \left(\frac{a_2}{T^2} + \frac{a_3}{T}\right) e_s(T), \tag{6.6}$$

where $a_1 = 58.1717$, $a_2 = 6938.67$ and $a_3 = -5.5189$, respectively, for $T > T_0$, and $a_1 = 28.5938$, $a_2 = 6309.64$ and $a_3 = -0.65706$, respectively, for $T \leq T0$ (Vardavas and Carver, 1984). In Penman's analysis, Δ is evaluated at T_a, the atmospheric temperature above the water surface.

Calculation of E_s

In equation (6.1), E_s (mm day^{-1}) is given by:

$$E_s = \frac{239 Q_n}{L \rho} \tag{6.7}$$

where ρ is the density of water (1 g cm^{-3}), L is defined by equation (6.3) and expressed in cal g^{-1}, and Q_n is the net all–wave flux (MJ m^{-2} day^{-1}) above the water surface, given by:

$$Q_n = \overline{F}^{\downarrow}_{sol} - \overline{F}^{\uparrow}_{ir}. \tag{6.8}$$

In the above equation, $\overline{F}^{\downarrow}_{sol}$ and $\overline{F}^{\uparrow}_{ir}$ represent the net downward flux and the net upward terrestrial flux, at the water surface, respectively.

Calculation of E_a

According to Penman (1948), E_a is given by:

$$E_a = f(\overline{u})[e_s(T_a) - e(T_a)], \tag{6.9}$$

where $f(\overline{u})$ is the wind function and $\overline{u}$ is the mean wind speed, $e_s(T_a)$ is the saturation vapour pressure at the water surface, evaluated at the air temperature T_a, and $e(T_a)$ is the vapour pressure at some height above the water surface. The wind function is either empirically determined or evaluated theoretically from similarity profile functions (Brutsaert, 2010), and for neutral conditions is given by:

$$f(\overline{u}) = \left(\frac{M_v}{M_d}\right) \frac{a_\nu k^2 \overline{u}}{D}, \tag{6.10}$$

with

$$D = R_d T_a \ln\left(\frac{z_2 - d_0}{z_{0\nu}}\right) \ln\left(\frac{z_1 - d_0}{z_{0m}}\right), \tag{6.11}$$

where k is the Von Karman constant, taken equal to 0.42, a_ν is the ratio of the eddy diffusivity for water vapour and the eddy viscosity, taken to be 1.13 (Pruitt et al., 1973). In equation (6.10), $M_v/M_d = 0.622$, R_d is the gas constant for dry air, z_1 is the level of the wind speed measurement and z_2 that for the water vapour pressure. For a smooth surface, such as a water surface, $d_0 = 0$ and the momentum roughness can be evaluated from:

$$z_{0m} = \frac{0.135 \nu}{u_*}, \tag{6.12}$$

with the roughness length for water vapour given by:

$$z_{0\nu} = \frac{0.624\nu}{u_*}. \tag{6.13}$$

The friction velocity u_* can be evaluated using the logarithmic wind profile law for mean wind speed:

$$\overline{u} = \frac{u_*}{k} \ln\left(\frac{z_2 - d_0}{z_{0m}}\right), \tag{6.14}$$

which from equation (6.12) reduces to:

$$\overline{u} = \frac{u_*}{k} \ln\left(\frac{z_2 u_*}{0.135\nu}\right). \tag{6.15}$$

Equation (6.15) can be solved for u_* using Newton–Raphson iteration given a wind speed measurement at height z_2. In the above, ν is the kinematic viscosity (m^2 s^{-1}) of air, which can be computed with reasonable accuracy from:

$$\nu = 2.964 \times 10^{-6} \frac{T_a^{3/2}}{p}, \tag{6.16}$$

given the atmospheric pressure p(mbar) and T_a(K). If $f(\overline{u})$ is expressed as $C_w\overline{u}$, then:

$$C_w = \frac{3966}{T_a \ln\left(\frac{z_2}{z_{0\nu}}\right) \ln\left(\frac{z_1}{z_{0m}}\right)}, \tag{6.17}$$

and so

$$E_a = C_w\overline{u}(1 - r_H)e_s(T_a), \tag{6.18}$$

where E_a is measured in mm day^{-1}, $\overline{u}$ in m s^{-1}, $e_s(T_a)$ in mbar and r_H is the relative humidity expressed as a fraction.

Estimation of the aerosol effect on potential evaporation

The estimation of the aerosol effect on potential evaporation was based on the same method used for the estimation of the aerosol DRE (Section 3.8) and the aerosol effect on J(O^{1}D) (Section 5.2). Specifically, PE was calculated separately by including and omitting the aerosol layer from the SW model. The aerosol effect on PE (ΔPE) is defined as the difference of these two outputs:

$$\Delta\text{PE} = \text{PE} - \text{PE}_{\text{no-aerosol}}. \tag{6.19}$$

6.2.2 Satellite and surface input data

The pre–processing procedure for the FORTH model MODIS Level 2 input data, described in Section 2.4.1, was repeated over each lake. The retrieved AOT over land was used in the present study, instead of the corresponding AOT product over ocean, due to the increased distance of the lakes from coastal areas. For the asymmetry parameter, however, which is not retrieved by MODIS over land, the size of the N×N km^2 area used for the estimation of each parameter over each lake, was increased from 50 km×50 km to 100 km×100 km, in order to include pixels over nearby seas, where the asymmetry parameter values are available.

Aerosol single–scattering albedo data were acquired from the GADS climatology database (Köpke et al., 1997). These data are available at 61 wavelengths, from which 38 fall into the 0.2 µm–10 µm region used by the model, and 8 different levels of relative humidity. They were linearly interpolated at the model wavelengths, while the model–computed relative humidity on a daily basis was used for the corresponding interpolation from the 8 humidity levels. Due to the availability of the GADS data only in winter and summer, these values were assigned to January and July, respectively, and the remaining monthly values were calculated based on linear interpolation from these two months.

Air temperature data, needed for the computation of PE, were calculated from the MODIS temperature and pressure profile data, by interpolating or extrapolating to the surface pressure level. Surface wind data, needed for the PE air component evaluation, were obtained from ground–based stations at three of the four lakes, as described in Section 6.2.4. Finally, net upwelling LW radiation data at the surface, needed for the computation of Q_n in Equation (6.8), and consequently E_s, were obtained from corresponding runs of the LW model (Section 6.2.5).

6.2.3 Lake surface reflectivity

The lake surface reflectivity was computed using the Fresnel reflection equation, omitting the correction for surface roughness, as described in Section 3.9. While n, the real part of the water refractive index, is assumed constant and equal to 1.333 in equations (3.48) and (3.49), Hale and Querry (1973) report a variation in n, especially in the NIR region (Figure 6.2). In this chapter, where only water surfaces are considered, the reflectivity was allowed to vary spectrally, depending on this spectral variation of n.

Figure 6.2 shows the spectral variation of n, according to Hale and Querry (1973), and the corresponding values used as input to the model. For the

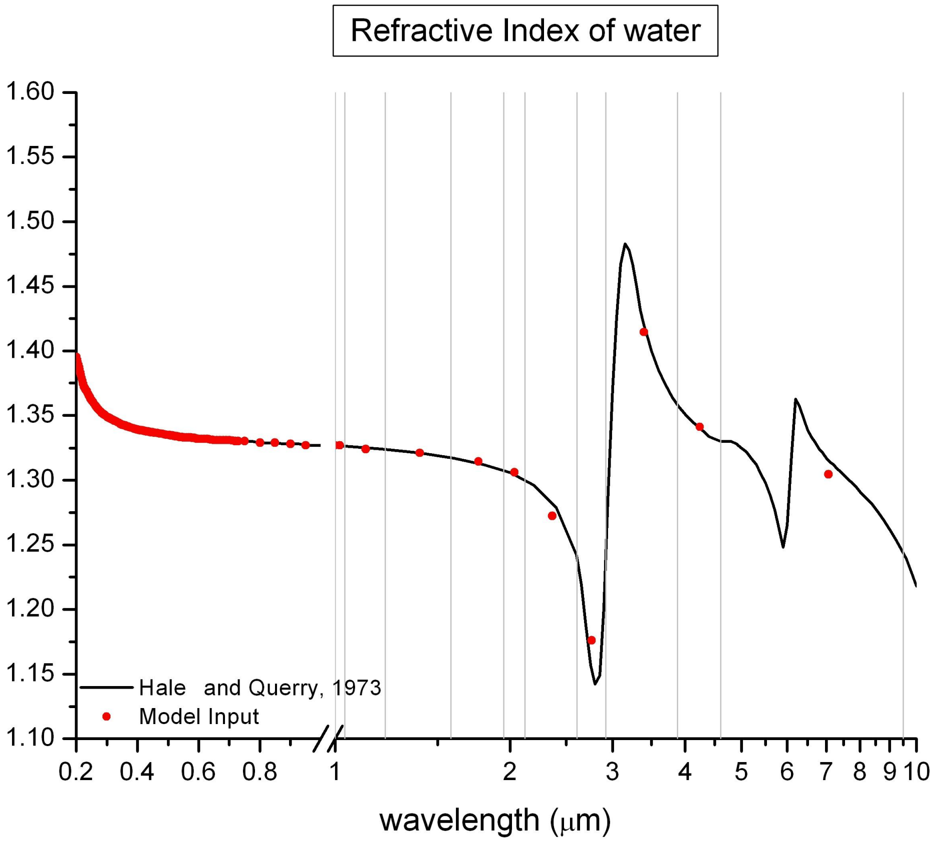

Figure 6.2: Spectral variation of the refractive index of water (n), according to data from Hale and Querry (1973) (black line). The vertical lines show the limits of the model NIR bands, while red dots correspond to the model input values of n in each wavelength and band.

derivation of the model input, linear interpolation was used in the 0.2–1 μm region, while for the NIR bands, a mean value was estimated, based on the data falling in each band. These values are also shown in Figure 6.2. In order to evaluate possible differences when using the spectrally varying n, instead of the constant value, the model was run with both methods over Marathonas lake, using both Terra and Aqua MODIS input data. Figure 6.3 shows the percent difference in the net DSR, which is used as input for the PE computation. The maximum difference values, equal to ±0.25%, are observed during summer and winter, respectively. Although this difference is insignificant, the spectrally varying method was used in this chapter.

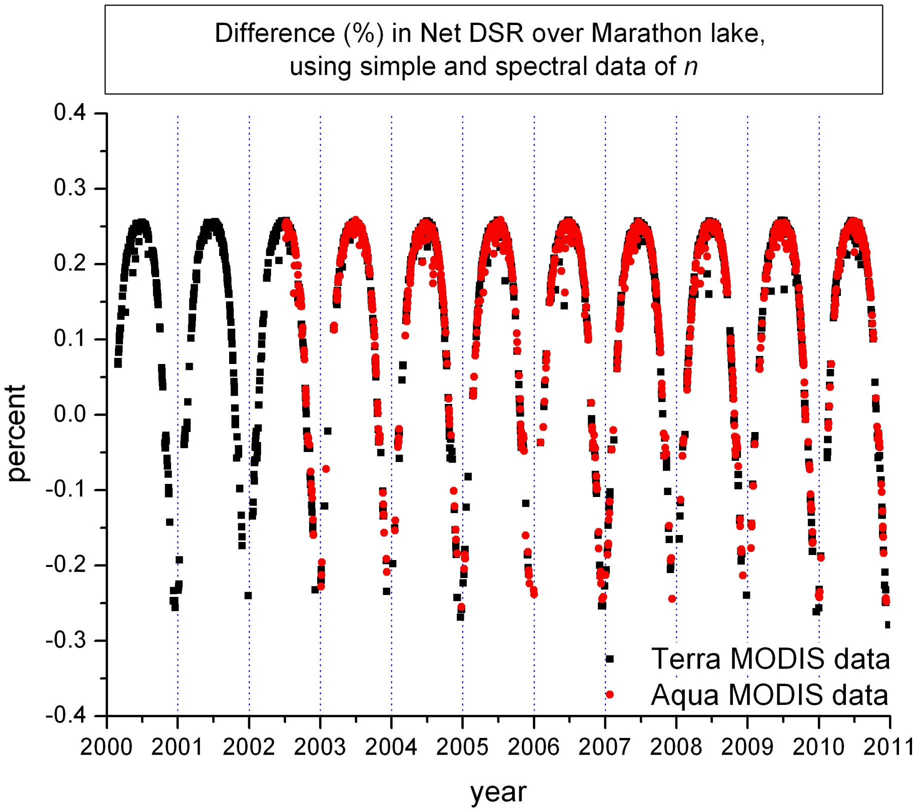

Figure 6.3: Time series of the percent difference in net DSR over Marathonas lake, using spectrally varying and constant values of n.

6.2.4 Wind data

Surface wind speed and direction data are available in Marathonas, Mornos and Yliki lakes, in 10–minutes and 1–hour averages, covering the periods 2002–2006 in Marathonas and 2002–2007 in Mornos and Yliki. Monthly mean values were calculated from the 1–hour averages and used as input for the computation of PE. Mean values on a monthly basis, calculated from the entire period of wind data availability, were also used for the months in 2001 and 2007/2008–2010, when station data were not available. In the case of Evinos lake, where no wind measurements exist, data from Mornos were used, due to their proximity (Figure 6.1) and their similar terrain morphology.

Figure 6.4 shows the average polar distribution of wind speed and direction in the three lakes, calculated in 10° intervals from the 10–minutes average data. Higher values of wind speed are reported in Mornos lake, and should probably be attributed to wind tunnel effects caused by the high

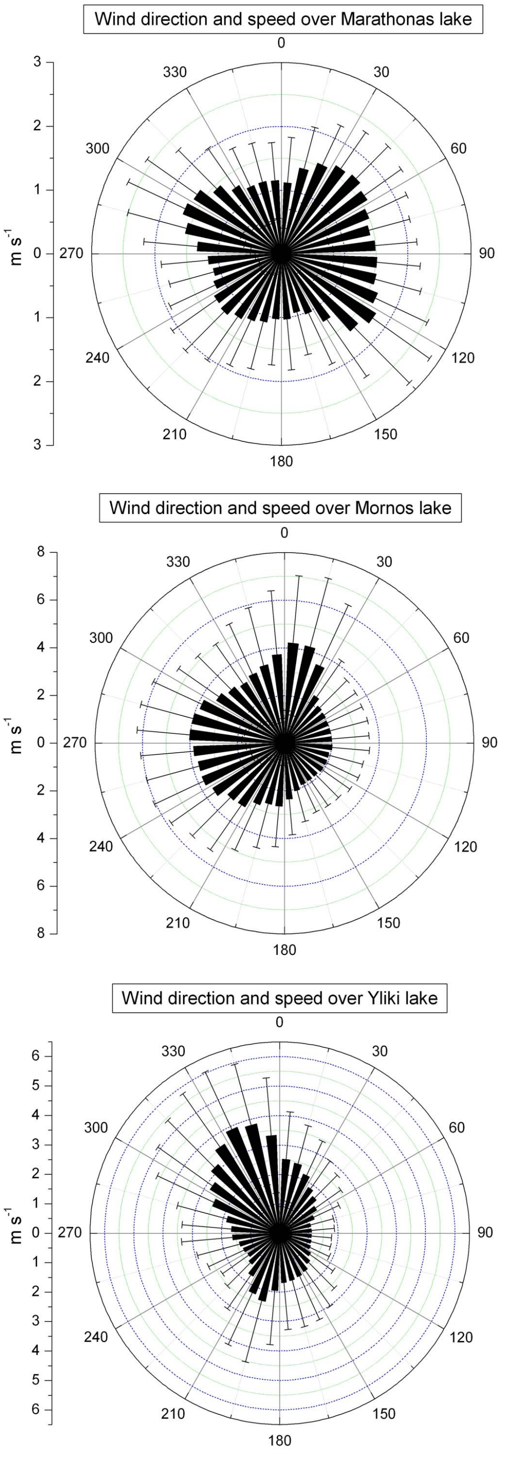

Figure 6.4: Average polar distribution of wind speed and direction over the lakes of Marathonas, Mornos and Yliki. Error bars represent the standard deviations from the calculated mean values in each 10° interval.

mountains and narrow valleys surrounding the lake. Differences in wind directions among the three lakes should also be attributed to differences in the morphology of the surrounding areas.

6.2.5 Net upwelling LW radiation at surface

The surface net upwelling LW radiation is included in the output parameters of the LW RTM, which was developed from the radiative–convective model of Vardavas and Carver (1984), for the computation of the terrestrial infrared radiation. The model version used for the computation of the data presented here, runs on a monthly basis and at 2.5° × 2.5° resolution. The vertical resolution is 5 mbar, from the surface up to 50 mbar, to ensure that the atmospheric layers are optically thin with respect to the Planck mean LW opacity, while the spectral resolution comprises 28 LW bands. Model input data came from the ISCCP–D2 and NCEP/NCAR data sets.

The atmospheric molecules considered by the LW model are H_2O, CO_2, CH_4, O_3, and N_2O. The sky is divided into clear and cloudy fractions, and three non–overlapping layers of low, mid and high–level clouds are considered. The model input data include cloud amounts, cloud scattering and absorption optical depths, cloud–top pressure and temperature (for each cloud type), cloud geometrical thickness and vertical temperature and specific humidity profiles. The LW model is described in more detail in Matsoukas et al. (2011), while a full presentation is given in Pavlakis et al. (2004). The model downwelling longwave radiation (DLR) has also been validated against BSRN station measurements for the entire globe (Pavlakis et al., 2004; Matsoukas et al., 2005).

The LW model input data and runs cover the period 2000–2008. Based on the geographical coordinates of the four lakes, two 2.5° × 2.5° pixels were identified, one covering Evinos and Mornos, and the other Marathonas and Yliki. The corresponding monthly surface net upwelling LW radiation data for these pixels were extracted, and used as input for the calculation of the potential evaporation. For the years 2009 and 2010, monthly climatologies from the 2000–2008 period were computed and used. The LW data were also analysed for possible trends during 2000–2008. Figure 6.5 shows the seasonal variation and the normalized anomaly time series of the surface net upwelling LW radiation in Evinos and Mornos (Figure 6.5a), and Marathonas and Yliki (Figure 6.5b). In both cases, the values range between $\sim$40 W m^{-2} in winter and $\sim$70 W m^{-2}. No statistically significant trend was found in either case.

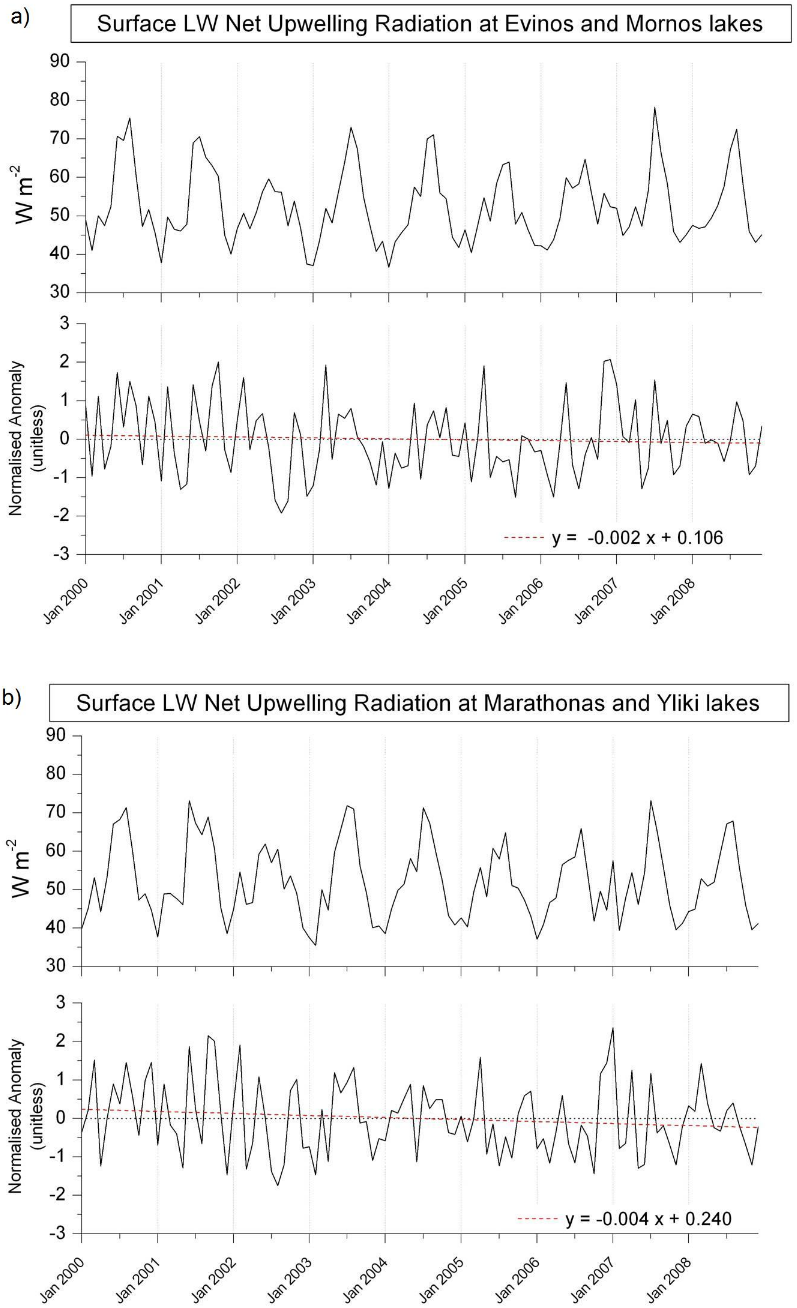

Figure 6.5: Time series of the surface net upwelling LW radiation in Evinos and Mornos (a), and Marathonas and Yliki (b) lakes, with each pair of lakes located within the same pixel used. The seasonal variation (upper panels) and the normalised anomaly (lower panels) are shown. The linear regression equations are also shown.

6.3 Results

6.3.1 Model DSR validation against surface measurements

The model–derived DSR was validated against corresponding surface measurements near Marathonas, Mornos and Yliki lakes. These measurements were available from pyranometers operated by the Athens Water Supply and Sewerage Company (EYDAP SA), for the periods 2002–2006 in Marathonas and 2002–2007 in Mornos and Yliki. Since the surface measurements were acquired from stations near the lakes, for the validation of the output DSR against ground–based measurements, the model was run using surface albedo data from MODIS. For the validation of the daily (24–hour) mean DSR, the average of measurements acquired every 10 minutes was compared against the daily mean model output DSR, estimated using separately Terra and Aqua MODIS input data.

Figures 6.6, 6.7 and 6.8, show the validation scatter plots over Marathonas, Mornos and Yliki, separately for Terra (a) and Aqua (b) data, along with the corresponding linear regression fits, determination coefficients and numbers of points used. The model daily mean DSR is in good agreement with the corresponding surface measurements, with a determination coefficient ranging between 0.8 and 0.9 in most of the cases, and slopes around 0.9. Several cases of the sparse points appearing in the upper left areas especially of the Aqua MODIS scatter plots, were further examined, and should be attributed to atmospheric conditions during the satellite overpass time, which failed to represent the daily mean conditions. Specifically, in these cases MODIS detected partial cloud cover, while clear–sky conditions prevailed almost throughout the day, as was deduced from the temporal distribution of the 10–min DSR measurements. These results explain the underestimation of the model DSR compared to station measurements, during these specific days.

Table 6.1: Determination coefficient (R^2) and slope validation results over Marathonas, Mornos and Yliki lakes, using averaged values of Terra and Aqua model output DSR.

Lake	R^2	slope
Marathonas	0.85	0.94
Mornos	0.75	0.79
Yliki	0.91	0.96

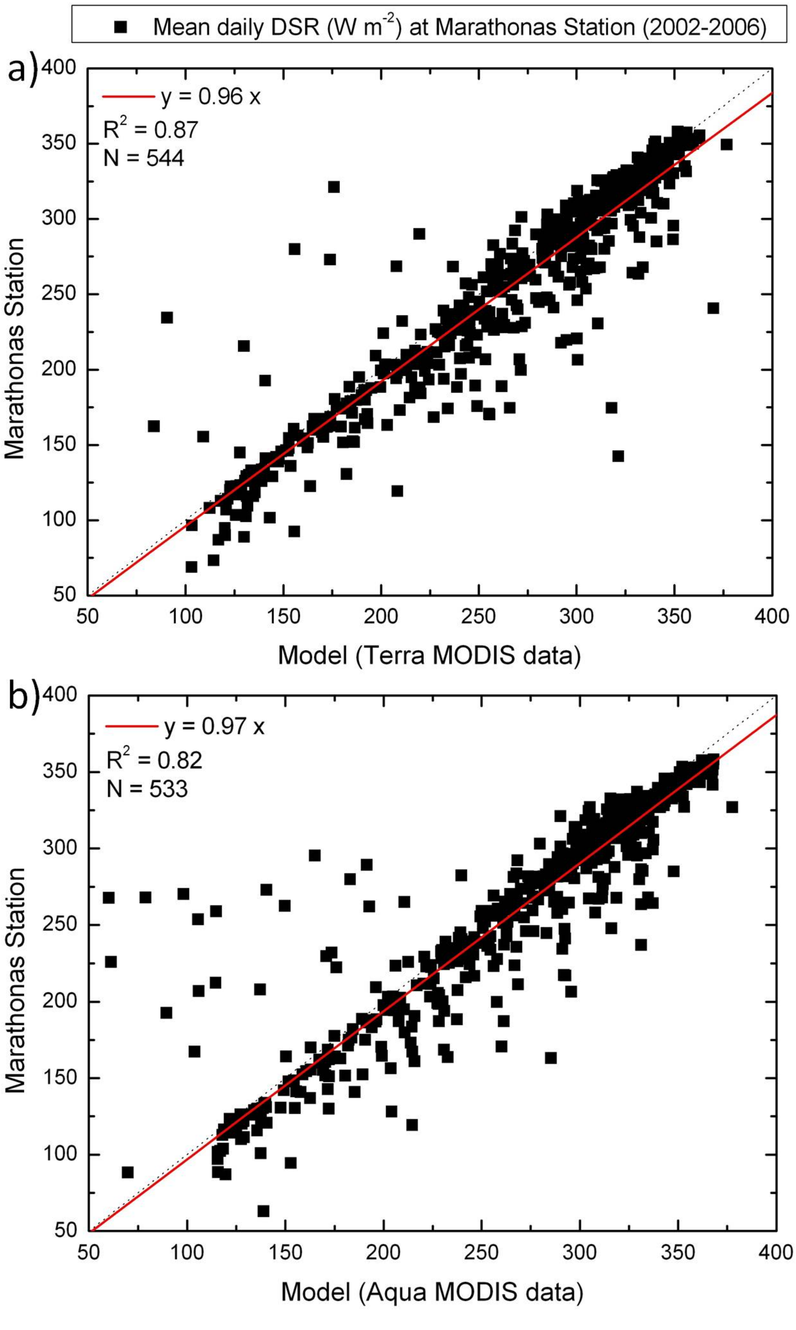

Figure 6.6: Scatter plots of the model daily mean DSR using Terra (a) and Aqua (b) data, against corresponding ground measurements from Marathonas, for the years 2002–2006. The red lines are the linear regression fits, with the equations, determination coefficients and number of points also shown.

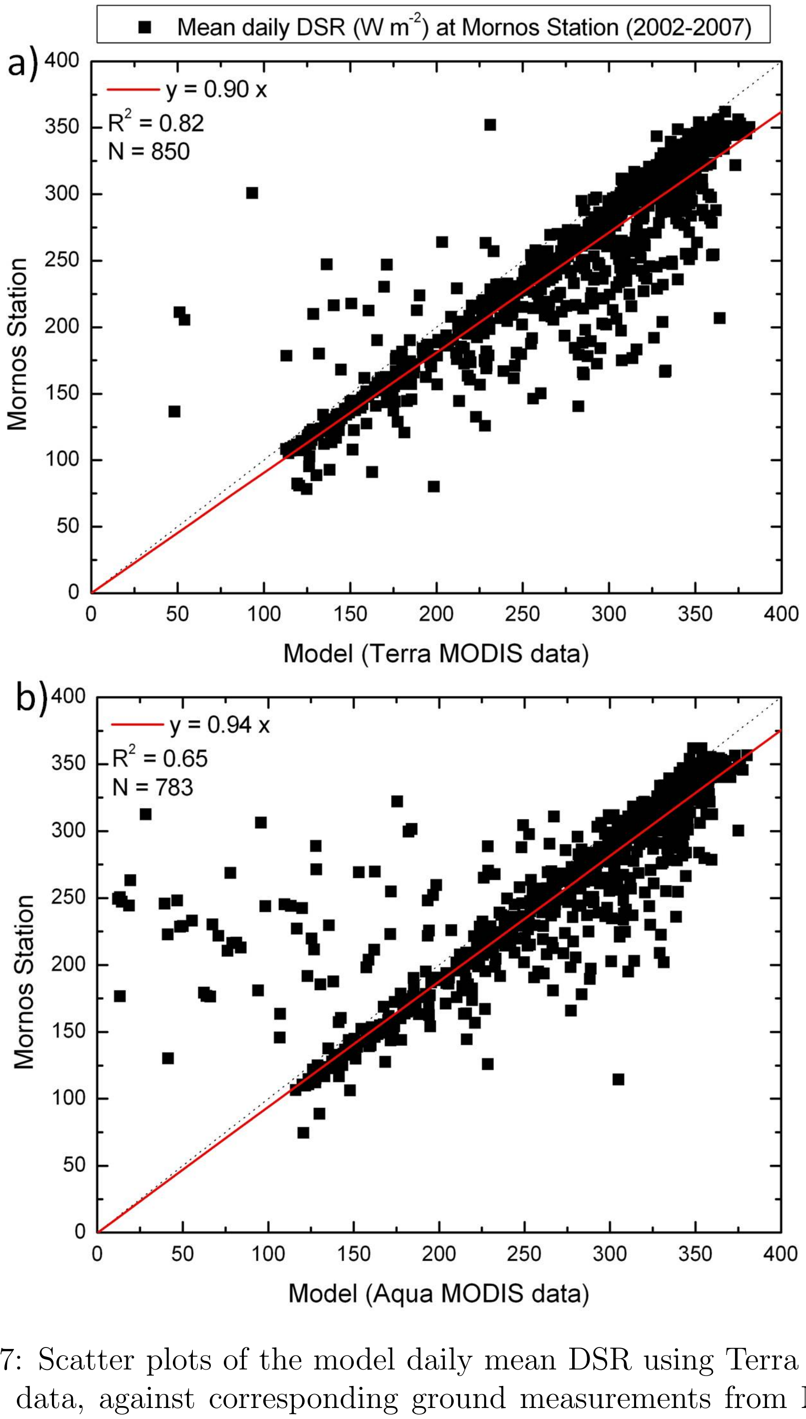

Figure 6.7: Scatter plots of the model daily mean DSR using Terra (a) and Aqua (b) data, against corresponding ground measurements from Mornos, for the years 2002–2007. The red lines are the linear regression fits, with the equations, determination coefficients and number of points also shown.

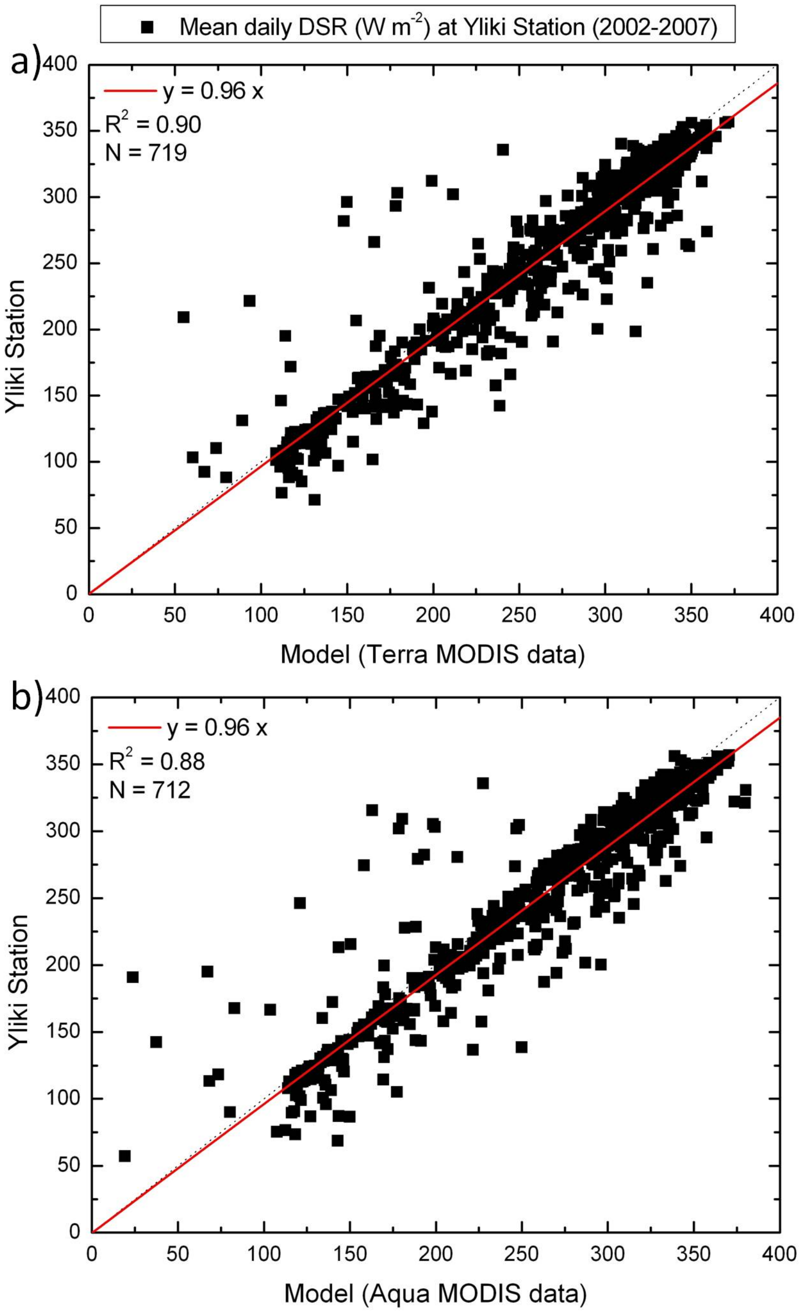

Figure 6.8: Scatter plots of the model daily mean DSR using Terra (a) and Aqua (b) data, against corresponding ground measurements from Yliki, for the years 2002–2007. The red lines are the linear regression fits, with the equations, determination coefficients and number of points also shown.

A validation was also performed using Terra and Aqua average model output DSR values, and gave similar determination coefficient and slope results, shown in Table 6.1. The model performance was also similar when MODIS Terra and Aqua averaged input data were used. Since the aim of the present study is the evaluation of daily mean values of the atmospheric radiation budget and the corresponding PE, it appears reasonable to use Terra and Aqua input, or the corresponding model output, average values, as more representative of the daily mean. The above mentioned validation tests, however, show that the slightly poorer performance of Aqua data in representing the daily mean, cause a reduction in the representativeness of the average input or output parameters, compared to Terra only data and corresponding model output. In fact, the determination coefficient value in the case of Mornos (R^2 = 0.75, Table 6.1), should be attributed to the poorer performance of the model output over this lake using Aqua MODIS data (Figure 6.7b). Hence, the results reported in the following sections were computed using Terra MODIS data, being the most representative of the daily mean, among the available data sets.

6.3.2 Seasonal characteristics of potential evaporation

Figure 6.10 shows the seasonal variation of the PE (in mm day^{-1}) and its components ($\mathrm{PE_{sol}}=(\Delta/(\Delta+\gamma))E_s$ and $\mathrm{PE_{air}}=(\gamma/(\Delta+\gamma))E_a$, according to Equation (6.1)), over the four lakes (left column), calculated from the daily mean values during the period 2001–2010. The seasonal contribution (in percent) of $\mathrm{PE_{sol}}$ and $\mathrm{PE_{air}}$ is also shown (right column). It is obvious from Figure 6.10 that the solar component dominates throughout the year, determining the variation of the total PE. Higher values of PE are observed during summer (June and July), reaching over 8 mm day^{-1} in most cases. During winter (December and January), when the available solar radiation reaches its minimum values, PE is less then 2 mm day^{-1} in all cases. The air component ranges between 0.4 and 1.7 mm day^{-1}, having higher values in July, in all four lakes. These summer maximum values of $\mathrm{PE_{air}}$ result as a combination of increased wind speed, reduced relative humidity and increased saturation vapour pressure, due to the increased air temperature (Equations (6.18) and (6.5), and Figure 6.9).

The contributions to PE range between ~70%–90% and ~10%–30% for $\mathrm{PE_{sol}}$ and $\mathrm{PE_{air}}$, respectively. While maximum contributions by $\mathrm{PE_{air}}$ are observed during winter, these should be attributed to the reduction of $\mathrm{PE_{sol}}$, instead of an increase in $\mathrm{PE_{air}}$, as can be seen in the left column of Figure 6.10.

Based on the seasonal PE results, the total evaporation on an annual

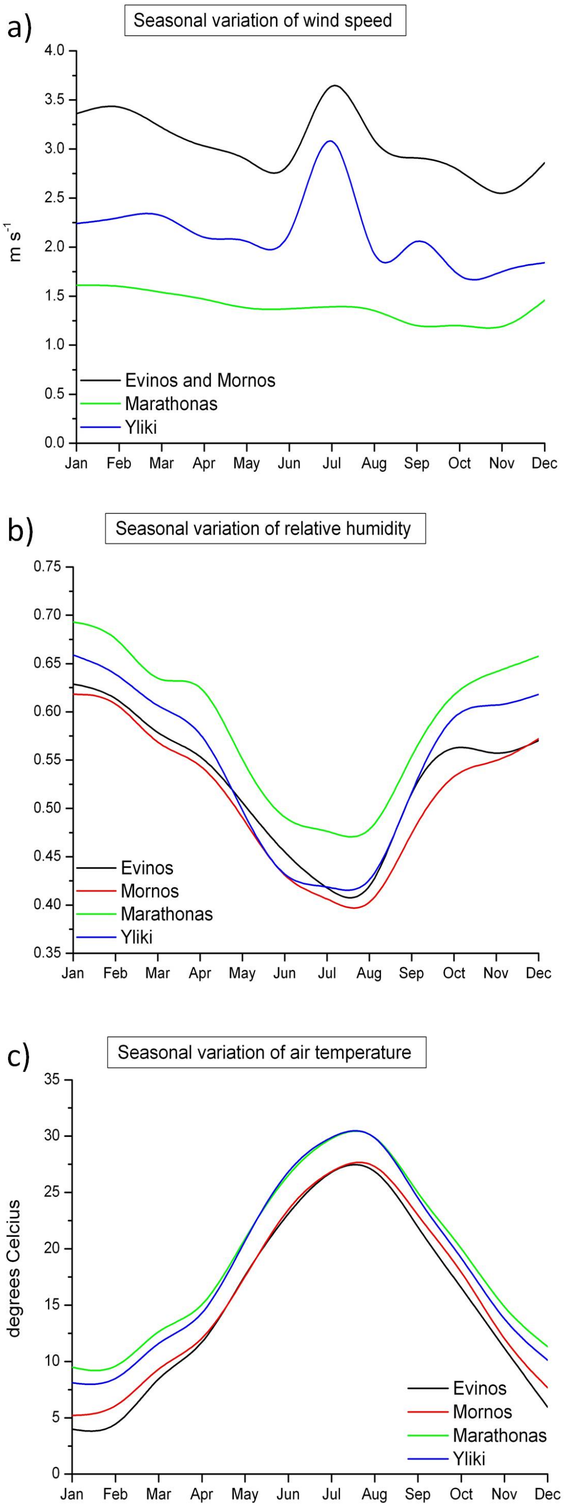

Figure 6.9: Seasonal variation of wind speed (a), relative humidity (b) and air temperature (c), over the four lakes, computed from the daily values.

Table 6.2: Total water (mm year^{-1}) lost through potential evaporation on an annual basis in Evinos, Mornos, Marathonas and Yliki.

Lake	mm year^{-1}
Evinos	1755.0
Mornos	1804.5
Marathonas	1619.5
Yliki	1704.4

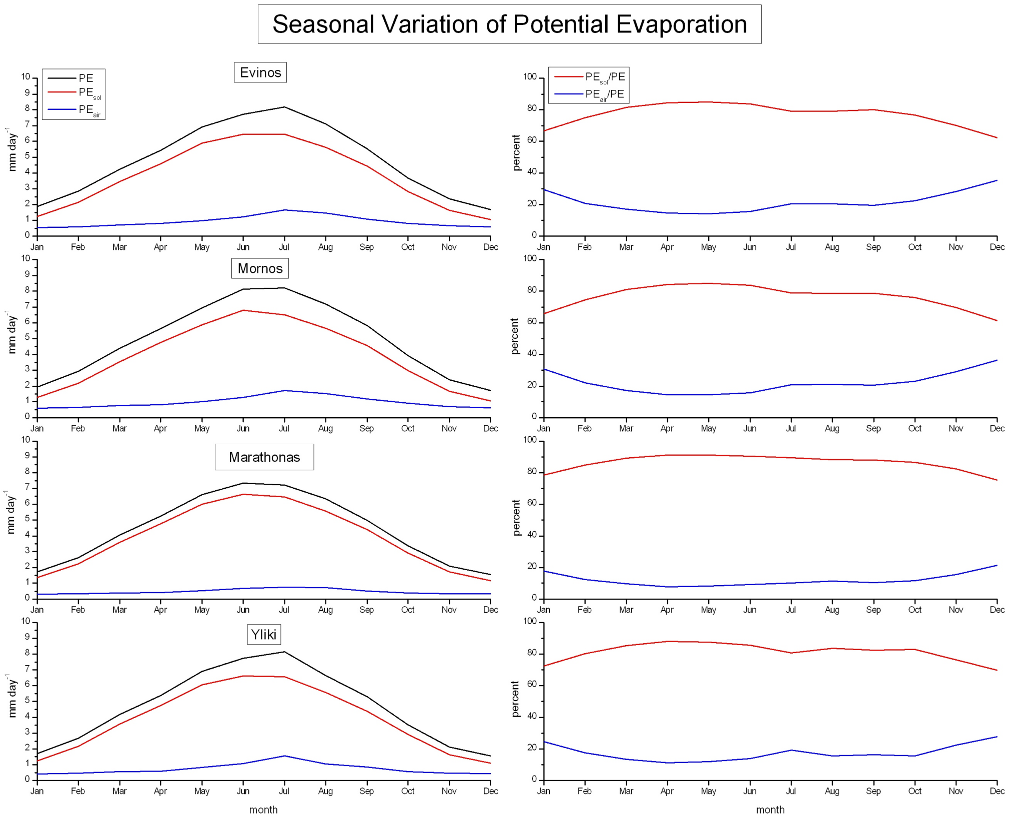

Figure 6.10: Seasonal values of PE, PE$_{sol}$ and PE$_{air}$ over the four lakes (left column), and the corresponding contributions of PE$_{sol}$ and PE$_{air}$ to the total PE (right column).

basis (mm year^{-1}) was calculated, by multiplying the monthly values (in mm day^{-1}), by the corresponding days in month. The results, (Table 6.2) show that Evinos and Mornos lose slightly more water due to evaporation on an annual basis, compared to Marathonas and Yliki. This difference should be attributed to the higher aerosol loads over Marathonas and Yliki, compared to Evinos and Mornos, which decrease the total water lost through evaporation as discussed in Section 6.3.5.

6.3.3 Aerosol daily effects on potential evaporation

The aerosol effect on PE, on a daily basis, during the period 2001–2010, is shown in Figures 6.11 and 6.12, in mm day^{-1} and %, separately for each lake. A seasonal variation is observed in all lakes, with ΔPE reaching peak values of about -1.5 and -2.0 mm day^{-1} in summer, at Evinos/Mornos and Marathonas/Yliki, respectively, with the lowest values occurring in winter. These summer extremes of ΔPE should be attributed to corresponding maxima in AOT, while the difference between Evinos/Mornos and Marathonas/Yliki is explained by the higher AOT values above the latter, due to their proximity to urban and industrial areas. This difference in the aerosol loads is also depicted in the mean ΔPE values, shown in Table 6.3, which is higher in Marathonas and Yliki, compared to Evinos and Mornos. The seasonal variation is not obvious in the time series showing ΔPE in percent (lower panels in Figures 6.11 and 6.12), since along with the decrease in AOT during winter, PE is also decreased, due to the seasonality of the SW radiation reaching the surface of each lake.

An analysis on ΔPE caused by dust events was also performed over all four lakes. The criteria for the identification of dust events were based on thresholds on the MODIS AOT values at 0.55 µm and the corresponding values of the Angstrom exponent (Å) over land (0.47 µm–0.67 µm), as described in Section 4.2.4. Applying these criteria and verifying the result through back–trajectory analysis, about 40 cases of dust events were detected over Evinos and Mornos, during the 10–year period examined, occurring mainly in spring and secondarily in autumn, in agreement with the results reported in Chapter 4. At Marathonas and Yliki, however, no dust event case was detected. This contradictory result should also be attributed to the proximity of these lakes to urban and industrial areas, as previously mentioned. Specifically, while the AOT meets the criterion of increased values on a frequent basis, the constantly polluted air, which is characterised by fine particles and high Å values, prevents Å from obtaining values lower than the applied threshold, which would characterise coarse particles of a dust event. This constant air pollution, which characterises the entire region between the

Table 6.3: Mean values of the aerosol effect on potential evaporation at the four lakes, during the period 2001–2010. Corresponding mean values during dust events are also shown for Evinos and Mornos.

Aerosol Effect on Potential Evaporation				
	All Days		Dust Events	
Lake	mm day^{-1}	%	mm day^{-1}	%
Evinos	-0.44	-6.73	-1.02	-15.83
Mornos	-0.44	-6.82	-1.00	-17.30
Marathonas	-0.61	-10.02	–	–
Yliki	-0.58	-9.25	–	–

cities of Athens and Thessaloniki, was also reported by Athanassiou et al. (2013), and was attributed to intense human activities in this area.

ΔPE during dust events over Evinos and Mornos is shown separately in Figure 6.11. While ΔPE does not exceed -7% over Evinos and Mornos on a mean basis, aerosols cause a decrase of ∼16–17% in PE during dust events (Table 6.3).

The aerosol effect on the PE rate on a daily basis, was also investigated based on the correlation of the MODIS AOT at 0.555 μm with ΔPE over each lake. Figure 6.13 shows the corresponding scatter plots for each lake, which present a similar behaviour. As a general rule, an increase in AOT by 0.1, causes a decrease in PE by about 3.5%–4%. Higher values of AOT and corresponding PE decrease, especially at Marathonas and secondarily at Yliki, compared to Evinos and Mornos, are also evident here.

6.3.4 Trends in potential evaporation and operating factors

Table 6.4 shows the percent change during the period 2001–2010 in PE over all four lakes, the solar and air components (PE_s and PE_a, respectively), and the factors and parameters that affect these changes. The trend was computed from the time series of the monthly mean values, using a threshold of 10 values per month, in order for the corresponding mean value to be used in the analysis as representative of the month. No statistically significant change in the 95% confidence interval was observed in PE; the results show that the four lakes can be grouped into two pairs (Evinos/Mornos and Marathonas/Yliki), based on their geographical proximity (Figure 6.1). PE has increased by ∼4–6% in Marathonas and Yliki, while it has decreased by

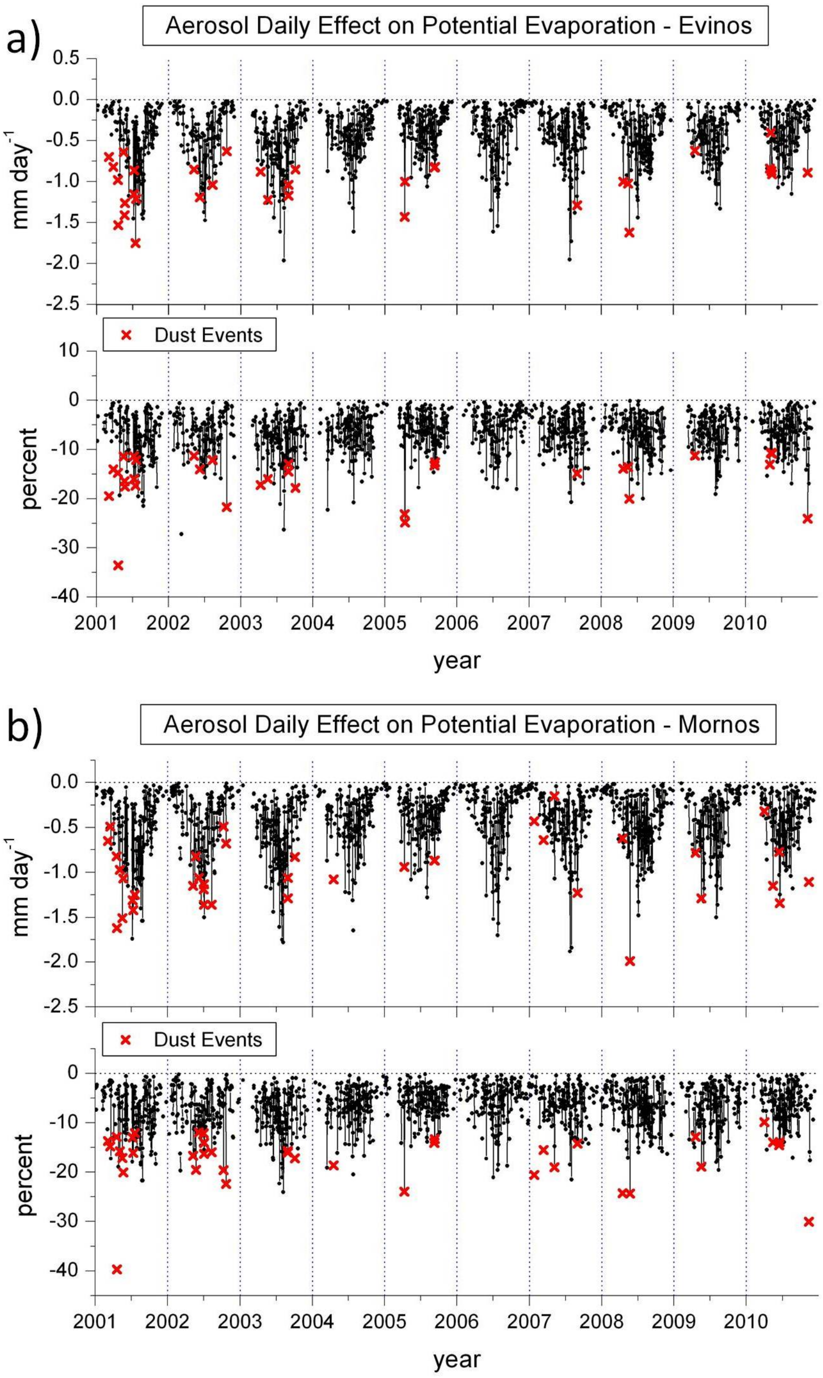

Figure 6.11: Time series of the aerosol mean daily effect on potential evaporation at Evinos (a) and Mornos (b) lakes, during 2001–2010, in mm day^{-1} (upper panels) and percent (lower panels). Values during dust events are also shown.

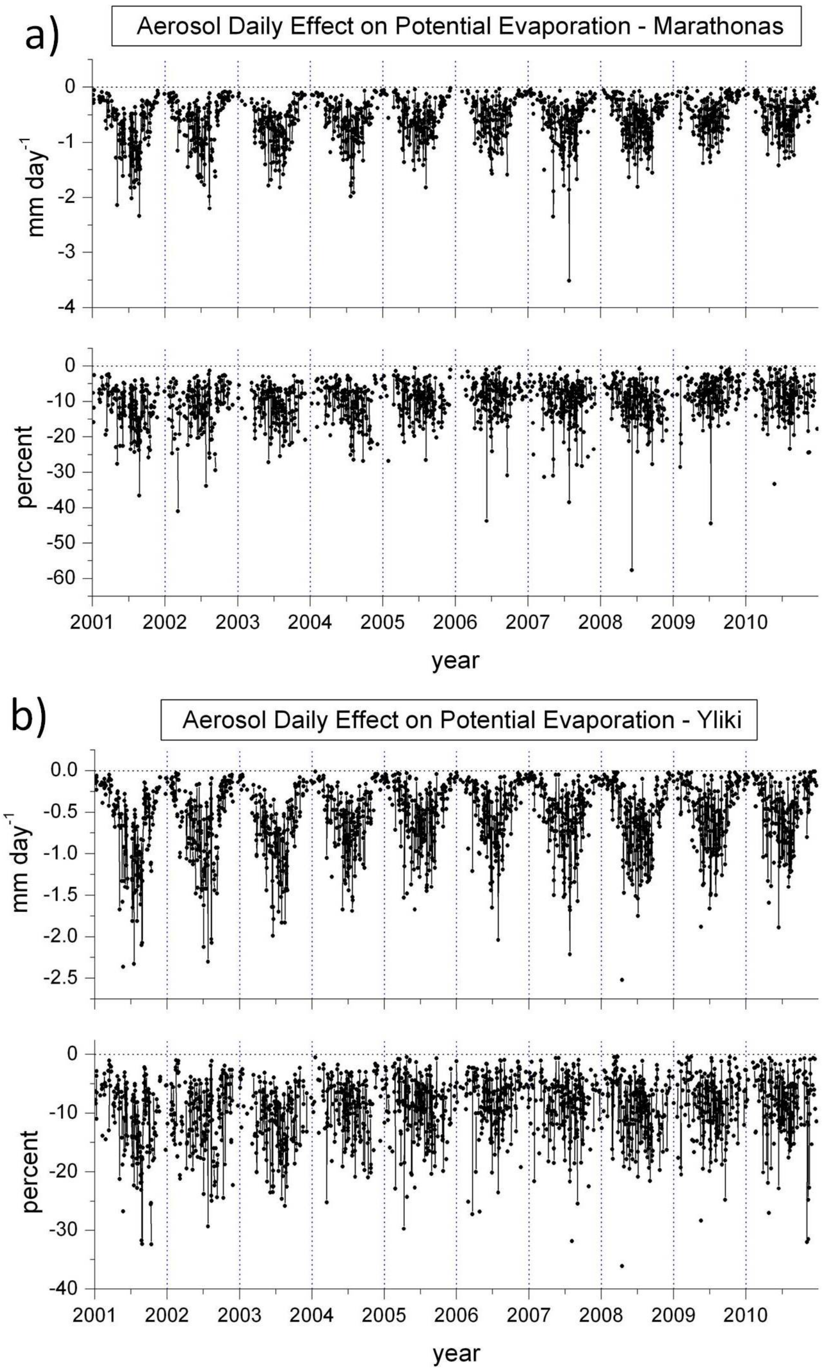

Figure 6.12: Time series of the aerosol mean daily effect on potential evaporation at Marathonas (a) and Yliki (b) lakes, during 2001–2010, in mm day^{-1} (upper panels) and percent (lower panels).

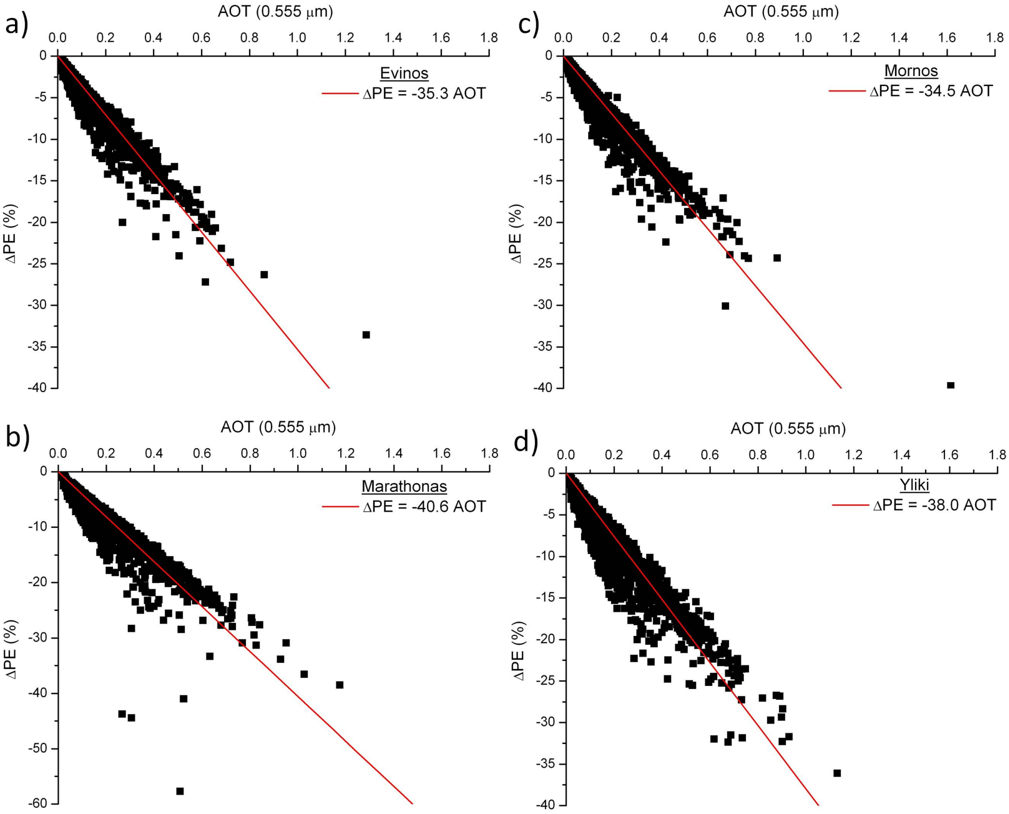

Figure 6.13: Scatter plots of the MODIS AOT values at 0.555 µm against corresponding ΔPE (%) over Evinos (a), Mornos (b), Marathonas (c) and Yliki (d), on a mean daily basis, during 2001–2010. Equations of the linear regressions (red lines) are also shown.

∼2–4% in Evinos and Mornos. The aerosol effect on PE has decreased substantially during this decade in all four lakes, ranging between -25.4% in Yliki and -40.4% in Marathonas. This decrease is explained by the corresponding substantial decrease in AOT, which is statistically significant in all cases. It should be noted that since PE_s dominates over PE_a (Section 6.3.2), changes in PE are driven primarily from corresponding changes in PE_s. Hence, the PE is decreasing in Evinos/Mornos and increasing in Marathonas/Yliki due primarily to the corresponding changes in the net DSR (and consequently DSR, according to Equations (6.7) and (6.8)).The decrease in PE_a by ∼15% over Marathonas and Yliki, which should be attributed to the statistically significant increase in relative humidity (r_H, Equation (6.18)), does not influence significantly the PE trend.

Table 6.4: Changes (%) in PE, its components and parameters affecting them at Evinos, Mornos, Marathonas and Yliki. Statistically significant changes at the 95% confidence level are shown in bold.

Trends 2001–2010 (%)													
Lake	PE	PE$_s$	PE$_a$	$\overline{F}_{sol}^{\downarrow}$	DSR	$\overline{F}_{ir}^{\uparrow}$	Aerosol Effect on PE	AOT	r_H	e_s	$\overline{u}$	T_a	Cloud fraction
Evinos	-3.88	-3.58	+6.23	-2.73	-2.51	+2.20	-27.10	**-28.18**	-2.46	+12.72	-1.15	+0.83	+12.90
Mornos	-2.08	-0.85	-3.12	-1.29	-1.00	+2.20	**-31.79**	**-36.14**	+5.24	+8.85	-1.15	+0.65	+12.44
Marathonas	+4.11	+6.15	-15.47	+4.41	+4.23	-1.70	**-40.43**	**-35.87**	**+10.62**	-3.32	-1.76	<0.01	-2.06
Yliki	+5.95	+8.35	-14.65	+4.27	+4.01	-1.70	-25.38	**-26.52**	**+14.60**	+1.83	-2.06	+0.10	+1.07

Table 6.5: Mean differences in DSR (Δ(DSR)) induced by variation (ΔV) of variable V (AOT and cloud fraction) at Marathonas lake.

V	ΔV	Δ(DSR)
AOT	-10%	+0.91±0.51%
AOT	-30%	+2.79±1.57%
Cloud fraction	+10%	-4.55±5.68%

While the decrease in AOT would be expected to increase the DSR, this trend is observed only in Marathonas and Yliki. A similar trend analysis on cloud fraction, showed that it remained practically unchanged over Marathonas and Yliki, while it has increased by ∼12% over Mornos and Evinos. These results imply different influences of aerosols and clouds over the two pairs of lakes, which were verified by a sensitivity analysis. This analysis was conducted over Marathonas lake, since the sensitivity results are expected to be similar for all lakes. Table 6.5 shows that a 30% decrease in AOT, which is of the order of the actual decrease observed over all four lakes, will increase the DSR by 2.79±1.57%, with higher values observed during summer months, which dominate the time series due to the applied threshold of 10 values per month. Thus, the PE increase over Marathonas and Yliki can be attributed to the decrease in AOT and the corresponding aerosol effect. According to Table 6.5, however, an increase in cloud fraction by 10% would reduce the DSR by almost 5%. These results imply that the cloud fraction increase by about 12% over Evinos and Mornos masked the DSR (and consequently PE) increase, arising from the reduction in AOT.

6.3.5 Aerosol effect on the water budget

Based on the monthly mean values of PE and ΔPE, and the maximum surface area of each lake, available from EYDAP SA data (Table 6.6), the surplus of available water in each lake, due to the presence of aerosols, was calculated on a seasonal basis. Figure 6.14 shows the amount of water (in 10^3 m^3) that would be lost through PE, if aerosols were absent. This amount peaks during summer over all lakes, when the aerosol effect is also maximum in absolute values (Figures 6.11 and 6.12). The differences among the lakes are caused by the corresponding differences in their surface areas, as shown in Table 6.6. Mean annual values of water lost through PE and water surplus due to ΔPE, shown in Table 6.6, were also calculated based on the seasonal values.

The time series of the total annual water surplus due to aerosols, calculated in each lake, is shown in Figure 6.15. Applying linear regression fits to

Table 6.6: Maximum surface areas and catchment areas of the four lakes (km^2), water lost due to natural lake evaporation (PE) and water surplus due to aerosols (ΔPE), and catchment rainfall. All water amounts are given in 10^6 m^3.

Lake	Maximum surface area	Catchment area	Water lost through PE	Water surplus due to ΔPE	Catchment rainfall
Evinos	3.60	352	6.3	0.4	429.1
Mornos	13.93	588	25.1	1.7	557.4
Marathonas	2.57	118	4.2	0.4	80.2
Yliki	27.74	2467	47.3	4.7	1598.6

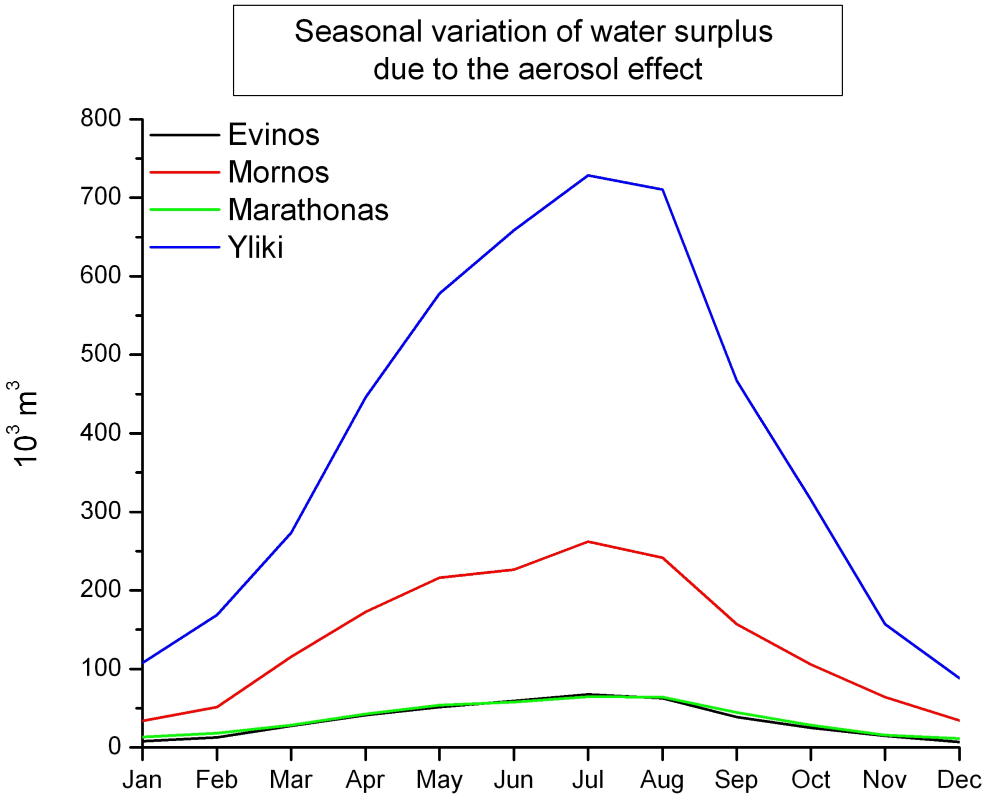

Figure 6.14: Seasonal variation of the water surplus available in each lake, due to the aerosol effect on PE.

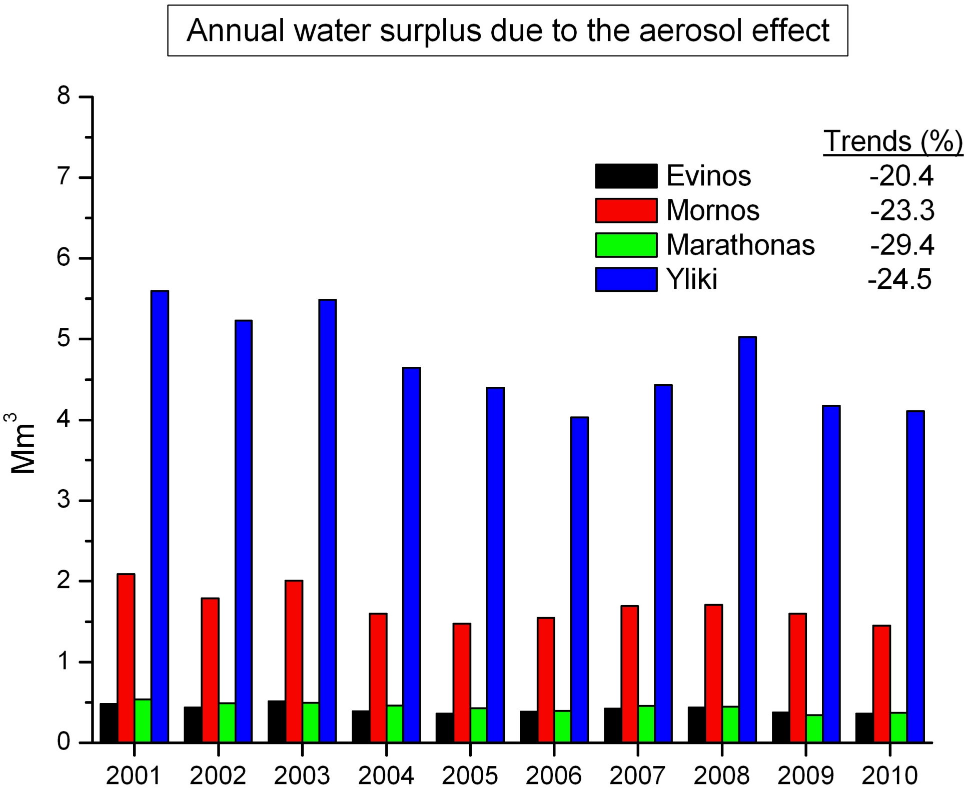

Figure 6.15: Inter–annual variation of the water surplus available in each lake, due to the aerosol effect on PE. The corresponding trends are given in Table 6.6

each lake time series, statistically significant decreasing trends of this water surplus were found in all lakes. These % changes are also given in Figure 6.15, and should be attributed to the corresponding significant decreasing trends of ΔPE, shown in Table 6.4.

Mean values of rainfall water, in mm year^{-1}, were also available from EYDAP SA over the four lakes. For the conversion in 10^6 m^3, this water amount was multiplied by the surface area of the entire catchment basin of each lake (shown in Table 6.6), instead of the water surface only, as in the case of the water surplus conversion. The computed values are also shown in Table 6.6.

These results show that, although the lake water lost through evaporation is increasing, due to the decreasing aerosol concentration over the lakes, this amount remains small compared to the catchment rainfall, although there will be also some reduction in catchment evaporation due to aerosols. The amount of the water surplus due to the presence of aerosols, however, becomes important when compared with the annual water consumption. According to data from EYDAP SA, the annual mean water consumption over the wider area of Athens during the last years was about 200 Mm^3. Hence, the annual water surplus due to the presence of aerosols, would suffice to supply water in the wider area of Athens for about 2 weeks, or about 3.5% of annual consumption.

6.4 Summary and conclusions

The daily mean Penman potential evaporation rate was computed at lakes Evinos, Mornos, Marathonas and Yliki, for the period 2001–2010. The lakes are located in Central Greece and constitute the main water supply for the city of Athens. The computation was based on the FORTH SW RTM, with MODIS Level 2 aerosol and atmospheric parameters input data, supplemented by aerosol single–scattering albedo data from the GADS database, FORTH LW RTM output fluxes and wind speed data from ground stations. This approach allowed the assessment of the aerosol effect on potential evaporation on a daily and monthly basis, and the evaluation of corresponding trends during the decade examined.

The model output DSR was validated against corresponding in situ measurements at three of the four lakes, showing very good agreement. Examination of the seasonal characteristics of PE showed that it is primarily driven by the radiation balance at the lake's surface, following the corresponding seasonal DSR curve, with maximum values during summer ($\sim$8 mm day^{-1}) and minimum in winter.

The aerosol effect was found to reduce the PE rate by about 7%–10% on a long–term mean basis, reaching 16%–17% during dust events. More intense ΔPE was reported over Marathonas and Yliki, explained by the higher aerosol loads in this region, due to the proximity to aerosol sources of human origin.

Differences between the pairs Marathonas/Yliki and Evinos/Mornos were also found in the decadal trends examined. While the AOT and the corresponding ΔPE have significantly decreased from 2001 to 2010 over all lakes, the PE increased, as expected, only over Marathonas and Yliki. Examination of other parameters affecting the PE, combined with a sensitivity analysis, showed that an increase in cloud cover by $\sim$12% over Evinos and Mornos counterbalanced the expected increase in DSR due to the decreased AOT, and led to a decrease in PE.

Comparisons showed that, although the amount of water lost through evaporation on an annual mean basis is small compared to the incoming rainfall, the amount of water surplus due only to the presence of aerosols, would suffice to cover the needs of the wider Athens area for about 2 weeks.

The results presented in this chapter highlight the ability of the FORTH RTM, combined with local scale data, to evaluate processes and effects influenced by the atmospheric radiation budget. The assessment of the PE is highly important both in the research of the water cycle, and for more practical reasons, including water use and management.

Bibliography

Athanassiou, G., Hatzianastassiou, N., Gkikas, A., and Papadimas, C.: Estimating Aerosol Optical Depth Over the Broader Greek Area from MODIS Satellite, Water, Air and Soil Pollution, 224, 1–14, doi:10.1007/s11270-013-1605-2, 2013.

Bengtsson, L.: The global atmospheric water cycle, Environmental Research Letters, 5, 2010.

Brutsaert, W.: Evaporation Into the Atmosphere: Theory, History and Applications, Environmental Fluid Mechanics, Springer, 2010.

Hale, G. M. and Querry, M. R.: Optical constants of water in the 200–nm to 200–micrometer wavelength region, Applied Optics, 12, 555–563, doi:10.1364/AO.12.000555, 1973.

Köpke, P., Hess, M., Schult, I., and Shettle, E. P.: Global Aerosol Data Set, MPI Report for Meteorology, Max–Planck–Institut für Meteorologie, 1997.

Matsoukas, C., Banks, A. C., Hatzianastassiou, N., Pavlakis, K. G., Hatzidimitriou, D., Drakakis, E., Stackhouse, P. W. J., and Vardavas, I.: Seasonal energy budget of the Mediterranean Sea, Journal of Geophysical Research, 110, 1–15, doi:10.1029/2004JC002566, 2005.

Matsoukas, C., Benas, N., Hatzianastassiou, N., Pavlakis, K. G., Kanakidou, M., and Vardavas, I.: Potential evaporation trends over land between 19832008: driven by radiative fluxes or vapour-pressure deficit?, Atmospheric Chemistry and Physics, 11, 7601–7616, doi:10.5194/acp-11-7601-2011, 2011.

Meehl, G. A., Stocker, T. F., Collins, W. D., Friedlingstein, P., Gaye, A. T., Gregory, J. M., Kitoh, A., Knutti, R., Murphy, J. M., Noda, A., Raper, S. C. B., Watterson, I. G., Weaver, A. J., and Zhao, Z. C.: Global Climate Projections, in: Climate Change 2007: The Physical Science Basis. Contribution of Working Group I to the Fourth Assessment Report of the

Intergovernmental Panel on Climate Change, edited by Solomon, S., Qin, D., Manning, M., Chen, Z., Marquis, M., Averyt, K. B., Tignor, M., and Miller, H. L., Cambridge University Press, Cambridge, United Kingdom and New York, NY, USA, 2007.

Pavlakis, K. G., Hatzidimitriou, D., Matsoukas, C., Drakakis, E., Hatzianastassiou, N., and Vardavas, I.: Ten–year global distribution of downwelling longwave radiation, Atmospheric Chemistry and Physics, 4, 127–142, doi: 10.5194/acp-4-127-2004, 2004.

Penman, H. L.: Natural Evaporation from Open Water, Bare Soil and Grass, Proceedings of the Royal Society of London. Series A. Mathematical and Physical Sciences, 193, 120–145, 1948.

Pruitt, W. O., Morgan, D. L., and Lourence, F. J.: Momentum and mass transfers in the surface boundary layer, Quarterly Journal of the Royal Meteorological Society, 99, 370–386, doi:10.1002/qj.49709942014, 1973.

Trenberth, K. E., Jones, P. D., Ambenje, P., Bojariu, R., Easterling, D., Tank, A. K., Parker, D., Rahimzadeh, F., Renwick, J. A., Rusticucci, M., Soden, B., and Zhai, P.: Observations: Surface and Atmospheric Climate Change, in: Climate Change 2007: The Physical Science Basis. Contribution of Working Group I to the Fourth Assessment Report of the Intergovernmental Panel on Climate Change, edited by Solomon, S., Qin, D., Manning, M., Chen, Z., Marquis, M., Averyt, K. B., Tignor, M., and Miller, H. L., Cambridge University Press, Cambridge, United Kingdom and New York, NY, USA, 2007.

Vardavas, I.: Modelling the seasonal variation of net all-wave radiation flux and evaporation in a tropical wet-dry region, Ecological Modelling, 39, 247–268, 1987b.

Vardavas, I. and Carver, J.: Solar and terrestrial parameterizations for radiative-convective models, Planetary and Space Science, 32, 1307–1325, 1984.

Appendices

Appendix A

Validation of MERIS/AATSR Synergy Algorithm AOT

[1] A new synergy algorithm has been recently developed, to retrieve AOT in high spatial resolution (1 km × 1 km), which may improve the study of aerosols at local scale (North et al., 2009). The algorithm combines spectral and angular information provided by the MERIS and the AATSR sensors, respectively, offering improved characterization of aerosol properties. Here, the MERIS/AATSR synergy algorithm AOT is validated by comparing the retrieved AOT with the respective AOT values observed at AERONET stations globally, considering different land cover types. Spatial patterns and differences between the MERIS/AATSR and the MODIS derived AOT are also investigated. Results indicate that the MERIS/AATSR synergy algorithm substantially improves the spatial resolution of the derived AOT and it is capable of retrieving AOT for most land cover types, with a good correlation relative to AERONET station measurements (R^2 ranges between 0.60 and 0.90, depending on the land cover type).

A.1 The MERIS/AATSR synergy algorithm for aerosol retrieval

MERIS and AATSR instruments were launched on board the Envisat satellite on March 1st 2002. MERIS is a medium resolution imaging spectrometer, operating in the solar reflective spectral range and possessing 15 spectral

---

[1] The results presented in Appendices A and B were based on research conducted in collaboration with Dr. Nektarios Chrysoulakis at the Regional Analysis Division of the Institute of Applied and Computational Mathematics, Foundation for Research and Technology–Hellas.

bands between 390 nm and 1040 nm. Three of these bands are dedicated to the retrieval of aerosol properties. The instrument's field of view around nadir covers a swath width of 1150 km across–track. The Earth is imaged with a spatial resolution of 300 m × 300 m (Full Resolution data), while Reduced Resolution data pixel size covers an area of 1.2 km × 1.2 km (ESA, 2011). Only Fine Resolution data are used in this study.

AATSR is a scanning radiometer with seven spectral bands in the visible, reflective infrared and thermal infrared regions. Special features of the AATSR include its use of a conical scan to give a dual view of the Earth's surface, thus improving the capacity for atmospheric correction. The AATSR swath covers approximately half of the MERIS swath (~ 500 km), with pixel sizes of 1 km × 1 km at the center of the nadir swath and 1.5 km × 1.5 km at the center of the forward swath. For the AATSR Level 1 products, forward pixels are resampled to 1.5 km^2 resolution, in order to be the same size as the nadir pixels (ESA, 2007).

The MERIS/AATSR synergistic algorithm for retrieval of aerosol properties has been described in detail by North et al. (2009). It consists of three major procedures: in the first, the MERIS and AATSR data collocation is performed, and a combined MERIS/AATSR Level 1b product is created, containing all the data that will be used as input to the algorithm. These data are resampled into the AATSR nadir view spatial resolution (1 km × 1 km) and cover the area where both data sets are available. The center of this area's swath coincides with the centers of the MERIS and AATSR swaths, while the width is equal to the AATSR swath width (~ 500 km)). The second step of the algorithm consists of a cloud screening procedure applied to the collocated product, while in the third the atmospheric correction and aerosol retrieval are performed. Specifically, a physical model of spectral change with view angle was developed to separate the angular effects of the surface into two components, a structural parameter that is dependent only on the viewing and illumination geometry and a spectral parameter that is dependent only on the wavelength. The angular reflectance of a wide variety of natural land surfaces fits this model, whereas reflectance that is a mixture of atmospheric and surface scattering does not fit it. As a result, the model can be used to estimate the degree of atmospheric contamination for a particular set of reflectance measurements and to find the atmospheric parameters which allow retrieval of a realistic surface reflectance. An iterative optimization procedure has been adopted based on the minimization of an error metric which is a function of both the MERIS derived spectral information and the AATSR derived angular information. Since the optimal AOT for a specific wavelength and aerosol model are defined, the respective Angstrom exponent (α) can be extracted. A two–stage optimization process is employed by the algorithm: 1) given a set of 21 satellite TOA radiances (from the 4 solar reflective AATSR bands – nadir and forward – and the 13 MERIS non–absorbing bands) and an initial guess of the atmospheric profile (which includes AOT at 550 nm and aerosol model), a corresponding set of surface reflectances is estimated; 2) testing of this set against a constraint results in an error metric, a minimum value of which corresponds to a realistic set of surface reflectances (and hence atmospheric profile). The procedure is repeated using a refined atmospheric profile, until convergence to an optimal solution is achieved. For the surface reflectance retrieval, an approximation of a RTM based on LUTs is used. The output of the algorithm includes AOT at 550 nm, α, aerosol model used and error estimates of AOT and α. The algorithm is capable of retrieving AOT over land and ocean, in spatial resolution reaching 1 km × 1 km.

A.2 Data and methodology

AOT data from AERONET stations around the globe were used, in order to examine the synergy algorithm performance under different surface conditions and aerosol sources. Global MERIS and AATSR data, provided by the European Space Agency, were also used. The study period covers two months (August–September 2011) and the global coverage of both satellite and station data ensure the acquisition of a data set suitable for the validation of the synergy algorithm AOT and the study of its spatial characteristics. MODIS Level 2 Collection 051 AOT data were also validated against the same stations and for the same period, allowing the comparison of the performance between the two algorithms. Finally, MODIS Level 2 AOT images were used, to compare the aerosol spatial patterns derived by the algorithm with a similar product that has been tested and validated in the past and is known to perform well (e.g. Levy et al., 2010; He et al., 2010; Misra et al., 2008). The MERIS/AATSR synergy algorithm was implemented by using the BEAM platform (Brockmann-Consult, 2011).

The MERIS/AATSR synergy algorithm is capable of retrieving aerosol properties in various spatial resolutions. Outputs with three different spatial resolutions were tested in the present study: 1 km × 1 km, 1.5 km × 1.5 km and 2 km × 2 km. For the validation of AOT against AERONET observations, the following procedure was followed: a) in each algorithm derived AOT map, the pixels corresponding to AERONET stations (validation points) were identified; b) a N × N pixels subset of the AOT map, centered on each validation point, was extracted; c) the mean AOT and standard deviation were computed, representing the average value of AOT and its local spatial variability, respectively; d) three subset sizes were tested (N = 1, N = 3 and N = 5); e) all possible combinations of the subset sizes with the above AOT spatial resolutions were performed and the test areas ranged between 1 km × 1 km and 10 km × 10 km; f) four AERONET-satellite observation time difference intervals were considered: simultaneous AOT observations and interpolated AERONET AOT observations from the time intervals of 20, 30 and 60 minutes centered on the satellite overpass time.

In each comparison, the AOT at 550 nm retrieved by the algorithm was compared to the AERONET AOT measured at the same wavelength. For several AERONET stations where measurements at this wavelength were not available, AOT was estimated by interpolation from measurements at 500 and 675 nm.

To minimize the effect of outliers in each data set, a robust regression analysis with bisquare weights was used, instead of the ordinary least square method (Maronna et al., 2006): the bisquare weights line fitting technique is a method which minimizes a weighted sum of squares, where the weight given to each data point depends on how far the point is from the fitted line. Points near the line get full weight, while points farther from the line acquire reduced weight. Thus the effect of outliers in the data set is minimized, compared to the ordinary least square fitting technique. In addition, only points lying between two standard deviations from the mean difference were considered, accounting for roughly 95% of each data set.

Table A.1: Land cover types considered and percentage of AERONET stations in each land cover type.

Land Cover Type	AERONET stations (%)
Croplands	13
Broadleaved	5
Needleleaved	10
Mixed vegetation	10
Shrubland/Grassland/Sparse	16
Urban areas	34
Bare areas	5
Water bodies	7

To examine if the algorithm's performance depends on the surface characteristics, the AERONET stations were classified into 8 classes, according to the land cover types of the respective areas. This categorization was based on the MERIS derived GLOBCOVER product (2009), which provides global land cover information at 300 m × 300 m spatial resolution (Bicheron et al., 2008). The 22 land cover types of GLOBCOVER were reclassified into 8 (Table A.1). A total of 123 AERONET stations were used and at least 5% of them corresponded to each land cover type (Table A.1).

The validation of MODIS derived AOT was performed using the above procedure, AERONET stations and time period, allowing the direct comparison of the performance of two aerosol retrieval algorithms. In the case of MODIS Level 2 AOT, the spatial resolution is 10 km × 10 km. The subset sizes tested (N = 1, N = 3 and N = 5) correspond to areas of 10 km × 10 km, 30 km × 30 km and 50 km × 50 km, respectively.

A.3 Results

A.3.1 Validation of the MERIS/AATSR AOT against measurements from AERONET stations

All tests showed that the algorithm's performance was relatively poor over mixed vegetation areas and water bodies. The overall performance of the algorithm, disregarding these two land cover types, indicated that the best correlation between the algorithm and the AERONET stations was achieved comparing the 1.5 km × 1.5 km pixel size with the simultaneous station values, with a correlation coefficient R = 0.79. The slope of the regression fit (0.72) reveals an AOT overestimation, compared to the station measurements, as shown in Figure A.1. This overestimation is enhanced by a group of points lying in the area where AERONET AOT is less than 0.1, while the synergy algorithm AOT is greater than 0.2. These points were found to correspond only to urban and sparse vegetation land cover types. A possible explanation of this overestimation is that, as these two land cover types enhance multiple scattering effects in the atmosphere, there is an increase in the atmospheric scattering signal estimated by the decoupling process of the algorithm, causing an overestimation in the corresponding AOT. The dashed and dotted lines in Figure A.1 represent the 1–1 line and the expected error lines of MODIS AOT ($\pm 0.05 \pm 0.15 \times \text{AOT}$, Levy et al., 2010), respectively. This error envelope appears to represent the synergy AOT results very well. While the algorithm performance using this pixel size remained almost invariant under different AERONET time intervals, the correlation coefficient using 6 km × 6 km spatial resolution (3 × 3 pixels of 2 km × 2 km size) was improved as the time interval is increased. Starting from a value of 0.71 when compared against instantaneous AERONET values, R reached 0.78 against the 1–hour mean AERONET value. This fact reveals that the mean AERONET

AOT calculated based on wider time windows was more representative of extended areas, as it was expected due to the motion of air masses.

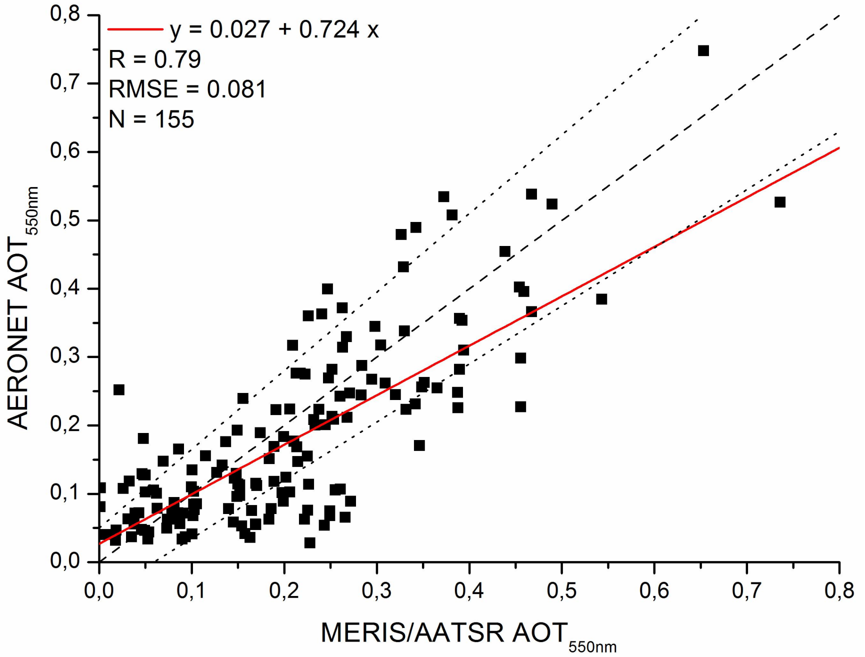

Figure A.1: Scatter plot of AOT (550 nm) from MERIS/AATSR synergy algorithm against corresponding AERONET station simultaneous values for all land cover types. The red line is the linear regression fit, with the equation, correlation coefficient, RMSE and number of points used shown at the upper left corner. The dashed and dotted lines are the 1–1 line and the MODIS AOT expected error lines, respectively.

Figure A.2 shows the scatter plots of the MERIS/AATSR synergy algorithm derived AOT against the simultaneous AERONET AOT values, with spatial resolutions that best fit station measurement data, for the six land cover types examined. This spatial resolution corresponds to a 1.5 km × 1.5 km pixel size for croplands (Figure A.2a) and needleleaved vegetation (Figure A.2c); 1 km × 1 km for broadleaved vegetation (Figure A.2b); 6 km × 6 km for sparse vegetation (Figure A.2d) and urban areas (Figure A.2e); and 10 km × 10 km for bare areas (Figure A.2f). The corresponding slopes, correlation coefficients, RMSEs and number of points used are also given. It is worth noting that in all cases, the MODIS AOT expected error (dotted lines) represents very well the synergy AOT results.

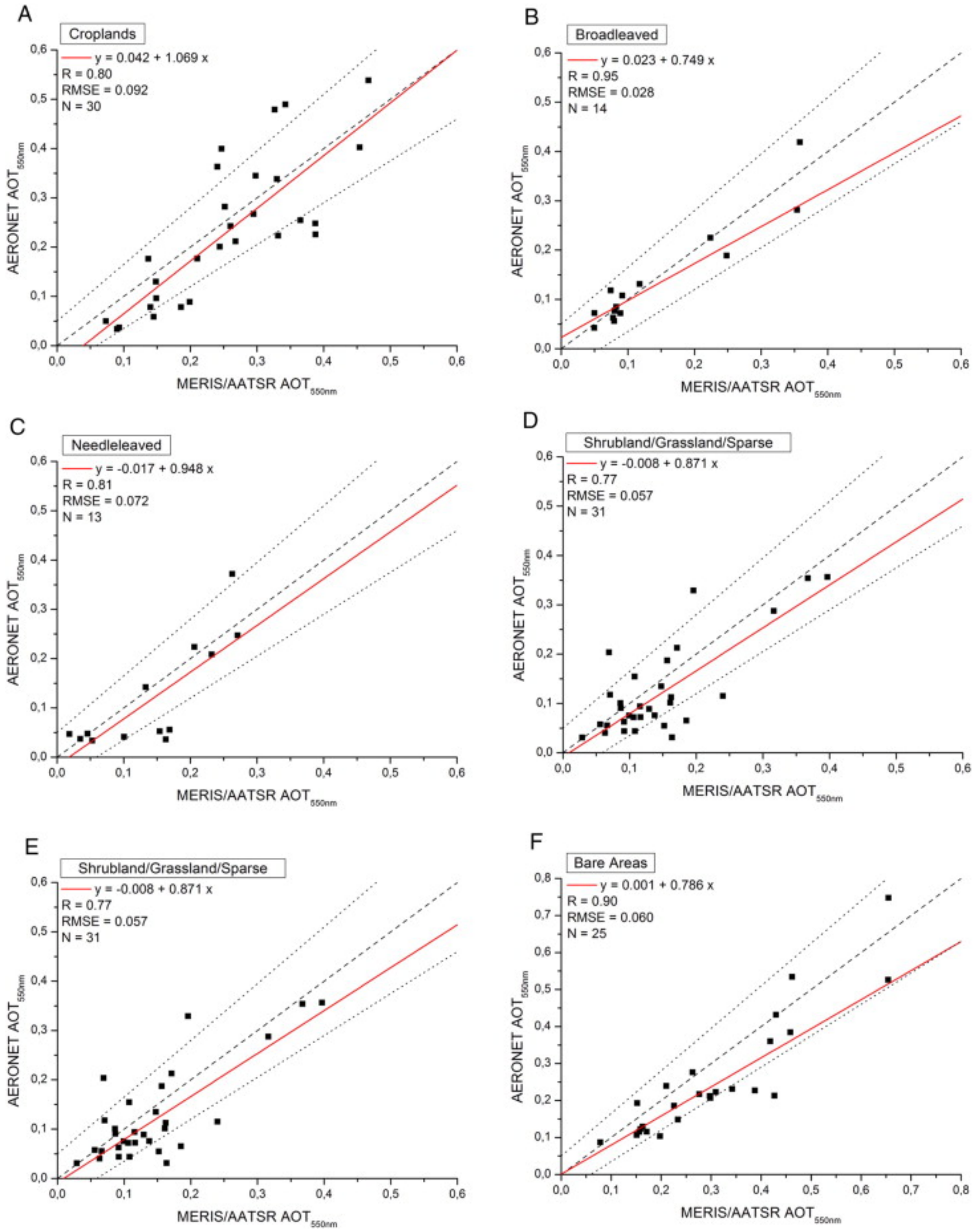

Figure A.2: Scatter plots of AOT (550 nm) from MERIS/AATSR synergy algorithm against simultaneous AERONET observations for croplands (a); broadleaved vegetation (b); needleleaved vegetation (c); sparse vegetation (d); urban areas (e); and bare areas (f). The red lines are the linear regression fits, with the equations, correlation coefficients, RMSEs and number of points used in each case shown at the upper left corners. The dashed and dotted lines are the 1–1 line and the MODIS AOT expected error lines, respectively.

In the case of croplands, the correlation coefficient and the RMSE obtained their maximum and minimum values, respectively, using the 1.5 km × 1.5 km pixel size, in all four time intervals tested. Comparing the maps of 1.5 km × 1.5 km pixels with the simultaneous AERONET values, the correlation coefficient was found at 0.8, with an RMSE equal to 0.09, while the slope of the fit (1.07) indicated a slight underestimation of the algorithm AOT compared to the corresponding AERONET values (Figure A.2a). Mean AOT values of a 5 × 5 pixel area (7.5 km × 7.5 km) also performed well, when compared to mean AERONET AOT values from 30 minutes time interval (R = 0.74, RMSE = 0.09, slope = 0.99).

In broadleaved vegetation areas, the best algorithm performance was achieved using the highest possible spatial resolution (one pixel of 1 km × 1 km), in all time intervals tested. The correlation was higher compared to the respective for croplands, with a value of 0.95, while the RMSE was reduced to 0.03 for all time intervals. The slope of the regression fit, which ranged between 0.75 and 0.78, showed a tendency of AOT overestimation (Figure A.2b). As in the case of croplands, wider areas (10 km × 10 km), with mean AOT values from 5 × 5 pixels of 2 km × 2 km size, performed good for 30–minutes and 1–hour mean AERONET AOT (R = 0.94, RMSE = 0.04, slope = 0.82 for both cases).

In needleleaved regions, the 1.5 km × 1.5 km pixel size performed better than all other spatial resolutions, and was almost invariant under all time intervals. While the correlation coefficient and RMSE were similar to those found in croplands (0.8 and 0.07, respectively), the slope (0.95) indicated no systematic tendency in the AOT retrieval over these areas (Figure A.2c).

The group of shrubland, grassland and sparse vegetation, along with the one regarding urban environments, showed a different behavior compared to the previously examined land cover types. In both cases, the best algorithm performance was achieved using a 3 × 3 pixels mean AOT of 2 km × 2 km size, corresponding to a 6 km × 6 km area, independently of time intervals. In the case of sparse vegetation (Figure A.2d), the correlation was fair, with a coefficient ranging between 0.70 and 0.77, a constant RMSE equal to 0.06 and a slope in the range of 0.80–0.87. In urban areas (Figure A.2e), although the RMSE was the same and the correlation was better (R = 0.78), slopes ranging between 0.72 and 0.76, indicating a systematic tendency of AOT overestimation.

For bare areas (practically deserts in the present study) the lowest RMSE (0.06) and best correlation coefficients (over 0.90) were found in 5 × 5 pixels mean AOT with 1 km × 1 km pixel size (equal to 5 km × 5 km area), with slopes of the regression fits ranging between 0.75 and 0.81 (Figure A.2f). The slopes were improved when mean AOT from 10 km × 10 km areas were considered, reaching values of 0.87 to 0.89. In these cases, the correlation coefficients remained almost unchanged (0.88), while the RMSEs slightly increased to 0.08.

A.3.2 Validation of MODIS Level 2 AOT against measurements from AERONET and comparison with the MERIS/ AATSR derived AOT

In order to compare between the two aerosol products, since the spatial resolution of the MODIS Level 2 AOT is 10 km × 10 km, the MERIS/AATSR product of the resolution of 10 km × 10 km (by averaging AOT in a 5 × 5 pixel area with pixel size 2 km × 2 km) was used. Furthermore, the performance of different MODIS AOT product spatial scales (30 km × 30 km and 50 km × 50 km) against AERONET observations was also examined. Disregarding land cover types, the overall performance of the two products was similar and both found to overestimate AOT, especially for large values, as can be seen from Figure A.3.The correlation coefficient was also fair for both data sets (0.75 for MODIS and 0.76 for MERIS/AATSR).

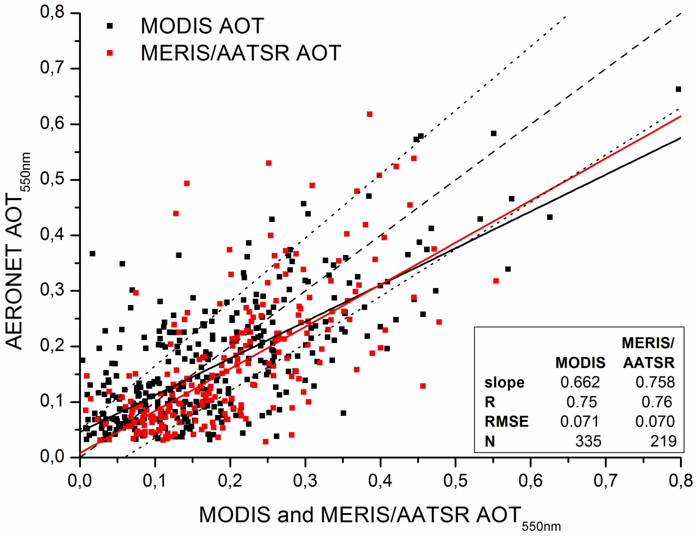

	MODIS	MERIS/ AATSR
slope	0.662	0.758
R	0.75	0.76
RMSE	0.071	0.070
N	335	219

Figure A.3: Scatter plots of AOT (550 nm) derived from MERIS/AATSR synergy algorithm and from MODIS Level 2 Aerosol Product versus simultaneous AERONET observations for all land cover types. The solid lines represent the linear regression fits, while the dashed and dotted lines are the 1–1 line and the MODIS AOT expected error lines, respectively.

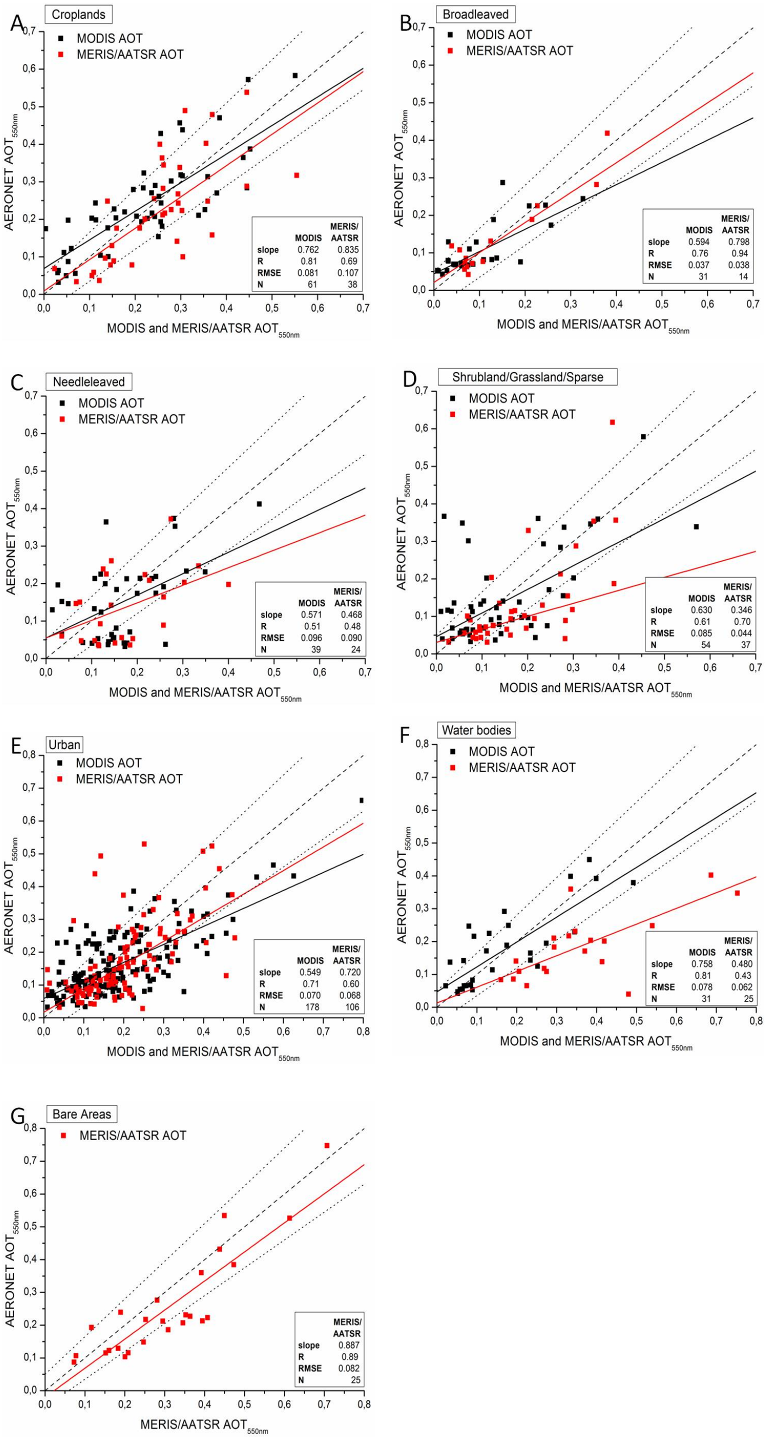

Figure A.4: As in Figure A.3, separately for each land cover type.

In croplands, the MERIS/AATSR product performed better for low AOT values as shown in Figure A.4a. In broadleaved vegetation, the MERIS/AATSR product performed much better than the MODIS product, in terms of slope and correlation coefficient (Figure A.4b). The performance of both products was relatively poor in the cases of needleleaved and sparse vegetation (Figures A.4c and A.4d), while in urban areas both performed fair (Figure A.4e). Important differences resulted over water bodies, where the performance of the MERIS/AATSR product was poor (Figure A.4f). In bare areas the MERIS/AATSR product performed well (Figure A.4g). MODIS Level 2 Collection 051 AOT product was used in this study, therefore the MODIS product over bare areas is not shown in Figure A.4g, because this product is provided by the Deep Blue Algorithm (Hsu et al., 2004, 2006).

The MODIS product performed better when a subset of N × N pixels of size 10 km × 10 km is compared against a mean AERONET AOT value of a time interval t, where N = 5 and t = 1 hour, as was also indicated by Ichoku et al. (2002). The present study confirmed this behavior of the MODIS aerosol product: using this spatial scale and time interval, the correlation coefficient was increased in most cases (croplands, broadleaved vegetation, urban areas and water bodies), the RMSE remained almost invariant and the slope was also increased, reducing the tendency for AOT overestimation.

A.3.3 Intercomparison of the spatial characteristics of the MERIS/AATSR synergy and the MODIS Level 2 AOT products

Two study areas were selected to compare the spatial characteristics of the AOT derived by MERIS/AATSR synergy algorithm and by MODIS Level 2 aerosol product. The selection criteria were: the high variability of land cover types; the sufficient spatial coverage from both products; and the minimum observation time differences. According to these criteria, the broader area of Cairo, Egypt, and a part of South Italy were selected. The land cover in both areas was extracted from GLOBCOVER as it was described in Section A.2 (Figures A.5a and A.6a). South Italy is dominated primarily by croplands and urban areas, as shown in Figure A.5a, while regions of mixed and sparse vegetation are also present. In Figure A.6a, the city of Cairo is depicted in orange, while two different land types dominate the area: croplands in the Nile delta region and bare areas (desert) elsewhere.

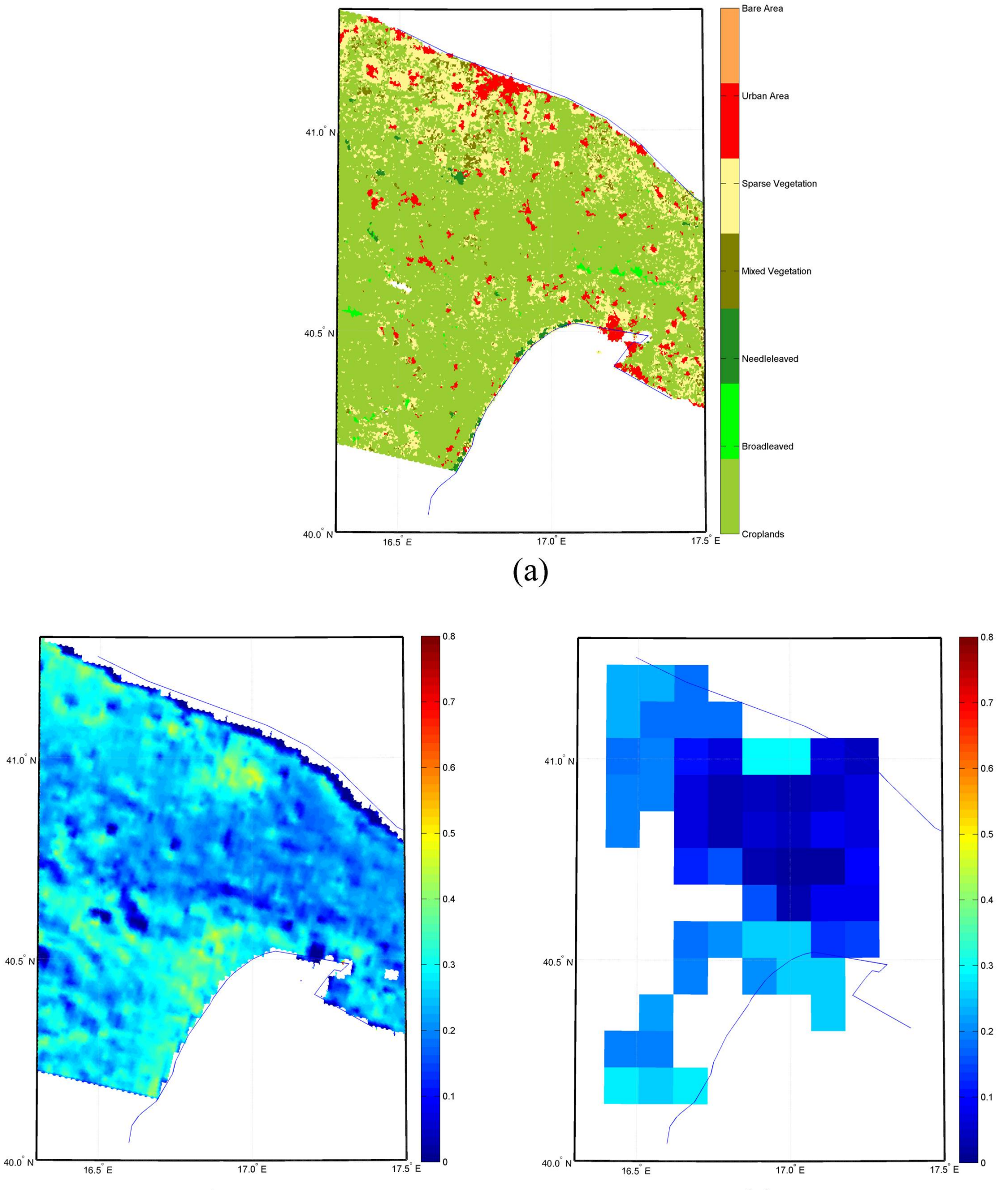

(a)

(b) (c)

Figure A.5: Land cover of the area in Southern Italy (a); spatial distribution of AOT (550 nm) for the same area, using MERIS/AATSR synergy algorithm (b); and MODIS Level 2 Aerosol Product data (c).

Figures A.5b and A.5c show the spatial distribution of the AOT at 550 nm in South Italy, derived from the MERIS/AATSR and MODIS, respectively. In the case of the MERIS/AATSR synergy AOT, a smoothing filter (3×3

pixel average) was applied to the data, while the initial spatial resolution is 1.5 km × 1.5 km. The MODIS AOT spatial resolution (Figure A.5c) is 10 km × 10 km. The two images were acquired with 2 minutes time difference (August 23, 2011, 09:18 UTC for MERIS/AATSR and 09:20 UTC for MODIS). Comparing the two maps, the differences in AOT spatial patterns are obvious: details in the first case (MERIS/AATSR) are more evident, while the spatial distribution of AOT suggests a possible connection with land cover types (Figure A.5a): higher AOT values are observed over urban areas (north coastline) and croplands (south coastline). Back–trajectory calculations, conducted using the HYSPLIT modeling system (Draxler and Hess, 1998), verify that airborne particles in the area should be attributed to local sources (Figure A.7a). Air masses transported from the Balkans in high altitude (3000 m) are not expected to transfer high aerosol loads. The low AOT values across the entire north coastline should probably be attributed to water contamination effects, where the algorithm was shown to have poor performance. In the case of MODIS (Figure A.5c), while the spatial variability is presented, the covered area is lower due to algorithm limitations, and the observed high AOT values cannot be directly assigned to local sources.

For Cairo, the two images (Figures A.6b and A.6c) were acquired with 23 minutes time difference (August 22, 2011, 08:17 UTC for MERIS/AATSR and 08:40 UTC for MODIS). In the case of MERIS/AATSR AOT (Figure A.6b), areas with high AOT values are located south of Cairo and over specific regions in the Nile delta. Back–trajectory analysis showed no specific transfer patterns (Figure A.7b): high aerosol loads were probably resulted by the city air pollution and the intense agricultural activities in the Nile delta area, while desert dust contribution in the total AOT should not be excluded. Regions with high AOT values are also found in the desert and were probably naturally generated (dust). Using the MODIS 10 km × 10 km AOT (Figure A.6c), the high aerosol load over the city of Cairo is also obvious, but lower values are observed in this case, due to the spatial averaging of the MODIS received radiance at the level of 10 km × 10 km. Similar behavior is observed in the area of Nile delta.

Both cases examined above show that using the higher resolution MERIS/ AATSR algorithm, more details on the spatial distribution and characteristics of AOT become evident. Specifically, high aerosol loads are better correlated with their possible sources (e.g. urban areas and cropland activities).

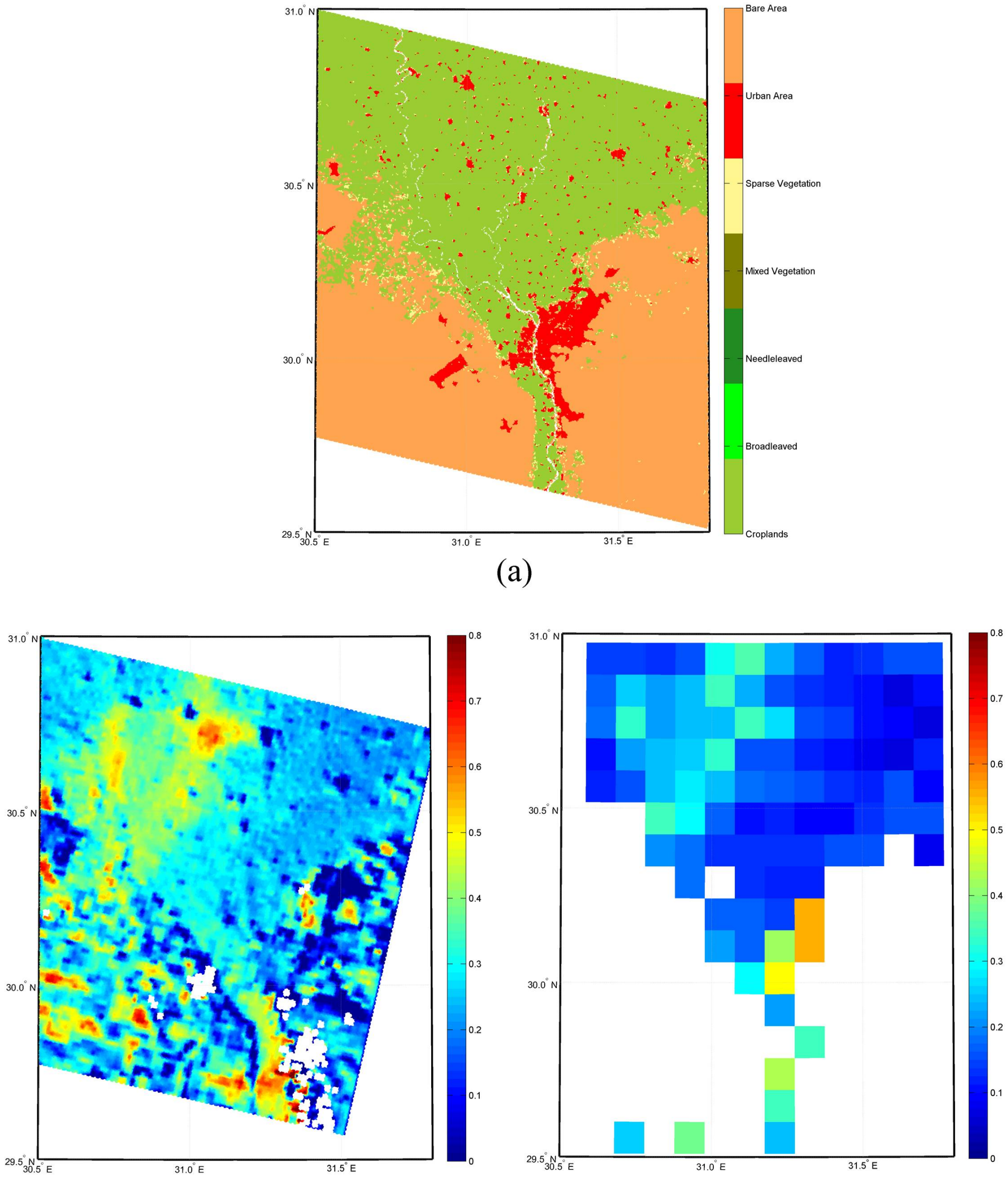

(a)

(b)

(c)

Figure A.6: Land cover of the wider Cairo and Nile delta area (a); spatial distribution of AOT (550 nm) for the same area, using MERIS/AATSR synergy algorithm (b); and MODIS Level 2 Aerosol Product data (c).

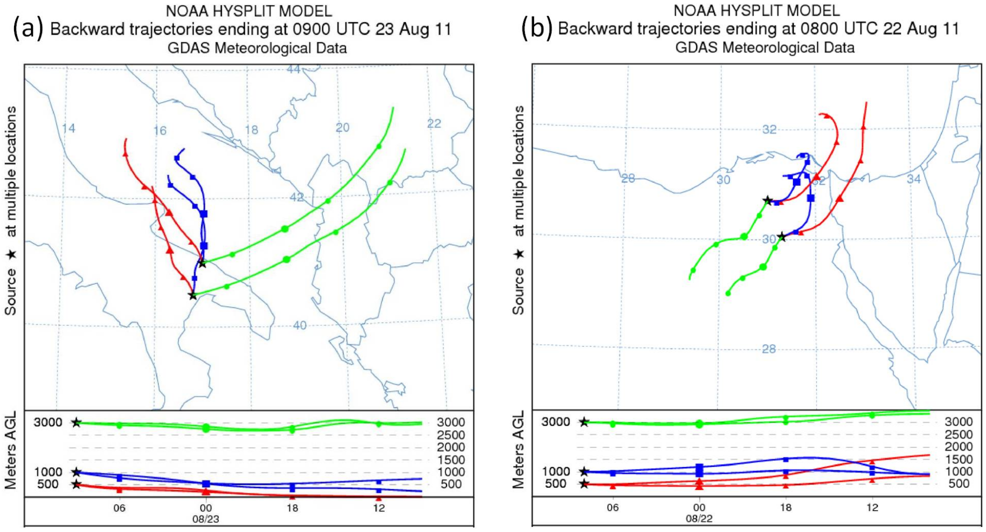

Figure A.7: Back–trajectory analysis from the HYSPLIT model, at 24 hour intervals, for air parcels terminating in South Italy (a) and Cairo and Nile delta (b) regions.

A.4 Summary and conclusions

The MERIS/AATSR synergy algorithm for AOT retrieval was validated against AERONET observations worldwide and compared against MODIS Level 2 AOT data. AERONET observations over eight different land cover types were used and the validation procedure was performed for each specific land cover type, as well as for the whole dataset.

The MERIS/AATSR synergy algorithm was capable of retrieving AOT in spatial resolutions reaching 1 km × 1 km. The comparison with AERONET observations revealed good performance of the algorithm in most of the land cover types. The best performance was achieved using 1.5 km × 1.5 km resolution. Relatively poor performance was found in mixed vegetation areas and water bodies, while the best correlations were achieved in broadleaved and bare areas. The comparison with MODIS Level 2 AOT values (10 km×10 km) indicated that the MERIS/AATSR product was more accurate than MODIS product in croplands, broadleaved and urban areas.

The intercomparison of the two AOT products revealed the advantages of the higher spatial resolution offered by the MERIS/AATSR synergy algorithm, and the possible correlations of AOT with local surface sources. This finding is important, since the synergy algorithm can be extended to the SLST (Sea and Land Surface Temperature Radiometer) and OLCI (Ocean and Land Color Instrument) sensors, on board the Global Monitoring for Environment and Security (GMES) forthcoming Sentinel–3 satellite mission (Berger et al., 2012).

It is therefore expected that the AOT derived by the synergy algorithm can be used in local scale studies, especially in urban areas, where the air quality mapping is of great importance for urban planning and public health. In this framework, the synergy algorithm may offer new possibilities in the ongoing effort to derive $PM_{2.5}$ concentrations in urban areas, using the satellite derived AOT.

Bibliography

Berger, M., Moreno, J., Johannessen, J. A., Levelt, P. F., and Hanssen, R. F.: ESA's sentinel missions in support of Earth system science, Remote Sensing of Environment, 120, 84–90, doi:10.1016/j.rse.2011.07.023, 2012.

Bicheron, P., Defourny, P., Brockmann, C., Schouten, L., Vancutsem, C., Huc, M., Bontemps, S., Leroy, M., Achard, F., Herold, M., Ranera, F., and Arino, O.: GLOBCOVER: Products Description and Validation Report, Toulouse: MEDIAS-France, 2008.

Brockmann-Consult: The Earth Observation Toolbox and Development Platform BEAM, 2011.

Draxler, R. R. and Hess, G. D.: An overview of the HYSPLIT 4 modelling system for trajectories, dispersion and deposition, Australian Meteorological Magazine, 47, 295–308, 1998.

ESA: AATSR Product Handbook, Issue 2.2, European Space Agency, 2007.

ESA: MERIS Product Handbook, Issue 3.0, European Space Agency, 2011.

He, Q. S., Li, C. C., Tang, X., Li, H. L., Geng, F. H., and Wu, Y. L.: Validation of MODIS derived aerosol optical depth over the Yangtze River Delta in China, Remote Sensing of Environment, 114, 1649–1661, 2010.

Hsu, N., Tsay, S.-C., King, M., and Herman, J.: Aerosol properties over bright–reflecting source regions, IEEE Transactions on Geoscience and Remote Sensing, 42, 557–569, doi:10.1109/TGRS.2004.824067, 2004.

Hsu, N., Tsay, S.-C., King, M., and Herman, J.: Deep Blue Retrievals of Asian Aerosol Properties During ACE–Asia, IEEE Transactions on Geoscience and Remote Sensing, 44, 3180–3195, doi:10.1109/TGRS.2006.879540, 2006.

Ichoku, C., Chu, D. A., Mattoo, S., Kaufman, Y. J., Remer, L. A., Tanré, D., Slutsker, I., and Holben, B. N.: A spatio-temporal approach for global validation and analysis of MODIS aerosol products, Geophysical Research Letters, 29, 8006, doi:10.1029/2001GL013206, 2002.

Levy, R. C., Remer, L. A., Kleidman, R. G., Mattoo, S., Ichoku, C., Kahn, R., and Eck, T. F.: Global evaluation of the Collection 5 MODIS dark–target aerosol products over land, Atmospheric Chemistry and Physics, 10, 10 399–10 420, doi:10.5194/acp-10-10399-2010, 2010.

Maronna, R., Douglas Martin, R., and Yohai, V.: Robust Statistics: Theory and Methods, Wiley Series in Probability and Statistics, 2006.

Misra, A., Jayaraman, A., and Ganguly, D.: Validation of MODIS derived aerosol optical depth over Western India, Journal of Geophysical Research: Atmospheres, 113, doi:10.1029/2007JD009075, 2008.

North, P., Grey, W., Heckel, A., Fischer, J., Preusker, R., and Brockmann, C.: MERIS/AATSR Synergy Algorithms for Cloud Screening, Aerosol Retrieval, and Atmospheric Correction. Algorithm Theoretical Basis Document Land Aerosol and Surface Reflectance ATBD. ESRIN Contract No. 21090/07/I–LG., 2009.

Appendix B

Estimation of Urban PM10 Concentration, based on MODIS and MERIS/AATSR Data

Airborne PM of both fine (PM2.5) and coarse (PM10) particles is used as an air quality indicator in urban areas. Examining the effects of PM on human health, numerous studies have found associations of PM with increased morbidity and mortality. High PM loads in urban areas, produced by local sources (e.g. transportation and industry), have been correlated with increased respiratory problems (e.g. Gent et al., 2009; Kappos et al., 2004; Pope et al., 2002; Atkinson et al., 2001), cardiovascular diseases (e.g. Franklin et al., 2006; Dominici et al., 2006) and decreased birth weights and lengths (e.g. Ballester et al., 2010; Bell et al., 2007).

PM monitoring is based primarily on ground measurements. Although station networks exist in large cities, point measurements do not provide information on spatial characteristics and distributions of PM over urban areas of interest. Temporal coverage of in situ PM measurements is also highly variable, depending on instrument operation period and functionality. These reasons have led to an ongoing effort for PM estimation using satellite remote sensing techniques.

The AOT is the satellite derived parameter most commonly used as the basis for PM estimation (e.g. Themistocleous et al., 2012). Several methods have been used to correlate the remotely sensed AOT with the surface measured PM. These include linear relations (e.g. Yap and Hashim, 2013; Retalis and Sifakis, 2010; Schaap et al., 2009; Kumar et al., 2007), statistical and chemical transport models (e.g. Kloog et al., 2012, 2011; Lee et al., 2012, 2011; van Donkelaar et al., 2011; van Donkelaar et al., 2006; van de Kassteele et al., 2006), multiple regression analysis (Gupta and Christopher, 2009a) and neural networks (Gupta and Christopher, 2009b). The major issue preventing a robust correlation between AOT and PM is that, while AOT refers to aerosols distributed over the entire atmospheric column, PM measurements regard suspending particles near the Earth's surface. Several studies have found that when information on the vertical profile of aerosols was included (available from either lidar measurements, or from boundary layer height estimations), the correlation between PM and AOT was significantly improved (e.g. van Donkelaar et al., 2011; Rohen et al., 2011; Schaap et al., 2009; Engel-Cox et al., 2006). Improvements have been also reported based on the inclusion of meteorological parameters that affect aerosol properties, including surface temperature (e.g. Gupta and Christopher, 2009a) and relative humidity (e.g. Koelemeijer et al., 2006).

Here, a multiple regression analysis technique is employed, for the estimation of PM10 over the broader urban area of Athens, Greece, based on satellite derived AOT and other related parameters, such as surface temperature, relative humidity and K–Index. The K–Index (George, 1960), an atmospheric static stability estimator, is used as a dichotomous estimator of the corresponding aerosol vertical mixing height. All parameters are available from MODIS sensors on board NASA's Terra and Aqua satellites, on a daily basis and at 5 km × 5 km spatial resolution (MODIS Level 2 Atmosphere Products, Section 2.2), spanning the period from March 2000 and July 2002 for Terra and Aqua MODIS, respectively. AOT is also available from MODIS Level 2 products at 10 km × 10 km spatial resolution (Section 2.2.1). For the implementation of the multiple regression analysis, in situ measurements of PM10 are used, available from a network of ground stations over the area of Athens, on a mean daily basis during 2007–2010. The same technique is tested for combined MERIS and AATSR observations, more specifically for AOT derived by the MERIS/AATSR synergy algorithm for aerosol retrieval (North et al., 2009 and Appendix A), at 1 km × 1 km spatial resolution and resampled at 5 km × 5 km spatial resolution to match with MODIS Level 2 parameters.

B.1 Data and methodology

The urban area of Athens is a region with considerable air pollution problems, as is characteristic of southern European cities, where air pollution effects are more severe, compared to northern European cities (Katsouyanni, 2012). The air pollution originates primarily from traffic and industry, while do-

Table B.1: Geographical coordinates of Athens PM10 monitoring stations.

Station	Latitude	Longitude
Aghia Paraskevi	37°59′42″	23°49′10″
Aristotelous	37°59′16″	23°43′39″
Goudi	37°59′04″	23°46′04″
Koropi	37°54′04″	23°52′44″
Lykovrissi	38°04′11″	23°46′35″
Maroussi	38°01′51″	23°47′14″
Pireas	37°56′36″	23°38′51″
Thrakomakedones	38°08′37″	23°45′29″
Zografou	37°58′11″	23°47′13″

mestic heating also becomes a major pollution factor during winter months. Athenians have recently turned to more traditional ways of residential heating, such as fireplaces, due to the high cost of diesel. For this reason, a significant increase of PM was observed in winter 2012 (Florou et al., 2013).

PM10 mass concentration (in µg m^{-3} is regularly monitored by the Greek Air Quality Monitoring Network of the Hellenic Ministry for the Environment, Physical Planning and Public Networks, which maintains several air quality monitoring stations in Greece. More information on this network can be found in Retalis and Sifakis (2010). In this study, the daily mean PM10 data from nine monitoring stations, located in the center of Athens and in suburban areas (Figure B.1), was used. The nine monitoring stations and their geographical coordinates are shown in Table B.1.

Satellite data used for the implementation of the multiple regression analysis include AOT, surface relative humidity (RH), surface temperature (STMP) and K–Index. There were several reasons why the parameters were included: surface temperature can enhance the photochemical reactions in the atmosphere and hence production of PM particles (Gupta and Christopher, 2009a), while relative humidity influences the hygroscopic growth of particles and consequently the estimated AOT relative to ground level PM, as the latter is measured at controlled RH (Paciorek et al., 2008; Liu et al., 2005). K–Index is a parameter generally used as a measure of the vertical temperature lapse rate and atmospheric static stability. The atmospheric static stability can be estimated using MODIS derived K–index spatial distributions (Chrysoulakis et al., 2003). Thus, the MODIS–derived K–Index is used in this study as an estimator of atmospheric static stability and therefore as a proxy to the corresponding aerosol vertical mixing height.

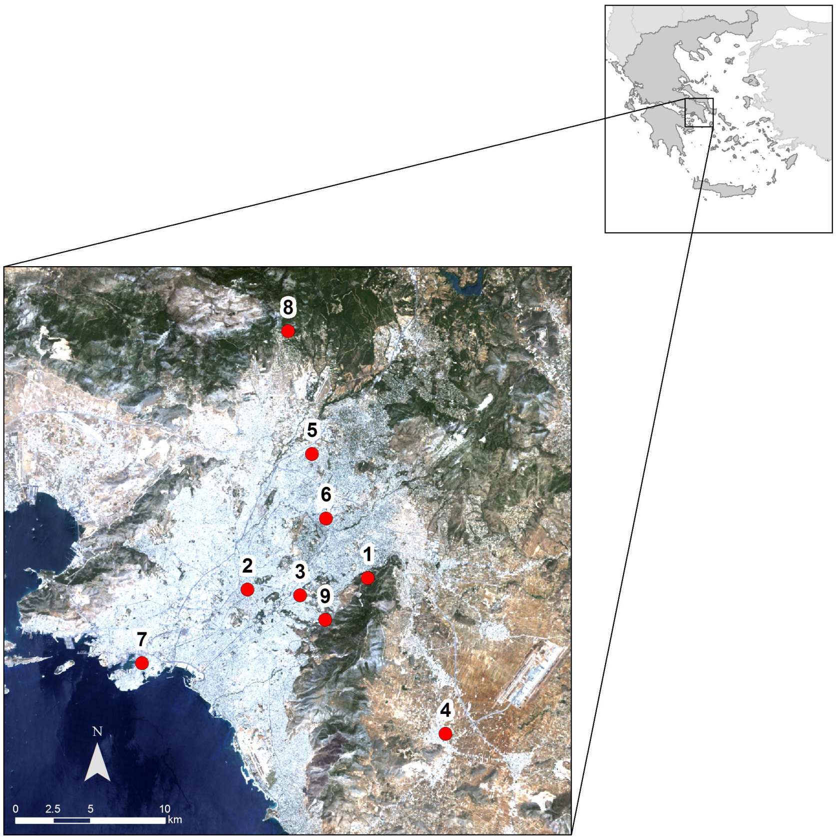

Figure B.1: The broader urban area of Athens and the geographical distribution of the Greek Air Quality Monitoring Network PM10 stations used (1: Aghia Paraskevi, 2: Aristotelous, 3: Goudi, 4: Koropi, 5: Lykovrissi, 6: Maroussi, 7: Pireas, 8: Thrakomakedones, 9: Zografou).

AOT is available from Terra and Aqua satellites MODIS Level 2 Aerosol Product on a daily basis and at spatial resolutions ranging between 10 km × 10 km (at nadir) and 20 km × 20 km (Section 2.2.1). The Terra and Aqua Athens overpass times range between 8:20–10:00 and 10:40–12:20 UTC, respectively. Mean values of Terra and Aqua MODIS AOT over the wider area of Athens, covering the 4–year period 2007–2010, were resampled to a regular 10 km × 10 km grid. MODIS Level 2 Product also includes the K–Index, and temperature and relative humidity profiles at 20 pressure levels, ranging from 1000 hPa to 5 hPa, and at 5 km × 5 km spatial resolution (Section 2.2.3). To estimate RH and STMP near the surface, surface pressure data was used, also available from MODIS and interpolated from the atmospheric profiles accordingly. RH, STMP and K–Index were resampled to a 5 km × 5 km grid, whereby four pixels correspond to one 10 km × 10 km AOT pixel. Furthermore, the MERIS/AATSR synergy algorithm for aerosol retrieval (North et al., 2009), implemented in BEAM software toolbox (Brockmann-Consult, 2011), was also used to derive AOT distributions for the same period at 1 km × 1 km spatial resolution (Appendix A). MERIS and AATSR data over Athens acquired simultaneously at a time interval ranging between 8:40–9:00 UTC. To match with the MODIS–derived STMP, RH and K–Index, mean values of the MERIS/AATSR synergy derived AOT were computed at 5 km × 5 km.

To implement the multiple regression analysis, a complete set of satellite data and corresponding surface PM10 measurements were required. The spatial resolution of satellite data was 10 km × 10 km (MODIS AOT) and 5 km × 5 km (rest parameters), whereas in situ PM10 measurements were point values, thereby making comparisons complicated. To analyse satellite–derived and in situ parameters on the same scale, the in–situ parameters were spatially interpolated over the whole study area, using the kriging method (Kitanidis, 1997). Regarding the PM10 data, available from all nine stations, kriging statistical indicators ensured the ability of the method to correctly simulate the spatial distribution of PM10 over the study area. Specifically, each kriging output PM10 spatial distribution was checked in order to satisfy the Q1 and Q2 statistical criteria, which correspond to the averages of the orthonormal residuals and the squared orthonormal residuals, respectively (Kitanidis, 1997): for days when Q1 and Q2 were not statistically significant in the 95% confidence interval of their probability density functions, the corresponding PM10 spatial distributions were rejected.

For the development of multiple regression equations, a subset of the final data set, comprising both PM10 (response variable) and satellite–derived parameters (predictor variables), was used, including only pixels coinciding with ground stations. Testing and validation of the statistical models were performed using the entire data set. The first approximation involved the development of a linear regression model for PM10:

$$\mathrm{PM10} = b_0 + b_1\mathrm{AOT} + b_2\mathrm{RH} + b_3\mathrm{STMP} + \epsilon, \qquad \text{(B.1)}$$

where PM10 is the mass concentration in $\mu\mathrm{g\ m^{-3}}$ (pixel value after the spatial interpolation), and AOT is estimated at 550 nm, separately from MODIS and MERIS/AATSR. The b_0–b_3 are regression coefficients for each predictor and ϵ is the error variable. Equation B.1 therefore assumes that PM10 mass concentration is a combination of the linear effects of AOT, RH and STMP. However, this linear parametric approach can be successful provided the assumed model is appropriate, since the linear functional forms are presumed a priori for the regression surface. When the relationship between the response and predictor variables is unknown or inexact, linear parametric regression can yield erroneous or even misleading results. Therefore, a non–parametric regression technique was used, which makes assumptions about the regression surface (Friedman and Stuetzle, 1981). As a result, the ACE algorithm, developed by Breiman and Friedman (1985), was used to estimate optimal transformations for both response and independent variables. The ACE regression model has the general form:

$$\theta(\mathrm{PM}) = \phi_1(\mathrm{AOT}) + \phi_2(\mathrm{RH}) + \phi_3(\mathrm{STMP}) + \epsilon \tag{B.2}$$

where θ is the function of the response variable and ϕ_1–ϕ_3 are functions of the predictors. Thus, this model replaces the problem of estimating the regression coefficients of the linear function by estimating the separate one–dimensional functions.

Last, the K–Index was used as a dichotomous predictor of atmospheric static stability, where, according to a K–Index threshold, the entire data set was divided in two separated cases of static stability and instability. Since threshold values of instability indices are not definite, but vary with geographical location, season and synoptic situation (Haklander and Van Delden, 2003), a range of K–Index values that could serve as thresholds for the case of Athens were tested, and the selection of the K–Index threshold was based on the maximization of the determination coefficient between the model–derived PM10 and the corresponding station measurements. Values of K–Index smaller than the defined threshold indicate higher atmospheric static stability, and hence aerosol trapping near the surface. Values of K–Index greater than this threshold imply atmospheric instability and therefore better aerosol mixing. The results were validated based on the above categorization based on K–Index.

B.2 Results and discussion

B.2.1 Multiple regression analysis using MODIS observations

Stepwise implementation of the linear multiple regression analysis using AOT, STMP, RH and K–Index from MODIS, resulted in the coefficient of determination (R^2) and the Root Mean Square Error (RMSE) values presented in Table B.2. R^2 values indicate that the AOT is the most important predictor of PM10, explaining more than 50% of the corresponding variance, while inclusion of RH contributes significantly to the improvement of both R^2 and

Table B.2: Determination coefficient (R^2) and RMSE results after stepwise implementation of MODIS–derived parameters.

MODIS	Linear Regression	
	R^2	RMSE (µg m^{-3})
AOT	0.53	10.2
AOT, RH	0.59	9.6
AOT, RH, STMP	0.61	9.4
	Non–Linear Regression	
AOT, RH, STMP	0.67	10.4
AOT, RH, STMP, K–index≥297 K	0.71	11.1

RMSE. However, inclusion of the STMP in the linear relationship results in minor improvements.

The linear relationship yielding the best correlation results is given by the corresponding equation shown in Table B.3. By applying the non–linear regression analysis, the correlation between predicted PM10 and in situ measurements is improved (R^2=0.67), while the RMSE is slightly increased. The non–linear relationships yielding the best correlation results are also shown in Table B.3. The improved correlation in this case indicates that PM10 is better estimated using non–linear relationships with the predictor variables. Since the input AOT over Athens has a mean value of 0.37 ± 0.21, ϕ_1(AOT) represents a small correction from the simple linear relationship. Figure 2a shows the contribution of ϕ_1(AOT) to the total PM10 concentration (black line), along with the histogram of AOT values found over Athens during the period examined. As shown in Figure B.2a, the contribution of AOT does not exceed the value of 30 µg m^{-3} in the majority of the cases.

In Figure B.2b, the shape of ϕ_2(RH) implies that for values of RH around 30%–35%, which correspond to the controlled conditions of RH during station measurements (Liu et al., 2005), the resulting PM10 remains almost unchanged when implementing ϕ_2(RH) in the computation. However, for larger and smaller RH values, the contribution of ϕ_2(RH) increases significantly. As Gupta et al. (2006) report, a change in RH from 50% to 80% causes a small increase in AOT values. However, there is no corresponding increase in in–situ PM10, since station measurements take place under controlled RH conditions. Thus, the resulting multiple regression algorithm corrects the higher AOT estimation due to the increased RH by decreasing the corresponding PM10 values. This behavior explains the contribution of

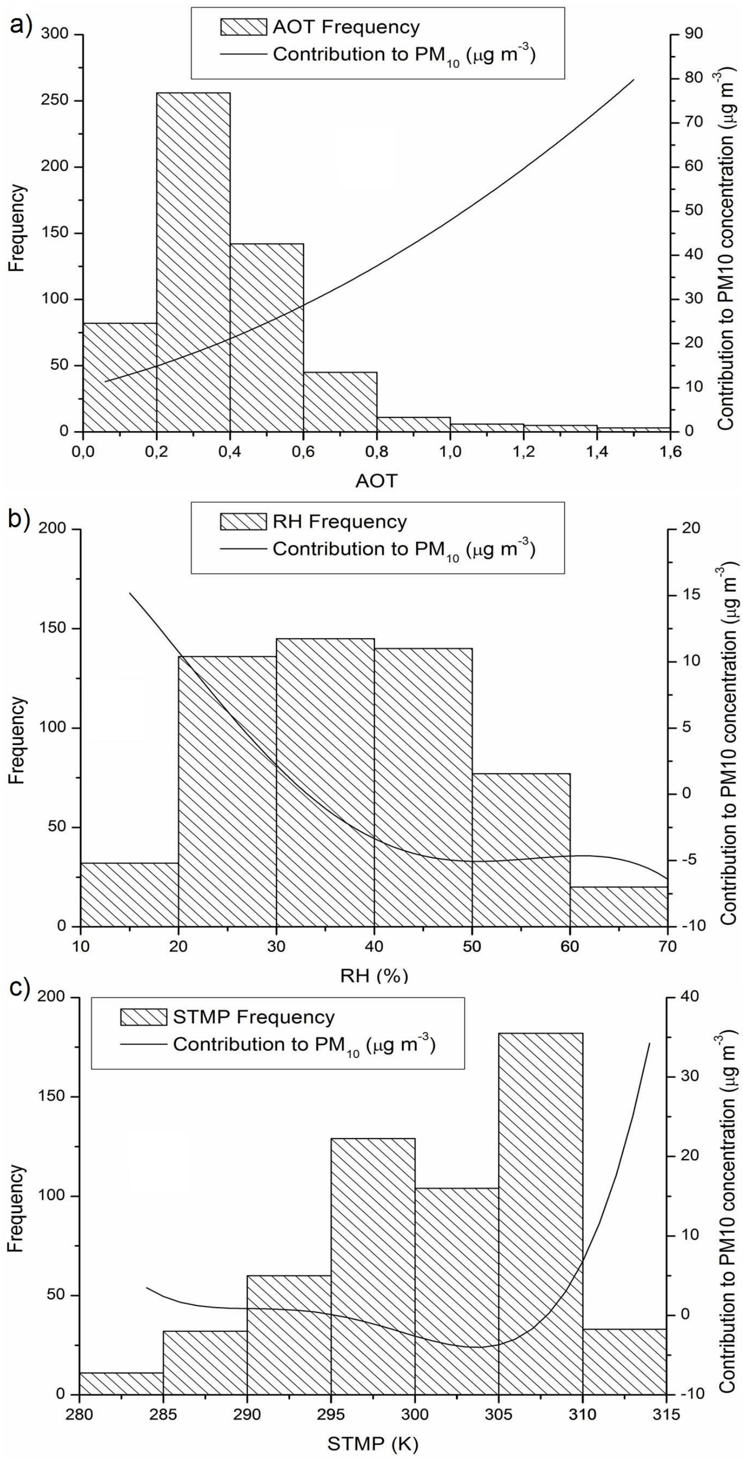

Figure B.2: Contributions of AOT (a), RH (b) and STMP (c), in total PM10 (μg m^{-3}) and corresponding histograms, showing their distribution during the period examined.

Table B.3: Multiple regression equations derived using MODIS AOT and meteorological parameters.

MODIS regression equations
Linear
$\mathrm{PM10} = 50.00\ \mathrm{AOT} - 0.58\ \mathrm{RH} - 0.37\ \mathrm{STMP} + 157.54$
Non–Linear
$\mathrm{PM10} = 17.2\ \phi_1(\mathrm{AOT}) + 18.5\ \phi_2(\mathrm{RH}) + 19.3\ \phi_3(\mathrm{STMP})$ $\phi_1(\mathrm{AOT}) = \mathrm{AOT}^2 + 1.2\mathrm{AOT} + 1.99$ $\phi_2(\mathrm{RH}) = -6 \times 10^{-7}\mathrm{RH}^4 + 9 \times 10^{-5}\mathrm{RH}^3 - 4 \times 10^{-3}\mathrm{RH}^2 + 2 \times 10^{-2}\mathrm{RH} + 1$ $\phi_3(\mathrm{STMP}) = 2 \times 10^{-5}\mathrm{STMP}^4 - 3 \times 10^{-2}\mathrm{STMP}^3 + 11.5\mathrm{STMP}^2$ $-2.3 \times 10^3\mathrm{STMP} + 1.7 \times 10^5$

ϕ_2(RH) in the PM10 estimation, whereby RH values ranging between 50% and 70% induce a reduction in PM10 concentration of about 5 µg m^{-3}. For similar reasons, low RH values are expected to have an increasing effect in PM10 concentration, as shown in Figure B.2b.

Although the inclusion of STMP in a linear relationship with PM10 slightly improved the overall correlation, as mentioned above, the non–linear relationship between PM10 and STMP is crucial for the performance of the model: including only ϕ_1(AOT) and ϕ_2(RH) in the PM10 estimation, the coefficient of determination increases to 0.61, whereas this coefficient increases to 0.67 if STMP is also included. The polynomial function of STMP, given in Table B.3, implies a rapid increase in PM10 with the temperature increase, especially for temperatures higher than 310 K, which occur only in summer. This PM10 dependence on temperature should be attributed to the effects of enhanced emission of particles from surface, and accelerated secondary particle formation in the atmosphere, when the air temperature increases (Gupta and Christopher, 2009a). However, as the histogram in Figure B.2c indicates, the contribution of STMP to PM10 is minimal in the majority of cases.

By implementing a K–Index threshold of 297 K, and using only values greater than this threshold (representing higher static instability), the correlation between station measurements and predicted PM10 is also improved, while the RMSE is slightly increased (last row in Table B.2). This result illustrates that better aerosol vertical mixing improves the correlation with the PM10 measured at the surface, in general agreement with Gupta and Christopher (2009a), who showed that an increased boundary layer height, corresponding to increased aerosol vertical mixing, results in better correlations with in situ PM2.5 measurements. K–Index is related to the atmospheric stability and therefore to the vertical mixing, since the height of the boundary layer increases in unstable conditions; however due to the turbulent movements that are permanent in the surface layer, the atmospheric instability favors also the horizontal (within the 10 km × 10 km grid cell of the MODIS–derived AOT spatial distribution) aerosol mixing. Therefore, better correlation of satellite observations with in–situ PM10 measurements are expected in case of unstable conditions, as shown in Table B.2 for high K–Index values.

B.2.2 Multiple regression analysis using MERIS and AATSR synergy derived AOT, supported by observations from MODIS

The same stepwise procedure, described in Section B.2.1, was used in the case of MERIS/AATSR synergy derived AOT and MODIS–derived STMP, RH and K–Index. Table B.4 shows the R^2 and RMSE results of the stepwise validation for linear and non–linear regression, while Table B.5 shows the linear and non–linear relationships yielding the best correlation results.

Table B.4: Determination coefficient (R^2) and RMSE results after stepwise implementation of MERIS/AATSR AOT and MODIS–derived parameters.

MERIS/AATSR	Linear Regression	
	R^2	RMSE (µg m^{-3})
AOT	0.37	9.2
AOT, RH	0.45	8.2
AOT, RH, STMP	0.45	8.3
	Non–Linear Regression	
AOT, RH, STMP	0.62	8.2
AOT, RH, STMP, K–index≥297 K	0.69	8.3

Although the stepwise validation results of Table B.4 show a poorer performance of the MERIS/AATSR synergy AOT, compared to MODIS AOT, which can be partially attributed to the time difference between the two satellites, the overall behavior of the linear approach is similar: AOT is the most important parameter in predicting PM10, with RH significantly improving the correlation and STMP yielding no significant improvement. A major difference arises when the K–Index threshold is implemented: the results are

Table B.5: Multiple regression equations derived using MERIS/AATSR AOT and MODIS meteorological parameters.

MERIS/AATSR regression equations
Linear
$\mathrm{PM10} = 55.17\ \mathrm{AOT} - 0.36\ \mathrm{RH} - 0.14\ \mathrm{STMP} + 82.14$
Non–Linear
$\mathrm{PM10} = 10.1\ \theta_1(\mathrm{AOT}) + 10.5\ \theta_2(\mathrm{RH}) - 2.9\ \theta_3(\mathrm{STMP})$
$\theta_1(\mathrm{AOT}) = 45.3\mathrm{AOT}^3 - 21.0\mathrm{AOT}^2 + 3.6\mathrm{AOT} + 39.4$
$\theta_2(\mathrm{RH}) = -1.3 \times 10^{-6}\mathrm{RH}^4 + 2.3 \times 10^{-4}\mathrm{RH}^3 - 0.014\mathrm{RH}^2 + 0.3\mathrm{RH} - 1.4$
$\theta_3(\mathrm{STMP}) = -7.4 \times 10^{-5}\mathrm{STMP}^3 + 0.065\mathrm{STMP}^2 - 19.1\mathrm{STMP} + 1858$

improved for K–Index values lower than the threshold, which correspond to atmospheric static stability, thus trapping of aerosols near the surface. A possible explanation of this opposite effect can be attributed to the higher spatial resolution of MERIS/AATSR AOT compared to MODIS AOT, which is the only difference between the two data sets, since, as previously discussed, the aerosol mixing in three–dimensional, low spatial resolution satellite–derived columnar AOT (such as MODIS AOT) will better correlate with surface PM under high aerosol mixing conditions, as has been also reported by Gupta and Christopher (2009a). However, as the spatial resolution of the satellite derived AOT product increases (MERIS/AATSR synergy derived AOT), the diffusion of aerosols in all directions is expected to reduce the correlation between the satellite derived AOT and the in–situ measured PM10, as shown in Table B.4.

B.2.3 Seasonal variation of MODIS–derived PM10 over Athens

Using the non–linear equation for the evaluation of PM10 derived from MODIS observations, daily maps of PM10 concentration over the broader area of Athens were produced for the period 2007–2010, calculating also the corresponding seasonal means. Figures B.3a, B.3b and B.3c feature the spatial distribution of the mean PM10 concentration during spring, summer and autumn, respectively. The coast line and the central municipality borders of the Athens urban area are also illustrated as black lines. The lowest PM10 values were found for winter, however, due to the enhanced cloud cover over Athens during winter, and the corresponding lack of MODIS derived AOT data, the few PM10 values found for winter could not ensure the representativeness of the corresponding seasonal mean value. For this reason, the winter mean PM10 values are not shown in Figure B.3.

The main PM10 characteristics shown in Figure B.3 are the intra–annual variation in its values, combined with an almost identical spatial distribution pattern in every season. The largest PM10 concentrations are found during summer over the entire area, while they are reduced during spring and autumn, obtaining even smaller values during winter (not shown here). This seasonal variation should be attributed to the prevailing weather conditions: increased insolation during summer favors the presence of PM10, the concentration of which is mainly reduced by dry deposition, while increased precipitation during the other seasons removes airborne particles (both wet and dry deposition). Figure B.3 also shows that PM10 concentrations are always higher in the central urban area of Athens, compared to the suburban areas, especially the south coastal area. However, the highest concentrations are found in the industrial areas of Elefsina and Thriasion located northwest. PM10 concentrations in these areas are always higher than the respective concentrations found at the city center.

B.3 Summary and conclusions

Multiple regression equations for the estimation of surface PM10 concentration over the broader area of Athens, Greece, were developed, based on satellite derived observations and in situ PM10 measurements.

Satellite parameters included AOT from MODIS and the MERIS/AATSR synergy, as well as RH, STMP and K–Index from MODIS. Both linear and non–linear equations were tested, showing that PM10 is better approximated using non–linear relationships. Stepwise validation revealed the relative importance of the parameters used, with AOT being the most important factor, followed by RH and STMP. Implementation of a K–Index threshold, as a proxy to aerosol vertical mixing height, resulted in promising outcomes, although the dependence on the spatial resolution should be further investigated.

Results based on the MERIS/AATSR synergy AOT are also promising, especially in view of the forthcoming ESA's Sentinel–3 satellite mission (Berger et al., 2012). The synergistic use of the Sea and Land Surface Temperature Radiometer (SLSTR) and the Ocean and Land Color Instrument (OLCI), on board Sentinel–3 satellite, is expected to provide improved AOT, RH, STMP and K–Index (or similar parameter) values. Furthermore, the Sentinel–3 series is expected to provide operational frequent observations, increasing its potential to support local scale studies related to urban

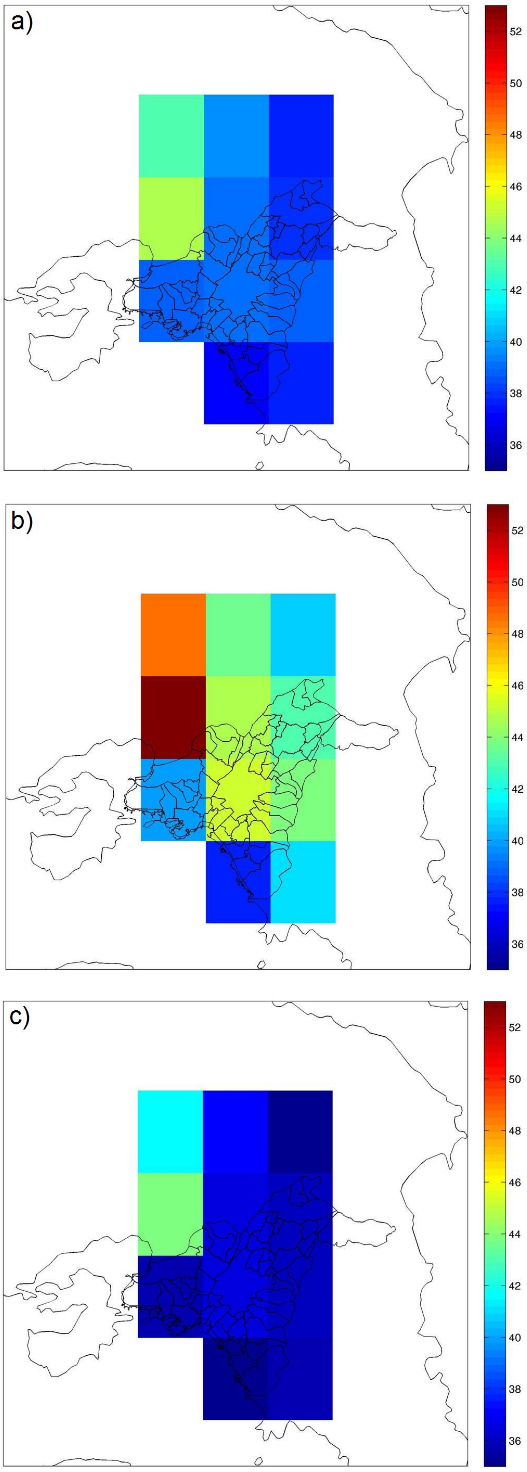

Figure B.3: Spatial distribution of the seasonal mean PM10 concentration (µg m^{-3}) over the broader area of Athens, during spring (a), summer (b) and autumn (c). The coast line and the central municipality borders are shown in black lines.

planning and public health.

Bibliography

Atkinson, R. W., Anderson, H. R., Sunyer, J., Ayres, J., Baccini, M., Vonk, J. M., Boumghar, A., Forastiere, F., Forsberg, B., Touloumi, G., Schwartz, J., and Katsouyanni, K.: Acute effects of particulate air pollution on respiratory admissions: results from APHEA 2 project. Air Pollution and Health: a European Approach, American Journal of Respiratory and Critical Care Medicine, 164, 1860–1866, 2001.

Ballester, F., Estarlich, M., Iñiguez, C., Llop, S., Ramón, R., Esplugues, A., Lacasaña, M., and Rebagliato, M.: Air pollution exposure during pregnancy and reduced birth size: a prospective birth cohort study in Valencia, Spain, Environmental Health, 9, 6, doi:10.1186/1476-069X-9-6, 2010.

Bell, M. L., Ebisu, K., and Belanger, K.: Ambient Air Pollution and Low Birth Weight in Connecticut and Massachusetts, Environmental Health Perspectives, 115, 1118–1124, 2007.

Berger, M., Moreno, J., Johannessen, J. A., Levelt, P. F., and Hanssen, R. F.: ESA's sentinel missions in support of Earth system science, Remote Sensing of Environment, 120, 84–90, doi:10.1016/j.rse.2011.07.023, 2012.

Breiman, L. and Friedman, J. H.: Estimating Optimal Transformations for Multiple Regression and Correlation, Journal of The American Statistical Association, 80, 580–598, 1985.

Brockmann-Consult: The Earth Observation Toolbox and Development Platform BEAM, 2011.

Chrysoulakis, N., Spiliotopoulos, M., Domenikiotis, C., and Dalezios, N. R.: Towards monitoring of regional atmospheric instability through MODIS/AQUA images, in: N. R. Dalezios and H. Dobesch (Editors): Proceedings of the International Symposium on GIS and Remote Sensing: Environmental Applications, pp. 155–166, 2003.

Dominici, F., Peng, R. D., Bell, M. L., Pham, L., McDermott, A., Zeger, S. L., and Samet, J. M.: FIne particulate air pollution and hospital admission for cardiovascular and respiratory diseases, The Journal of the American Medical Association, 295, 1127–1134, doi:10.1001/jama.295.10.1127, 2006.

Engel-Cox, J. A., Hoff, R. M., Rogers, R., Dimmick, F., Rush, A. C., Szykman, J. J., Al-Saadi, J., Chu, D. A., and Zell, E. R.: Integrating lidar and satellite optical depth with ambient monitoring for 3–dimensional particulate characterization, Atmospheric Environment, 40, 8056–8067, doi: 10.1016/j.atmosenv.2006.02.039, 2006.

Florou, K. K., Pikridas, M., and Pandis, S. N.: Wintertime Air Pollution and the Greek Financial Crisis, in: EGU General Assembly Conference Abstracts, vol. 15 of *EGU General Assembly Conference Abstracts*, p. 7091, 2013.

Franklin, M., Zeka, A., and Schwartz, J.: Association between PM2.5 and all–cause and specific–cause mortality in 27 US communities, Journal of Exposure Science and Environmental Epidemiology, 17, 279–287, doi:10.1038/sj.jes.7500530, 2006.

Friedman, J. H. and Stuetzle, W.: Projection Pursuit Regression, Journal of the American Statistical Association, 76, 817–823, 1981.

Gent, J. F., Koutrakis, P., Belanger, K., Triche, E., Holford, T. R., Bracken, M. B., and Leaderer, B. P.: Symptoms and Medication Use in Children with Asthma and Traffic–Related Sources of Fine Particle Pollution, Environmental Health Perspectives, 117, doi:10.1289/ehp.0800335, 2009.

George, J. J.: Weather forecasting for Aeronautics, Academic Press, New York, pp. 409-415, 1960.

Gupta, P. and Christopher, S. A.: Particulate matter air quality assessment using integrated surface, satellite, and meteorological products: Multiple regression approach, Journal of Geophysical Research, 114, 1–13, doi:10.1029/2008JD011496, 2009a.

Gupta, P. and Christopher, S. A.: Particulate matter air quality assessment using integrated surface, satellite, and meteorological products: 2. A neural network approach, Journal of Geophysical Research, 114, 1–14, doi:10.1029/2008JD011497, 2009b.

Gupta, P., Christopher, S. A., Wang, J., Gehrig, R., Lee, Y., and Kumar, N.: Satellite remote sensing of particulate matter and air quality assessment over global cities, Atmospheric Environment, 40, 5880–5892, doi:10.1016/j.atmosenv.2006.03.016, 2006.

Haklander, A. J. and Van Delden, A.: Thunderstorm predictors and their forecast skill for the Netherlands, Atmospheric Research, 67–68, 273–299, 2003.

Kappos, A. D., Bruckmann, P., Eikmann, T., Englert, N., Heinrich, U., Höppe, P., Koch, E., Krause, G. H. M., Kreyling, W. G., Rauchfuss, K., Rombout, P., Schulz-Klemp, V., Thiel, W. R., and Wichmann, H. E.: Health effects of particles in ambient air, International Journal of Hygiene and Environmental Health, 207, 399–407, 2004.

Katsouyanni, K.: Short–term health effects of particulate air pollution with special reference to the needs of southern European countries, Chemical Industry and Chemical Engineering Quarterly, 18, 675–679, doi:10.2298/CICEQ120104110K, 2012.

Kitanidis, P. K.: Introduction to Geostatistics: Applications in Hydrogeology, Stanford–Cambridge Program, Cambridge University Press, 1997.

Kloog, I., Koutrakis, P., Coull, B. A., Lee, H. J., and Schwartz, J.: Assessing temporally and spatially resolved $PM_{2.5}$ exposures for epidemiological studies using satellite aerosol optical depth measurements, Atmospheric Environment, 45, 6267–6275, doi:10.1016/j.atmosenv.2011.08.066, 2011.

Kloog, I., Nordio, F., Coull, B. A., and Schwartz, J.: Incorporating Local Land Use Regression And Satellite Aerosol Optical Depth In A Hybrid Model Of Spatiotemporal PM2.5 Exposures In The Mid–Atlantic States, Environmental Science & Technology, 46, 11 913–11 921, doi:10.1021/es302673e, 2012.

Koelemeijer, R. B. A., Homan, C. D., and Matthijsen, J.: Comparison of spatial and temporal variations of aerosol optical thickness and particulate matter over Europe, Atmospheric Environment, 40, 5304–5315, doi:10.1016/j.atmosenv.2006.04.044, 2006.

Kumar, N., Chu, A., and Foster, A.: An empirical relationship between PM2.5 and aerosol optical depth in Delhi Metropolitan, Atmospheric Environment, 41, 4492–4503, doi:10.1016/j.atmosenv.2007.01.046, 2007.

Lee, H. J., Liu, Y., Coull, B. A., Schwartz, J., and Koutrakis, P.: A novel calibration approach of MODIS AOD data to predict $PM_{2.5}$ concentrations, Atmospheric Chemistry and Physics, 11, 7991–8002, doi: 10.5194/acp-11-7991-2011, 2011.

Lee, H. J., Coull, B. A., Bell, M. L., and Koutrakis, P.: Use of satellite–based aerosol optical depth and spatial clustering to predict ambient PM2.5 concentrations, Environmental Research, 118, 8–15, doi:10.1016/j.envres.2012.06.011, 2012.

Liu, Y., Sarnat, J. A., Kilaru, V., Jacob, D. J., and Koutrakis, P.: Estimating Ground–Level PM 2.5 in the Eastern United States Using Satellite Remote Sensing, Environmental Science & Technology, 39, 3269–3278, doi:10.1021/es049352m, 2005.

North, P., Grey, W., Heckel, A., Fischer, J., Preusker, R., and Brockmann, C.: MERIS/AATSR Synergy Algorithms for Cloud Screening, Aerosol Retrieval, and Atmospheric Correction. Algorithm Theoretical Basis Document Land Aerosol and Surface Reflectance ATBD. ESRIN Contract No. 21090/07/I–LG., 2009.

Paciorek, C. J., Liu, Y., Moreno-Macias, H., and Kondragunta, S.: Spatiotemporal associations between GOES aerosol optical depth retrievals and ground–level PM2.5, Environmental science & technology, 42, 5800–5806, 2008.

Pope, C. A. I., Burnett, R. T., Thun, M. J., Calle, E. E., Krewski, D., Ito, K., and Thurston, G. D.: Lung cancer, cardiopulmonary mortality, and long–term exposure to fine particulate air pollution, The Journal of the American Medical Association, 287, 1132–1141, doi:10.1001/jama.287.9.1132, 2002.

Retalis, A. and Sifakis, N.: Urban aerosol mapping over Athens using the differential textural analysis (DTA) algorithm on MERIS–ENVISAT data, ISPRS Journal of Photogrammetry and Remote Sensing, 65, 17–25, doi: 10.1016/j.isprsjprs.2009.08.001, 2010.

Rohen, G. J., von Hoyningen-Huene, W., Kokhanovsky, A., Dinter, T., Vountas, M., and Burrows, J. P.: Retrieval of aerosol mass load (PM_{10}) from MERIS/Envisat top of atmosphere spectral reflectance measurements over Germany, Atmospheric Measurement Techniques, 4, 523–534, doi: 10.5194/amt-4-523-2011, 2011.

Schaap, M., Apituley, A., Timmermans, R. M. A., Koelemeijer, R. B. A., Leeuw, G. D., and Unit, C. C.: Exploring the relation between aerosol optical depth and PM2.5 at Cabauw , the Netherlands, Atmospheric Chemistry and Physics, pp. 909–925, doi:10.5194/acp-9-909-2009, 2009.

Themistocleous, K., Hadjimitsis, D. G., Retalis, A., and Chrysoulakis, N.: The development of air quality indices through image–retrieved AOT and PM10 measurements in Limassol Cyprus, In: Proceedings of SPIE Remote Sensing 2012: Remote Sensing of Clouds and the Atmosphere XVII and Lidar Technologies, Techniques, and Measurements for Atmospheric Remote Sensing VIII., Proc. of SPIE Vol., 85 340B–85 340B–13, doi:10.1117/12.974701, 2012.

van de Kassteele, J., Koelemeijer, R., Dekkers, A., Schaap, M., Homan, C., and Stein, A.: Statistical mapping of PM10 concentrations over Western Europe using secondary information from dispersion modeling and MODIS satellite observations, Stochastic Environmental Research and Risk Assessment, 21, 183–194, doi:10.1007/s00477-006-0055-4, 2006.

van Donkelaar, A., Martin, R. V., and Park, R. J.: Estimating ground–level PM2.5 using aerosol optical depth determined from satellite remote sensing, Journal of Geophysical Research, 111, 1–10, doi:10.1029/2005JD006996, 2006.

van Donkelaar, A., Martin, R. V., Levy, R. C., da Silva, A. M., Krzyzanowski, M., Chubarova, N. E., Semutnikova, E., and Cohen, A. J.: Satellite-based estimates of ground-level fine particulate matter during extreme events: A case study of the Moscow fires in 2010, Atmospheric Environment, 45, 6225–6232, doi:10.1016/j.atmosenv.2011.07.068, 2011.

Yap, X. Q. and Hashim, M.: A robust calibration approach for PM_{10} prediction from MODIS aerosol optical depth, Atmospheric Chemistry and Physics, 13, 3517–3526, doi:10.5194/acp-13-3517-2013, 2013.

List of Figures

List of Tables